1-1-2016

Magnetic Fields in Molecular Clouds: The Blastpol and Blast-Tng Experiments

Nicholas Galitzki
University of Pennsylvania, galitzki@sas.upenn.edu

Magnetic Fields in Molecular Clouds: The Blastpol and Blast-Tng Experiments

Abstract
The Balloon-borne Large Aperture Submillimeter Telescope for Polarimetry (BLASTPol) was a suborbital experiment designed to map magnetic fields in order to study their role in star formation processes. BLASTPol made detailed polarization maps of a number of molecular clouds during its successful flight from Antarctica in 2012. The data reduction and analysis efforts over the three years following the flight have produced a number of important scientific results. The next-generation BLAST instrument (BLAST-TNG) will build off the success of the previous experiment and continue its role as a unique instrument and a test bed for new technologies. With a 16-fold increase in mapping speed, BLAST-TNG will make larger and deeper maps. Major improvements include a 2.5 m carbon fiber mirror that is 40% wider than the BLASTPol mirror and more than 3000 polarization sensitive detectors. BLAST-TNG will observe in the same three bands as BLASTpol at 250, 350, and 500 microns. The telescope will serve as a pathfinder project for microwave kinetic inductance detector (MKID) technology, as applied to feedhorn coupled submillimeter detector arrays. The liquid helium cooled cryostat will have a 28-day hold time and will utilize a closed-cycle 3He refrigerator to cool the detector arrays to 270 mK. This will enable a detailed mapping of more targets with higher polarization resolution than any other submillimeter experiment to date. My thesis describes the 2012 instrument and results while also outlining the motivation for BLAST-TNG and the instrumental design and initial testing.

Degree Type
Dissertation

Degree Name
Doctor of Philosophy (PhD)

Graduate Group
Physics & Astronomy

First Advisor
Mark Devlin

Second Advisor
Gary Bernstein

Keywords
balloon-borne, cryogenics, instrumentation, interstellar medium, polarimetry, submillimeter

Subject Categories
Astrophysics and Astronomy

MAGNETIC FIELDS IN MOLECULAR CLOUDS: THE BLASTPOL AND BLAST-TNG EXPERIMENTS

Nicholas Galitzki

A DISSERTATION

in

Physics and Astronomy

Presented to the Faculties of the University of Pennsylvania

in Partial Fulfillment of the Requirements for the degree of Doctor of Philosophy

2016

Supervisor of Dissertation

_____

Mark J. Devlin, Professor of Astronomy and Astrophysics

Graduate Group Chairperson

_____

Marija Drndic, Professor of Physics and Astronomy

Dissertation Committee:

Masao Sako, Associate Professor of Physics and Astronomy

Gary Bernstein, Professor of Astronomy and Astrophysics

James Aguirre, Assistant Professor of Physics and Astronomy

Joshua Klein, Professor of Physics and Astronomy

Acknowledgements

Thank you to the many people who have been there as advisers, colleagues, friends, and family throughout my PhD studies, you all made the process that much easier to get through and I greatly appreciate it.

I have been incredibly lucky to have such a great adviser, Mark Devlin, and to have had the opportunity to work in his research group. The advice he has provided over the years has been invaluable in shaping me as a researcher and has allowed me to launch a strong career in astrophysics. I would also like to thank Jeff Klein who is ever ready to share his vast depths of knowledge and puns with me and all students in our lab to help us achieve our goals. Also, I never would have gotten through it all without my favorite Italian postdoc, Elio!

I would also like to thank my colleagues at collaborating universities who served as mentors during my graduate studies, especially Barth Netterfield, Giles Novak, and Philip Mauskopf.

A special mention to my fantastic classmates from the 2010 entering year, it's been real. A special thanks to T.J. McSorley and Mark Giovinazzi from Drexel University for their help and many hours of hard work on getting Layla ready.

I also thank the businesses that have kept me fed and caffeinated through the years. Picnic for its consistent good eats, Joe for your steady supply of coffee, (Mexican) Mikey's for much needed happy hours, and Nelson's for late night eats and a steady supply of gummy candies for sugar fueled SolidWorks sessions.

Lastly, thanks to my coffee mug that saw me through my thesis writing as shown in Figure 0.1 along with all the coffee shops in which I spent many days writing this thesis as described in Table 0.1.

Figure 0.1: The coffee mug that got me through writing my thesis with regular doses of delicious caffeine. During the approximately three and a half months of writing my thesis I averaged four cups of coffee or tea each day from the 20 oz. vessel. Cummulatively I drank nearly 250 liters out of the coffee mug which happily coincides with the volume of the helium tank I designed.

Café	Coffee (Out of 5)	Food (Out of 5)	Ambiance (Out of 5)	WiFi	Plugs
Ants Pants	4.5 ± 0.3	$5.0^{+0.0}_{-0.2}$	4.1 ± 0.3	Sometimes	Poor
Charter House	4.1 ± 0.4	3.5 ± 0.5	4.3 ± 0.5	Yes	Good
Elixr Coffee	4.4 ± 0.4	4.1 ± 0.4	4.4 ± 0.4	Yes	Good
Good Karma (Walnut St)	3.1 ± 10.9	4.0 ± 0.5	3.0 ± 0.2	Yes	Good
Good Karma (22nd St)	3.0 ± 1.0	4.0 ± 0.5	4.5 ± 0.3	Yes	Excellent
Good Karma (South St)	3.0 ± 1.0	4.0 ± 0.5	3.9 ± 0.3	Yes	Good
Green Line (Clark Park)	3.0 ± 1.0	4.0 ± 0.5	$5.0^{+0.0}_{-0.3}$	None	Good
Green Line (Powelton St.)	3.5 ± 0.5	4.0 ± 0.5	4.2 ± 0.5	Yes	OK
Green Line (Locust St.)	3.0 ± 1.0	4.0 ± 0.5	3.8 ± 0.4	Yes	OK
Green Line (40th St)	3.0 ± 1.0	4.0 ± 0.5	3.9 ± 0.3	Yes	Excellent
La Va	3.8 ± 0.6	4.3 ± 0.4	4.6 ± 0.3	Sometimes	Poor
Little Spoon	4.4 ± 0.3	4.7 ± 0.3	4.3 ± 0.3	Yes	Good
Magpie	4.4 ± 0.5	4.8 ± 0.2	4.1 ± 0.5	Yes	Poor
Mugshots	4.8 ± 0.2	4.0 ± 0.5	4.5 ± 0.3	Yes	Good
Picnic	3.0 ± 1.0	4.8 ± 0.2	4.2 ± 0.3	Unknown	Poor
Rival Bros	4.8 ± 0.2	3.1 ± 1.0	4.1 ± 0.4	Unknown	Good
Sabrinas (Powelton St.)	4.4 ± 0.3	$5.0^{+0.0}_{-0.2}$	3.9 ± 0.3	Yes	Excellent
Toast	4.1 ± 0.5	4.1 ± 0.5	3.6 ± 0.2	Yes	Good
Ultimo	4.2 ± 0.6	3.2 ± 0.4	4.2 ± 0.3	Yes	Poor
Waterfront Gourmet	3.2 ± 1.0	4.2 ± 0.5	3.5 ± 0.5	Sometimes	Good

Table 0.1: A brief overview of coffee shops in which I wrote my thesis. Special mentions include Mugshot's couches, Good Karma's dollar coffee refills, Green Line (Clark Park)'s excellent location, and Sabrina's (Powelton) great food.

Layla

What'll you do when you get lonely
And nobody's waiting by your side?
You've been running and hiding much too long
You know it's just your foolish pride

Layla, you've got me on my knees
Layla, I'm begging, darling please
Layla, darling won't you ease my worried mind

I tried to give you consolation
When your old man had let you down
Like a fool, I fell in love with you,
Turned my whole world upside down

Layla, you've got me on my knees
Layla, I'm begging, darling please
Layla, darling won't you ease my worried mind

Let's make the best of the situation
Before I finally go insane
Please don't say I'll never find a way
And tell me all my love's in vain

Layla, you've got me on my knees
Layla, I'm begging, darling please
Layla, darling won't you ease my worried mind

Layla (Layla) you've got me on my knees
Layla, I'm begging, darling please
Layla, darling won't you ease my worried mind
-Dominos (1970)

ABSTRACT

MAGNETIC FIELDS IN MOLECULAR CLOUDS: THE BLASTPOL AND BLAST-TNG EXPERIMENTS

Nicholas Galitzki

Mark J. Devlin

The Balloon-borne Large Aperture Submillimeter Telescope for Polarimetry (BLASTPol) was a suborbital experiment designed to map magnetic fields in order to study their role in star formation processes. BLASTPol made detailed polarization maps of a number of molecular clouds during its successful flight from Antarctica in 2012. The data reduction and analysis efforts over the three years following the flight have produced a number of important scientific results. The next-generation BLAST instrument (BLAST-TNG) will build off the success of the previous experiment and continue its role as a unique instrument and a test bed for new technologies. With a 16-fold increase in mapping speed, BLAST-TNG will make larger and deeper maps. Major improvements include a 2.5 m carbon fiber mirror that is 40% wider than the BLASTPol mirror and more than 3000 polarization sensitive detectors. BLAST-TNG will observe in the same three bands as BLASTpol at 250, 350, and 500μm. The telescope will serve as a pathfinder project for microwave kinetic inductance detector (MKID) technology, as applied to feedhorn coupled submillimeter detector arrays. The liquid helium cooled cryostat will have a 28-day hold time and will utilize a closed-cycle ^{3}He refrigerator to cool the detector arrays to 270 mK. This will enable a detailed mapping of more targets with higher polarization resolution than any other submillimeter experiment to date. My thesis describes the 2012 instrument and results while also outlining the motivation for BLAST-TNG and the instrumental design and initial testing.

Contents

List of Tables

List of Figures

Chapter 1

Introduction

Understanding the star formation process is an important field of modern astrophysics but it lacks key observational evidence to resolve the role of turbulence and magnetic fields in the early stages of cloud collapse. The The Balloon-borne Large Aperture Submillimeter Telescope for Polarimetry (BLASTPol) and The Balloon-borne Large Aperture Submillimeter Telescope - The Next Generation (BLAST-TNG) experiments examine the direction and magnitude of polarized light emitted by elongated dust grains that are aligned with the local magnetic field. They observe in the submillimeter part of the spectrum over three wavelength bands centered on 250, 350, and 500 μm to proved spectral coverage across the blackbody peaks of cold molecular clouds. From observing magnetic fields and the spectral response of polarized light in star forming regions we can better understand the role that magnetic fields play in the stellar nurseries of the Milky Way.

The data from the 2012 flight of BLASTPol has greatly increased our understanding of the regions we observed (see Fissel et al., 2015). For the 2012 data reduction I led the effort to deconvolve the electronics signal from the time stream, flat field the detector response in the time ordered data, and a variety of other important analysis tasks. I have also led a number of the scientific analysis efforts such as working with

complementary data from the Herschel space observatory which has proved incredibly useful in getting the most out of the BLASTPol data. However, BLASTPol only had the capability to observe a handful of targets in depth leaving much to be discovered.

BLAST-TNG is being designed and built with a larger mirror, field of view, and cryostat than BLASTPol allowing for higher resolution imaging, faster scan speeds, and more than twice the cryogenics hold time. It will also be a pathfinder mission for polarization sensitive microwave kinetic inductance detectors (MKIDs), a new detector technology that is very promising for submillimeter astronomy. I have designed and overseen the production and testing of the optics, the cryogenic system, and other components of the instrument. My experience on the BLASTPol 2012 campaign has also proved useful for designing and implementing tests of the instrumental performance to prepare BLAST-TNG for a successful Antarctic campaign and flight in 2017.

I will first describe the scientific case that motivates the experiments in Chapter 2 which describes the properties of dust grain alignment in the interstellar medium (ISM) and how that process allows us to observe magnetic fields in GMC. In chapter 3 I will discuss the status of the BLASTPol instrument when I joined the project along with the subsequent modifications and test that were performed prior to the 2012 flight as well as a description of the flight performance. In Chapter 4 I will describe the data reduction process to get from the time ordered data (TOD) obtained during the flight to fully processed and scientific quality maps that we then used for our primary scientific analysis and results as described in Chapter 5. The results obtained form the 2012 campaign were compelling enough to warrant the funding and construction of a new telescope BLAST-TNG.

The design of BLAST-TNG is described in Chapter 6 with a focus on the portions of the project which I was most directly involved in. Following the design and construction of these components a series of tests were completed and are described

in Chapter 7. Additionally there will be a short description of future work that will be done in the lead up to the launch of BLAST-TNG from Antarctica.

Chapter 2

Magnetic Fields in Molecular Clouds

2.1 Galactic Star Formation

An important goal of modern astrophysics is to understand the star formation process and especially the factors that regulate the star formation rate in molecular clouds and galaxies as a whole. Recent progress includes using observations of dust emission and extinction, which show how core mass distribution correlates with observed stellar mass distribution (Nutter and Ward-Thompson, 2007). There are also many results from the *Herschel* data. One example is evidence that filamentary structures are common in molecular clouds and that higher density filaments preferentially break into pre-stellar cores (André et al., 2010; Hill et al., 2011). However, there are many questions concerning the star-formation process and the evolution of cloud structure that remain to be addressed (McKee and Ostriker, 2007). Examples include whether the lifetimes of molecular clouds and their internal structures are equal to (Vázquez-Semadeni et al., 2006) or larger (Netterfield et al., 2009; Blitz et al., 2007; Goldsmith et al., 2008) than the turbulent crossing time. To have lifetimes longer

than crossing times would require a supporting mechanism to counteract gravity. Current ideas to explain this discrepancy point to a support process that slows the formation and evolution of pre-stellar cores in molecular clouds. The two dominant theories that strive to explain this effect focus on turbulent forces and magnetic fields (McKee and Ostriker, 2007). In the case of turbulence-controlled star formation, motion within the clouds dissipates dense regions before they can reach a critical stage of collapse. Alternatively, magnetic fields could provide support that could affect the collapse process. Numerical simulations have shown magnetic fields in clouds can drastically alter star formation efficiencies and the lifetimes of molecular clouds (Li et al., 2010; Hennebelle et al., 2011). The current consensus leans toward a situation where both processes are important with the relative degree of influence dependent on the environment being studied (Nakamura and Li, 2008, 2011). In order to resolve the relative importance of these two competing mechanisms we need turbulent flow information and measurements of magnetic field orientation and strength.

Knowledge of magnetic fields and their interaction with molecular cloud structure is still fairly limited. Zeeman splitting observations have produced measurements of the field strength along the line of sight, but are limited to bright regions. Optical extinction polarization observations have produced measurements of magnetic field pseudo-vectors, but only in areas of low extinction (Crutcher and Osei, 2010; Falgarone et al., 2008). The most promising method for detecting magnetic fields over large ranges of dust column density is with FIR and submillimeter polarimetry (Hildebrand et al., 2000; Ward-Thompson et al., 2000, 2009). Spinning dust grains preferentially anti-align with the local magnetic field and emit modified blackbody radiation that is polarized orthogonally to the local magnetic field. BLASTPol is the first instrument capable of creating degree-scale polarization maps of molecular clouds with sub-arcminute resolution and a mapping speed that has allowed it to cover multiple targets during each flight. BLASTPol data enables direct compar-

ison between polarization maps and numerical simulations (Ward-Thompson et al., 2000) and shows agreement with previous observations of molecular cloud polarization (Ward-Thompson et al., 2009; Li et al., 2006).

2.2 Magnetic fields in star forming regions

BLASTPol was designed to determine magnetic field structure and how it correlates with molecular cloud features. Theoretical models suggest that if magnetic fields are strong enough to have a significant role in GMC morphology there would be a number of observable effects. In low-density regions, slightly ionized gas which is not gravitationally bound encounters no resistance to flow along field lines but encounters significant resistance perpendicular to field lines (Nagai et al., 1998). The flows along field lines can give rise to the filamentary structure parallel to magnetic fields lines in the lower density regions.

Higher density regions of molecular clouds will preferentially contract along field lines onto self-gravitating sheets creating dense structures that are perpendicular to the magnetic field orientation (Palmeirim et al., 2013). We would therefore expect to observe a correlation between column density contours, as a measure of GMC structure, and the magnetic field direction. With enough data points from a cloud, these two parameters can be examined for correlations that can be compared to predictions from theories and simulations. Extensive work has been done to simulate GMC evolution with varying magnetic fields and turbulent parameters to explore the significance of observations as shown in Figure 2.1 (Soler et al., 2013). By comparing empirical models derived from observations with those generated by simulations, we have a robust method to constrain the role magnetic fields and turbulence play in different star forming regions in our galaxy.

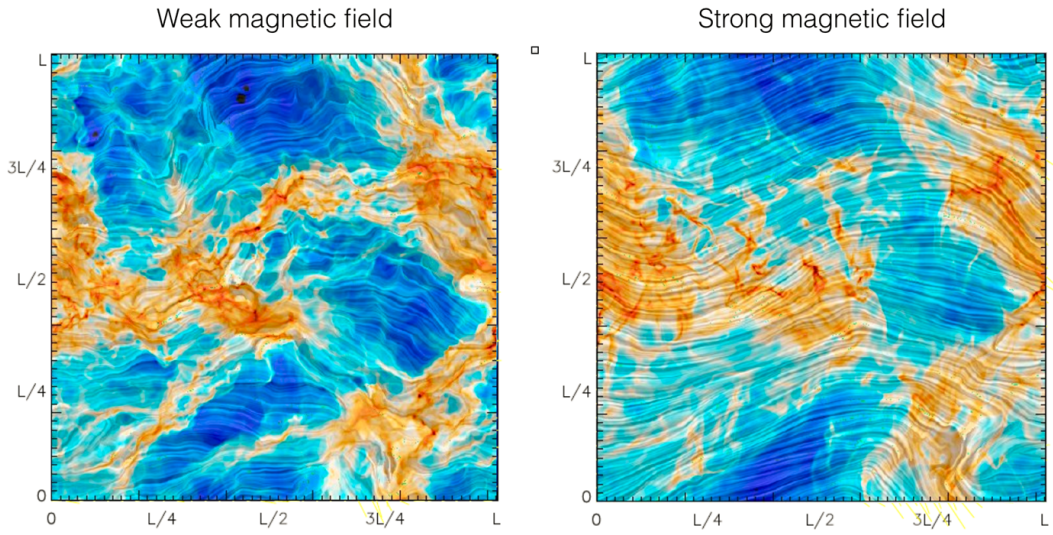

Figure 2.1: Figure from Soler et al. (2013) of simulations of a molecular cloud with a fixed initial turbulent component and a set magnetic field strength that is varied between runs. Color shows the logarithm of the column density along the LOS with higher column density structures in red and lower in blue. A line integral convolution is performed between the column density map and the magnetic field psuedo-vectors which produces the striations (Cabral and Leedom, 1993). Left: The case with a weak magnetic field that is much lower than the turbulent energy. Right: A simulation with a much stronger magnetic field that dominates the turbulent energy. The correlation of field with structure is readily apparent and is the basis on which statistical methods of analysis are constructed to compare observations with simulations.

2.3 Observing Magnetic Fields

Polarization of the ISM was first discovered in visible wavelengths by observing the polarized extinction of starlight by the dust in the ISM which was quickly realized to be from asymmetric grain alignment to local magnetic fields (see Hall, 1949; Hiltner, 1949). Some years later it was predicted that the dust would not only absorb background light but also emit it in the FIR which was confirmed by additional observations (Stein, 1966; Cudlip et al., 1982). Since these series of discoveries the polarization from aligned grains has been probed to high sensitivity in the ultra-violet (UV), visible, infra-red (IR), and FIR in a number of different regions and environments demonstrating the ubiquity of magnetic fields in our galaxy and uncovering

information about the role they play.

Dust grains preferentially align with the local magnetic field and emit polarized light along their long axis which is orthogonal to the local magnetic field, a process described in detail in Section 2.3.1. Submillimeter polarimetry of molecular clouds measures the polarization of light along the LOS through the cloud. By examining the dispersion of vector angles, combined with complementary observations with spectral surveys to determine a velocity dispersion in the cloud, the local magnetic field strength can be estimated using a method pioneered in Chandrasekhar and Fermi (1953) and shown in Equation 2.1 from the same paper.

$$H = \sqrt{\frac{4}{3}\pi\rho}\frac{v}{\alpha} \tag{2.1}$$

Where H is the magnetic field strength, ρ is the density of the diffuse material, v is the root-mean-square velocity of the turbulent motion, and α represents the mean angular deviation of the measured polarization signal. Making actual measurements of the strength is difficult due to the fact that the molecular clouds and ISM are optically thin at submillimeter wavelengths. Experiments sample all populations along the LOS making it difficult to separate out the various components that contribute to the polarized signal. Additionally, calculating field strength requires accurate observations of both the turbulent component and the dispersion of the magnetic field angles of a specific target. This has been done but tends to be difficult on large scales with multiple complex objects, such as across an entire GMC. Measuring the field strength remains a goal of our experiments and can be accomplished by combining our extensive polarization maps with follow up observations of spectral data to determine velocity structure. However, our primary science concentrates on examining correlations of magnetic field direction with cloud characteristics such as temperature and density structure.

A number of prior experiments have mapped magnetic field pseudo-vectors using submillimeter polarimetry. Notable earlier efforts include the Submillimeter Common-User Bolometer Array (SCUBA), Hertz, and the Submillimeter Polarimeter for Antarctic Remote Observing (SPARO) instruments (Matthews et al., 2009; Dotson et al., 2010; Li et al., 2006). They were able to make maps of magnetic fields in the galaxy, but only over relatively small regions as ground based observations tend to be limited in sensitivity by atmospheric effects. More recently the *Planck* project[1] has released all sky maps of polarized emission from galactic dust which has made massive contributions to the field of study as well as providing a useful calibration for future experiments (Planck Collaboration et al., 2015). However, all of these experiments have either lacked the resolution to make sub-arcminute resolution maps of magnetic fields or lacked the sensitivity to map entire GMC providing the motivation for an additional experiment to fill this experimental gap that will prove useful in completing the picture of star formation in our galaxy and determining the properties of the polarized dust emission spectra.

2.3.1 The Theory of Radiative Alignment Torque

A number of complementary physical processes allow us to observe magnetic fields with submillimeter polarimetry. The first is the existence of dust grains in the ISM that have a population of grains large enough to absorb light from the UV to the IR and re-emit in the submillimeter through FIR. The dust grains must then spin up and align to the local magnetic field which is predicted to occur through a process called Radiative Alignment Torque (RAT). The RAT model is currently the favored mechanism for dust grain alignment as it agrees the best with observations over a wide

[1] *Planck* (`http://www.esa.int/Planck`) is a project of the European Space Agency (ESA) with instruments provided by two scientific consortia funded by ESA member states and led by Principal Investigators from France and Italy, telescope reflectors provided through a collaboration between ESA and a scientific consortium led and funded by Denmark, and additional contributions from NASA (USA).

range of environments (see Andersson et al., 2015). There are other alignment models that work in certain types of regions but struggle to explain all of the alignment effects that have been observed.

The RAT grain alignment procedure is best described in two stages. The first stage, called internal alignment, aligns the angular momentum vector of the dust grain with the grain's primary short axis. The second part of the process brings the angular momentum axis of the grain into alignment with the magnetic field direction. The combination of the two processes yields the observed polarized emission in the FIR from the grain's long axis perpendicular to the local magnetic field.

In the RAT method, incident light on the surface of the dust grain creates a torque on the grain that directly leads to both processes occurring. The requirements for this torque to be generated are a helicity in the dust grain's shape that gives the grain a differential absorption cross section between left hand circular polarized light and right hand circular polarized light. Additionally, the incident light needs to be anisotropic or the torques will simply cancel out. For simplicity, this torque is separated into two components, a spin up torque, H, that operates to spin the grain around its principle axis, and an alignment torque, F, that serves to align the grain with the magnetic field as shown in Figure 2.2 (Lazarian, 2007).

Internal alignment occurs due to the Barnett effect (Barnett, 1915) in which the spin of a paramagnetic solid causes free electron's spins to flip and induce magnetic moments in the solid that are aligned with the angular momentum vector. Equation 2.2 describes the effect, where χ is the magnetic susceptibility of the material, γ is the gyromagnetic ratio, and Ω is the angular momentum and the principle variable in the equation.

$$M = \chi\Omega/\gamma \tag{2.2}$$

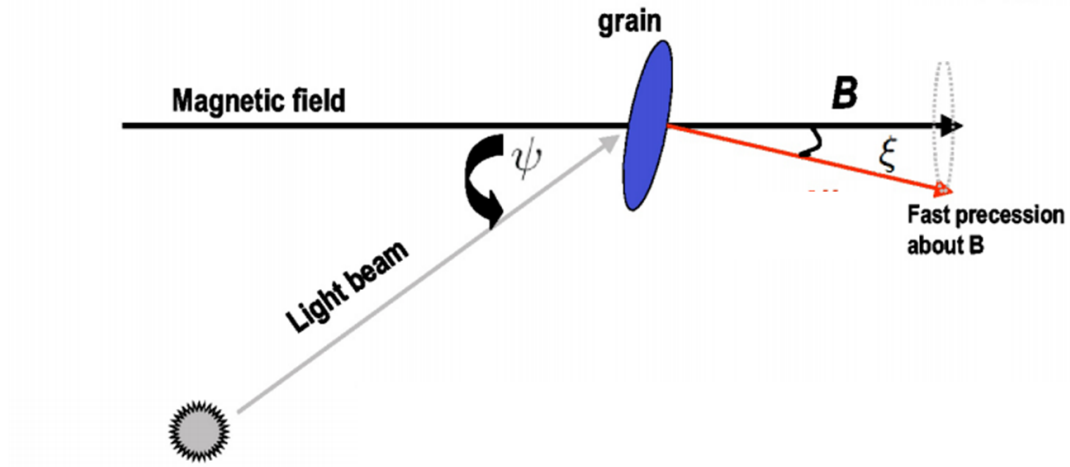

Figure 2.2: Diagram from Lazarian (2008) showing the main components necessary for alignment by radiative torque. An incident light beam hits a dust grain with a helicity that has a different cross section to left hand circular polarized light versus right hand circular polarized light. The incident radiation spins the dust grain around its short axis at which point any dipole moment inherent to the grain precesses around the magnetic field causing alignment with the long axis of the grain perpendicular to the magnetic field direction.

If the grain's angular momentum and principle spin axis are not aligned, the grain's principle axis will precess about the angular momentum vector in the well understood force-free motion of a symmetric top. The precession of the grain requires that the induced magnetic moments from the Barnett effect must also precess within the material which causes them to lag behind, dissipating thermal energy in the process of trying to stay aligned. In this way rotational energy is transferred from the grains motion around the angular momentum component not aligned with the principle axis into the spins of the electrons where it is lost thermally. The process creates a mechanism for the grain to reach its lowest energy state with the primary angular momentum aligned with the primary short axis of the dust grain, a mechanism first proposed in Purcell (1979) and shown in Figure 2.3. The lowest energy state is described by Equation 2.3 in which θ is the angle between the primary spin axis and the angular momentum axis and $I_{\|}$ is the moment of inertia about the primary short

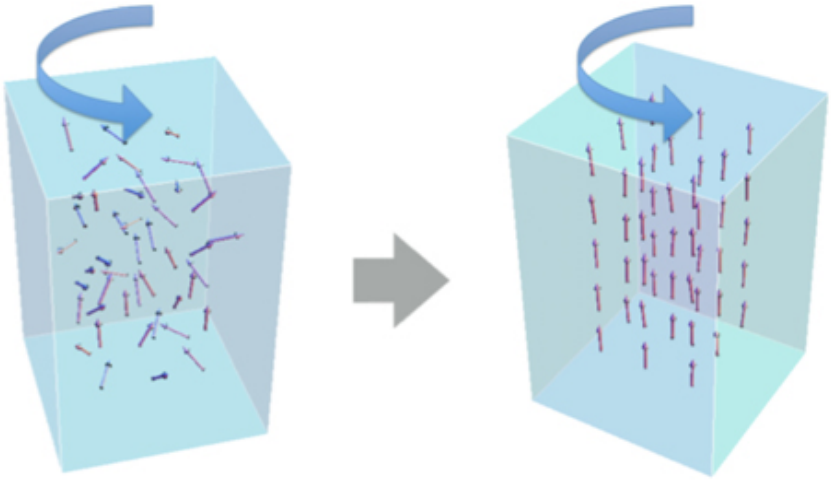

Figure 2.3: An illustration of the Barnett effect from Matsuo et al. (2015). On the left hand side is a paramagnetic material in which the free electron spins are randomly oriented. Once the solid is rotated as in the right hand image, the electron spins preferentially flip to become aligned with the spin axis of the solid which has two primary effects, a magnetic moment is induced in the grain by the aligned spins and angular momentum is transferred from the solid to the electrons (Barnett, 1915).

axis such that $I_{\parallel}/I_{\perp} > 1$ which implies low attractor energy states where $\theta = 0$ or π (Roberge, 2004).

$$E_{rot}(\theta) = \frac{J^2}{2I_{\parallel}} \left[1 + \left(\frac{I_{\parallel}}{I_{\perp}} - 1 \right) \sin^2 \theta \right] \tag{2.3}$$

After internal alignment is complete the dust grain will spin about its primary axis. Due to the Barnett effect the grain will have a magnetic moment that will Larmor precess around the local magnetic field. At this point it is important to recall the alignment torque F from the incident light beam. On the part of the precession where the angle between the grain axis and the incident radiation is largest, F will also be largest and will act to reduce the angle between the grain spin axis and the magnetic field. On the opposite side of the precession where the angle between the grain axis and the incident light is smaller, F will act in the opposite direction to push the grain axis away from the magnetic field, but F will be smaller in this case than

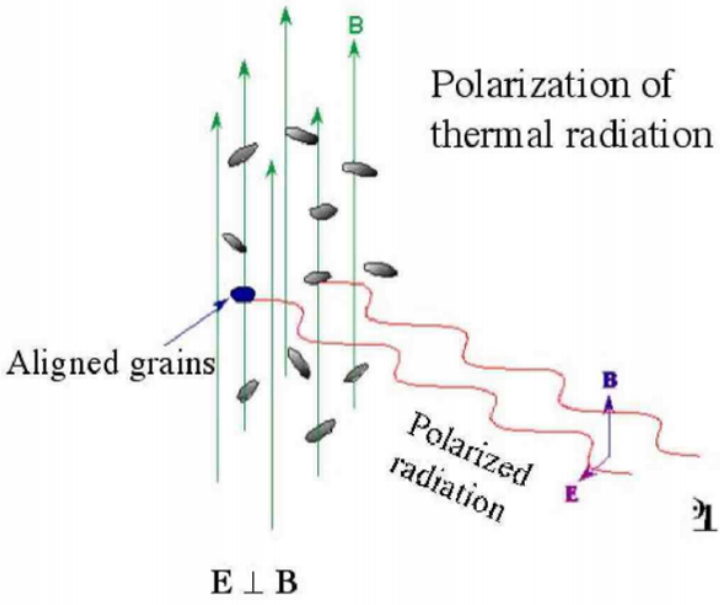

Figure 2.4: Diagram from Lazarian (2007) that demonstrates the fFIR emission from aligned dust grains that results in a polarized signal. The fraction of the signal that is polarized, $p = P/I$, is a function of the efficiency of the grain alignment to the magnetic field and of the grain shape as no grain will emit light entirely in one polarization direction.

in the former and so the net result as the grain precesses is for the angle between the principle grain axis and the magnetic field to go to zero over time. This was shown to be a stable attractor point in Lazarian (2007) for all ranges of orientation angles between the grain, incident radiation, and magnetic field. It is at this stage that the grain becomes useful for observing the local magnetic field as shown in Figure 2.4. Additional details on the RAT process and the observations that support it can be found in the comprehensive review Andersson et al. (2015).

The larger dust grains (> 0.01 μm) in dense GMC equilibrate at temperatures in the range of 10-40 K, whereas smaller dust grains tend to absorb and emit light via a different process at much shorter wavelengths than those observed by BLASTPol. The grains that are observed by BLASTPol emit thermally with a modified blackbody

spectrum described in Hildebrand (1983). The light is emitted preferentially along the long axis of the dust grains which, for the portion of the population that is aligned, translates to a polarized signal that is orthogonal to the magnetic field. The observed polarized emission can reach levels up to approximately 15% of total emission.

The precise mechanism that aligns the dust grains is not fully understood (Lazarian, 2007). Dust grain theories predict different sizes, shapes, and compositions that can have distinct effects on the polarization spectra. Multiband polarization measurements are therefore extremely useful in providing constraints for dust grain models which is another of the principle science goal of BLASTPol and BLAST-TNG.

Additionally, there are a number of experiments currently observing the polarized Cosmic Microwave Background (CMB) signal in a search for B-mode patterns that could show evidence of primordial gravity waves caused by inflation (see Smith et al., 2009). In order to measure these fluctuations with a high degree of confidence, foreground Galactic dust contamination must be very well understood. Observing regions in the submillimeter that are being used by CMB polarization experiments will help to constrain foreground models, allowing for more detailed probes of inflation (Planck Collaboration et al., 2015).

2.4 Current models

An extensive amount of effort has been put into observing dust grain extinction and emission from the UV through the FIR in order to gain a comprehensive understanding of the behavior of the dust spectral dependance and environmental variations. Despite extensive observations, a complete picture has yet to emerge to describe grain alignment. However, the behavior in the UV through the IR is fairly well modeled by the Serkowski curve (see Serkowski et al., 1975) given in Equation 2.4. The Serkowski curve describes the behavior of an extensive portion of the extinction

spectrum with two important parameters, K and λ_{max} that describe the characteristic width. Constraining the two parameters has led to several important results. Despite considerable unpolarized extinction from dust at shorter wavelengths, the polarized extinction percentage drops off rapidly which indicates a much lower fraction of the small dust grains align with the magnetic field. Kim and Martin (1994) found the sharp fall towards the UV end of the spectrum to be indicative that grain sizes smaller than $\sim 0.01\,\mu$m were poorly aligned as illustrated in Figure 2.5.

$$p(\lambda) = p_{max} \cdot \exp\left[-K \ln^2\left(\lambda_{max}/\lambda\right)\right] \tag{2.4}$$

Unfortunately, this relationship does not extend to results from FIR emission observations, and in general the polarization spectrum of the longer grain emission wavelengths lacks data given the difficulty of making observations through the atmosphere. Additionally, some models exist for submillimeter polarization emission but none can completely describe the observed behavior (Draine and Fraisse, 2009). An example of the predicted emission in the submillimeter part of the spectrum is shown in Figure 2.6. It is this lack of information and models that The Balloon-borne Large Aperture Submillimeter Telescope (BLAST) hopes to address by increasing the amount of available data points by several orders of magnitude in a variety of galactic environments.

Once we have observed the polarized light we must review current theories, models, and simulation results to see how they align with our observations. The ISM and GMCs are optically thin to submillimeter emission so observations along the LOS give the average of the magnetic field direction through the entire target and any background objects. This places a preference on GMCs that are near to us, so we can resolve smaller scale structures and can more easily obtain strong signal to noise measurements. Additionally, nearby GMC can be more easily separated from

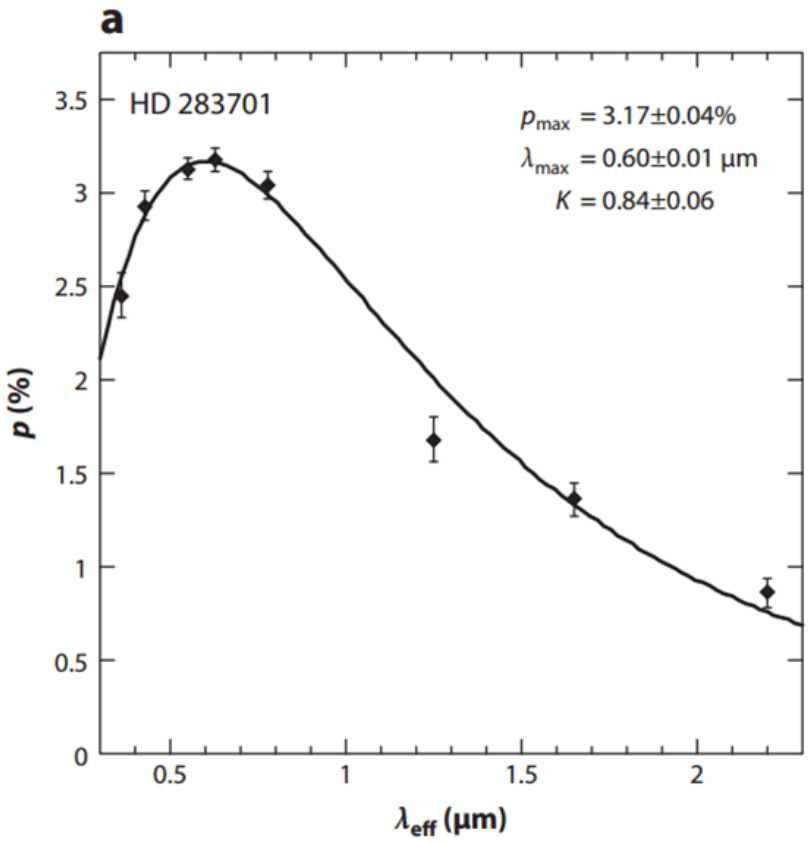

Figure 2.5: A figure shown in Andersson et al. (2015) that serves as an example of the Serkowski curve using data points obtained in Whittet et al. (1992) from the star HD 283701. The curve accurately describes the extinction of starlight from aligned dust grains in the ISM between the observer and the observed star. Such a well defined relation does not exist for the FIR emission from aligned dust grains prompting additional observations to refine models in this part of the spectrum.

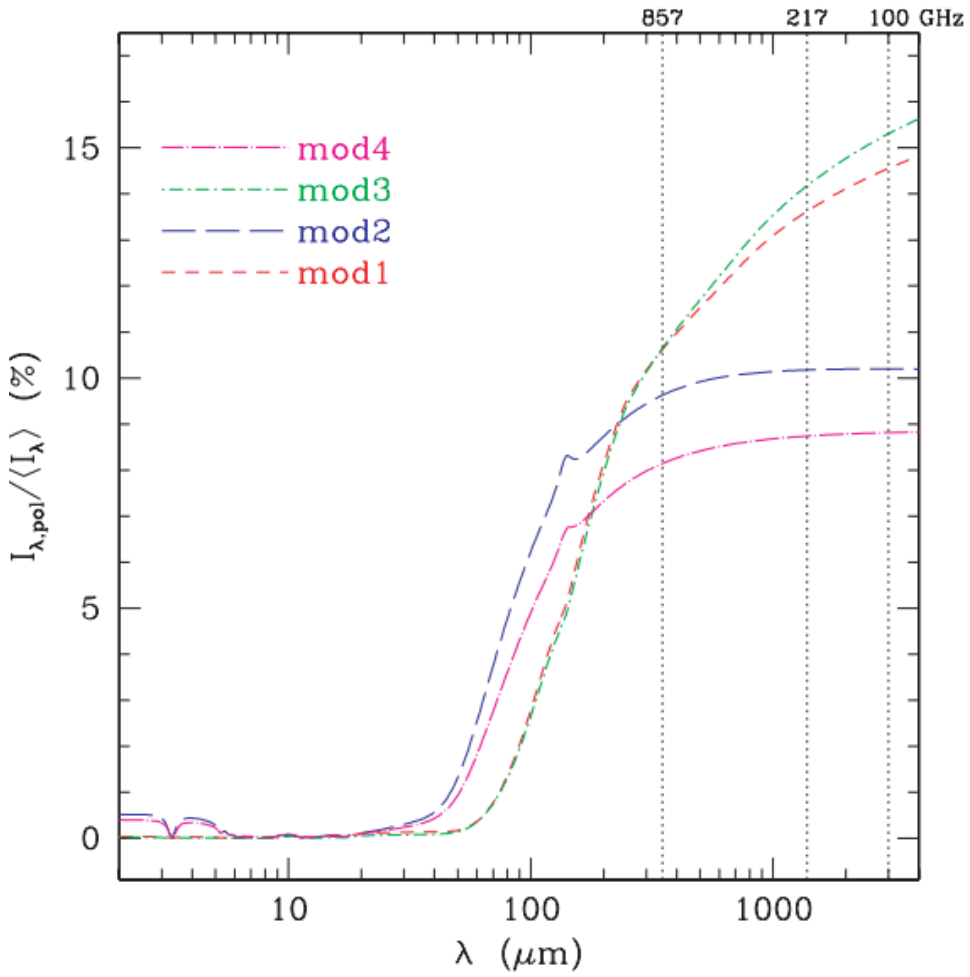

Figure 2.6: A figure from Draine and Fraisse (2009) showing model predictions for the submillimeter polarization emission. On the Y axis is the predicted percentage polarization of the thermal emission while the X axis shows its wavelength dependance. Two classes of models are clearly seen, where Model 1 and 3 have aligned silicate based grains and unaligned carbanaceous grains while in Model 2 and 4 both carbanaceous and silicate type grains are aligned with the local magnetic fields. In the portion of the spectrum covered by BLAST, 200 to 600 μm, the model types can be differentiated by polarization spectrum observations. It should, however, be noted that the models were designed for relatively diffuse regions and not for the spectral behavior in GMC. It should also be noted that the lack of alignment below 40 μm is due to small grains not being aligned in these models.

background sources. To make source separation simpler we pick targets that are off the galactic plane to minimize the amount of signal from the diffuse ISM and distant molecular clouds that could confuse our measurements. Even with intelligent selection of sources, we must dedicate significant analysis effort into removing background sources of contamination to make sure our results are intrinsic to the GMC being observed. The BLASTPol flight in 2012 and subsequent analysis was able to address these issues using a variety of methods discussed in subsequent chapters. The data has yielded important results that are being used to guide new models of dust emission and magnetic fields in GMC.

Chapter 3

BLASTPol 2012 Instrument and Flight

BLASTPol(Fissel et al., 2010) was a 1.8-meter Cassegrain telescope with three bolometric arrays operating over 30% bandwidths centered on 250, 350, and 500 μm, which had 139, 88, and 43 bolometric detectors with diffraction limited resolution of $30''$, $42''$, and $60''$, respectively. It flew at altitudes of $> 38,000$ meters from stratospheric helium balloons developed and provided by National Aeronautic and Space Administration (NASA)in order to get above interference caused by atmospheric water vapor. Flight times of balloon-borne missions are typically several weeks during which astronomical observations are done continuously. The instrument must be able to operate autonomously during flight in case communications break down and so observations are done via a smart scheduling process which observes targets as they come into the range of angles the telescope can safely cover. The telescope is able to determine its position with an array of pointing sensors which use star positions, encoders on motor axles, the position of the sun, the strength and direction of the magnetic field, and several other effects in order to determine both the direction the telescope is looking as well as the scan velocity at a given moment. The pointing

information is then fed back into a set of pointing motors that slew the telescope along the desired scan direction. Working in balloon-borne astronomy requires a large breadth of skills and knowledge to make sure all parts of the instrument work in harmony together for a successful flight.

3.1 Antarctic Ballooning

The unique field of balloon-borne astronomy is driven by the benefits of performing experiments above the atmosphere without the cost and time of launching a satellite. Ballooning also provides an opportunity to test pathfinder technology for space based applications in a near space environment. For the BLASTPol and BLAST-TNG experiments we gain a tremendous amount in sensitivity by getting above the submillimeter extinction caused by atmospheric water vapor as can be seen in Figure 3.1. Additionally, being above $> 99.5\%$ of the water vapor means we experience very small changes in atmospheric transmission over our scan elevations allowing us to map much larger regions of sky than possible from observatories at lower elevations.

The primary reason balloons are launched from Antarctica is due to the 24 hours of sunlight present during the Austral summer launch season. The constant sunlight creates a relatively stable thermal environment for the balloon resulting in smaller expansion and contraction cycles of the gas inside. This reduces the drift in altitude of the balloon over the course of the day which in turn greatly reduces any diurnal systematics from the change in atmospheric loading. The plentiful sunlight also affords us two other advantages over flights from latitudes with a day night cycle. We are able to power our instruments with a relatively small amount of batteries that are continuously charged by solar arrays and we can use pin hole sun sensors to locate the sun with respect to the instrument giving us another method of determining our azimuthal pointing.

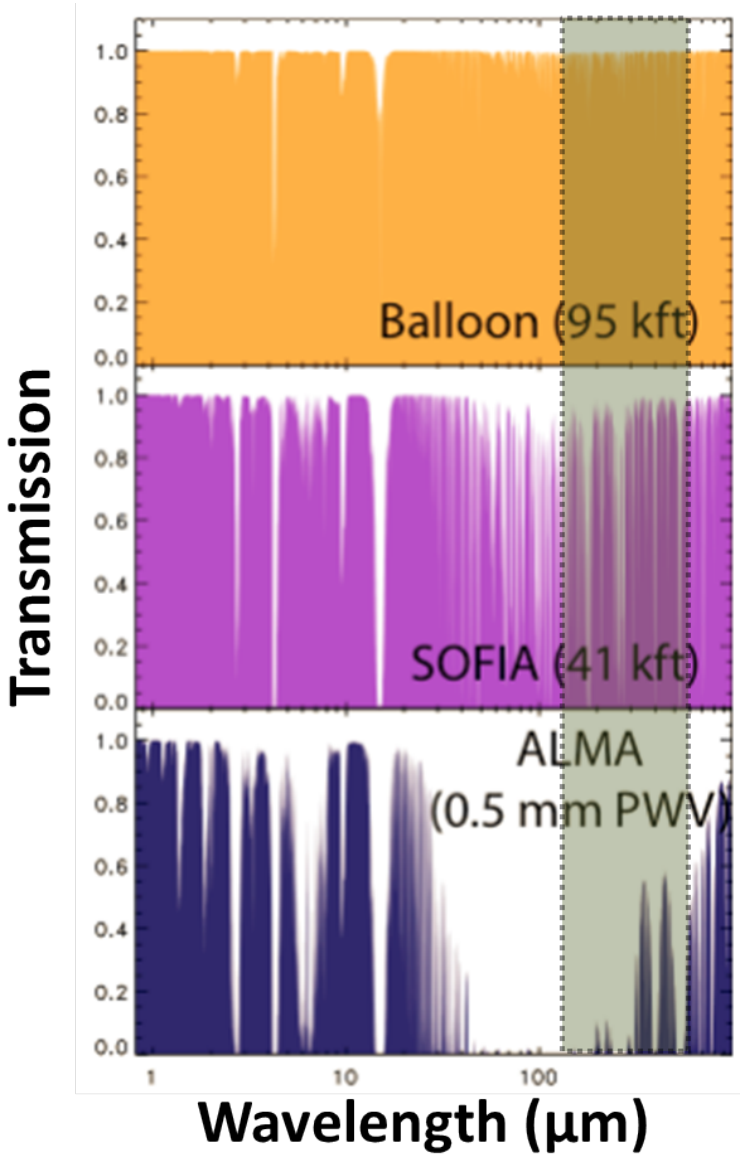

Figure 3.1: A figure from Miller et al. (2014) showing the transmission spectra at various altitudes representative of balloon-borne, stratospheric airplane, and ground based observatories, from top to bottom. The advantage of balloon-borne observation in the highlighted BLASTPol portion of the spectra is clearly evident.

There are several other additional benefits of flying in Antarctica. During the Austral summer, circumpolar air currents set up that ensure the balloon-borne payloads stay over the continent during their flight, circling around approximately every two weeks. The huge advantage this offers is the release and landing of the payload is done over the continent allowing for the complete recovery of the data and instrumental package. Due to this fact we do not have to transmit all our data down during the flight but can instead store it on hard drives for recovery. Since a majority of the instrument is retrieved relatively undamaged within a year of launch, payloads can, and have been, refitted for subsequent launches on timescales as short as two years as was the case with BLASTPol.

One of the primary challenges of balloon-borne missions is also created by the continuous sunlight. The ambient light level seen by our star finding cameras is relatively high requiring extensive baffling and additional filtering to enable them to find pointing solutions during the flight. The other main problem the sunlight presents is the intense thermal environment at float altitudes. With so little atmosphere, we can not rely on convective cooling which necessitates extensive efforts to model the thermal behavior of all the telescope components at our float altitude and design our instrument to reflect as much sunlight away as possible while creating windows to space to radiate heat created by power dissipating in the electronics.

It is for these benefits and trade offs that we fly an Antarctic balloon-borne payload as the optimal setup for our instrument and the type of science we hope to examine. The following sections examine the BLASTPol instrument in more detail.

3.2 Instrumental Design

BLAST (Fissel et al., 2010; Pascale et al., 2008; Marsden et al., 2008) flew from Kiruna, Sweden, in 2005 and from McMurdo, Antarctica, in 2006 (Truch et al., 2009).

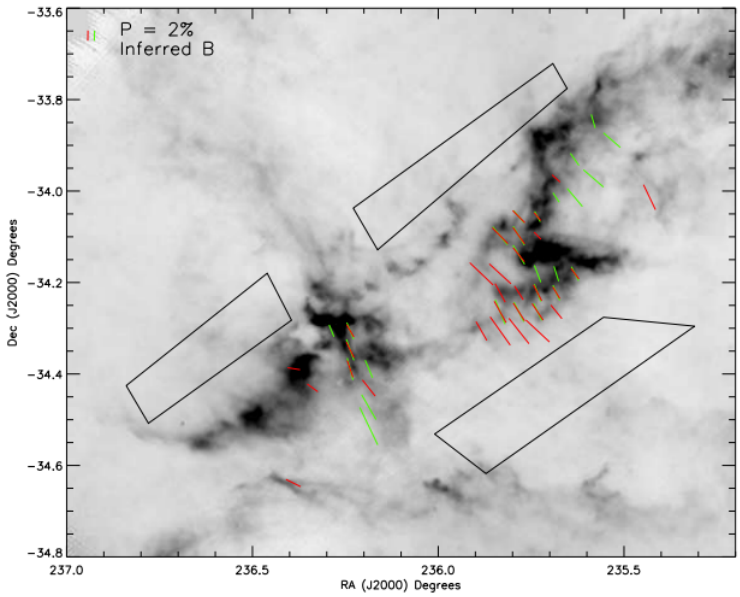

Figure 3.2: Magnetic field pseudo-vectors obtained during the BLASTPol 2010 Antarctic flight (Matthews et al., 2014). The image is of the Lupus I star forming region with the intensity map provided by *Herschel* SPIRE 350μm measurements. Boxed areas denote reference regions used in deriving the polarization pseudo-vectors which are then rotated by 90° to show inferred magnetic field pseudo-vectors. The length of the lines indicates the degree of polarization as dictated by the key in the upper left. Red and green pseudo-vectors show 500 and 350 micron measurements, respectively.

It successfully served as a pathfinder mission for *Herschel*'s SPIRE instrument by flying and testing a similar detector and focal plane design (Griffin et al., 2010). BLAST made a number of high profile observations, which included a high resolution map of the Vela C molecular cloud complex and confusion limited FIR observations of the GOODS South region (Devlin et al., 2009; Marsden et al., 2009; Pascale et al., 2009; Patanchon et al., 2009; Viero et al., 2009; Wiebe et al., 2009; Netterfield et al., 2009).

BLASTPol was created by modifying the BLAST instrument, which is described in detail in Fissel et al. (2010); Pascale et al. (2008); Marsden et al. (2008). In order to make BLAST polarization sensitive, a polarizing grid was placed at the

entrance to each feedhorn on all three arrays and a stepped Half Wave Plate (HWP), described in Moncelsi et al. (2014), was added to the optical configuration. The optical layout is shown in Figure 3.6 with the optical component parameters listed in Table 6.3. The telescope uses a Ritchey-Chrétien configuration with an aluminum 1.8-m diameter primary mirror attached to a 40-cm aluminum secondary mirror. The secondary mirror is actuated to allow for active focusing during the flight to adjust to the differential thermal contraction of the support structure. The telescope beam is reimaged by the cold optics ($\sim$1.5 K), which are situated in an Offner relay configuration. The light is split by two dichroic filters into the science bands at 250, 350, and 500 μm (Ade et al., 2006). The focal planes are held within a cryostat cooled by liquid helium and liquid nitrogen, which has a hold time of approximately 13 days. The total field of view (FOV) of each array is $14'$x $7'$. The arrays are kept at 290 mK by a closed-cycle ^{3}He refrigerator. Each pixel is made of a Neutron Transmutation Doped (NTD) thermistor glued to a silicon-nitride "spider-web" absorptive element (Bock et al., 1998), which is coupled to a smooth-walled conical feedhorn (Chattopadhyay et al., 2003) spaced at $2f\lambda$ (Griffin et al., 2002).

The BLAST experiments have a history of serving as test beds for balloon-borne telescope technology that have produced significant improvements in the field during its years in operation. The BLASTPol flights in 2010 (Pascale et al., 2012) and 2012 (Galitzki et al., 2014b) proved the potential for this type of instrument to observe Galactic polarization and map magnetic fields. However, the 2010 instrumental performance was limited by a melted IR blocking filter that greatly complicated polarization analysis. During takeoff the telescope payload spins unpredictably under the balloon and at one particular pointing angle the IR intensity from the sun proved too much for the filter which caused it to melt. The effect of this failure was an unpredictable and skewed beam shape from the instrument that made it difficult to reconstruct observed images and especially difficult to recover accurate polarimetry

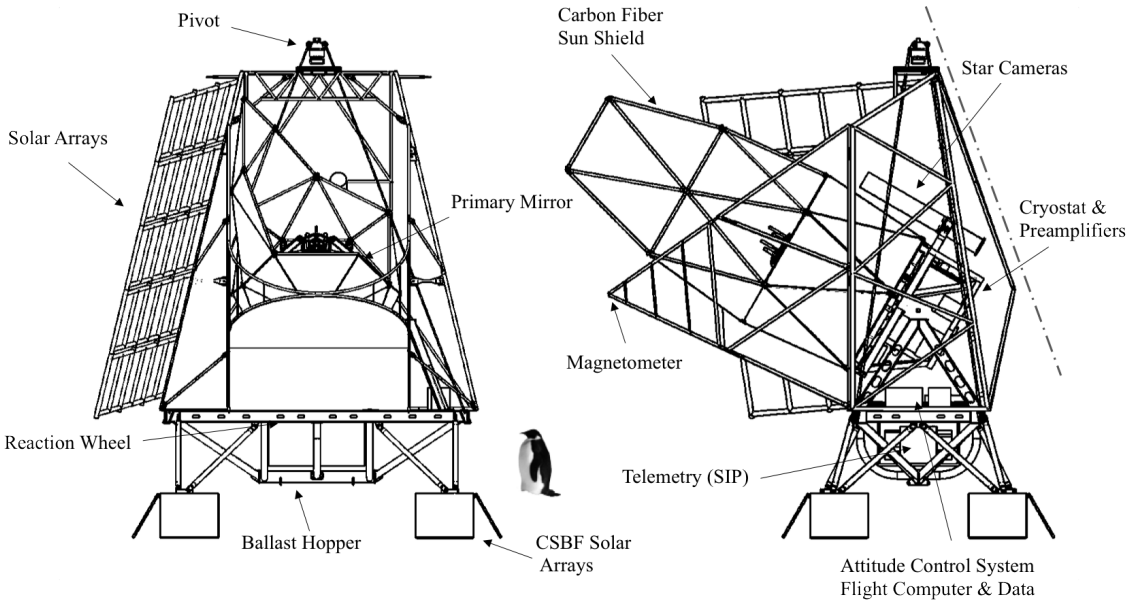

Figure 3.3: Front and side schematic drawings of the BLASTPol gondola with a 1 m tall Emperor penguin shown for scale. Dimensions of the frame are largely determined by NASA requirements that correspond to the size of the highbay facilities used in Antarctica as well as the capabilities of the launch vehicle shown by the dot-dashed line which shows the 20° avoidance zone required to prevent accidental contact at launch. All the primary components of the telescope are shown along with the sunshields and solar arrays. The sunshields are primarily on the right side of the telescope to allow observations to be made within 44° of the Sun while the left side is left largely open to allow heat generated by the electronics to radiate to space.

measurements. The abnormal beam shape was smoothed with a Gaussian kernel to remove beam dependent artifacts which reduced the resolution to $\sim 2.5'$ (Matthews et al., 2014). A significant portion of the data from 2010 was also rejected due to contamination by intermittent systematic noise likely caused by the satellite communication system, Tracking and Data Relay Satellite System (TDRSS), and motor current cross talk which effectively reduced integration time on the targets. Despite these significant hurdles, the 2010 flight yielded interesting scientific results as illustrated with a magnetic field map of the Lupus I cloud in Figure 3.2.

After the 2010 flight, most of the BLASTPol hardware was recovered and it was quickly decided to fly again in 2012 with largely the same instrument with only minor

improvements. The main component that needed to be replaced was the aluminum frame on which the telescope is mounted, referred to the gondola as a whole, with an inner frame that moves in elevation and an outer frame that hangs from the balloon flight train and scans in azimuth. Once the new inner and outer frames arrived at The University of Pennsylvania (UPenn), the instrument was reassembled. This required attaching the cryostat, primary and secondary mirrors, motors, and electronics and then engaging in a new round of testing and upgrades to confirm the rebuilt instrument performed as designed and would be less susceptible to issues experienced in the previous flight.

During the second flight of BLASTPol from Antarctica in 2012 we made degree-scale maps of a number of nearby molecular clouds and were able to obtain a vast improvement on the number of polarization pseudo-vectors over the 2010 flight. The 2012 maps cover multiple targets and contain thousands of pseudo-vectors which can be seen in the Vela C map shown in Chapter 5 (see Fissel et al., 2015). The design and testing of BLASTPol from the point at which I joined the project prior to the 2012 Antarctic flight will be described in the following sections. Additional details of the 2012 instrument and flight can be found in Angilè (2013).

3.2.1 Detectors

The polarization sensitive detector arrays at all three wavebands compose the detecting element of the telescope around which everything else is built. The detectors were made from NTD germanium thermistors which were attached to a silicon nitride micromesh "spider-web" which allows for fine tuning of the thermal time constant of the device, good coupling to incoming light, and a low cross-section to cosmic rays (Bock et al., 1998). The detectors were determined to be photon noise limited, as defined in Equation 3.1, where η is the bolometer absorption efficiency, T_A is the antenna

Band		250 μm	350 μm	500 μm
Number of detectors		149	88	43
Nominal FWHM	[arcsec]	36	42	60
Bolometer Optical NEP	[$WHz^{1/2}$]		3.0×10^{-17}	
Time Constant	[ms]		2	
Spectral Noise	[$\mu VHz^{1/2}$]	3	2.6	2.5
1/f Knee	[mHz]	55	52	56
Responsivity	[$V/MJySr^{-1}$]	1.13×10^{-7}	2.64×10^{-7}	5.18×10^{-7}
Sensitivity	[$MJySr^{-1}s^{1/2}$]	1.54	0.74	0.52
Beam area	[deg^2]	1.13×10^{-4}	1.54×10^{-4}	3.14×10^{-4}
Noise Equivalent Flux Density [NEFD]	[mJy/beam $s^{-1/2}$]	53.13	34.79	49.75
depth [1σ, 5 hr, $1deg^2$]	[MJy sr^{-1}]	2.05	1.25	0.44
depth [1σ, 50 hr, $1deg^2$]	[MJy sr^{-1}]	0.65	0.40	0.14
Polarization Sensitivity [0.5% Pol., 5 hr, $1deg^2$]	[MJy sr^{-1}]	410.66	249.94	87.56
Polarization Sensitivity [0.5% Pol., 50 hr, $1deg^2$]	[MJy sr^{-1}]	129.86	79.04	27.69
Instrumental Polarization	[%]	0.71	0.10	0.16
Polarization Efficiency	[%]	80	77	85

Table 3.1: BLASTPol loading, noise, and nominal sensitivities from Angilè (2013)

temperature, and $\Delta\nu$ is the bandwidth. Additional parameters of the BLASTPol detectors can be seen in Table 3.2.1 and an image of the detector construction can be seen in Figure 3.4.

$$NEP_{photon} = 2\eta k_B T_A \sqrt{\Delta\nu} \tag{3.1}$$

The detectors were read out by supplying an AC bias voltage at ∼200 Hz which suppresses low frequency noise from sources including thermal fluctuations and microphonics in the cabling. The changes in resistance of the bolometer from the input optical signal are read out as changes in voltage which is amplified at a cold 130 K stage by junction field-effect transistor (JFET) circuits and then further amplified and bandpass filtered in a warm electronics box before the signal is ported to an analog to digital converter (ADC) to create to a digital signal. The digitized voltage is then sent to a field programmable gate array (FPGA) on a separate board which performs the lock-in to the AC signal, additional filtering, and sends the resultant DC voltage to the flight computer to be recorded. A schematic showing a single

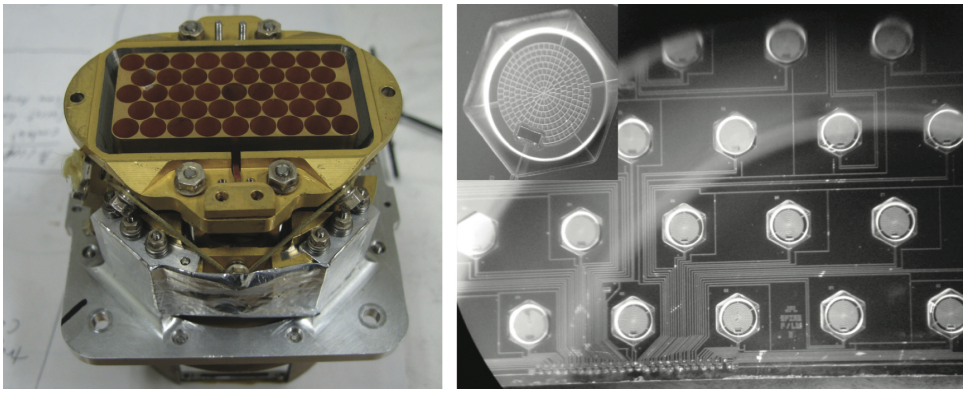

Figure 3.4: Left: The 500 μm array assembly showing the output of the feedhorn array with the polarizing grid removed. Right: A microscopic image of the 500 μm detectors with an inset showing a zoomed in view of a signal detector element showing the characteristic "spider-web" structure. Image from Angilè (2013).

bolometer readout circuit is shown in Figure 3.5.

3.2.2 Optics

The detectors are coupled to smooth walled conical feedhorns that are optimally spaced at $2f\lambda$. The feedhorn arrays are illuminated at the focus of the cold optics which are enclosed in and attached to a box that is cooled to 1 K. This box is offset from the 4 K coldplate by Torlon supports to provide a strong mechanical attachment with minimal thermal conductivity. The cold optics follow a modified Offner relay design with three spherical re-imaging mirrors as shown in Figure 3.6. This configuration allows us to change the focal ratio to $f/5$ allowing us to install additional optical components including the two low pass dichroic filters. The first dichroic filter reflects light onto the 250 μm array, defining its lower frequency boundary while an additional filter in front of the feed array and polarizing grids defines its high frequency boundary. The second dichroic filter reflects the light to the 350 μm array which defines its low frequency boundary with its high frequency edge determined by the cutoff of the 250 μm dichroic. The light that passes through both dichroics then

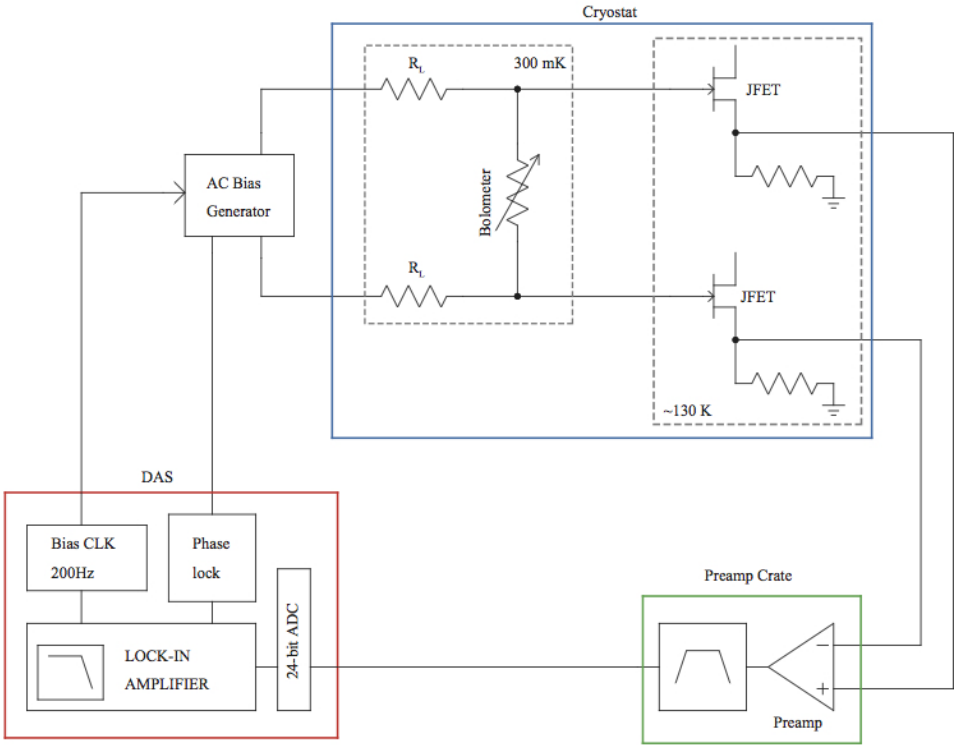

Figure 3.5: Schematic representation of the bolometer read-out electronics from Angilè (2013).

reaches the 500 μm array at the re-imaged Cassegrain focus where the high frequency edge is defined by the 350 μm dichroic and the low pass is defined by the feedhorn frequency cutoff. By this method we are able to simply define the bandpasses of all three detector arrays in a configuration that allows us to observe all three bands on the same patch of sky simultaneously. Figure 3.7 shows an image of the cold optics assembly.

An additional advantage of the Offner relay configuration lies in the M4 mirror which is at an image of the primary. By under-sizing M4 and placing an absorptive hole in its center, we define the illumination of the primary mirror which is under-illuminated to avoid edge effects, while also blocking light from the path of the central hole in the primary. We are also able to place a calibrator lamp (Hargrave et al., 2006)

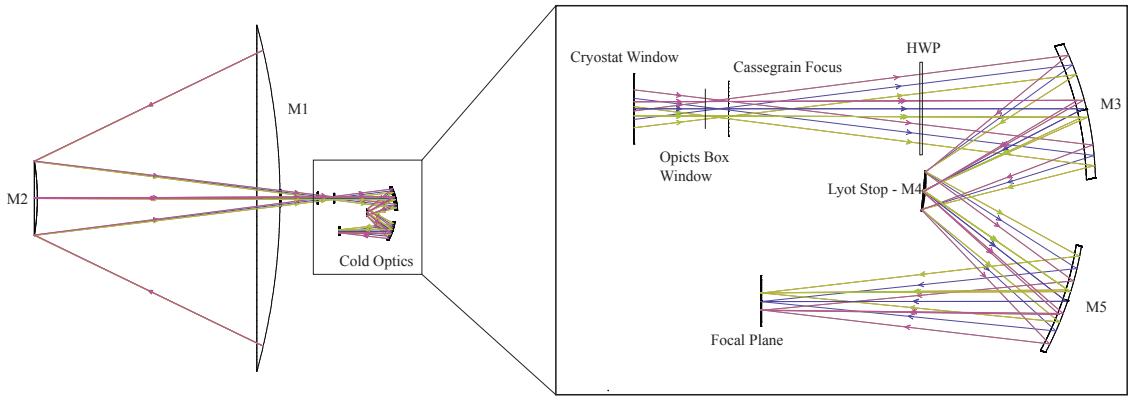

Figure 3.6: The optical layout of the BLASTPol telescope and receiver is shown on the left with the 1.5 K optics, located within the cryostat, shown in the expanded view on the right. The image of the sky formed at the input aperture is re-imaged onto the bolometer detector array at the focal plane. The mirror M4 serves as a Lyot stop which defines the illumination of the primary mirror for each element of the bolometer array. The three wavelength bands are separated by a pair of dichroic beam splitters (not shown), which are placed between M5 and the focal plane. The sapphire half-wave plate is shown, placed ∼19 cm behind the focus of the telescope, between the Cassegrain focus and M3.

in the center of M4 that illuminates all the arrays simultaneously. Pulses from the calibrator lamp allow us to correct for drifts in responsivity of the detectors over the course of the flight as described in Chapter 4.

The longer light path prior to the M3 mirror provides a convenient placement for the HWPR which contains a sapphire HWP manufactured by Cardiff University with an anti-reflective coating (see Moncelsi et al., 2014). Rotation of the HWP in steps provides polarization rotation during the flight allowing each detector to sample both directions of the Q and U Stoke's parameters. Having each detector sample each component allows us to remove polarization effects introduced by the cold optics and the detectors themselves which ensures the polarization signal that we sample is from the sky. However, the HWP position is only rotated between scans of a target which is on a time scale much longer than the detector response necessitating an additional step to address polarization systematics. We do so by alternating the

Table 3.2: Summary of BLASTPOL Optical Characteristics

Effective Focal Length	Antenna Efficiency	Emissivity	Telescope f#	Cold Optics f#	
9 m	80 %	0.06	5	5	
Geometry	M1	M2	M3	M4	M5
Nominal Shape	Parabola	Hyperbola	Sphere	Sphere	Sphere
Conical Constant	-1.029	-2.853	0.000	0.000	0.000
Radius of Curvature	4.186 m	1.154 m	348.6 mm	174.3 mm	348.8 mm
Aperture	1.816 ∅ m	0.399 ∅ m	95×75 mm	36.8 ∅ mm	95×75 mm

polarizing grid direction by 90° on adjacent pixels which provides fast sampling of both linear polarization components. The combination of these two strategies yields a polarimeter with relatively low polarization systematics.

3.2.3 Cryogenics

The detector arrays are cooled via a closed cycle ^{3}He absorption refrigerator manufactured at UPenn which provided enough cooling power to keep the detector arrays at 300 mK for 76 hours. The refrigerator was cycled by heating the charcoal element to drive the ^{3}He gas out of the charcoal and onto a condensing section provided by a 1 K intercept. The condensed liquid would then refill the ^{3}He reservoir. Cycling the system was a process that took approximately 1.5 hours.

The 1 K temperature stage uses a pumped pot of ^{4}He that is constantly refilled from the main helium tank via a small capillary tube. The ^{4}He pot was manufactured as a 110 mL toroidal tank that fit around the ^{3}He refrigerator to provide the intercept condensing stage as well as to provide an easy mounting point for straps to cool

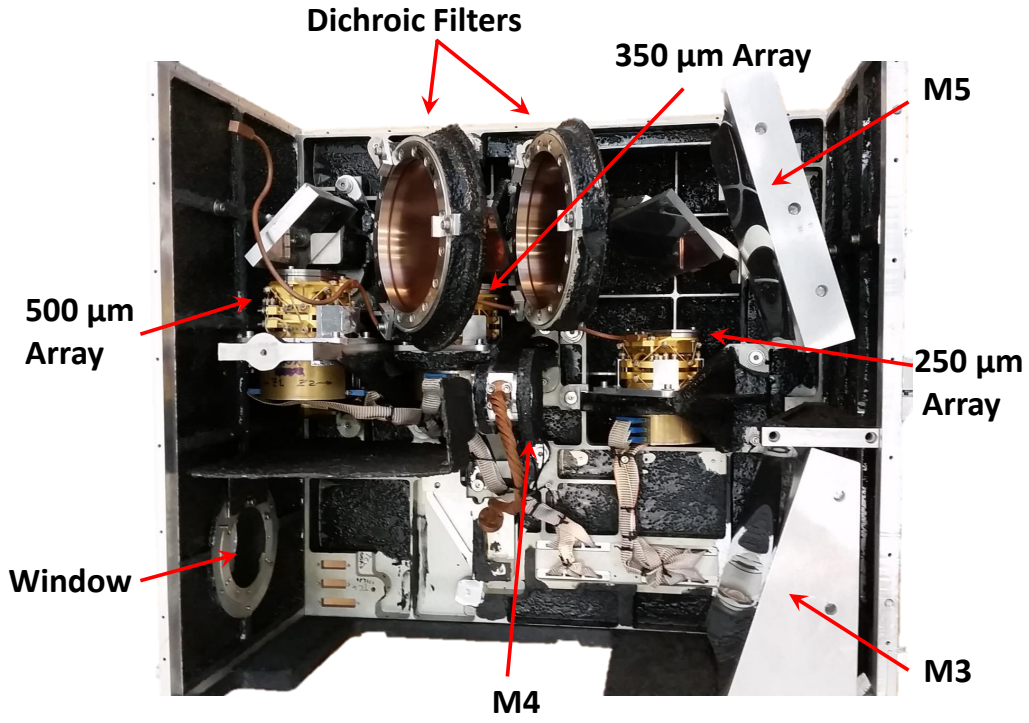

Figure 3.7: Image of the interior of BLASTPol cold optics box where the near side and top have been removed. It should also be noted that the HWPR mounted to the cold plate at 4 K and not the optics box, instead being placed in the optical path through the hole in the bottom of the optics box once the box was mounted in the cryostat.

the optics box to 1 K. The ^{4}He refrigerator slowly filled after ^{3}He refrigerator cycles. When the ^{4}He reservoir became completely full we would notice a small jump in temperature due to the fact that the full pot had a much smaller surface area from which to pump on. The ^{3}He refrigerator and ^{4}He refrigerator assembly had been used in prior flights and was reused for this flight without significant modification. A vent line for the pump pot was attached to a vacuum pump while in the lab and had a motorized valve attached in the flight configuration which was opened post launch and ascent to the near vacuum of the balloon float environment to provide a passive pumping system for the ^{4}He pot.

The cryostat, made by Precision Cryogenics[1], has a primary Helium tank with a 43 L capacity. The Helium cooled stage was then surrounded by a shield layer that used a copper intercept on the helium vent line which was cooled by the boil off vapor from the helium tank. This vapor cooled shield (VCS) had typical temperatures of 35 K and was itself surrounded by a toroidal liquid nitrogen tank with a capacity of 55 L which provided an intermediate temperature stage at 77 K. A detailed view of the cryostat can be seen in Figure 3.8.

The primary vent lines for the He and liquid nitrogen (LN2) tanks vented to atmosphere in the lab through ports in the top of the cryostat. A TAVCO[2] pressure control valve and a motorized valves were attached to each vent port for launch which allowed us to switch between venting to atmosphere or through the TAVCO. Other components on the top of the cryostat were the HWPR motor with a ferro-fluidic shaft feedthrough and two vacuum ports to allow for rapid vacuum pumping of the cryostat volume prior to cool downs.

The cryostat also had a window on the front that was made of high density polyethylene (HDPE) with anti-reflective coating applied at Cardiff University. Additional filtering elements provided by Cardiff University included IR blocking filters placed in front of the window and on the LN2 stage. On the VCS and helium stage windows, low pass edge (LPE) filters were attached to further reduce the amount of optical loading on the detectors from light outside the detector bandpasses.

During the 2010 launch the IR filter in front of the window melted due to excessive loading from the sun during ascent to launch altitude during which we cannot control azimuthal pointing. To remedy this, a shutter system was created that was mounted to the inner frame that swing an aluminum shutter up between the cryostat and the primary mirror to block incident radiation during ascent. If power to the shutter was

[1]Precision Cryogenic Systems Inc., 7804 Rockville Rd., Indianapolis, IN 46214
[2]Tavco, Inc, 20500 Prairie St., Chatsworth, CA

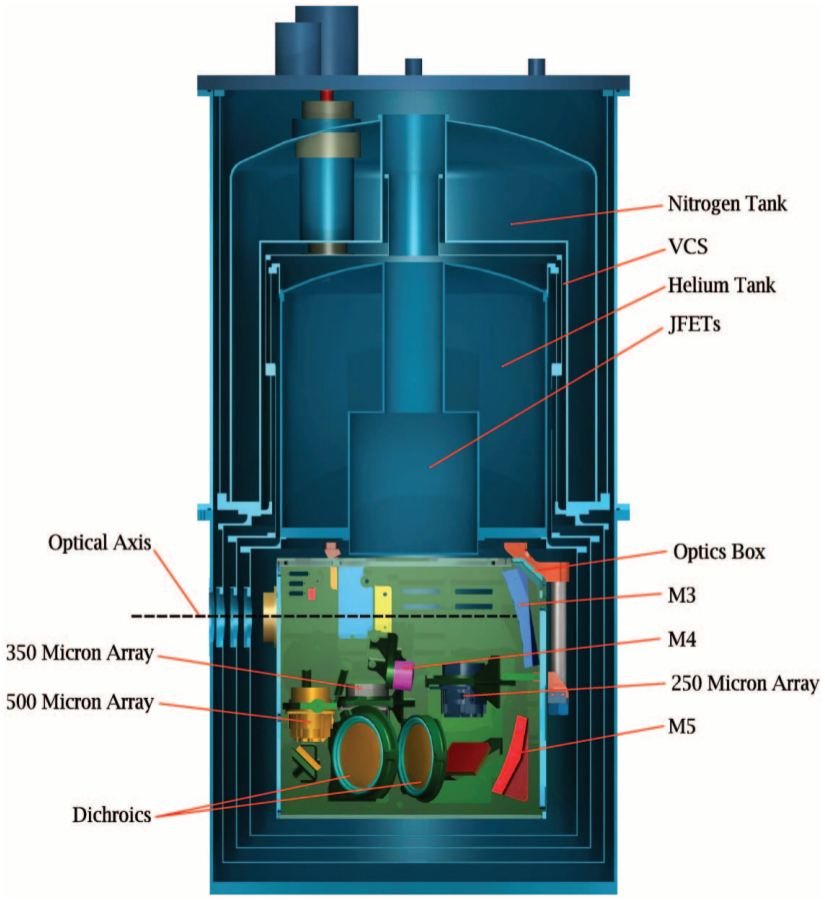

Figure 3.8: An image of the BLASTPol cryostat cut away view showing all the main thermal layers and cryogenic tanks as well as illustrating how the cold optics fit into the assembly.

lost it would automatically drop to its base 'open' state to ensure low risk of any failure of the shutter blocking observations.

3.2.4 Telescope Alignment

The primary mirror was attached to the inner frame via three mounting bolts with G10 washers which were used to thermally isolate the primary mirror from the inner frame to reduce temperature drifts in the mirror. M1 thermal stability was further accomplished by attaching Multi-Layer Insulation (MLI) blankets to the back of the

primary mirror. In the previous 2010 flight the secondary mirror had been attached directly to the edge of the primary mirror via four carbon fiber support struts. In 2012 the configuration was altered to three support struts which were directly attached to the inner frame. The secondary mirror had three stepper motor actuators attached to the M2 mount while the mirror itself was offset from the mount via three leaf springs. This allowed us to adjust the alignment of M2 with M1 which we checked by using a bore site laser mounted in the middle of M2 which reflected off a target mounted in a fixture in the center of the primary mirror. When M1 and M2 were properly aligned the laser would reflect off the center of the target back to the center of M2. The actuators on M2 also allowed us to actively adjust the focus in flight. During the flight we would observe a point like source and adjust the focus to maximize the Gaussian peak response in the detectors. After initial focusing, the temperatures of M1, M2, and the struts between the mirrors were monitored. The offset between M2 and M1 along the optical axis was adjusted if the temperature fluctuations were determined to cause a change in the focus.

The cryostat was mounted with an aluminum interface piece that bolted to the top of the cryostat and to the inner frame. The inner frame was a hexagonal structure which couples the cryostat to the primary and secondary mirrors and interfaced with the elevation pivot driven by the elevation motor. The cryostat mounting piece provided an adjustable interface between the cryostat and the frame which allowed us to adjust in X, Y, and Z as well as angle to M2 which was performed after M2 had been aligned with M1. Checking the alignment of the cryostat was done in a similar mnanner to the M1 and M2 alignment process with the M2 bore site laser hitting a reflector mounted on the cryostat. The cryostat reflector had previously been aligned to the optical beam projected out from the cryostat cold optics. This allowed us to align the M1 and M2 optical axis correctly with the cryostat optical axis by adjusting the crysotat position until the incident beam hit the center of the

target and the reflected laser beam returned to the center of the secondary mirror.

3.2.5 Pointing Control

Pointing in elevation was accomplished via a direct drive motor mounted on the axis of the inner frame. The inner frame was dynamically balanced with lead weights prior to elevation pointing. Additionally, there was a liquid balance system installed that would pump liquid from a tank placed low on the frame to one placed high on the frame to counteract the boil off of the cryogens over the course of the flight. This prevented the elevation motor current from saturating at its limit of around 10 amps.

The inner frame axis was offset from the outer frame by two pyramidal structures. The outer frame fine azimuthal pointing was accomplished using a 1.5 meter diameter reaction wheel made of three inch thick aluminum honeycomb with brass plugs placed along its circumference. The reaction wheel was velocity limited necessitating a pivot motor which was used to transfer excess angular momentum to the balloon to prevent saturation of the reaction wheel. The pivot motor was also used for coarse pointing when quick shifts in azimuth were commanded. The pivot motor was mounted between the balloon flight train and the four support cables mounted at each corner of the outer frame.

Pointing control was accomplished primarily with two star cameras that could find pointing solutions roughly every few seconds. To determine pointing information between star camera solutions we had six fiber optical gyroscopes, with two mounted on each of the elevation, yaw, and roll axes. The gyroscopes make precision measurements of angular velocity but have a random walk of $4''/\sqrt{s}$ which dictates how frequently the star cameras must generate a pointing solution. Additional pointing instruments included sun sensors that used the sun's location to find pointing in azimuth, inclinometers on both the outer and inner frames to measure elevation and

tip/tilt of the entire telescope, a magnetometer to measure azimuth in relation to Earth's magnetic field, and GPS to determine absolute location which was provided through NASA hardware. Additional details on the BLASTPol pointing systems can be found in Gandilo et al. (2014).

Several tests were performed in Antarctica to provide absolute calibration between all of the pointing control systems. One such procedure was done on a wooden platform away from the main buildings called the "dance floor". The telescope was placed on the dance floor with a link to allow us to control the instrument and record data. A number of people then physically spun the telescope through several 360 rotations in both directions. This allowed us to fully calibrate and debug the magnetometer and sun sensor pointing performance prior to the flight.

3.2.6 Electronics

Two flight computers received all the data and wrote it to disk while also sending out commands to control the various components. They were overseen by a watchdog circuit that dictated which computer was in charge, with the capability to switch computers in case of a failure or reboot. The two primary control systems run by the flight computers were the data acquisition system, which controls the cryostat and the detector readout, and the attitude control system, which communicates with the various gondola hardware including motors and pointing sensors.

To power the telescope we ran off of four batteries that were charged on the ground via a power supply and then switched over to Morningstar[3] charge controllers that regulated the voltage from the set of 15 solar panels that provided continuous charging during the flight. It was observed in pre-flight operations that changes in the current supplied to the primary pointing motors caused an anomalous pickup in the detector channels most likely due to poor grounding control. This issue was resolved

[3]Morningstar Corp., 8 Pheasant Run, Newton, PA

by separating the power systems into an outer frame system that supplied power to the computers, the motors, and most of the control and pointing systems.

A separate power system was made to supply power to the cryostat, readout electronics, and most other components on the inner frame. The split was simplified by the fact that the two systems had nearly identical requirements besides a smaller power consumption from the inner frame systems. For each system we connected two batteries in series along with a charge controller. The solar panels were split into a set of nine, to charge the outer frame system as the motors needed more overhead, and six panels to charge the inner frame power system.

3.2.7 Preflight Tests

After the instrument was reassembled it had to undergo a battery of characterization tests. The cryostat was tested separately to make bandpass and polarization property measurements of the cold optics and detectors. The bandpass of the instrument with all filters in place was measured with a FTS. The FTS optics are mounted inside a vacuum chamber with an input window for the signal from a LN2 cooled source. The signal then goes through the FTS optics before exiting through a second window that was coupled to the cryostat. Nitrogen was pumped into the air gap between the FTS window and the cryostat window to reduce the level of atmospheric absorption lines which can contaminate the bandpass measurement. The setup is shown in Figure 3.9.

We would measure the FTS interference pattern which is then processed to create a bandpass graph for each of the detector arrays. In principal the bandpass would look like a square step function for each array but in reality the filters did not produce a perfect response which can be seen in Figure 3.10. Due to our measurement method, some atmospheric lines could be seen as absorption spikes and noise in the

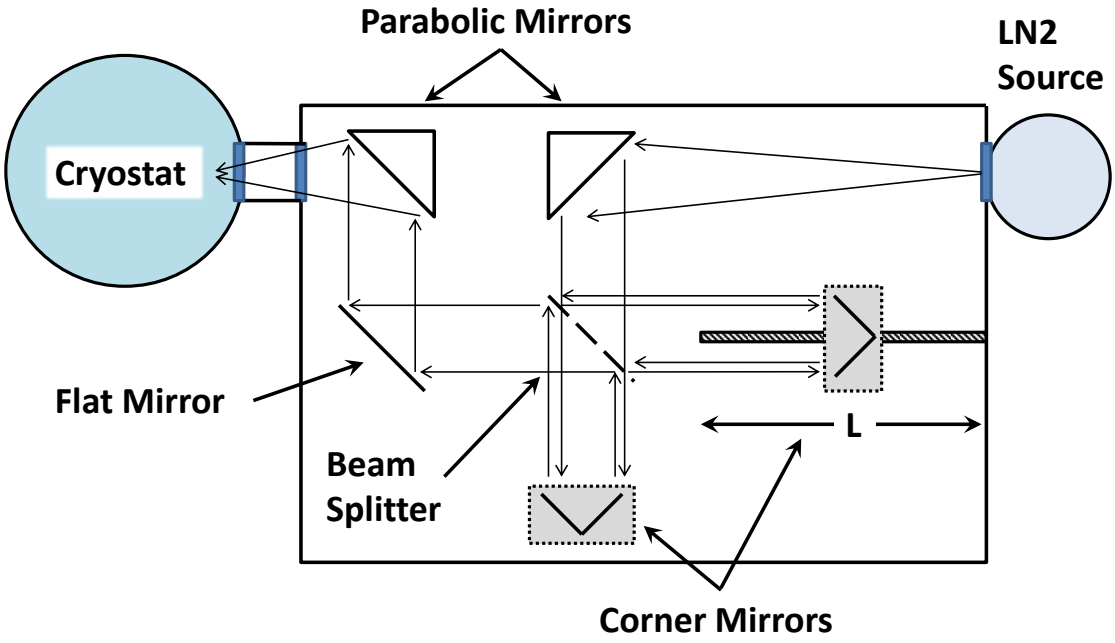

Figure 3.9: A schematic view of the FTS setup used to determine the spectral bandpass of BLASTPol. The design is based on that of a polarizing Martin-Puplitt interferometer. A liquid nitrogen source is placed at the focus of the first parabolic mirror at the entrance window to the FTS. The parabolic mirror collimates the beam before it goes through a beam splitter to two corner mirrors, one of which is on a moveable stage that can move a distance $L = 20\,\mathrm{cm}$. The beams from each of the corner mirrors then recombine and reflect off a flat mirror before being refocused by a second parabolic mirror identical to the first. The cryostat is placed such that the FTS focus is at the same point as the Cassegrain mirror focus. The FTS has a focal length of 60.96 cm with $f/\# = 4.8$. The path length of the mirror sets the frequency resolution to be $\nu_R = c/4L \approx 0.75\,\mathrm{GHz}$. The stage was moved by $3\,\mu\mathrm{m}$ steps, the motor step limit, at the detector sampling frequency of 100 Hz which maximized the signal-to-noise of the measurement.

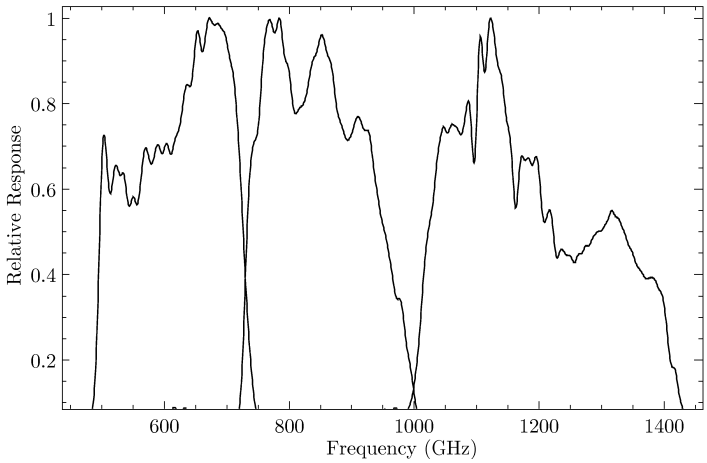

Figure 3.10: The spectral response of the three BLASTPol channels normalized for unit peak transmission. A FTS with a liquid nitrogen source was used to measure the bandpass.

measurement. The bandpass measurement is extremely important for future calibration efforts as it was used to characterize the spectral and intensity response of our detector arrays. Further details of preflight tests on the cold optics can be found in Angilè (2013).

After the cold optics have been characterized, we mount the receiver on the telescope to couple it to the warm optics which consist of M1 and M2. The primary test we conduct on the ground in the complete optical configuration is making beam maps. To create the maps we had to shift the telescope's focus into the near field as atmospheric absorption prevented us from viewing any source in the telescope's far field. We offset M2 by inserting aluminum blocks approximately three centimeters thick on the M2 mount to create a focus at 100 m where we place a chopped LN2 source that was moved across the detector field of view with a stepper motor XY stage. Fine tuning of the focus is accomplished with the active focus actuators on the secondary mirror. This allows us to create a map of the beam for each detector in the 500 μm channel as a check of the performance of the optics. Due to atmospheric attenuation we are unable to create similar maps in the other two telescope bands

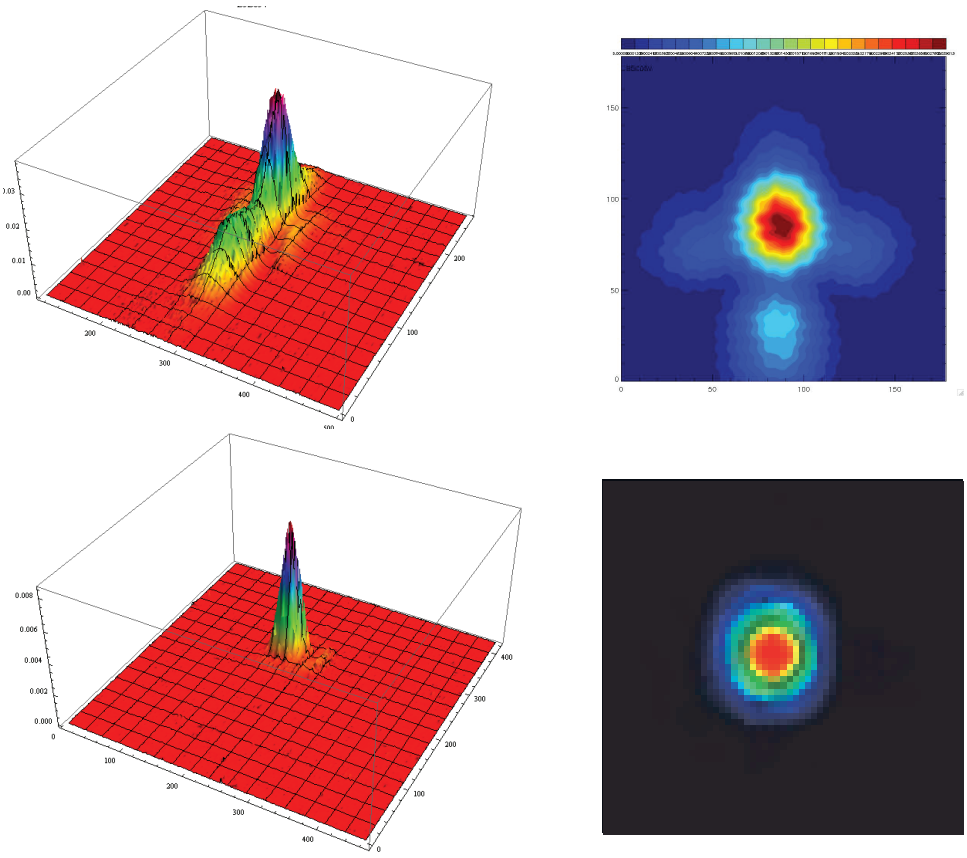

Figure 3.11: Reconstruction of the BLASTPol beam in one of the central pixel of the 500 μm array. Top: The beam shape before the fix implemented for the 2012 flight. The side lobe is $\sim$ 30% of the power of the main lobe. Bottom: The resultant beam shape after adjustments to the secondary mirror mounting scheme (Angilè, 2013).

which means we can only confirm that the beam shape is diffraction limited at our lowest resolution channel.

The first set of beam maps made in 2012 at UPenn yielded an odd shape that was seen before in the 2010 campaign showing a significant side lobe, with $\sim$30% of the total power, approximately one arcminute below the main beam. We found the side lobe was dependent on how we mounted the secondary mirror to the primary mirror by making beam maps for multiple configurations. We then mapped the surface of the mirror shape under different loading scenarios using a FARO device, a laser tracker able to determine the location of target retro-reflectors with an error of $\sim$ 10 μm per

meter away from the target. In the 2010 flight the secondary mirror was attached via four carbon fiber struts directly to the rim of the aluminum primary mirror. In this configuration the bottom strut ended up supporting the bulk of the weight which was enough force to deflect the primary mirror edge causing its shape to deform resulting in the reflection of a significant amount of power into a separate peak below the main beam. The deformed shape of the mirror is illustrated in Figure 3.12. We solved this problem by switching to a M2 mounting configuration using three of the original carbon struts mounted directly to the inner frame instead of to the edge of M1. The alteration was effective in removing the side lobe to levels below what we could measure with 500 μm near field beam maps as shown in Figure 3.11.

3.3 Polarimetry

Each detector array has a photo-lithographed linear polarizer (Figure 3.13) mounted to the front of the feedhorn block. The polarizing grid orientation rotates by 90° from one pixel to the next along each row with the rows parallel to the nominal scan direction. This alignment allows for sampling of either a Q or U Stokes parameter on a timescale that is much shorter than the array's common mode $1/f$ noise knee at 0.035 mHz (Pascale et al., 2008). The sampling timescale of the Stokes parameter is ∼0.125 s, which is determined by the detector separation, 45″ at 250 μm, and typical scan speed of $0.1^{\circ}\mathrm{s}^{-1}$. The field at the end of each feedhorn is approximately Gaussian, which results in very small leakage in polarization between adjacent pixels, estimated to be less than 0.07% (Moncelsi, 2011).

Rotation of the HWP is used to modulate the polarization signal. Linearly polarized light from a target is sampled at four pre-determined HWP positions which allows each pixel to observe I and both directions of the Q and U Stokes parameters during the course of a scan. Stepping the HWP allows us to remove polarization sys-

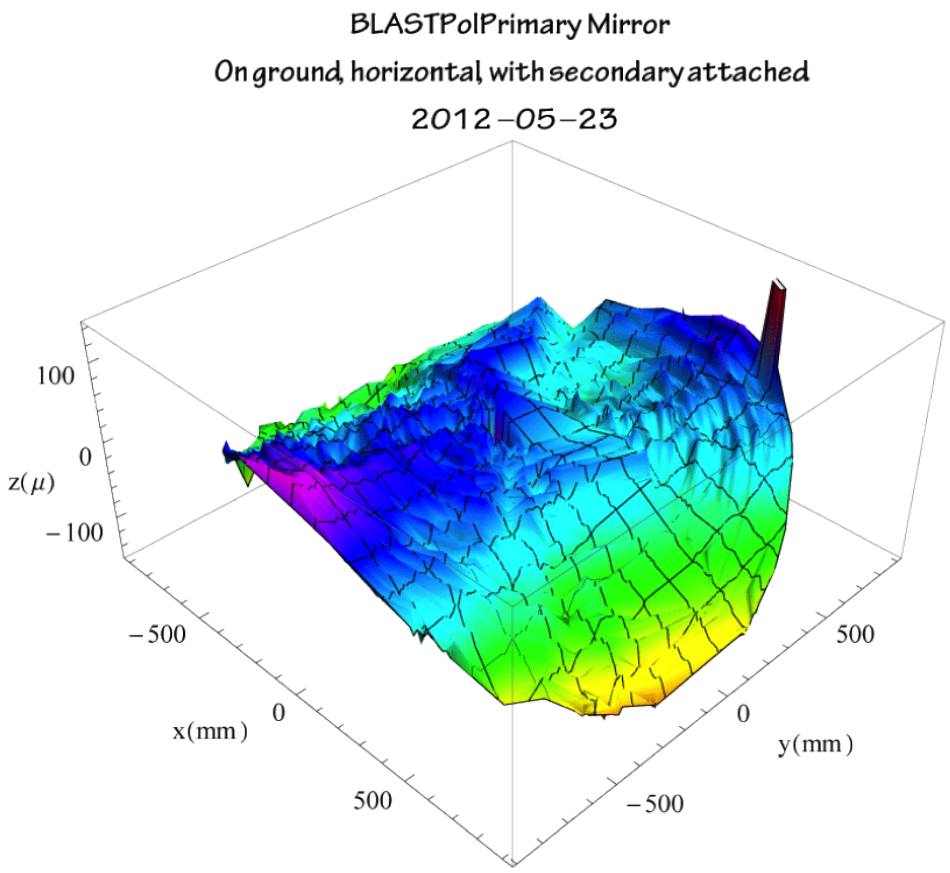

Figure 3.12: Exaggerated 3-D reconstruction of the primary mirror surface when it is subject to the weight and stress induced by the secondary mirror and supporting carbon fiber struts in the configuration used in 2010. The shape accounts for the strong sidelobe below the main beam that was observed in 2010 and in pre-flight tests in 2012 prompting a change in mounting strategy.

tematics from the cold optics and detectors. The HWP used in BLASTPol (Moncelsi et al., 2014) has a 10 cm diameter aperture and is made from five layers of 500 μm thick sapphire, which are glued together with a 6 μm layer of polyethylene. The outer faces of the HWP have a metal-mesh anti-reflective coating (Zhang et al., 2009).

The HWP is driven by a gear-train connected by a G-10 shaft to a stepper motor mounted on the exterior of the cryostat. The shaft is sealed via a vacuum ferromagnetic feedthrough[4]. The HWP is stepped between four set angles (0°, 22.5°, 45°, and

[4]Ferrotech Corporation: 526 S. Jefferson St., New Castle, PA 16101

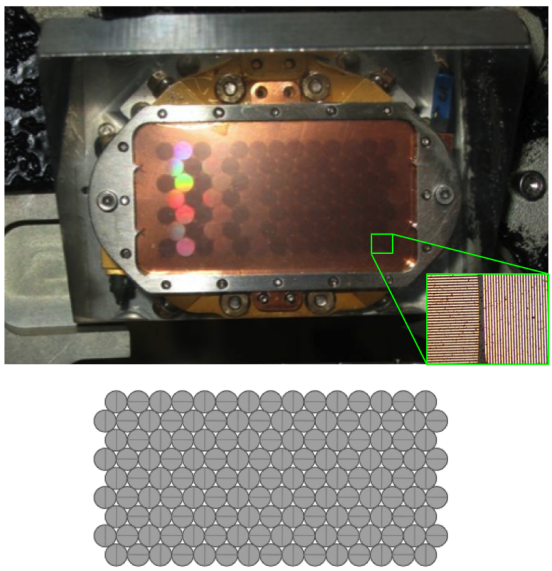

Figure 3.13: Top: A photo of the 350 μm array photo-lithographed polarizing grid which is mounted in front of the detector array. The inset is a detail of the grid between two neighbor pixels. Bottom: A cartoon of the grid layout which shows the alternating polarization angle for each detector. With this design we are able to sample one Stoke parameter (Q or U) in less than one second.

67.5°) after each completed scan of a source in elevation. The position is determined by an absolute reading from a 4 K potentiometer on the rim of the HWPR mount, combined with the stepper-motor encoder. Due to some parts of the potentiometer reading poorly in pre-flight tests, the positions used in the 2012 flight were offset from the positions in the 2010 flight by 15.12°. A detailed description of the HWP design and performance is included in Moncelsi et al. (2014).

We conducted pre-flight ground tests to characterize the polarization properties of the instrument, using a chopped heated source placed directly in front of the receiver window, in order to fill all pixels. Instrumental polarization (IP) is defined as the polarization signal induced by the telescope optics on incoming un-polarized light (Novak et al., 1989). To determine the expected IP of the array in pre-flight tests a vertical polarization grid is mounted between the chopped source and the window. The HWP is fully rotated generating a cosine response which is fit to find

the rotation angle of the HWP that maximizes the response in pixels measuring vertical polarization. The position is set as the zero angle and then the polarizing grid is removed and the polarized signal for each detector is measured at each of the HWP flight positions (0∘, 22.5∘, 45∘, and 67.5∘) which establishes a baseline IP for all detectors. Additionally, the IP of the entire optics assembly including M1 and M2 is measured in flight by observing a calibrator source at two parallactic angles. The IP of the detectors will be the same for both observations whereas any polarization from the source will rotate. Any small net polarization of the light can be subtracted out during the analysis stage to remove contamination by the instrument's optics. The IP was determined to be less than 1% for all three arrays.

Polarization efficiency (PE) is defined as the polarization measured when looking at a completely polarized light source. PE was measured in a second test where we polarized the source with a polarizing grid tilted at 45° with respect to the incident beam placed between the chopped source and the cryostat window. The grid is then rotated generating a sinusoidal response in the detectors that would have minimumm values of zero if the PE were 100%. $q = Q/I$ and $u = U/I$ are then calculated at several fixed angles of the grid and used to fit a circle in q and u space from which the PE is generated for each wavelength. This was observed to be 80%, 77%, and 85% for the 250, 350, and 500 micron arrays, respectively. Lower PE at shorter wavelengths is expected, due to the large spectral range observed (Moncelsi et al., 2014) and the fact that the instrument was optimized for performance at 500 μm, as motivated by scientific considerations.

In addition to polarization tests we also make far field beam maps of the detectors. Beam maps are made by scanning a LN2 point like chopped source across the detector FOV with a XY stage mounted 2 meters away from the cryostat in the rough location of the secondary mirror. Maps are then produced comparing the XY stage's position to the signal received at each detector by which we can map out the response through

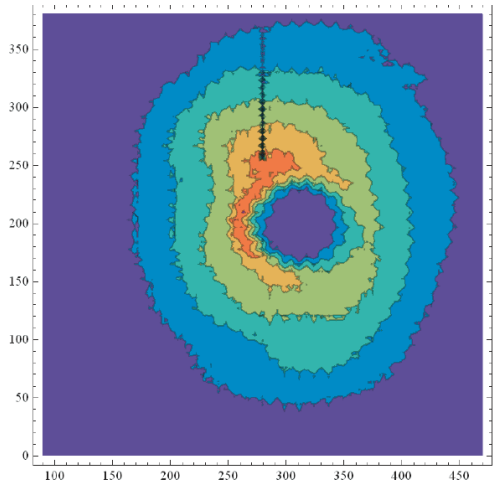

Figure 3.14: A map created between the 2010 and 2012 flights demonstrating the Gaussian like response of the detectors from a chopped LN2 source positioned two meters from the cryostat in the detector far field. The source is scanned across the detector FOV and the response is mapped recreating the vignetted beam through the cold optics. The hole in the center of the Gaussian is created by the vignetting from M4 that determines the illumination of the primary mirror. The fact that the hole is centered demonstrates that the detector array is correctly aligned with the cold optics.

the cold optics. The response should be a Gaussian beam with a hole in the center and sharp edges due to the vignetting from M4. A slight asymmetry in the 2D Gaussian is expected due to the polarizing grids mounted in front of the detector arrays. An image of the observed response measured prior to the 2012 flight is shown in Figure 3.14.

3.4 Flight

After integrating NASA hardware components and obtaining flight approval in Palestine, TX, our instrument was shipped directly to Antarctica via trucks, ships, and finally an airplane which took it from Christchurch, New Zealand to McMurdo base in Antarctica. We met the instrument there in early November for reassembly, testing, and confirmation of flight readiness. For the Antarctic 2012 campaign,

Figure 3.15: Image of BLASTPol in the seconds immediately after launch showing the fully assembled flight configuration of the telescope.

cooling the cryostat and reassembling the flight systems went quite smoothly. We also made beam maps in the telescope near field and confirmed similar performance to measurements made at UPenn and in Texas prompting us to make no additional changes to the optical system. After extensive testing of the entire system together with pointing control, readout, communication, and data recording we were ready to enter into flight ready status as approved by NASA after which no changes in the instrument configuration are allowed. BLASTPol was successfully launched on December 25th 2012. An image of the payload immediately after launch is shown in Figure 3.15.

Post launch, monitoring of the payload is begun so that we can take control of the balloon systems as soon as possible. The first $\sim$24 hours of the flight are the most critical as during that period we have a high data download rate using line of site

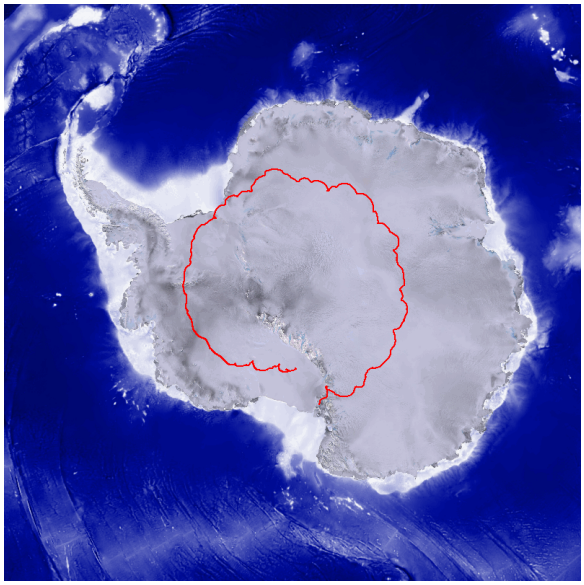

Figure 3.16: Flight path around Antarctica for the 2012 LDB flight of BLAST-Pol. The scallop features correspond roughly with diurnal cycles. (Source http://www.csbf.nasa.gov/antarctica/payloads.htm)

communication with the telescope. The higher rate allows us to monitor significantly more detector and sensor channels than later in the flight when we use lower data rate satellite communications. After we stabilized at flight altitude our first task was to begin pointing at calibrator sources to adjust the focus of the instrument to make sure our response is maximized in the 250 μm band which has the tightest Gaussian peak. Approximately six hours into the flight one of the star cameras suffered a critical hard drive failure which eliminated it as a pointing sensor. We continued pointing control with the remaining star camera and made our initial maps of Saturn which we used to establish the optimal focal position of the secondary mirror.

Once we completed initial calibration procedures a schedule file was uploaded to execute our optimal scan strategy. The schedule file is created by a program which finds the optimal scanning strategy to get the desired coverage of our targets throughout the flight. The primary scanning strategy during flight is a slow raster scan with a constant elevation velocity while moving back and forth across the tar-

get in azimuth, which works well for extended sources. A typical BLASTPol raster scans across targets in azimuth at a speed of $\sim 0.1^{\circ}\mathrm{s}^{-1}$ with an elevation scan speed calculated to change the elevation by 1/3 the array FOV in one crossing. The scan rates are determined by the size of the target, the detector FOV, and our desire to make a complete pass of a target in approximately 15 minutes to allow for HWP moves. Additionally, our scan scheduling is designed to scan across a target at two parallactic angles to create good cross-linking which vastly improves the quality of maps that can be made. The optimal schedule file is dependent on the launch date, as some sources are positioned in the sky to have better viewing either late or early in the flight, and latitude, as some targets are relatively low or high in the sky making them difficult to observe from some latitudes. The schedule file allows the telescope to operate autonomously in the event that we lose communication with it.

It was additionally realized early on that a feature labeled as "popcorn noise" in 2010 which manifested itself as random spikes in the detector signal was due to the TDRSS antenna. This system was subsequently turned off unless we absolutely needed its additional bandwidth, done periodically to understand the state of the pointing and control systems. Otherwise control and feedback was done over the lower bandwidth Iridium satellite system that did not introduce additional noise into our detector response.

The flight and scheduling went well with steady observations of our primary targets and calibrator sources until about six days into the flight after which our second star camera suffered an irrecoverable hard drive failure. After the failure we had to rely on coarse pointing sensors for pointing control and decided to make wide area maps of targets that were opposite the sun as the best low risk option available to us. The large scans were roughly centered on the Vela C and Puppis regions.

After 12 days of observing our cryogens ran out signaling the end of our science data acquisition after which the inner frame was locked in place at 45 degrees and

Table 3.3: BLASTPOl 2012-2013 Primary Target Observations

Target	Type	Distance (pc)	Size (deg^2)	Time Obs. (hrs)
Vela C	GMC	∼700	12	61.30
Carina Nebula	GMC	∼2300	2	4.62
G331	GMC	∼7000	2	4.05
IRAS 08470-4243	Point	∼700	0.1	2.58
Lupus I	Dark Cloud	∼155	1	15.27
Puppis	MC	∼1900	0.4	13.73

the shutter was closed. 16 days into the flight the payload was released from the balloon to a soft landing on its back on the ice sheet between McMurdo and the South Pole as shown in Figure 3.16. Subsequent recovery operations obtained all of our primary equipment including the cryostat, mirrors, electronics systems, and most importantly, the science hard drives. The inner and outer frame and the aluminum sun shield structures were left behind for recovery by the South Pole traverse that picked them up later and then shipped them back to UPenn for a delivery in mid 2014. An overview of the sources that we were able to observe during the 2012 flight are shown in Table 3.3.

Chapter 4

BLASTPol 2012 Data Reduction

The data reduction pipeline used for the 2012 data analysis has its roots in the original BLAST experiment as much of the instrument, including the detectors, is the same. Additional steps were developed to handle the polarization data components after the 2010 BLASTPol flight. Once we had the data from the 2012 flight we took the existing pipeline and improved on it to create the highest quality data products possible. The pipeline is described in detail in Pascale et al. (2008); Patanchon et al. (2009). A schematic of the 2012 process is shown in Figure 4.1.

The first steps in the analysis include flagging contaminated data from cosmic rays, glitches, and noise from TDRSS antenna. Cosmic rays are high energy radiation which occasionally hit a detector which results in a high signal to noise spike in the detector's TOD. The TDRSS contamination is due to reflections from the antenna signal off our sunshields sporadically reaching the detectors resulting in an increased noise level. The contamination source was recognized early in the flight and only affected a small percentage of the data. The data and flags are then passed to the deconvolution routine after which detectors are corrected for drifts in responsivity, using the signal from a calibrator lamp that is flashed every $\sim$15 minutes. Common-mode detector response from changes in elevation pointing along with other artifacts

inherent to the data are then removed in the detector pre-processor.

The cleaned data is initially processed by the **naivepol** map maker which uses a binning method to generate preliminary I, Q, and U maps. IP is determined by examining maps made of the same polarized source at different sky rotations and is then subtracted from subsequent data products. The initial maps are also used to flat-field all detectors in an array relative to a chosen pixel using aperture photometry from one of our calibration targets. Additionally, the naive maps are used to determine pointing offsets and to characterize the beam shape in each of the bands.

Once all of the primary pipeline steps have been completed the resultant data sets are processed into final maps by an ideal map maker, Time Ordered Astrophysics Scalable Tools (TOAST), as described in detail in Benton (2015). The map maker produces Stokes I, Q, and U maps from which a polarization pseudo-vector and polarization fraction can be extracted. A pseudo-vector contains magnitude and angle information but has a 180 degree degeneracy in the angle. The angle of the vector is then rotated by 90° to get the correct orientation of the magnetic field as described in Section 2.3 and Figure 2.4. The magnetic field and polarization data are then analyzed using a variety of simulations and jackknife consistency checks to determine uncertainty levels of the polarization strength and orientation. Pseudo-vectors that do not pass these tests are rejected. The rigorous consistency checks on our polarized data is described in detail in Matthews et al. (2014); Fissel et al. (2015).

4.1 Data Reduction

The data on the recovered hard drives from the flight comes in a raw TOD format with the DC voltage amplitude of the bolometer, as described in Section 3.2.1, sampled at 100 Hz. In addition to the data from the bolometers, there is data from pointing sensors, thermometry, motors, and other components that need to be an-

alyzed to understand and control for systematics from the flight. The first year of the data analysis effort was spent understanding and removing systematics. Data that was contaminated in an irrecoverable manner was flagged and ignored by the mapmakers. Flagged items included spikes from cosmic rays, sudden shifts in voltage level from HWPR moves, areas around calibration spikes, areas for which the pointing solution could not be determined, and portions of the TOD that had excessive noise due to other factors. Over the flight data used for our analysis, $\sim$8% of the data was flagged.

4.1.1 Electronics Transfer Function Deconvolution and Spike Removal

The detector signals undergo two important processes in the warm readout electronics before they are written as data. First, a bandpass filter in the pre-amplifier stage is applied that uses a 85Hz bandwidth biquad bandpass centered on the 200 Hz AC bias voltage frequency. Next a lock-in is performed to the AC bias using the reference to produce a DC voltage to which an anti-aliasing filter is applied before the DC voltage is written to disk. The combination of the bandpass and anti-aliasing filters are referred to as the electronics transfer function which must be corrected for in the pipeline to restore high frequency information. This is done through the use of a Fast Fourier Transform (FFT) as the transfer function is convolved with the signal from the detector. The transfer function is divided out in Fourier space before before the detector frequency response undergoes a FFT back into the time domain as shown in Equation 4.1 where F is the Fourier transform of the function, f is the transfer function, and g is the desired signal. After the deconvolution of the transfer function a new low pass filter is applied to remove excess high frequency noise. The filter only affects the response above 30 Hz which, at a scan speed of $0.1^{\circ}/s$, corresponds to

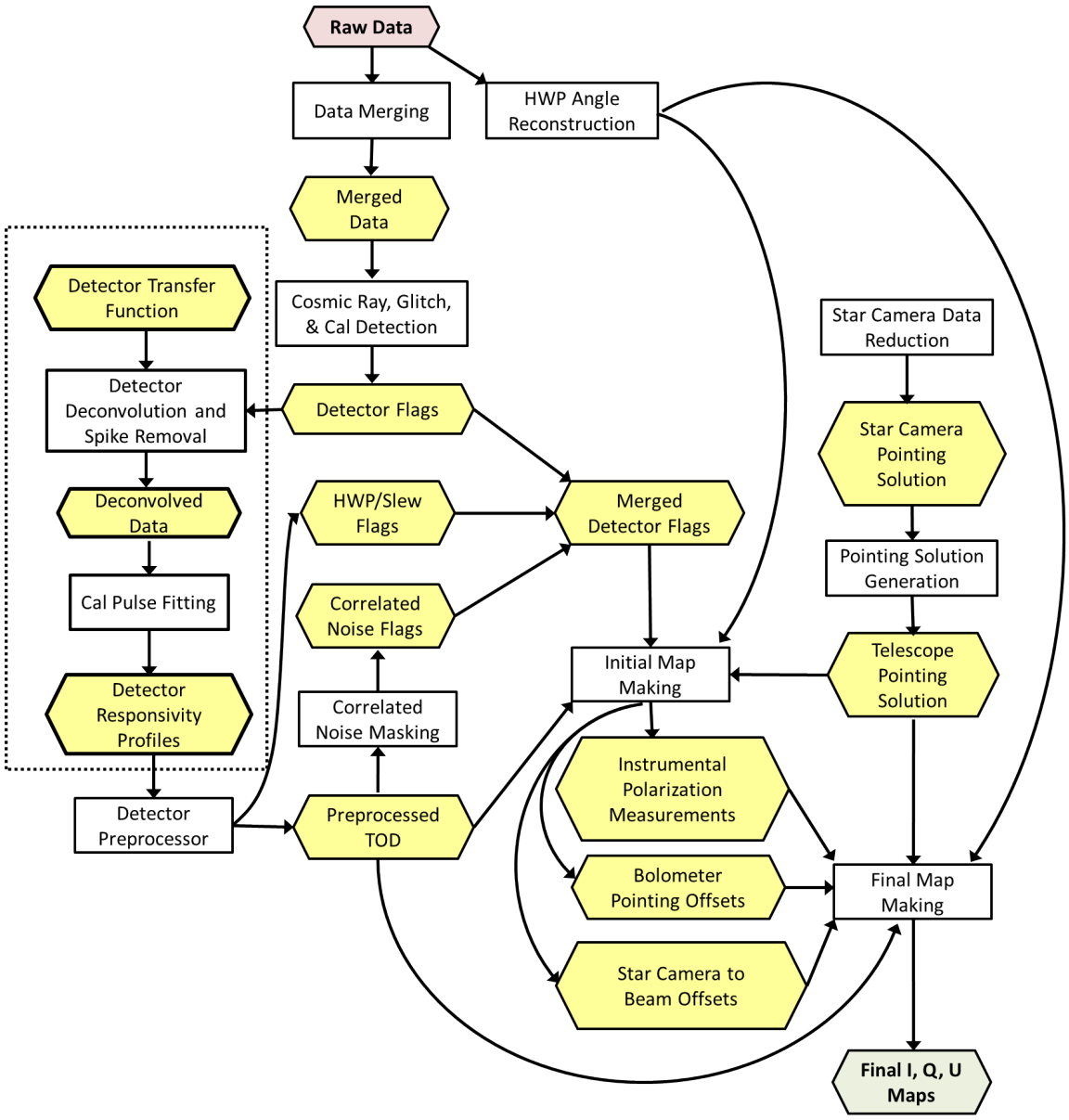

Figure 4.1: An illustration of the BLASTPol 2012 data reduction pipeline with shaded hexagons representing data products and rectangles representing data reduction processes (Fissel, 2013). The boxes within the dashed region represent the portion of the pipeline that I was responsible for that is discussed in more detail in Section 4.1.

features smaller than 12″ which is smaller than our best diffraction limited resolution and so the filter does not remove any resolvable features.

$$F(f * g)/F(f) = F(f) \cdot F(g)/F(f) = F(g) \rightarrow FFT \rightarrow g(t) \tag{4.1}$$

All sharp changes in signal response must be removed prior to the application of the FFT that is applied to the TOD to prevent ringing around the features in the TOD when the reverse transform is applied. Spike like features include Calibrator Lamp Pulses, cosmic ray hits, and HWPR are identified in a flagging field given as an input to the deconvolution code. Flagging of calpulses and HWPR moves were simple as their on/off state was recorded in a separate data field to allow for easy identification. However, cosmic ray spikes required iterating the process of flagging and deconvolution several times as the flagging program occasionally failed to identify a spike which would cause a high amplitude ringing in the detector channel after the deconvolution was run. All bolometer channels were then visually inspected to identify missed spikes which were then fed back into the flagging system.

Once all flags were set properly, the deconvolution program would cut out the flagged regions and perform linear fits with an applied white noise spectrum across the flagged regions to prevent ringing. As these sections were flagged there was no subsequent risk of the patched areas of the TOD being used in the data analysis. Additionally, the program would output several sets of deconvolved data, one in which all flagged items were replaced with linear white noise fits, one in which calpulses and HWPR moves were added back in, and one in which all flagged items including cosmic ray hits were added back in to the data after the removal of the transfer function. The multiple data sets for each bolometer time stream were created for use in other pipeline procedures prior to map making. A visual of the results of the processing stages of the pipeline is shown in Figure 4.2.

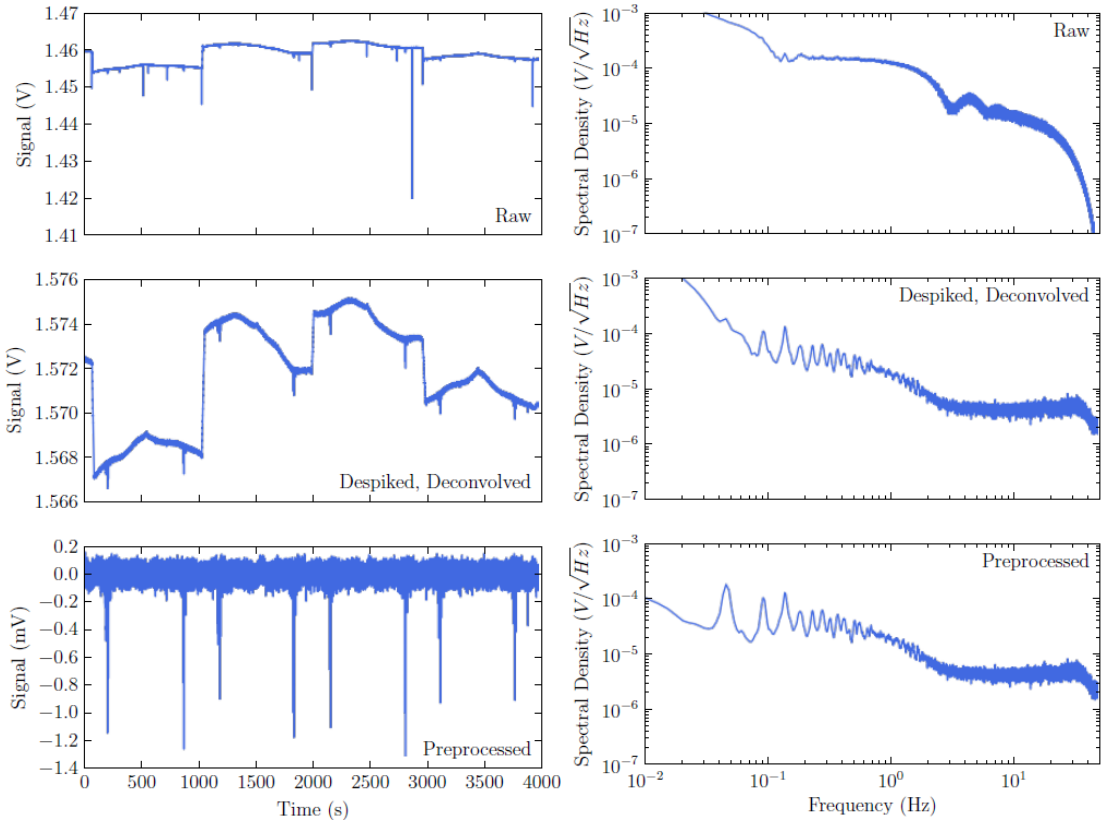

Figure 4.2: Figures from Benton (2015) illustrating the effect of the deconvolution and despiking process on a typical bolometer as well as from the additional pre-processing of the data time stream. The left column shows the TOD from a representative one hour scan period of Vela C while the right column shows the respective noise spectra of the data. In the top row, raw data with cosmic ray spikes and calpulse responses can be seen as well as steps caused by HWPR moves. The noise spectra shows evidence of the 0.1 Hz $1/f$ knee as well as the transfer function filtering. The second row TOD shows the removal of spikes with the retention of steps from HWPR moves while the noise spectra shows the flattening to white noise over most the spectral range with the drop above 30 Hz from the low pass filter. The bottom row shows the pre-processed data that is ready to be put into a map maker. The HWPR steps have been removed as well as drifts dependent on the pointing elevation along with other effects that generally manifest as low frequency noise sources. The remaining peak signal is from scans across the bright RCW36 region.

4.1.2 Calibrated Detector Response Flat Fielding

The next task in the pipeline was the flat fielding of the individual bolometer channels. During the course of the flight the DC voltage level of the detectors drifts in response to changes in the detector environment. The drift is most highly correlated with the temperature of the 300 mK refrigerator bath which changes by several millikelvin throughout the flight due to changes in elevation viewing angle, and other systematics. To remove these drifts from the TOD we use calpulses. Drifts in the height of calpulses are entirely due to changes in detector responsivity as the load provided by this lamp is extremely consistent (Hargrave et al., 2006). In previous analysis cycles this drift had been removed by looking at the height difference between adjacent calpulses and then fitting a spline between them to create a responsivity correction factor that the detector data was divided by to normalize the calpulses response height.

The height of a calpulse is determined by fitting it to a template pulse shown in Figure 4.3. The template is chosen from a quiet region of scan data for a reliable central pixel with a different template chosen for each array. The amplitude from the fit of the calpulse is used for correcting the data as it is directly related to the responsivity of the detector which is linear over the power range provided by the calpulse. The procedure as originally conceived for the BLAST data reduction after the 2005 and 2006 flights is further described in Wiebe (2008); Truch (2007); Truch et al. (2009).

During the 2012 data analysis efforts, I took on the task of improving the flat fielding process. Previous analysis had relied on very basic fitting functions to determine the responsivity correction between calpulses. However, this provided only a rough estimate which was generally effective as changes in responsivity were quite small. With the HWPR moves we were concerned about larger drifts in the detector

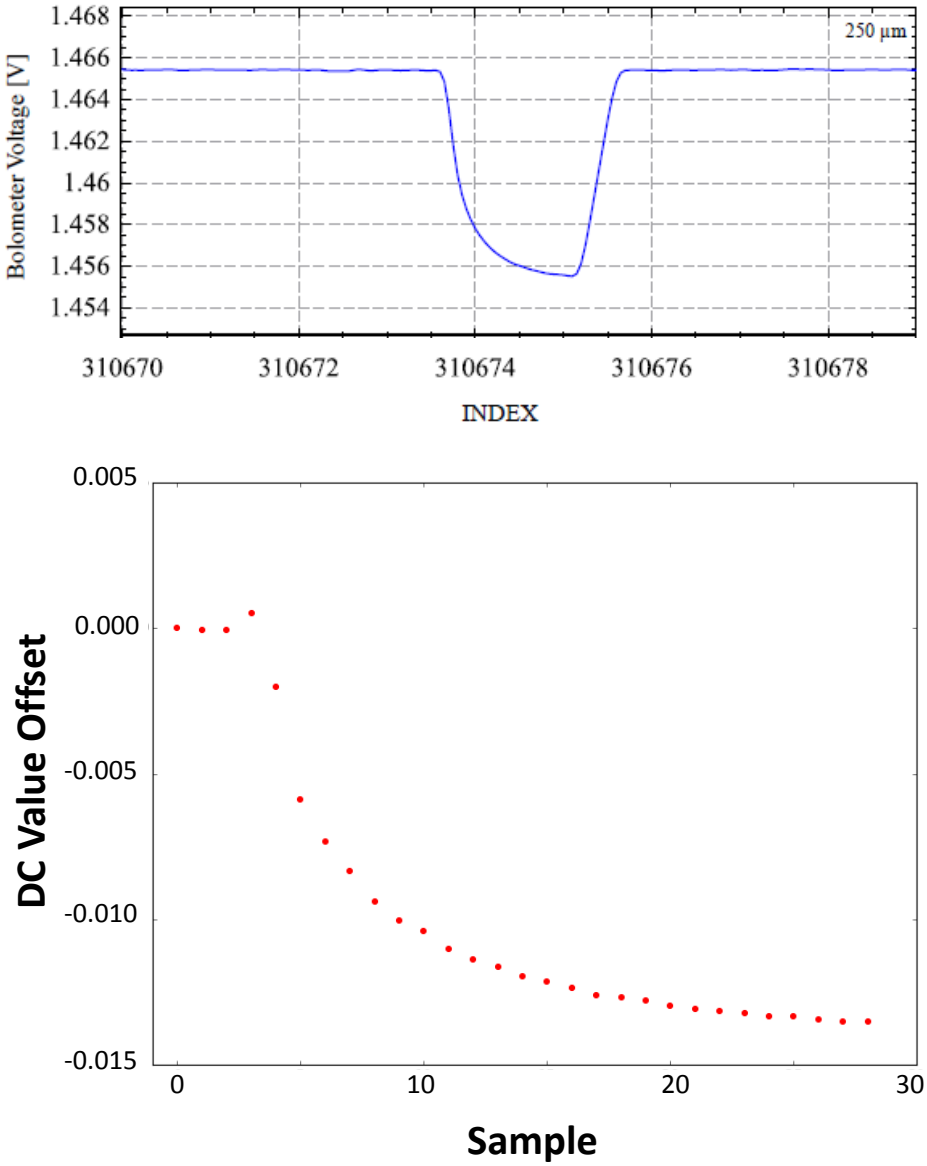

Figure 4.3: Top: A calpulse from the central bolometer of the 250 μm array (Angilè, 2013). The bottom panel shows the data points used for the 250 μm calpulse profile to which all calpulse from the 250 μm array were fit to determine their amplitude. The points are shown from the moment the lamp was turned on to the moment it was turned off and do not show the detector channel returning to its DC level as that is not included in the fit. The samples are collected at 100 Hz giving a pulse duration of $\sim$1/3 of a second.

responsivity and felt we could do a better job of correcting the responsivity on a sample by sample basis. To accomplish this task we examined correlations between calpulse height and potential sources that could cause the detector response to drift from which a high correlation was found to the DC detector level immediately prior to the pulse as shown in Figure 4.4. By making a linear fit to the correlation we could then predict the height of a calpulse anywhere in the TOD from the DC level of the detector response and use the information to normalize the power response of the entire detector time stream. The linear fits typical had uncertainties $< 1\%$ while calpulse heights would vary by up to 10%.

Normalization is accomplished by recognizing that a pulse in power dP on the detector has a corresponding voltage pulse dV which varies linearly with the DC voltage level, V_{DC} (See Equation 4.2). From these assumptions we can set up a differential equation and solve for the logarithmic function that converts the DC voltage level to the input power on the detector (See Equation 4.3). In this manner, we are able to eliminate drifts in the responsivity.

$$\frac{dV/V_0}{dP/P_0} = A * V_{DC} + R_0 \tag{4.2}$$

$$\frac{V_0}{P_0} P(V_{DC}) = \frac{1}{A} \log(A * V_{DC} + R_0) + C \tag{4.3}$$

The absolute calibration of the detectors is done at a later stage so P_0 and V_0, which are normalizing constants, can be ignored along with C as the offset is arbitrary. A and R_0 are values determined from the calpulse fit to V_{DC} which is performed for each channel separately as shown in Figure 4.5. The success of this method was measured by examining the height of the calpulse post this analysis (Figure 4.6) which showed a much tighter distribution compared to the raw data and the previous method.

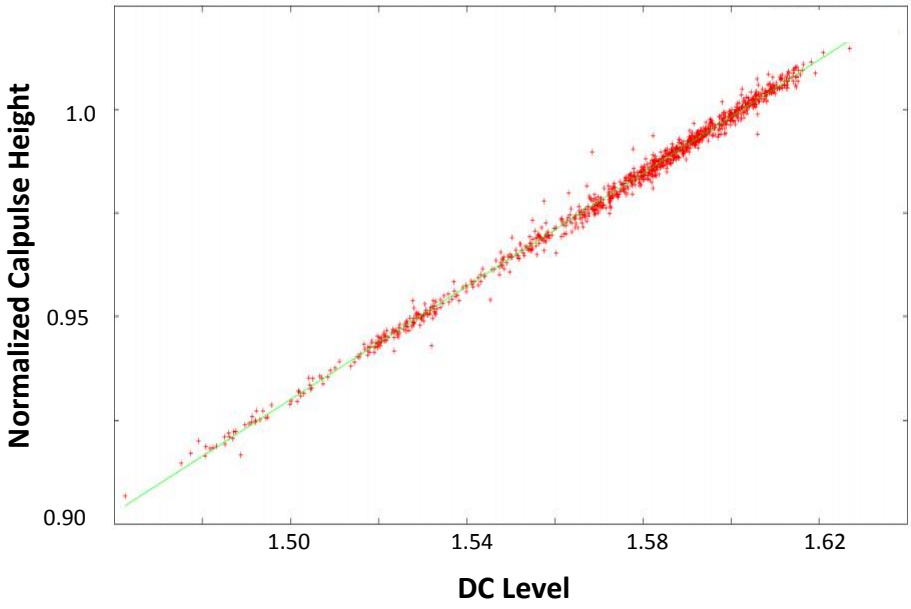

Figure 4.4: A typical linear fit result to the calpulse height and DC level of a central bolometer from the 500 μm array demonstrating the tight correlation observed. Outlying points from early in the flight and near fridge cycles have been removed.

4.1.3 Additional Data Reduction Performed

4.1.3.1 Pre-processor

Prior to initial maps being made, the TOD is run through a pre-processor which performs a number of vital tasks. There is an elevation dependent drift in the detector loading likely due to change in the quantity of atmospheric gas we are looking through as our pointing elevation changes. To remove it, the loading is modeled as function proportional to $\csc(\theta_{EL})$ which was shown to work well to remove the elevation dependent drifts in scans across targets.

The sudden shift in a detector's DC level due to HWPR moves must also be removed. The HWP's physical properties are not uniform across its diameter meaning each detector samples a different section of the HWP which changes after every move

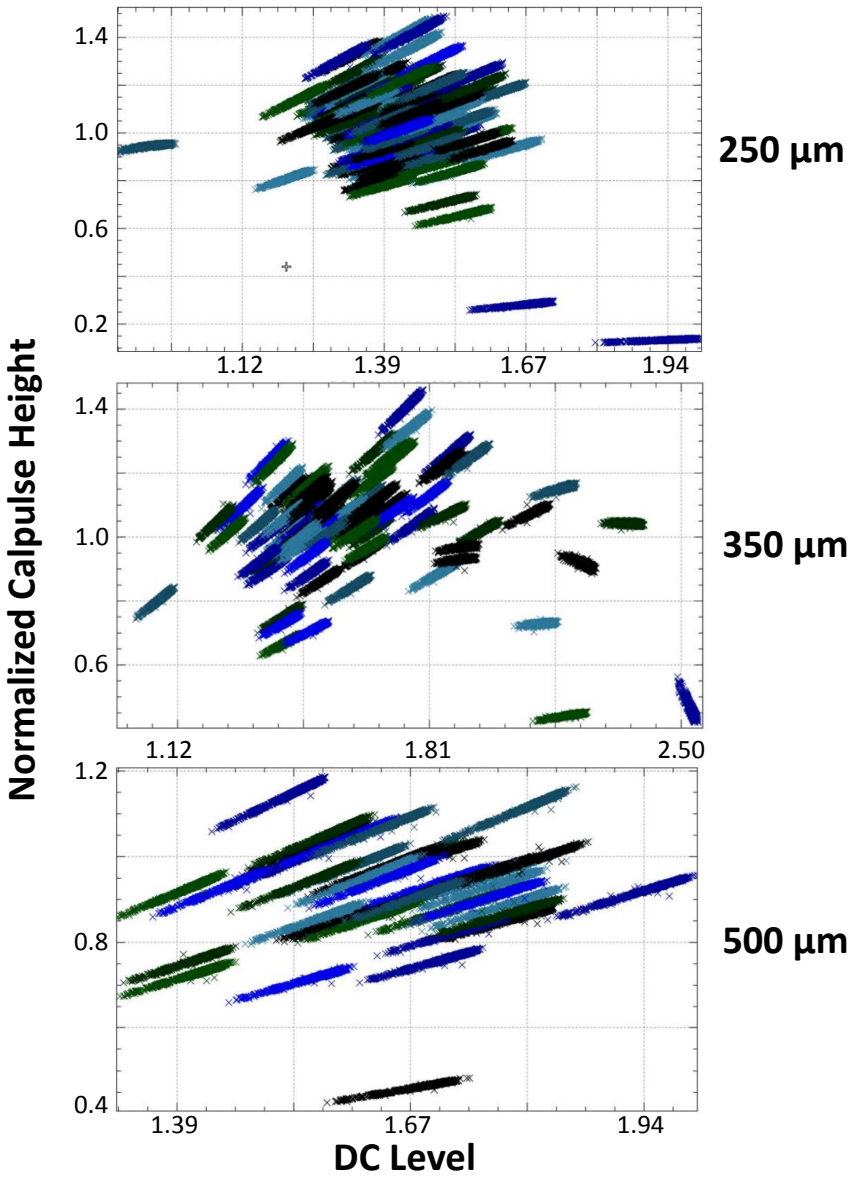

Figure 4.5: Normalized calpulse amplitudes versus the DC level for all bolometers as separated by array. The high correlation can be seen in all channels with most bolometers exhibiting similar responses. The different offset levels could be from differing illumination across the array by the calibrator or the fact the bolometers share a bias and the optimization of the bias level is done for an array and not individual bolometers. The similar slopes in all detectors are indicative of the responsivities between detectors being nearly identical. Some anti-correlated channels are observed in the 350 μm array which were filtered out as bad channels due to the observed deviation.

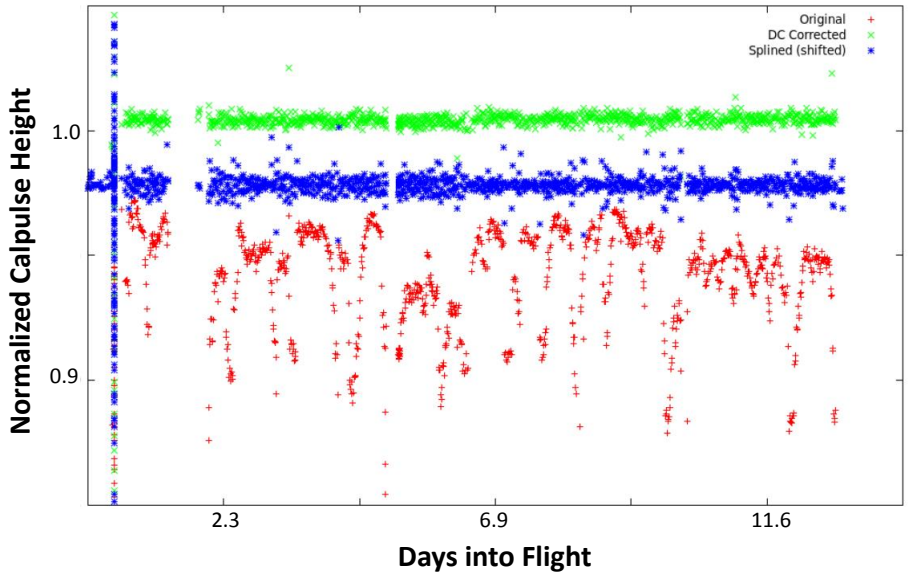

Figure 4.6: Normalized calpulse heights for the entire flight for a central bolometer in the 350 μm array. The red points show the heights from the flight data prior to flatfielding, the blue points show the normalized heights using the previous method of flatfielding, and the green points show the results from the new method developed for the 2012 data with standard deviations of $\lesssim 0.02$, $\lesssim 0.01$, and $\lesssim 0.005$, respectively. The much tighter distribution demonstrates the effectiveness of the method at providing consistent flatfielding for the entire time stream. The spike near the beginning of the flight is from calpulses commanded during scans of Saturn during which bias levels were adjusted along with higher than normal signal causing anomalous readings. Those points were excluded from the fitting procedure.

and causes the shift in response. A fit to the detector TOD with a function using two exponential functions was used to remove the drift after HWPR moves to allow us to recover data as close to the move as possible. The two functions used different time constants with one constrained to shorter time periods of ∼10's of seconds and the other constrained to longer periods of ∼ 100's of seconds. The fits used only the first 30 seconds of data after a move to ensure the larger response at short timescales was fit well.

The residual from the subtraction of the pre-processor fits is removed with a 5 mHz

high pass pass filter which reduces the signal below the $1/f$ knee of the detectors in a regime with no useful signal for BLASTPol. The filter also serves to eliminate any discontinuities that remain in the data which would cause issues for further analysis steps that use a FFT. Finally, the pre-processor replaced the linear fit white noise filled gaps inserted by the deconvolution with a bolometer noise model created by analyzing the noise spectrum from flight data.

4.1.3.2 Pointing Offsets and Array Flat Fielding

From the pre-processed data, maps are made with the simple **naivepol** map maker which makes accurate intensity maps that are used in several other pipeline processes. In Section 4.1.2 the individual detector's responsivities were corrected, however, the responsivity of detectors varies over the array. The entire bolometer array is flat fielded with respect to each other such that no channel contributes either a higher or lower signal than the rest of the array. The array flat fielding was done by performing aperture photometry from observations of a calibrator source, Compact calibration source IRAS 08470-4243 (Mickey). The aperture photometry was done in a circle of $2.5'$ to fully encompass the distorted beam we observed, with a background level subtracted from the average value in annulus of $2.5'$ to $3.0'$. The central bolometer's value was then taken and all the other bolometers were normalized to this bolometer such that after flat fielding the array would have the same photometric response for each detector, as shown in Figure 4.7.

The maps of the calibrator Mickey were also used to determine the pointing offset between individual detectors as well as the initial pointing offset between the arrays and the star cameras. The Mickey maps were made frequently during the flight with sufficient coverage to make beam maps for each detector. The central peak of each map was used to determine the individual detector's pointing which could then be compared to the pointing of other detectors in the array. The pointing offset between

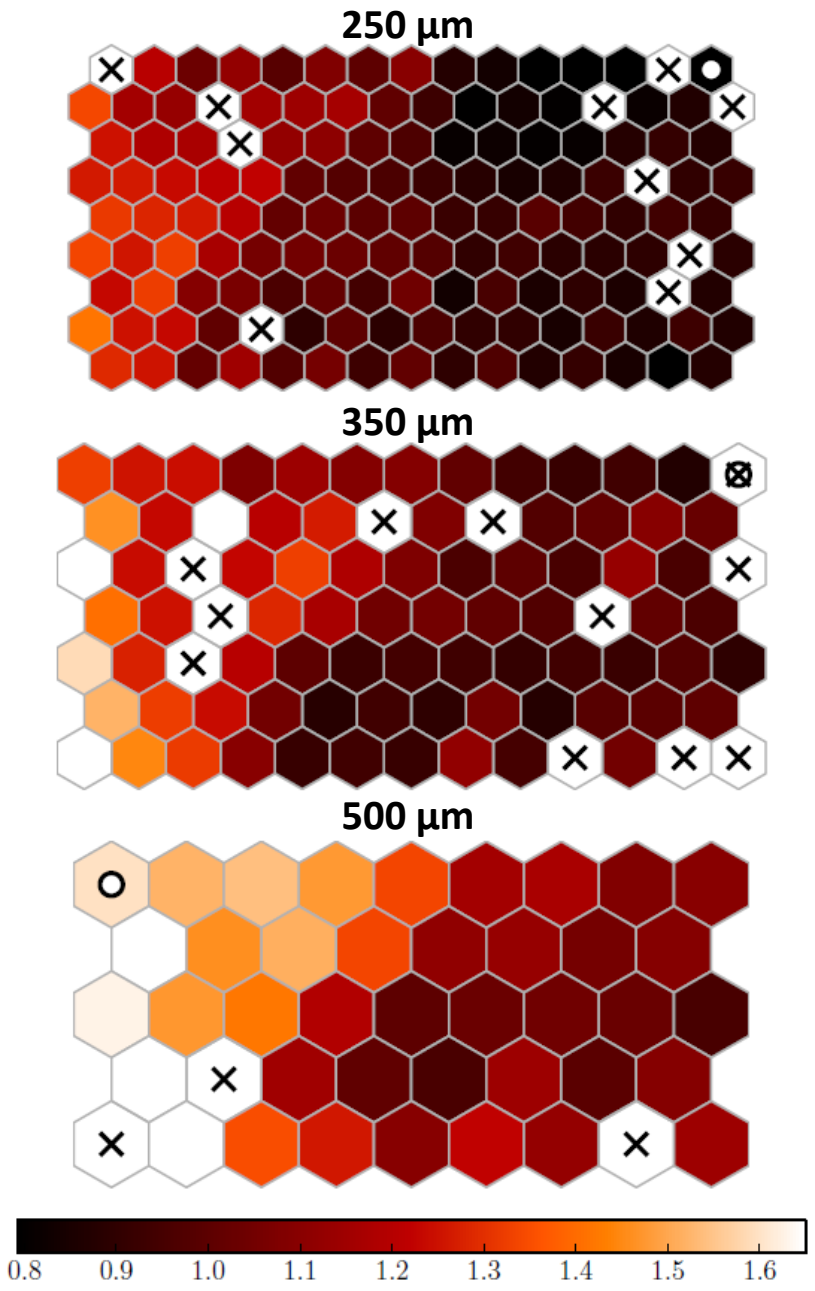

Figure 4.7: An image of the flat fielding coefficients used to adjust the gain on each individual detector to normalize them to the central pixel of each array. Coefficients were determined from observations of the calibration source Mickey. × indicates pixels that were determined to be bad while ∘ indicates the pixel indexed as the first in each array as described in Benton (2015).

individual detectors did not move significantly over the flight due to the rigidity of the cold optic's structure. The star camera's pointing frame is described by the pointing solution it generates from which the bore site of the telescope and of the detector arrays differs with a time dependence due to thermal fluctuations in the framework as well as changing mechanical loading at different pointing elevations. The pointing offsets between the star camera pointing solution and the detector's observations of Mickey were used to establish a baseline offset which was improved on with maps from the Herschel SPIRE instrument.

We spent long periods between observations of Mickey scanning targets at different pointing elevation and azimuth. This required us to create source dependent pointing offsets between the arrays and the pointing solution. We took Herschel observations of our targets with known pointing and put them through a simulated observing routine to create simulated BLASTPol maps which were then compared to the actual BLASTPol maps to determine an offset. The offset solution was then fed back into the simulated observations and the process repeated until the two converged to a pointing offset better than $10''$. The technique is described in greater detail in Gandilo (2015).

4.1.3.3 Beam Shape Analysis

From the **naivepol** maps we are also able to analyze our beam pattern in all three bands. During the testing prior to flight, detailed in 3.2.7, we were able to perform beam maps of the entire optical system only at the $500\,\mu$m band due to atmospheric attenuation that makes beam mapping at 250 and $350\,\mu$m unfeasible. The tests are primarily to determine the proper focus of the instrument prior to flight but have served to determine beam abnormalities. However, we only know our full beam characteristics at all three bands after post-flight analysis. From individual bolometer maps of Mickey we found our beam was significantly distorted as shown in Figure 4.8, likely due to warping of the cold or warm optics from previous flights and

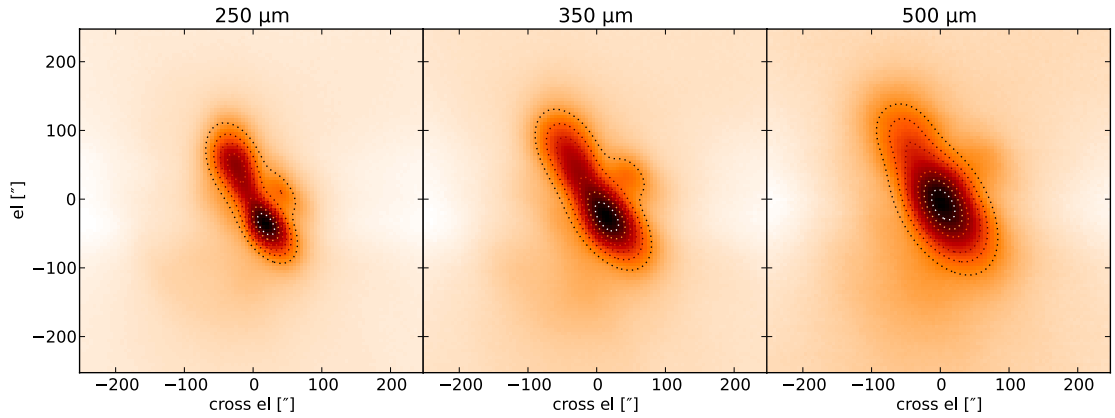

Figure 4.8: The reconstructed beam shape from observations of Mickey with 250, 350, and 500 μm shown from left to right. The 250 and 350 μm shapes are well described by three elliptical Gaussians which fit the two primary lobes as well as a much fainter third lobe on the right side. The 500 μm shape can be described by a single elliptical Gaussian. The contours represent the result of the fits to the beam shapes and can be seen to accurately reproduce the power distribution. These maps were made with data from all the bolometers and do not show the variation between pixels.

their subsequent hard landings in Antarctica. As part of the analysis we performed fits of the beam shape with the hope of deconvolving it from the maps to gain higher resolution. However, we found that the shape varied across the array and also had a time dependent component making it difficult to make a beam model over the course of a target scan.

Instead, we performed fits to the beam shapes using three elliptical Gaussians for the 250 and 350 μm channels and a single elliptical Gaussian model for the 500 μm array to determine the approximate beam shape for each detector during a scan. For our first round of publications we used a method described in Fissel et al. (2015) to smooth out the beam shape to the width of the long axis in order to create 2.5′ resolution maps with a nearly Gaussian beam profile as shown in Figure 4.9. Additional work is ongoing to reconstruct maps that would have a higher resolution closer to the short axis of the elongated beam.

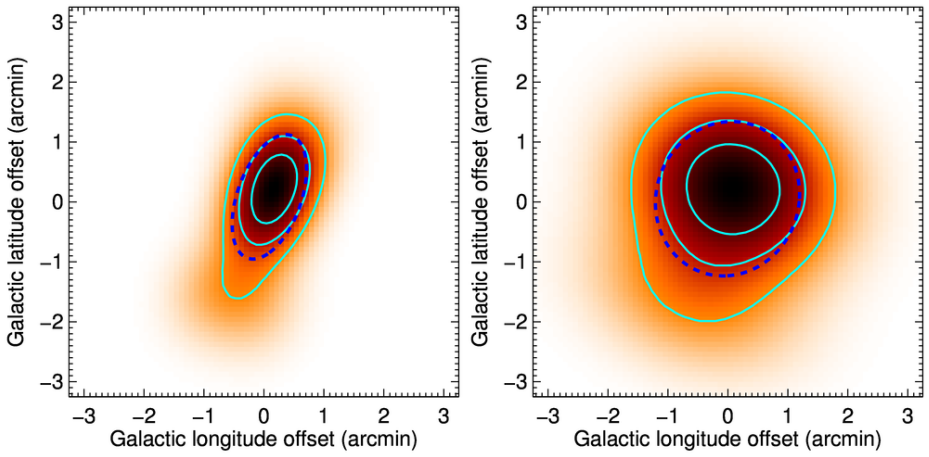

Figure 4.9: Left: The beam model at 500 μm for the Vela C map which shows the distorted elliptical Gaussian shape. Right: The beam shape post convolution with a smoothing kernel described in Fissel et al. (2015). The cyan contours show the level of the signal at 25, 50, and 75% of peak brightness. The FWHM of the elliptical Gaussian fit to the model is shown with the dashed blue line.

4.2 BLASTPol Map Making

Pre-processed TOD data is next fed into the map making programs to produce intensity and polarization maps of our targets. There are a variety of map making tools used to produce the highest quality images possible. The simplest tools are **naivepol** and **naivemap** which can create total intensity and polarization maps, respectively. The naive map makers use a high pass filter to greatly simplify the ideal map maker problem. However, this biases the result as the filter discards both noise and signal. The naive map makers are still quite useful in creating quick maps that can be used in the data reduction process as mentioned above.

Another tool used is **simsky** which takes telescope pointing data and an input map and then simulates the BLASTPol observations of the map to create a simulated TOD. The simulated data can then be fed into any map maker to allow the result to be compared to the original map, whether that be a BLASTPol map or a Herschel map. **simsky** is used for a variety of purposes including refining noise models, improving

map reconstruction, and checking pointing solutions.

The optimal map maker that was used for BLASTPol is TOAST (Kisner, 2014) which solves for the generalized least squares map and is highly modular making it easily adaptable to different experiments. One of the primary products needed to make maps with TOAST is a well constrained model of the power spectral density of the BLASTPol detector noise. The method to produce this along with other details of the implementation of the map maker can be found in Benton (2015). Output products of the map maker were scrutinized for accuracy through direct comparison with *Planck* intensity maps and SPARO polarization maps which generally showed strong agreement. TOAST would output I, Q, and U maps which were ready for scientific analysis, along with a covariance matrix that could be used for uncertainty calculations.

4.2.1 Polarization maps

All the linear polarization information is contained within the first three elements of the Stoke's vector S. I represents the total intensity and Q and U contain the information of the linear polarization of the light. V is the component that encases the circular polarization information which is not relevant to our science and to which our detectors are insensitive. From the Stoke's parameters we are able to reconstruct the polar coordinate representation of the polarization as shown in Equations 4.4 through 4.7.

$$S = \begin{bmatrix} I \\ Q \\ U \\ V \end{bmatrix} \tag{4.4}$$

$$P = \sqrt{Q^2 + U^2} \tag{4.5}$$

$$p = \frac{P}{I} \tag{4.6}$$

$$\phi = \frac{1}{2} \arctan\left(\frac{U}{Q}\right) \tag{4.7}$$

P is the magnitude of the polarization, p is the polarization fraction, and ϕ is the angle of the polarization on the plane of the sky. Due to the fact that p is a positive definite quantity the noise in Q and U can lead to an over estimate of the polarization magnitude. To address this issue P and p are debiased before maps are created with methods drawn from Plaszczynski et al. (2014) and shown in Equations 4.8 and 4.9.

$$P_{debias} = P - \frac{\sigma_P}{2P} \tag{4.8}$$

$$p_{debias} = p - \frac{\sigma_P}{2PI} \tag{4.9}$$

σ_P is the variance in P calculated from the elements of the I, Q, and U covariance matrix produced by TOAST. p_{debias} will be referred to as p from this point forward.

4.2.2 Background Subtraction

BLASTPol observes targets that are on scales of 10's of degrees at most meaning the maps lack the information to find a zero point and instead have some arbitrary offset. Additionally, the dust emission observed is optically thin which necessitates great care in separating out the signal intrinsic to the target from the galactic background. As such, the BLASTPol maps do not use an absolute calibration for most of the analysis and instead rely on a method of background subtraction to set an artificial zero point which removes the signal extrinsic to the target. To determine the background offset level a reference region is created off of the main target in a low signal area with good cross-linking, described in Section 3.4, to ensure a reliable

measurement. An average value for I, Q, and U is taken in the reference region and subtracted from the entire map from which the p, P, and ϕ maps are generated. The polarization pseudo-vectors determined for the target are then relative to the subtracted background. In this way the offset issue is solved while also separating the signal of the desired target from the background galactic emission. This is especially pertinent as it has been discovered by previous experiments as well as BLASTPol that the polarization fraction is inversely proportional to the column density. This means that while the overall background intensity is much lower off the cloud than on it, the polarization fraction can be significantly higher, up to 15%, in these regions which requires a much more careful subtraction of the polarized background signal.

For the Vela C analysis the process was taken a step further with two types of reference regions created to generate conservative and aggressive subtraction methods. In the conservative subtraction case an average flux in I, Q, and U is taken from a diffuse region off the main cloud and subtracted from the map. In the aggressive subtraction case a region is defined on both sides of the cloud and a plane is fit between these two regions. This was done in an attempt to characterize the change in emission as a function of distance from the galactic plane and is a more aggressive cut as the reference regions are closer to the cloud and have a higher intensity signal. An intermediate method was also made which is a combined average of the two subtraction methods. The aggressive method also defined the bounds of a validity region between the two reference region bars on either side of the cloud. The plane fit was only valid in this zone and so only points in that region were considered for further analysis. Additional cuts were also made based on signal to noise of the polarization fraction, of the intensity, and for agreement in angle ϕ between the wave bands for a given pixel as described in more detail in Fissel et al. (2015); Gandilo et al. (2015). The Vela C map along with reference regions is shown in Figure 4.10.

An inherent issue with the background subtraction method is found in regions

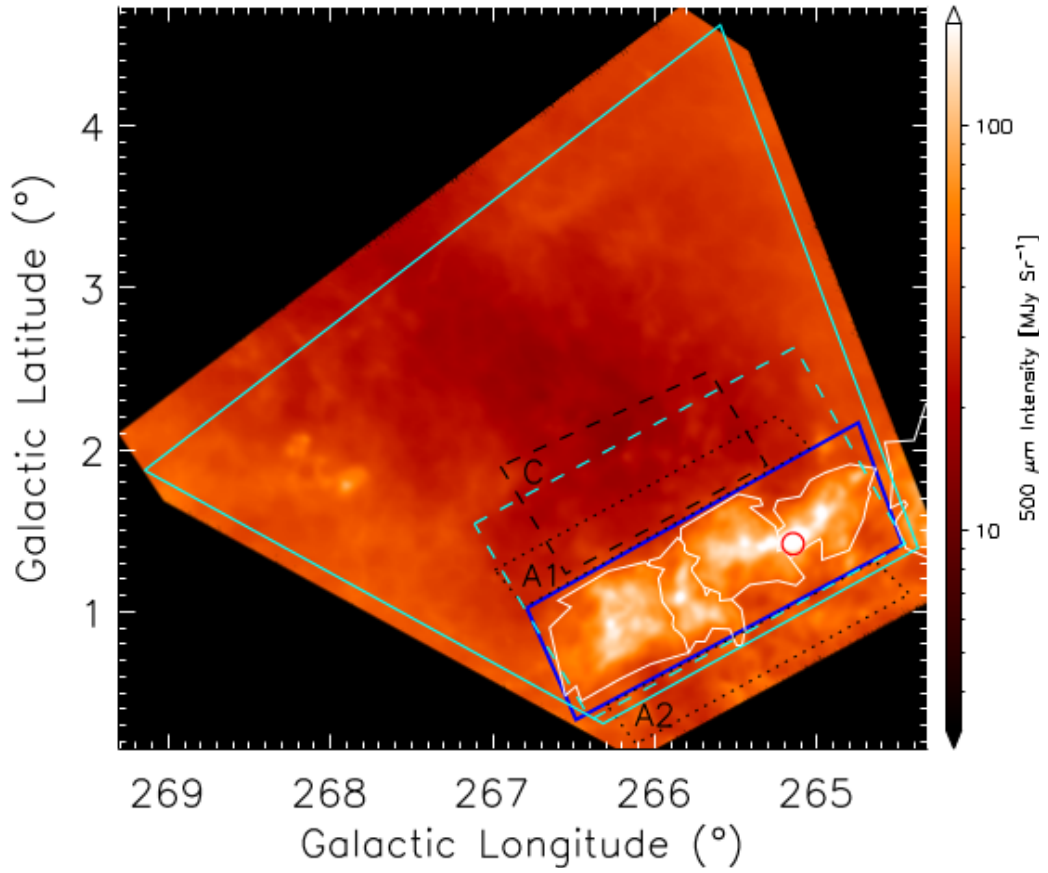

Figure 4.10: This map shows the area covered by the mapping of the Vela C GMC from the BLASTPol 2012 flight. On it are shown the regions with robust data as well as the reference regions used for background subtraction. Region C is used for a conservative background subtraction method whereas regions $A1$ and $A2$ are used in the more agressive planar fit background subtraction method and are used to define the boundaries of a validity region inside of which polarization data can be used for analysis. Additionally, the red circle indicates the area excluded from analysis around the HII source, RCW36, which is an internally heated region with active star formation.

where I is close to the background level which causes $p = P/I$ to artificially diverge as I goes to zero. To address this issue a cut is made to exclude areas below a certain A_V to eliminate the possibility of including divergent points. However, doing so means we cannot analyze the data from the observed diffuse regions using the background subtraction method. In order to do so we have worked to establish an absolute calibration which can be accomplished by using *Planck* High Frequency Instrument (HFI) data with intensity corrections supplied by the 545 GHz and 857 GHz channels which nearly align with the BLASTPol 500 and 350 μm channels requiring limited color corrections. However, polarization data does not exist for these channels and so corrections in Q and U must be done with projected values from *Planck*'s 353 GHz channel. The projections rely on dust models that are not entirely understood and will require careful analysis to avoid biasing. Efforts to do so are ongoing with more detail in Benton (2015).

4.3 Herschel Map Making

We used Herschel maps both as a more detailed map of intensity, as it has a higher resolution than BLASTPol, and for spectral energy distribution (SED) fitting to create maps of hydrogen column density and dust temperature. We worked with the three SPIRE bands that correspond to the BLASTPol bands for maps and also included the PACS instrument's 160 μm band for SED fitting purposes. Herschel maps were generated using the Scanamorphos map maker (Roussel, 2013) and additional reduction and manipulation was done in The Herschel Interactive Processing Environment (HIPE). All maps were obtained through the Herschel Science Archive which makes all Herschel data public. The particular data sets I used were obtained in parallel mode observations in which the PACS and SPIRE instruments image the sky simultaneously with a small offset between the center of their FOV. All such

data sets were comprised of at least two scans of the region which generated good cross-linking and a high signal to noise map resulting in some of the highest quality images available for submillimeter astronomy.

The absolute offset of the maps was obtained for the SPIRE bands with the **zeroPointCorrection** task in HIPE which uses methods similar to Bernard et al. (2010) and Juvela et al. (2011). It determines an absolute calibration of the Herschel maps by comparing to maps produced by the *Planck* HFI which can then be used for comparison to BLASTPol maps and for more accurate results from using **simsky**. However, at the time of processing the correction task was unavailable for the 160 μm maps which led us to develop a method of background subtraction similar to that used for the polarization maps to process the Herschel maps for SED fitting as described in Chapter 5.

The last step in preparing the maps prior to SED fitting was to convert them to the same resolution and pixel size to allow a pixel by pixel SED fit. We used the Gaussian smoothing task in the HIPE interface as well as Gaussian smoothing routines in **python** where the smoothing kernel was determined by Equation 4.10. I created sets of smoothed maps for all wavelengths at several resolutions including the $35.2''$ resolution of Herschel's 500 μm channel, the $2.5'$ resolution of BLASTPol, and the $5'$ resolution of *Planck*.

$$\sigma = \frac{\sqrt{35.2^2 - R^2}}{P \times 2 \times \sqrt{2 \times \log 2}} \tag{4.10}$$

P is the pixel size of 2.85, 4.5, 6.25, and $9''$ for the 160, 250, 350, and 500 μm channels, respectively, and R is the resolution of the bands as given in the Spectral and Photometric Imaging Receiver (SPIRE) handbook (Valtchanov, 2014) of 13.6, 17.6, 23.9, and $35.2''$ for the 160, 250, 350, and 500 μm bands, respectively. The maps were then re-gridded using a linear two dimensional interpolation function to

determine values from the 160, 250, and 350 μm maps at the pixel locations of the 500 μm map (Egg et al., 2016).

Maps of Vela C at each wavelength at their highest available resolution are shown in Figure 4.11. Maps smoothed to the $5'$ resolution of *Planck* can be seen in Figure 4.12. Additionally, Figure 4.13 shows 500 μm images at $35.2''$ resolution produced for analysis of a number of other targets observed by BLASTPol that are currently undergoing scientific analysis in preparation for publication.

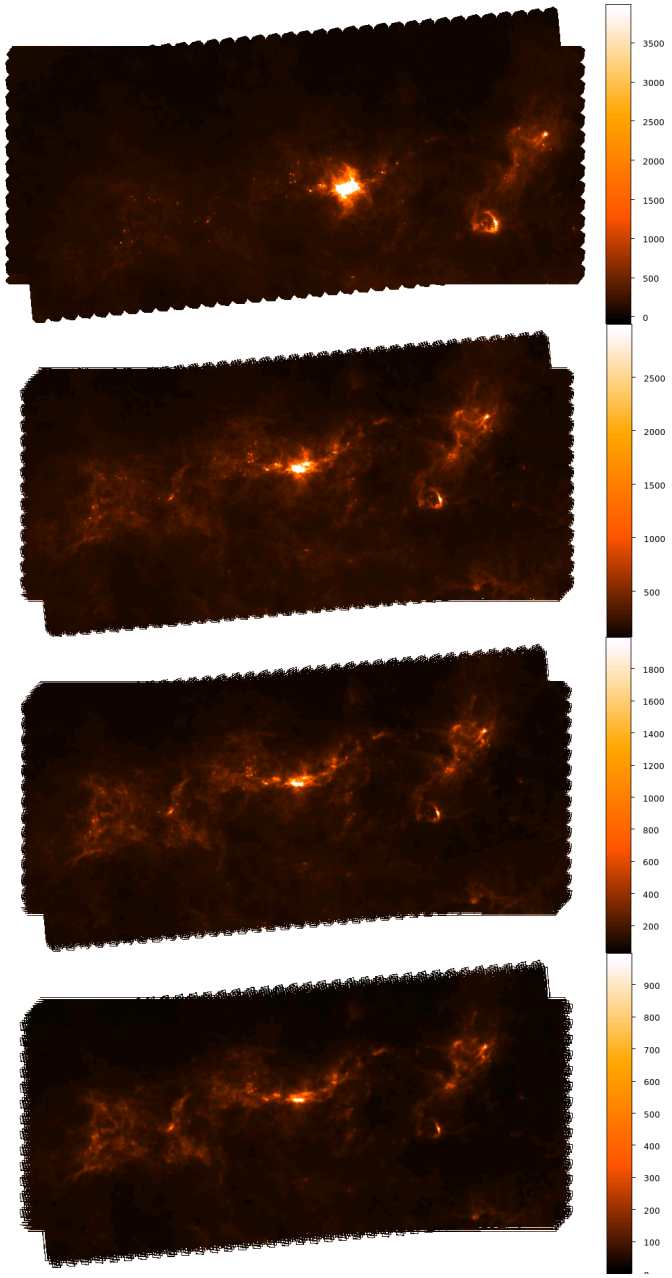

Figure 4.11: The images are, from top to bottom, 160, 250, 350, and 500 μm Herschel images of the Vela C GMC at their diffraction limited resolution of 13.64, 17.6, 23.9 and 35.2$''$, respectively. Images were produced using the Scanomorphos map maker with post-processing conversion of units to MJy/sr for all maps.

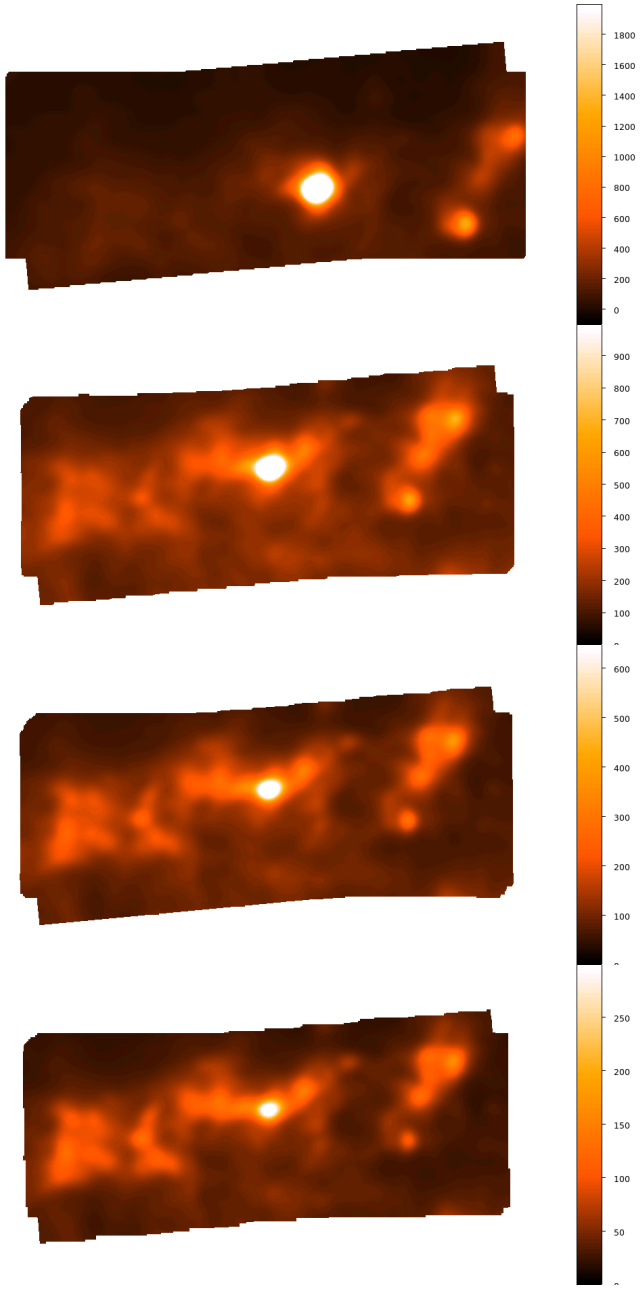

Figure 4.12: The images are from top to bottom 160, 250, 350, and 500 μm Herschel images of the Vela C GMC smoothed with a Gaussian kernel to 5′ resolution. Images were produced using the Scanomorphos map maker with post-processing conversion of units to MJy/sr for all maps.

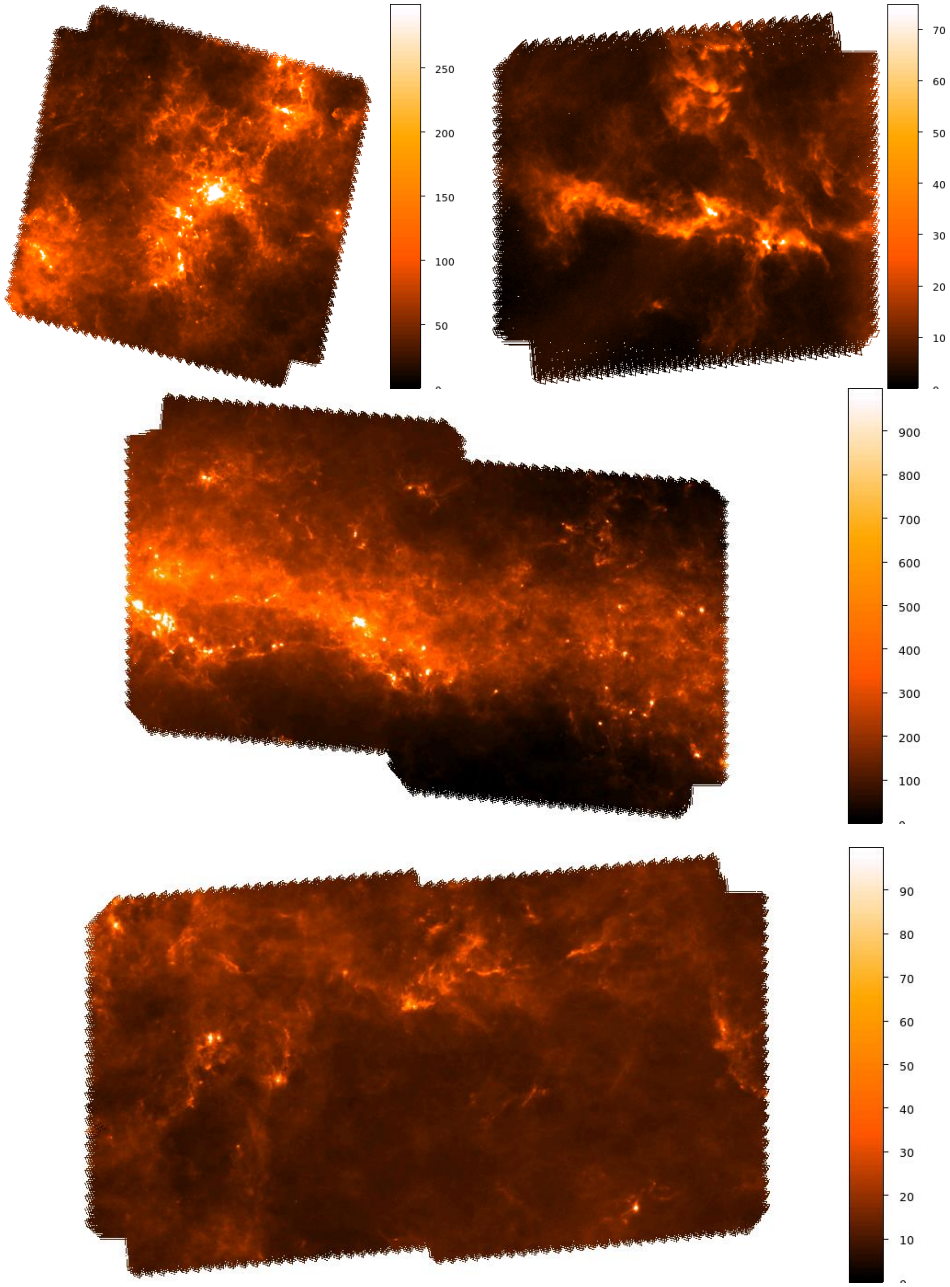

Figure 4.13: Herschel maps produced using the Scanomorphos map making procedure of four of the primary targets observed by BLASTPol. The top left image is of the Carina nebula complex, the top right image is of the Lupus molecular cloud, the middle image is of the G331 molecular cloud, and the bottom image shows a portion of the Puppis cloud complex.

Chapter 5

BLASTPol 2012 Scientific Analysis

5.1 Data products overview

Once the I, Q, and U maps as well as the P, p, and ϕ maps had been made for the Vela C, Carina, Puppis, and Lupus molecular clouds we could begin the scientific analysis of our data. Of the targets observed, the data coverage and cross linking was strongest on Vela C and Carina, thus the majority of our analysis has been focused on these two targets. The map of Vela C created with BLASTPol data is shown in Figure 5.1. Other targets will be examined in future work as they require additional analysis efforts to remove systematics due primarily to limited time spent observing them. The lower signal to noise and limited cross linking on these targets makes it create high quality map.

To complement our maps of the two primary regions, we also obtained *Planck* polarization maps at 353 GHz (850 μm) an example of which is shown in 5.2. The maps recently became publicly available which gave us access to calibrated I, Q, and U maps, albeit at a significantly lower resolution of $5'$. The maps were used as a check that our vectors were in agreement with a major experiment, to provide a means of absolute calibration, and as an additional data point for polarization spectra

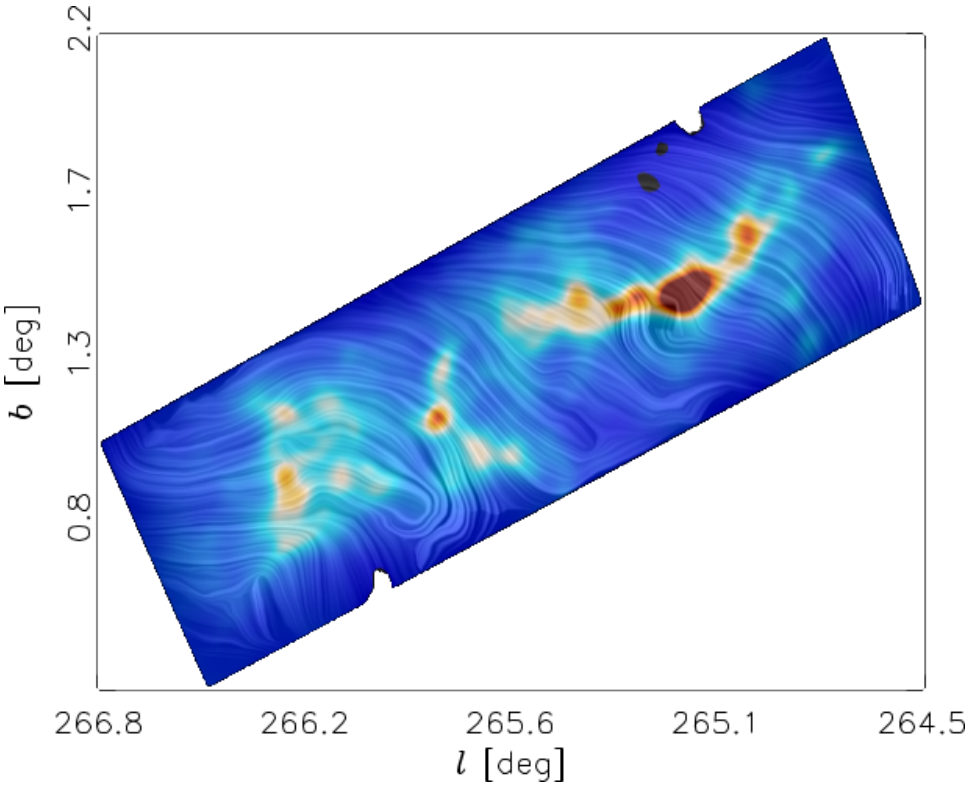

Figure 5.1: An image formed from the line integral convolution (Cabral and Leedom, 1993) of the intensity map at 500 μm, colorscale, and the orientation of the magnetic field on the plane of the sky, captured in the striations (Fissel et al., 2015). The relation between the structure and the magnetic field undergoes further statistical analysis to glean information about how the two are related. The image uses magnetic field information prior to any cuts on signal to noise of the measurements and thus is illustrative of the detail BLASTPol is capable of but cannot be used for quantitative analysis.

measurements.

The final complimentary component used for our analysis were the Herschel intensity maps that I compiled. The maps are important as an in band calibration of intensity since Herschel measurements have significantly higher resolution than BLASTPol as well as better calibration as shown in Figure 5.3. In addition to the usefulness of the intensity maps, I refined a SED fitting method that allowed me to create atomic Hydrogen column density maps and dust grain temperature maps from fits to the PACS 160 μm map and the SPIRE 250, 350, and 500 μm maps. These

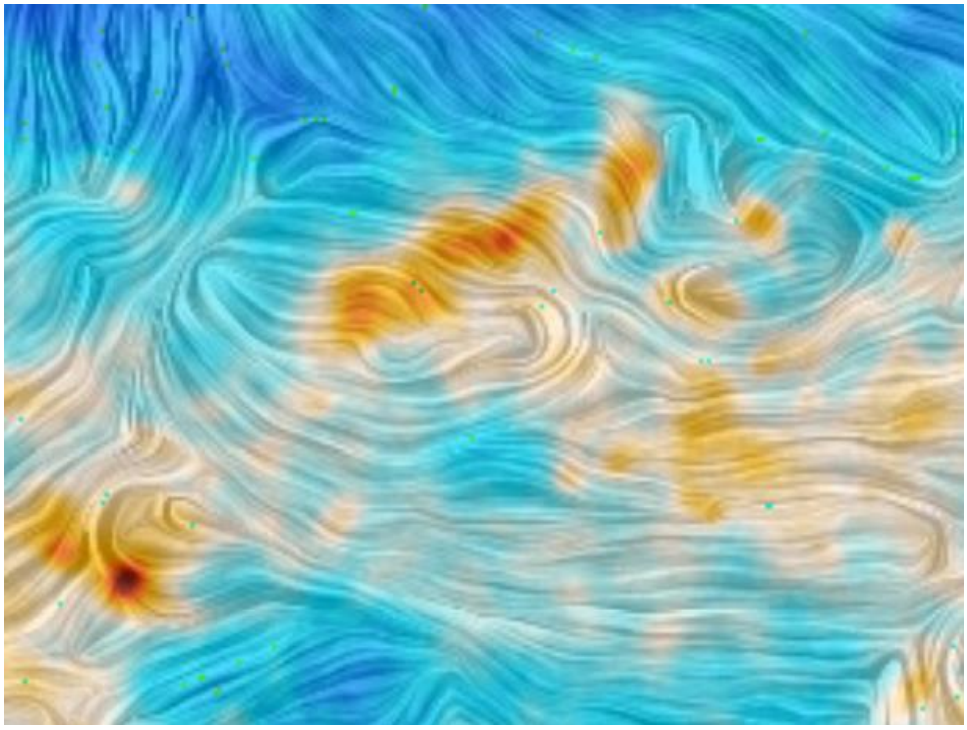

Figure 5.2: A map of the Vela GMC at 850 μm which also shows the background level that comes from unresolved galactic ISM and Gum nebula emission. The colors represent intensity with high intensity in red and low intensity in blue while the striations are produced by the same method described in Figure 5.1. The map was created with *Planck* data for comparison with BLASTPol data, courtesy Juan D. Soler.

maps have been very useful as a complementary component to the BLASTPol maps as a number of predictions of dust alignment mechanisms and magnetic field interactions are dependent on cloud environment. For instance, knowing the column density of a cloud allows us to understand the structure as well as to compare models of dust grain alignment with our observations. Additionally, the temperature of the cloud is indicative of the source of heating, whether it be internal heating by active star formation or external heating from the inter-stellar radiation field (ISRF). The temperature components can also play an important role in determining the shape of the polarization spectra as it has been theorized that steep drops and rises previously observed in the spectrum around 350 μm could be from multiple temperature

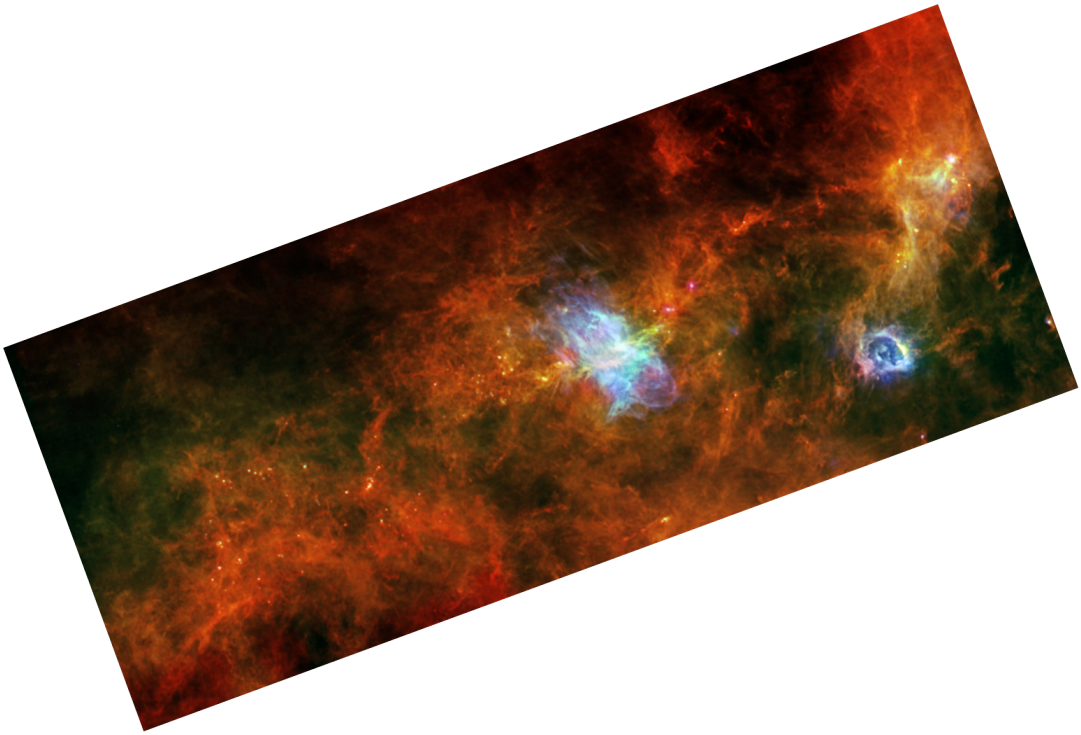

Figure 5.3: A color map of the Vela C GMC created from the 160, 250, and 350 μm Herschel bands which are shown in blue, green, and red, respectively. Map is from Hill et al. (2011).

components along the line of sight (Hildebrand et al., 1999).

5.2 SED Fitting

A SED function describes a modified blackbody emission spectra where a blackbody function as described by Planck's Law is:

$$B_\nu(\nu, T) = \frac{2h\nu^3}{c^2} \frac{1}{\exp \frac{h\nu}{kT} - 1} \tag{5.1}$$

ν is the frequency of light, h is Planck's constant, k is Boltzmann's constant, and T is the temperature of the blackbody. The basic blackbody function is then adjusted to accurately describe the emission from dust grains. The equation that was fit in

our basic two free parameter models is as follows:

$$F(\nu) = \frac{N_H}{N_0} * \left(\frac{\nu}{\nu_o}\right)^{\beta} B(\nu, T) \tag{5.2}$$

The primary modifications to the blackbody function include a spectral index β that controls for the dependence of the grain emissivity on frequency in different regimes of blackbody emission (Erickson et al., 1981; Schwartz, 1982). For dust emission in the submillimeter for regions that lie within the low temperature range we observe, $\lesssim 50\,\mathrm{K}$, it is generally assumed $\beta = 2$ which corresponds to silicate grain populations (Gezari et al., 1973). Fitting β independently is notoriously difficult due to the fact that it has a degeneracy in the fit with T such that increasing one can be compensated for by decreasing the other creating an anti-correlation between β and T that has no bearing on the physical properties of the cloud (Tabatabaei et al., 2014; Kelly et al., 2012). As such, values are typically chosen for β between 1.0 and 2.0 as determined by more in depth studies of the SED function. Our analysis also tends to be less affected by the degeneracy as we examine trends in T and are less sensitive to its absolute value.

Additionally, the function is modified by a calibrated parameter from Hildebrand (1983) that is a function of optical depth of the cloud. This free parameter N_H/N_0 is unitless and accounts for the fact that the amount of flux scales directly as the amount of dust along the LOS. The units of Hydrogen column density come from a calibration constant that uses a predefined ratio of dust emission to hydrogen column density provided by previous observations. $N_0 = 1.2{*}10^{25}$ atom/cm^2 is the calibration provided by Hildebrand (1983) for ν_o equivalent to $\lambda_o = 400\mu$m. Examples of the fitting function in action can be seen in Figure 5.4.

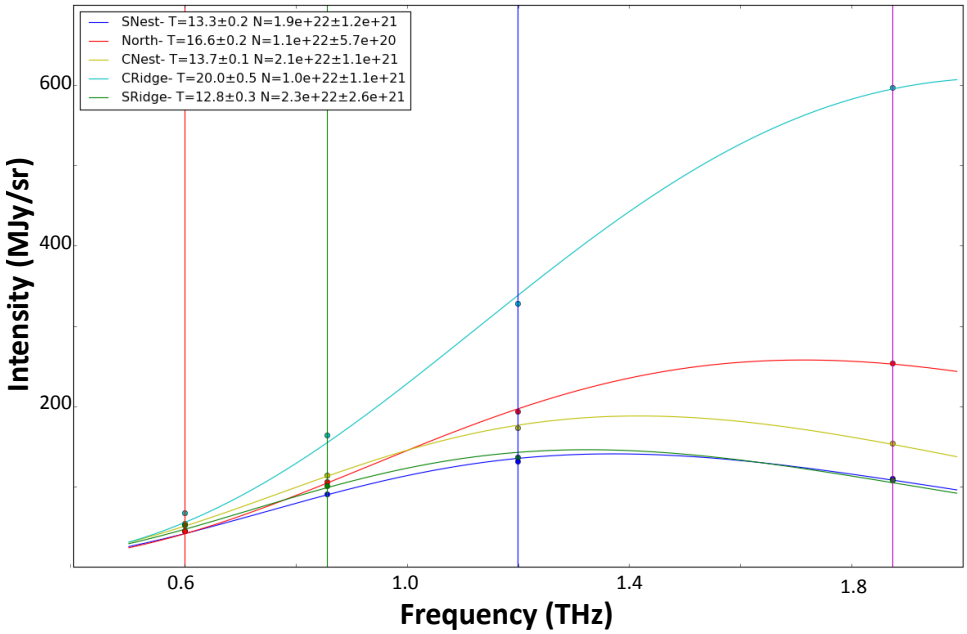

Figure 5.4: SED fits with temperature and column density as free parameters are shown for all of the primary regions of the Vela C GMC. Points represent averaged intensity values for the entire region in each band post subtraction of the average background level in reference region 1. The points were used to test the effectiveness of adjustments in the fitting program. Error bars on the points were not used in the analysis to weight the fits as the trends examined with temperature and column density are driven by the spread and the uncertainty of our polarization measurements. The vertical lines emphasize the observation bands at 500, 350, 250, and 160 μm from left to right.

5.2.1 SED Maps

To create the SED fits the maps were fit pixel by pixel using the methods described in Hill et al. (2009, 2010, 2011) and using the dust opacity law from Hildebrand (1983). The fit was done using **SciPy**'s curve fit package that uses non-linear least squares to fit the data to the SED function (Jones et al., 2001–). It should be noted that the curve fit routine required initial guesses for the values of the fit in order for the fitting routine to converge on reasonable timescales. For each target a set of four to six initial values were provided such that solutions could be found in a variety of temperature

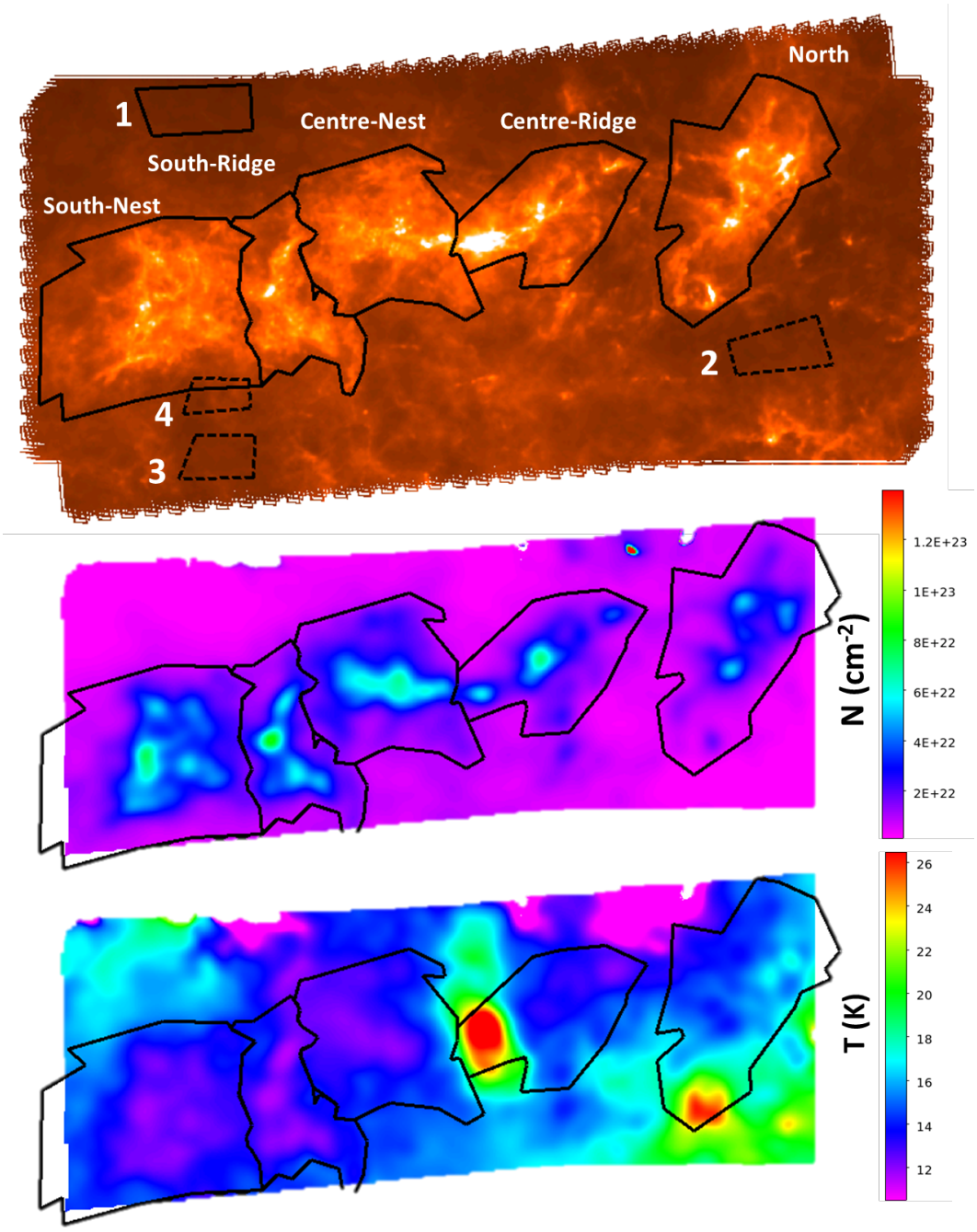

Figure 5.5: Top: The Vela 500 μm Herschel intensity map with reference regions 1-4 used in Figure 5.9 along with regions used for analysis and defined in Hill et al. (2011). The hydrogen column density map (middle) and dust temperature map (bottom) were both derived from two component SED fits after applying background subtraction from Region 1 to the Herschel maps.

and column density regions. Each set of initial values was evaluated by the program and the one with the lowest uncertainty from the fit was used. Uncertainties were caclulated from the diagonal elements of the returned covariance matrix. This proved to be much more efficient than increasing the number of iterations for the curve fitting routine to perform. Changes to the initial guess sets did not affect the values produced by the fit but were able to increase the number of pixels for which the fit could converge on a solution.

The results of the fit were visually compared to maps from Hill et al. (2011) and Rebolledo et al. (2016) and were found to be in close agreement. Maps demonstrating the results of the two parameter fit model are shown in Figure 5.5.

5.2.2 Three Component SED Model

In order to better understand the environment in the observed GMC, efforts were made to include a Rayleigh-Jeans component in the fitting function. A separate component would allow us to distinguish sight lines along which there were two populations of dust at noticeably different temperatures. The Rayleigh-Jeans approximation to the black body function would fit hotter cloud components that would be in the Rayleigh-Jeans limit over our observational bands. The approximation conveniently combines the Rayleigh-Jeans column density, N'_H, and temperature, T' components into a single unknown variable, $B = N'_H T'$, which can be used as a free parameter by simplifying Equation 5.2 after adding in a Rayleigh-Jeans component that is similarly scaled with number density and spectral index, yielding Equation 5.3.

$$F(\nu) = \frac{1}{N_0} * \left(\frac{\nu}{\nu_o}\right)^{\beta} \left(N_H B(\nu, T) + \frac{2k\nu^2}{c^2} B\right) \tag{5.3}$$

By using Equation 5.3 we can explore the temperature structure of clouds by looking for sight lines along which the Rayleigh-Jeans component contributed a significant

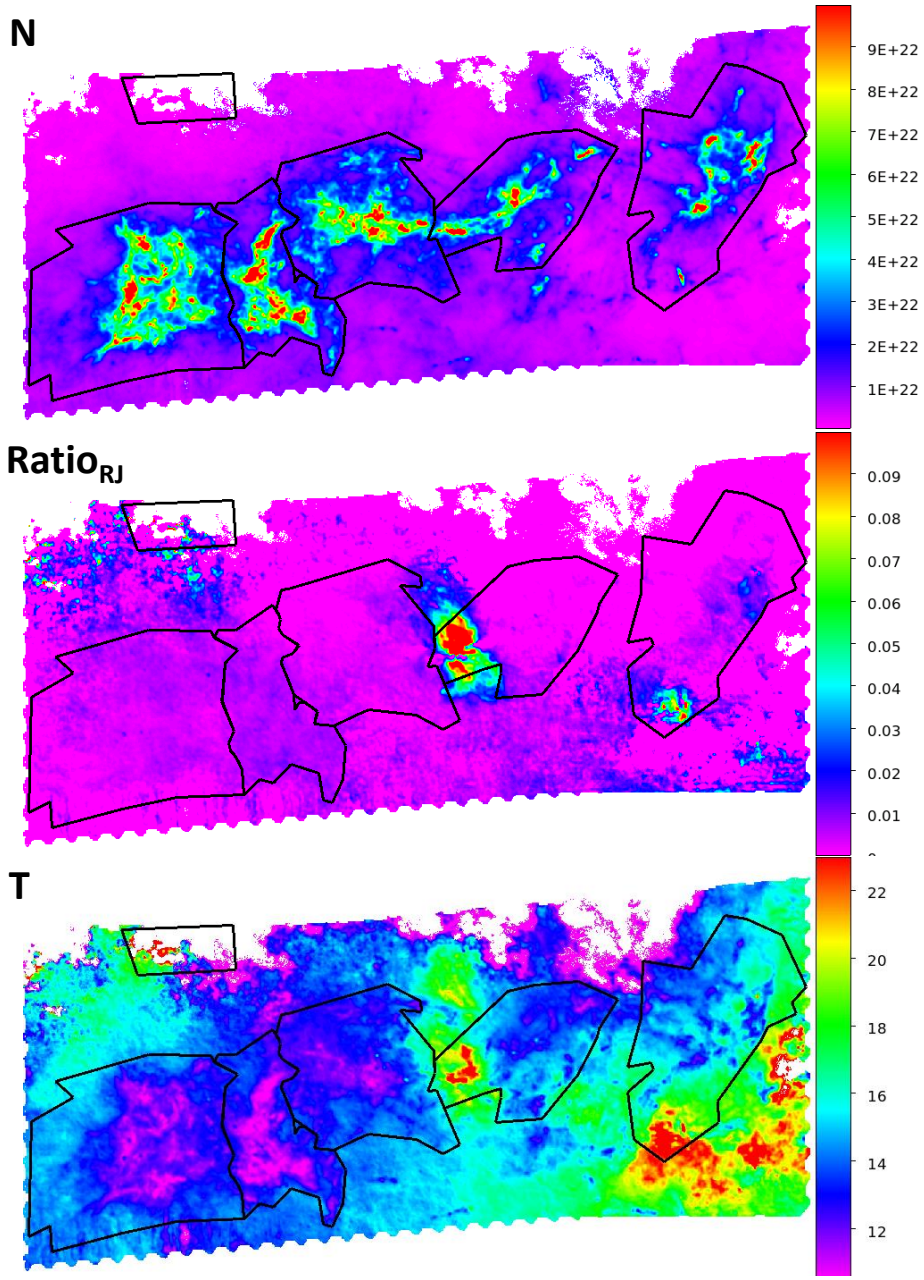

Figure 5.6: Vela C GMC maps derived from the Herschel intensity maps. Top: The map of column density of atomic hydrogen. Middle: A map of the calculated flux from the Rayleigh-Jeans component of the equation divided by the total calculated flux at 500 μm . Bottom: The map of dust temperature. The intensity maps input into the fits have been smoothed to the Herschel 500 μm channel's resolution of 35.2″.

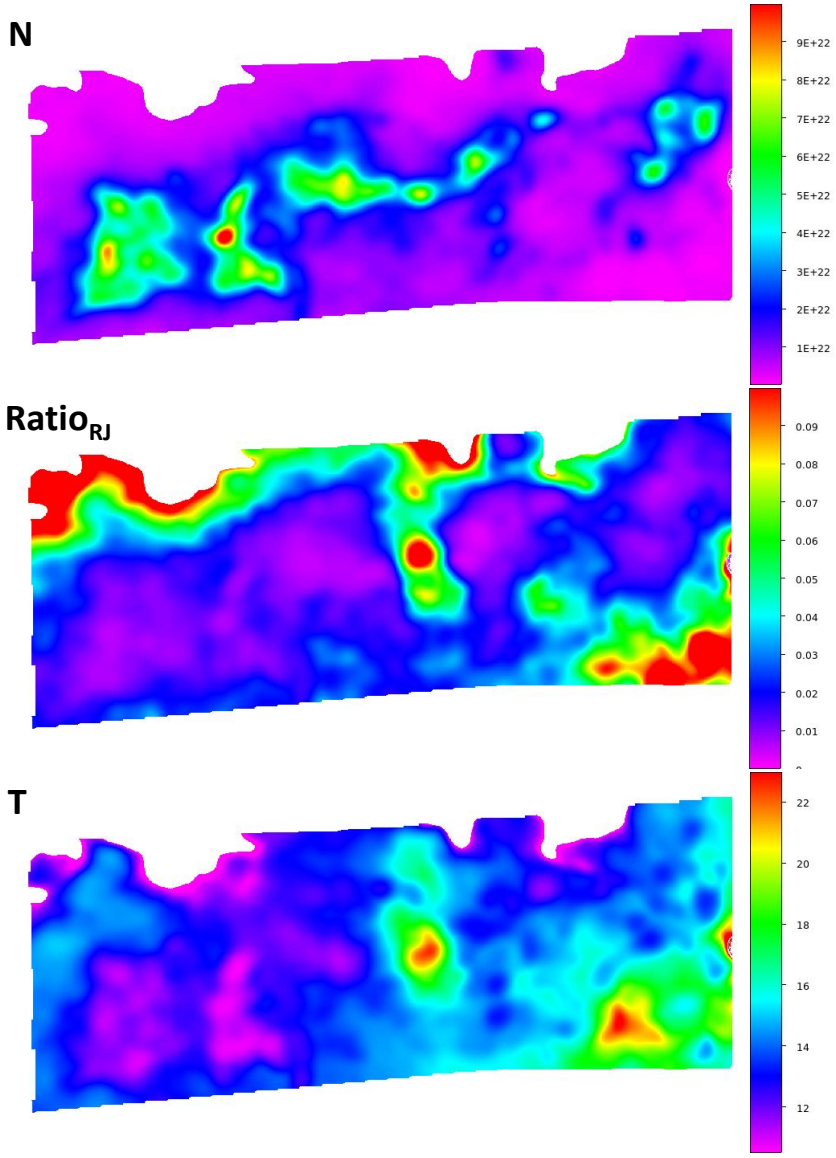

Figure 5.7: Vela C GMC maps derived from the Herschel intensity maps. Top: The map of column density of atomic hydrogen. Middle: A map of the calculated flux from the Rayleigh-Jeans component of the equation divided by the total calculated flux at 500 μm . Bottom: The map of dust temperature. The intensity maps input into the fits have been smoothed to the best BLASTPol resolution of 2.5′.

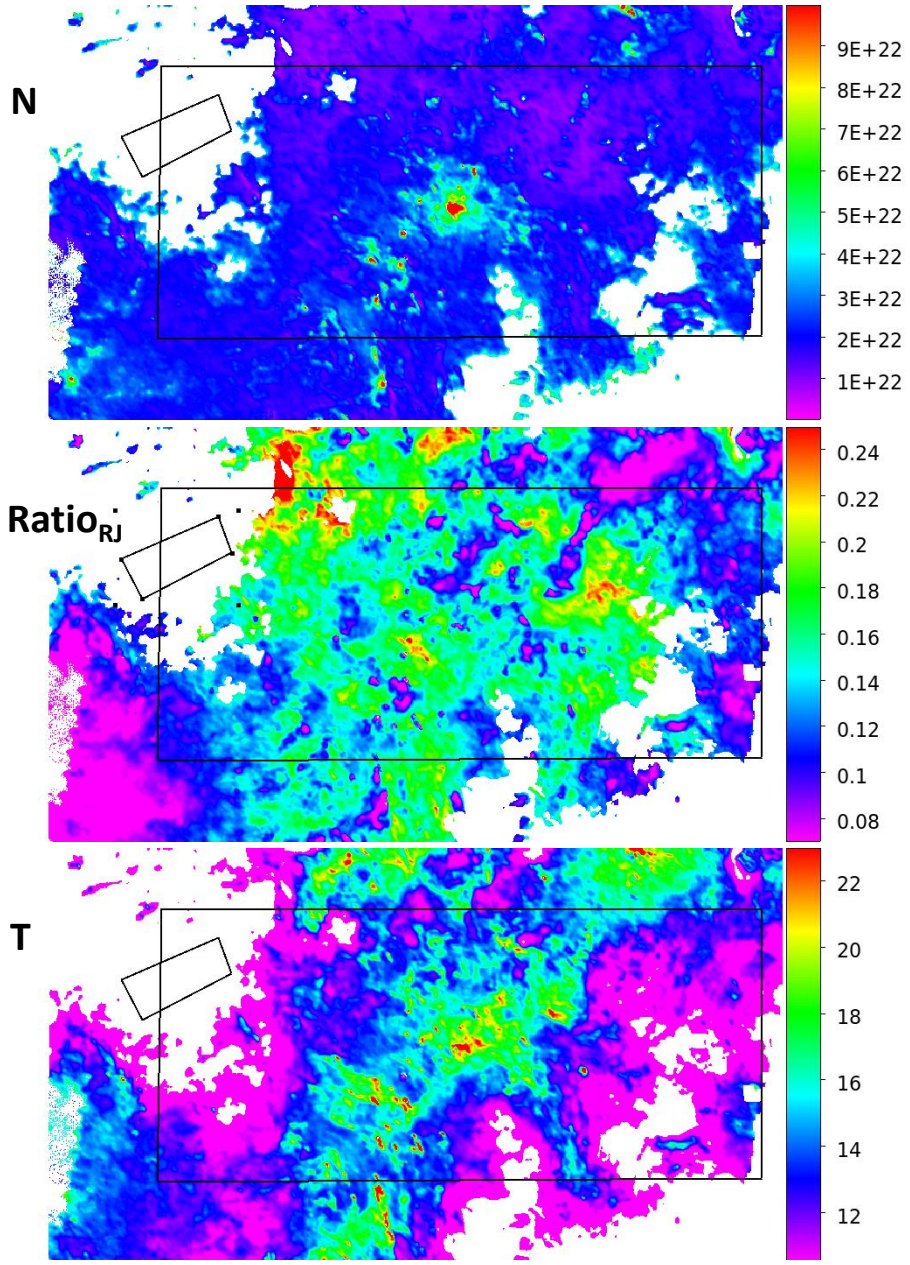

Figure 5.8: Carina GMC maps derived from the Herschel intensity maps. Top: The map of column density of atomic hydrogen. Middle: A map of the calculated flux from the Rayleigh-Jeans component of the equation divided by the total calculated flux at 500 μm . Bottom: The map of dust temperature. The maps are at the 35.2$''$resolution of the 500 μm channel of the Herschel SPIRE instrument. The small box in the upper left corner of each map is the reference region used to remove the background in the intensity maps prior to fitting. The larger box shows the area covered by BLASTPol.

fraction of the flux. The fractional dependence was determined to be the best way to describe the behavior of the function as the absolute temperature or column density of the Rayleigh-Jeans component cannot be computed with the information provided by the fit. Results of the three component fit can be seen in Figure 5.6 and Figure 5.8 where T, N, and B are free parameters. Maps were created at multiple resolutions so they could be used in combination with BLASTPol data at $2.5'$ resolution which was accomplished by smoothing the intensity maps prior to the fit being performed. A result of a smoothed map can be seen in Figure 5.7.

5.3 Primary Scientific Results

5.3.1 Radiative Shielding

Very early on in the analysis we found that the column density and temperature had a very strong anti-correlation which could be indicative of thermal shielding in the densest parts of the clouds. This correlation was confirmed by examining a plot of the $250\,\mu$m flux to the $500\,\mu$m flux as shown in Figure 5.9. In the figure there is a noticeable bend in the otherwise linear relationship between the two fluxes. Since the clouds are optically thin in the submillimeter, the flux measures all the dust along the LOS and therefore increased flux correlates to increased column density. However, after the bend we notice that the $500\,\mu$m flux increases more than the $250\,\mu$m flux. The simplest explanation of this feature is that the dust in the denser regions is colder which gives an excess amount of flux in the longer $500\,\mu$m band over the shorter wavelength $250\,\mu$m band. It is in essence a very basic test of the shift in the peak of the SED function. This premise is confirmed by plotting lines of constant temperature but variable column density calculated from Equation 5.2 onto the plot to show that for those fluxes the temperature decreases after the bend.

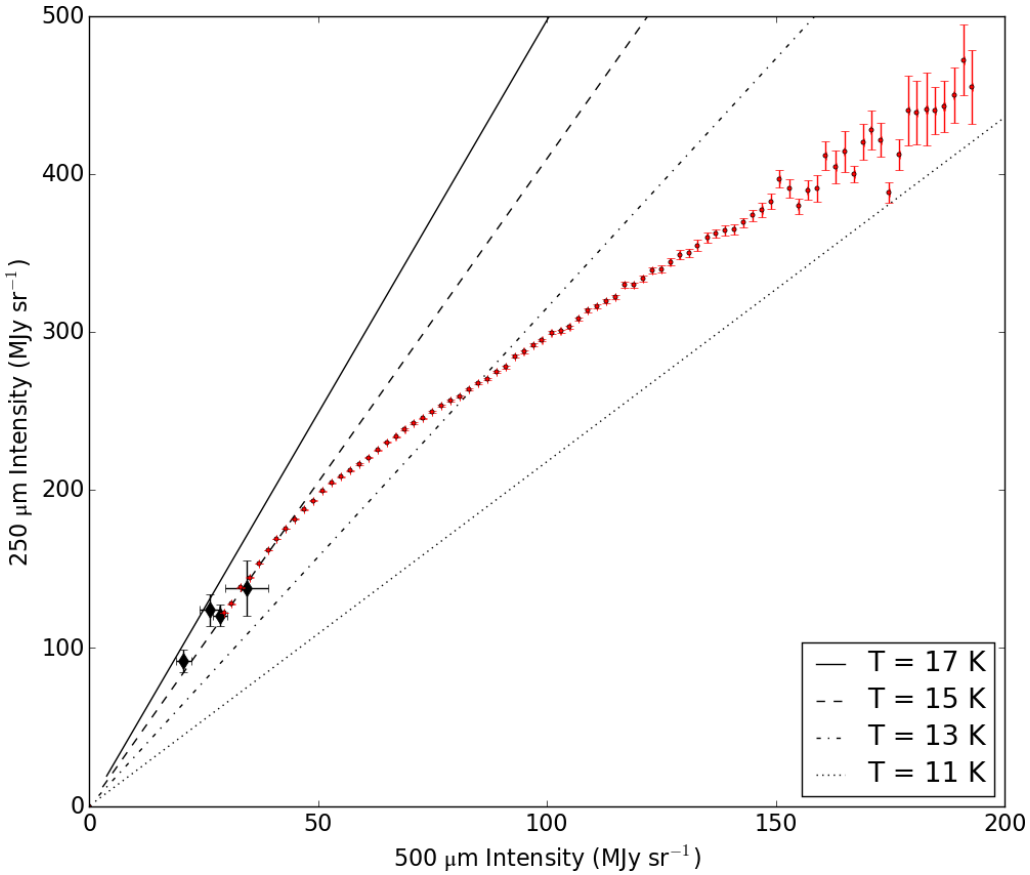

Figure 5.9: The plot shows evidence of radiative shielding as the bend is above the background regions indicating a trend towards colder temperatures at higher column densities along the line of sight. The four background regions as described in Figure 5.5 are shown with black diamonds that are regions 1, 2, 3, and 4 from left to right. Error bars are determined from the spread of the binned data.

An alternative explanation for the trend could be that of a uniform cold cloud in front of a warm background. The scenario is reasonable given the ISM that can be seen in Figure 5.2 is warmer ($\sim$ 50 K) than most regions of Vela C. To convince ourselves this was not the case while also removing the background from the maps of our analysis we tested the fits after subtracting average values from several reference regions. These regions were chosen to be in environments with a variety of column density and temperature values from what is assumed to be the background Gum nebula emission that is not associated with the Vela C cloud. Removing the reference

region flux essentially sets a new origin in Figure 5.9 and is equivalent to subtracting the background, leaving only flux from dust in the Vela C cloud. As can be seen in Figure 5.9, the reference region averages, even those placed agressively, reposition the origin to a point significantly below the bend in the flux ratio, reinforcing the conclusion that the observed T and N anti-correlation is an intrinsic component of the Vela C molecular cloud. The confirmation of radiative shielding in these types of regions is a significant result in and of itself and is a very important factor in characterizing the cloud environment. The background subtraction method we developed was also carried over to SED fitting as we remove the average flux from reference region 1 from the Herschel maps prior to performing the SED fit.

Determining the method of heating in the cloud has helped us separate Vela C into two types of regions, ISRF heated areas which exhibit radiative shielding and internally heated areas which exhibit signs of active star formation. The criterion to separate the two types of regions is determined by plotting T vs. $\log N$ which has a linear correlation for ISRF regions and no correlation in internally heated regions combined with higher temperatures. Outliers representing internally heated areas are identified by iteratively applying Chauvenet's criterion (Chauvenet, 1863) to the linear fit to the T and $\log N$ data (Fissel et al., 2015). The primary internally heated region is a compact HII source called RCW36 located in the Centre-Ridge shown in Figure 5.5. The ISRF heated portions of Vela C occupy a much larger section of the cloud and can be found in the Centre-Nest, South-Ridge, and South-Nest regions of the cloud, also defined in Figure 5.5. In the analysis covered in this chapter, an area around RCW36 shown in Figure 4.10 is excluded from the analysis both to concentrate on ISRF analysis and due to filtering tests that indicated unreliable data around RCW36 as described in Fissel et al. (2015).

5.3.2 Correlations of polarization fraction with T, N, and cloud structure

Our primary science comes from examining the magnetic field information and polarization fraction as they relate to measures of the environment including column density, structure, and temperature. Correlations that are discovered can then be used to describe physical processes in the cloud as well as to provide a relationship to constrain the parameter space of models. Additionally, results are compared to simulations that can vary magnetic field and turbulence parameters to create projected observations of GMC. The comparisons can help determine the most likely environmental conditions in the observed clouds.

Soler et al. (2013) provides an example of simulations done to identify observable effects of super-critical or sub-critical magnetic fields and also developed the method of histograms of relative orientations (HRO) analysis used in Planck Collaboration et al. (2016). The HRO examines the angle between the magnetic field pseudo-vector and iso-density contours. The contours trace out lines of constant column density and allow us to examine how the magnetic field is related to structures within the cloud. By making the HRO for several number density bins, the interaction of the magnetic field with cloud structure can be explored for different environments within the cloud. One of the primary predictions from simulations is that in less dense regions of a cloud the magnetic field will be parallel with the iso-contour lines while in denser regions the field will be perpendicular to iso-contour lines as discussed in Section 2.2. This was observed for several of the targets in Planck Collaboration et al. (2016). HRO analysis of BLASTPol targets is ongoing (Soler *et al.* in preparation).

A second measure of how the magnetic field directly interacts with the cloud morphology is a parameter S, angular dispersion, shown in Figure 5.10. To determine S, a pixel's polarization direction is compared to the direction of the polarization in

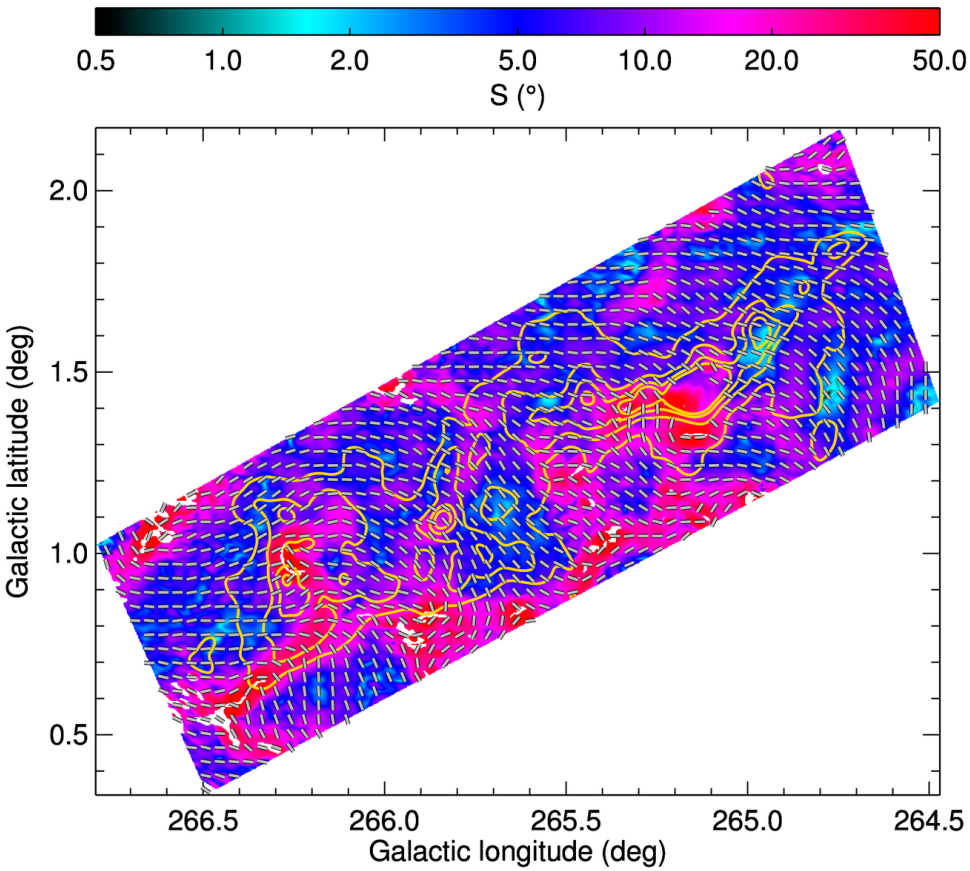

Figure 5.10: The vectors show sub-sampled magnetic field direction on the plane of the sky while the color indicates the level of angular dispersion as described in Section 5.3.2. Figure is from Fissel et al. (2015).

pixels on an annulus around the chosen pixel. In this case dispersion in polarization angle and magnetic field angle are equivalent as the measurement is invariant between the 90 degree rotation between the two. The root mean squared (RMS) deviation in the polarization-angle, $\psi(\vec{x})$, for a given pixel with an annulus of radius δ is found with Equation 5.4 where $\vec{x}$ is the position at which the dispersion is calculated and S_{xi} is defined in Equation 5.5. As S is positive definite is must be debiased via Equation 5.6.

$$S^2(\vec{x}, \delta) = \frac{1}{N} \sum S^2_{x_i\, i=0}^{\;\;N} \tag{5.4}$$

$$S_{x_i} = \psi(\vec{x}) - \psi(\vec{x} + \vec{\delta}_i) \tag{5.5}$$

$$S_{db}^2 = S^2(\delta) - \sigma_S^2 \tag{5.6}$$

If the direction of the pseudo-vectors is similar to the pixel, the angular dispersion is said to be low and is indicative of a uniform magnetic field direction. Alternatively, a high angular dispersion value points to either a rapidly changing magnetic field direction or a highly disordered field. The map of S is one of the primary results of the BLASTPol data as it encapsulates information on the magnetic field orientation on the plane of the sky for an entire molecular cloud at high resolution. S is derived from thousands of magnetic field pseudo-vectors which represents order of magnitude improvements over previous experiments.

The map of angular dispersion is compared to maps of column density and polarization fraction to determine a relation between the three parameters. It is important to distinguish between different types of environments and so in the analysis presented here the internally heated region around RCW36 is excluded, concentrating instead on the radiative shielded regions of the cloud heated by the ISRF. The coverage used can be seen in the map of the polarization fraction at 500 μm in Figure 5.11. The combined data is shown in 5.12 from which we were able to generate a fit to all three variables that serves to constrain models of GMC. The result of the two dimensional fit is shown in Equation 5.7 which effectively distills the highest impact results from the BLASTPol 500 μm maps into a single important empirical equation.

$$p(N, S) = p_0 N^{-0.45 \pm 0.1} S^{-0.6 \pm 0.02} \tag{5.7}$$

The observed inverse correlation between p and S is fairly intuitive. One would expect that in areas where the field is either disordered or changing direction quickly the LOS will sample field vectors at multiple orientations and in this way some of

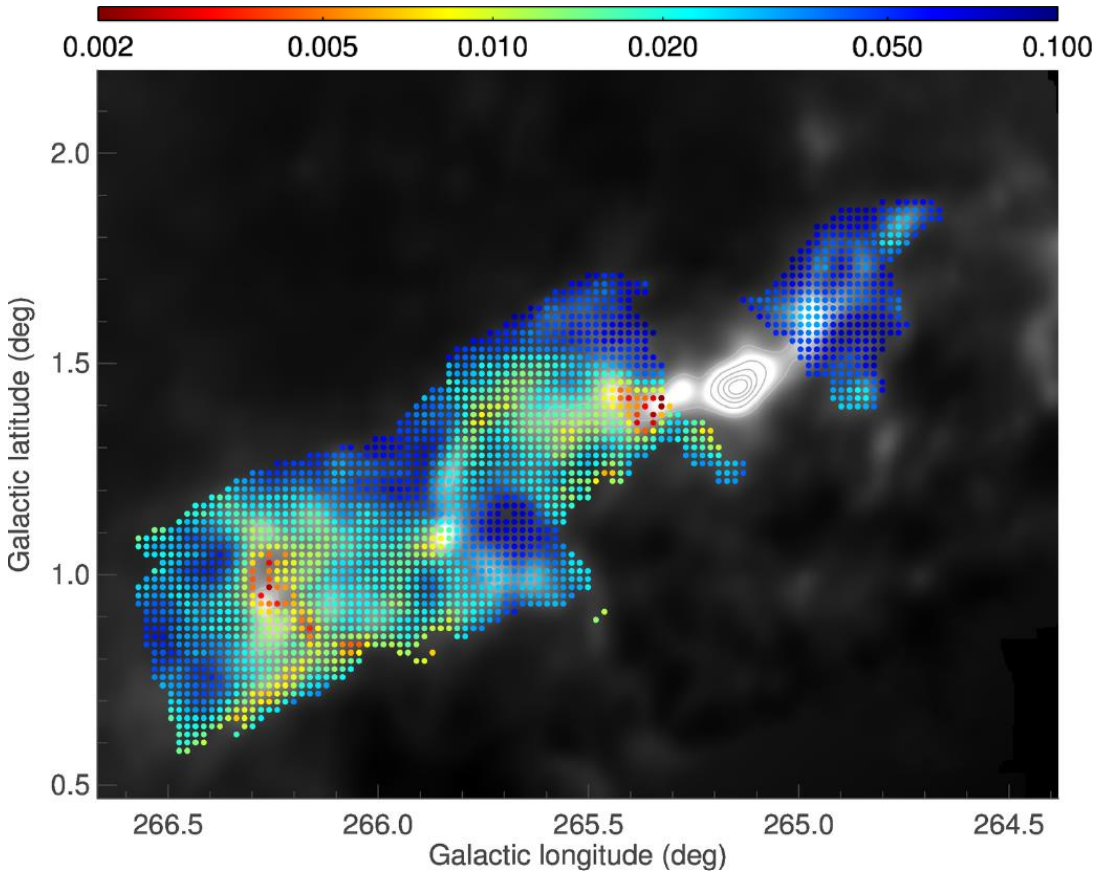

Figure 5.11: The colored pixels are the derived polarization fraction at 500 μm from ISRF heated regions overlaid on a 500 μm intensity map of the Vela GMC shown in grayscale. Figure is from Fissel et al. (2015) which describes the data selection criteria in more detail.

the polarized signal will cancel out resulting in the observed anti-correlation. The inverse relationship between p and N paints a somewhat more complex picture. On the one hand it could be a similar effect as with S, where sight lines with a higher column density are inherently examining more parts of the cloud that could potentially be disconnected form one another and have magnetic field vectors at different angles causing the cancellation of the polarized signal. Another possibility is that the alignment efficiency of the grains with the magnetic field drops in cloud interiors. In this case the radiative shielding of the cloud reduces the amount of incident radiation on grains deep within the cloud limiting the effectiveness of RAT.

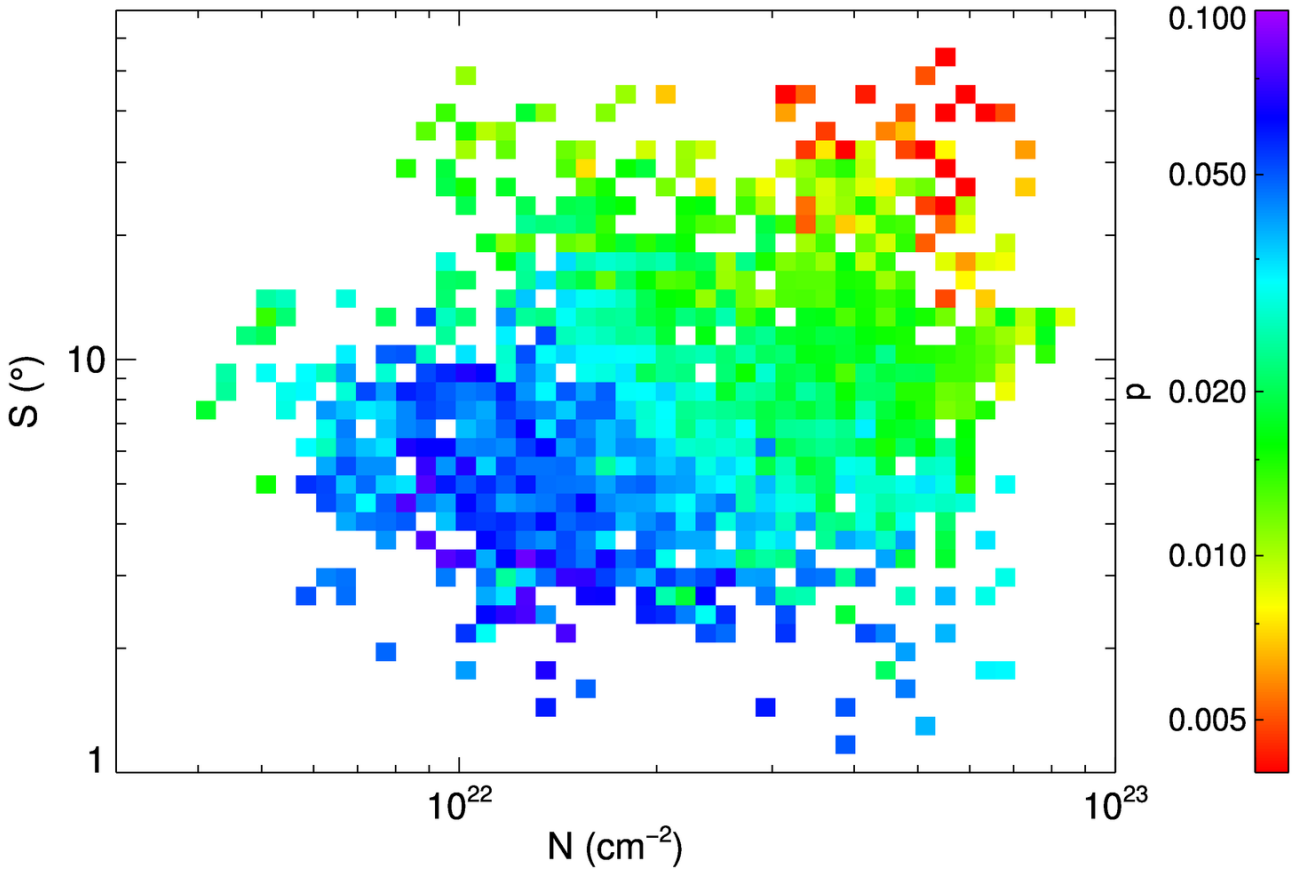

Figure 5.12: The color scale shows the median p value in bins of number density, N, and angular dispersion, S, plotted against both N and S for ISRF heated regions. As p decreases from blue to red, both N and S increase on a logarithmic scale which led to the creation of an empirical model with a two-variable power-law relation. Figure is from Fissel et al. (2015).

From our data analysis efforts we have found an empirical model relating the polarization fraction to both cloud structure and the magnetic field direction which will be used to constrain numerical simulations of GMC, a primary goal of BLASTPol. However, this trend may vary in other clouds and environments and as such, the two-variable power-law fit should be repeated with data from a variety of targets to further constrain models and simulations (Fissel et al., 2015).

5.3.3 Polarization Spectra of Vela C

Looking into the spectral response of the polarized dust emission can tell us a great deal about the population of dust grains including size distribution, shape, and composition. In order to discern between the possibilities there have been extensive efforts to model the spectral response while varying any number of the aforementioned parameters. However, most models are only loosely constrained in the FIR and submillimeter part of the spectrum due to the sparseness of available data which has resulted in no currently available comprehensive model. BLASTPol data provides a robust contribution to the field of study with the polarization spectra we are able to produce across our three bands which will help refine models. Additionally, maps at 850 μm from *Planck* were used to increase our spectral coverage. However, doing so required smoothing all BLASTPol maps to the *Planck* resolution of 5′.

In order to create a spectrum we first calculated ratios of p relative to the 350 μm band to allow easy comparison of the shape of the spectra to other studies. This also removes the variability between studies of the absolute magnitude of the polarization fraction. Once maps of p_{250}/p_{350}, p_{500}/p_{350}, and p_{850}/p_{350} had been made, a rigorous set of cuts were performed to ensure only the highest signal to noise and most reliable data was used. To reduce the possibility that different detector bands are sampling different point along the LOS, points were removed where the polarization angle ϕ differs by more than 10 degrees between any two of the maps. Additionally, a cut was done to remove low signal to noise points where $p < 3\sigma_p$ in any of the four bands observed. The analysis is also restricted to specified regions, for example in Gandilo et al. (2015) only points within the Hill et al. (2010) regions were used which effectively provided a cutoff of $A_V < 7$. Additionally, the region around RCW36 was masked in the analysis discussed here.

The polarization spectra resulting from the p ratio maps is shown in Figure 5.13.

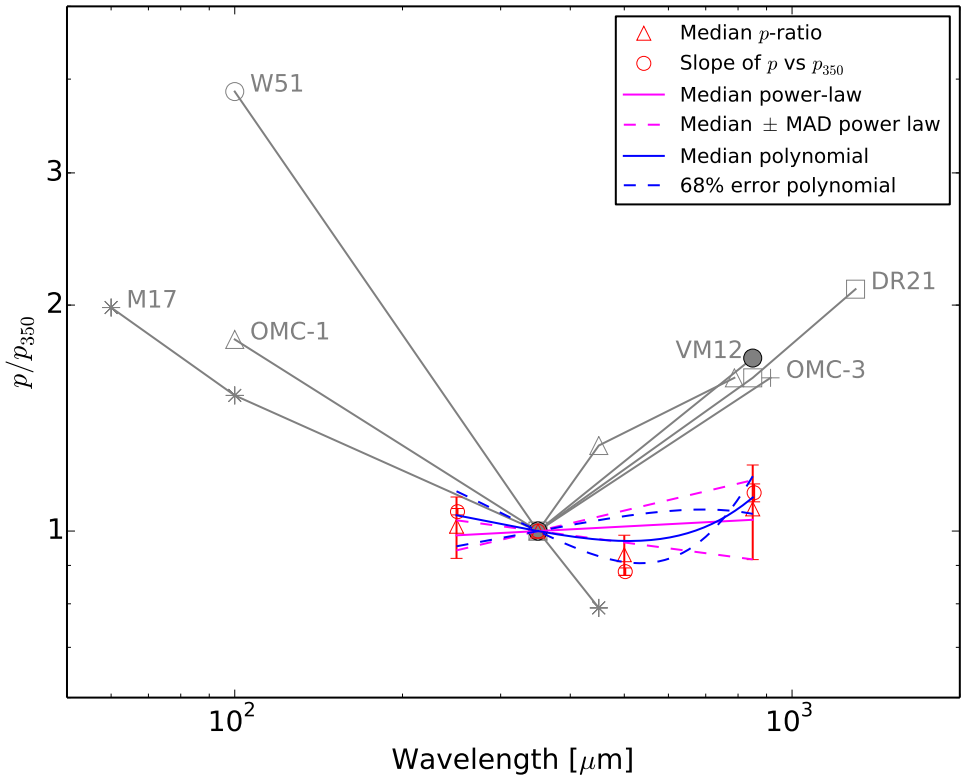

Figure 5.13: Red data points are derived from BLASTPol maps with the 850 μm point from the *Planck* polarization map. The distribution over the whole cloud is used to derive the points and their errors as detailed in Gandilo et al. (2015). The gray points are from previous studies.

The p ratio points and error bars were determined in two ways. In the first the median of all points in the ratio map was taken and then a median of the distribution around the median was taken to determine error bars, referred to as Median Absolute Deviation (MAD). As an additional check to ensure the robustness of the polarization spectra shape, a linear fit was performed to p_{250} vs. p_{350}, p_{500} vs. p_{350}, and p_{850} vs. p_{350} to determine the ratios with error bars derived from the uncertainty in the fit.

The result of the spectral analysis is very interesting as it predicts a flat polarization spectra in the Vela GMC around 350 μm whereas previous studies had found a steeply falling or rising spectrum as seen in the gray data points in Figure 5.13. In

Hildebrand et al. (1999) it was postulated that the steep spectrum was caused by dust grains with at least two temperature components along the line of sight. In this case the rise to shorter wavelengths is due to the warmer dust grain component experience better alignment. This possibility fits with RAT as the warmer component would likely be exposed to a more intense radiative environment which would increase the efficiency of RAT for that environment.

In Vaillancourt et al. (2008) it was proposed that the rise at longer wavelengths could also be consistent with a two temperature component model with the additional effect of different grain emissivities explaining the rising spectrum. For both these arguments it is important to note that the gray data points in Figure 5.13 were generally looking at clouds that showed stronger evidence of internal heating than the regions we examine in Vela C. Therefore, in the other studies there may be two temperature components along the line of sight, cooler areas of the cloud that were ISRF heated along with a hot component heated internally by active star forming regions. Additional research could focus on discerning the temperature components along the LOS in these clouds in an attempt to better constrain the environments that were sampled by the polarization measurements.

In the case of Vela C, after excluding RCW36, we expect to be sampling a single ISRF heated dust grain population with most the intensity coming from the high column density portion that is internal to the cloud and radiatively shielded. In such a case of a single population of dust grains we would not expect to see any change in the efficiency of grain alignment with wavelength in our spectral range which serves well to explain the relatively flat spectrum observed. Our result is significant as it is one of the first submillimeter measurements that both demonstrates a flat spectrum and has complementary data sets that allow us to understand the environment being measured.

5.3.4 Future polarization spectrum analysis

I have undertook the project of using additional data sets, such as the three component Herschel maps, combined with BLASTPol polarization maps in order to further explore the spectral structure within Vela C which is part of ongoing analysis (Galitzki *et al.*in preparation). We are primarily interested in regions of Vela C that might deviate from a flat polarization spectrum and are concentrating our analysis efforts there. For example, regions with a Rayleigh-Jeans component are more likely to have dust grain populations at two temperatures along the LOS and therefore we might expect them to deviate from the flat spectrum. Regions with two components are identified in part with the ratio calculate in Equation 5.8.

$$F_{ratio} = F(\nu)_{RJ}/F(\nu)_{Total} = \frac{\left(\frac{2k\nu^2}{c^2}B\right)}{\left(N_H B(\nu,T) + \frac{2k\nu^2}{c^2}B\right)} \tag{5.8}$$

We are also exploring other methods of identifying regions with non-flat polarization spectra in part by examining maps calibrated to *Planck* instead of using background subtraction. Doing so has expanded the region we are able to examine which gives us a larger data set with a wider range of environments. An example of an expanded area we are using is shown in Figure 5.14. Additionally, we are including RCW36 sight lines in the analysis to ensure we are looking at a variety of environments.

BLASTPol data will continue to produce high impact results in addition to those that have already been published. However, a great deal more can be accomplished by observing additional regions at higher resolution. Better data sets will allow us to more easily distinguish between different environments within the cloud and will allow us to establish the polarization dependance across a variety of regions. With an improved experiment we will be able to further explore the relationship between magnetic field and structure. We will also be able to pursue the goal of tracing the

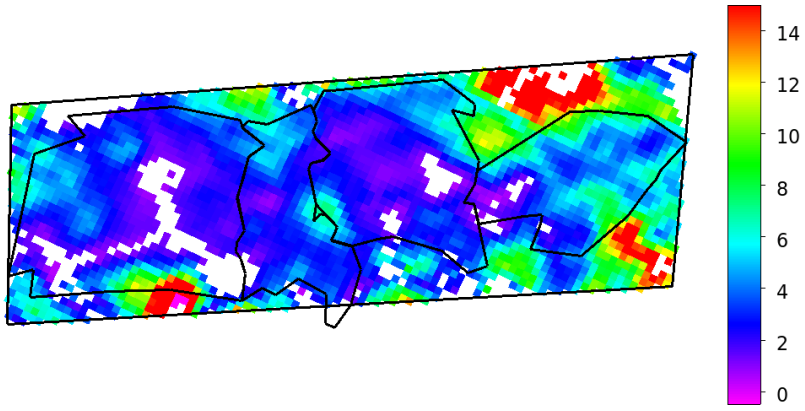

Figure 5.14: A map of all polarization percentage points at 500 μm inside the validity region defined by the aggressive planar fit background subtraction methods. The points have undergone 3 sigma cuts on p as well as angle agreement between ϕ of better than 10 degrees between all three BLASTPol bands. The map is at a resolution of 3′ that has been sub-sampled with 1.5′ pixels. The map is an example of the type of data products that will be used in future analysis to build on previously published results.

magnetic field from GMC through filamentary structures and down into proto-stellar cores that are embedded in the cloud. In order to achieve these goals we have begun construction of BLAST-TNG.

Chapter 6

BLAST-TNG Design

6.1 Instrument Overview

BLAST-TNG will continue the legacy of BLASTPol with the construction of an entirely new instrument. The design incorporates many successful elements from previous ballooning experiments. It is based around a 2.5 meter primary mirror which provides diffraction-limited observations in three 30% fractional bands at 250, 350, and 500μm. The 22$'$ diameter FOV is larger than BLASTPol's which led to a proportional increase in the size of the optics necessitating the construction of a new cryostat. The cryostat has been designed to have a longer hold time of 28 days, versus the 13 day hold time of BLASTPol. The previous cooling system used both helium and nitrogen, however, for BLAST-TNG we have switched to an entirely liquid helium system that utilizes two vapor cooled shields (VCSs) to provide additional thermal isolation. BLAST-TNG will also serve as a pathfinder instrument for microwave kinetic inductance detectors (MKIDs) (Day et al., 2003), which have never been flown before. The development of MKID arrays for astronomy is an extremely active area of detector research, and flight testing them will be a significant milestone. The design of the instrument is shown in Figure 6.1 and detailed in Galitzki et al. (2014a).

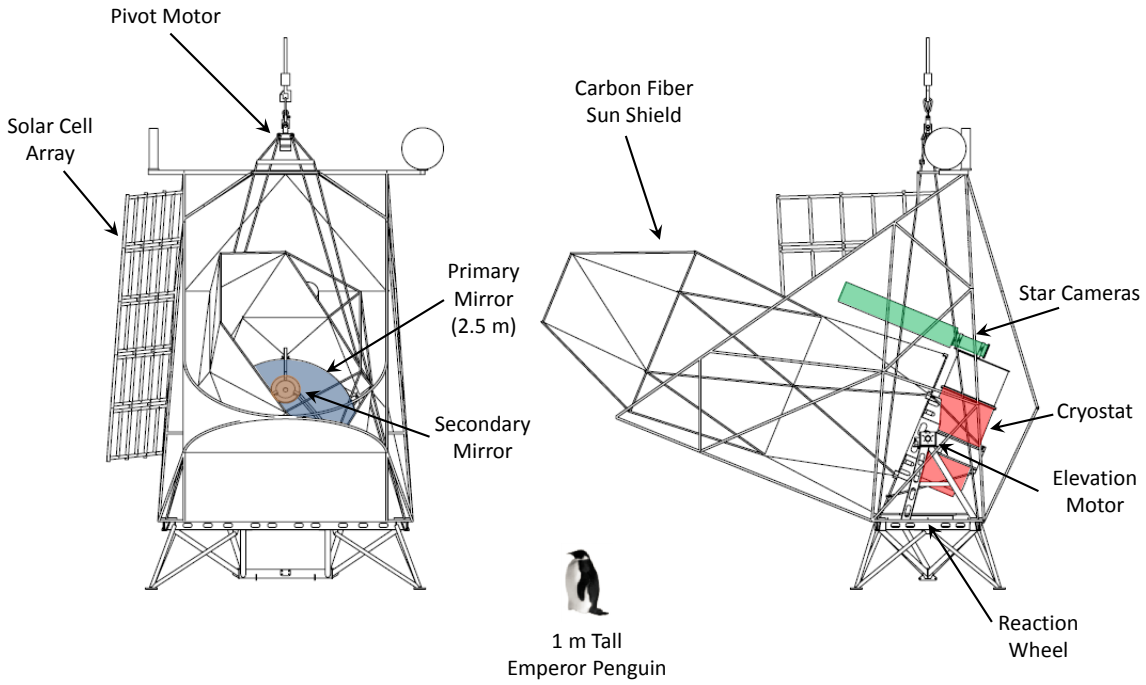

Figure 6.1: The front and side views of the BLAST-TNG telescope in its flight configuration. The cryostat, mirror optics bench, and star cameras are attached to an inner frame that moves in elevation. An extensive carbon fiber sun shield also attaches to the inner frame to shield the optics at our closest pointing angle of 35° to the sun.

6.2 Pointing Systems and Electronics

A number of the BLAST-TNG pointing and electronics systems are inherited from or based on components successfully flown previously with BLAST and BLASTPol. We will be using a very similar pointing sensor suite to determine telescope attitude, including star cameras, gyroscopes, and sun sensors (Gandilo et al., 2014). Pointing of the telescope will use the same strategy of a precision pointed inner frame that moves in elevation, supported by an external gondola that scans in azimuth. However, the computer and electronics systems have undergone a major overhaul to reduce reliance on legacy components that are either outdated or difficult to maintain.

6.2.1 Pointing System

The pointing in azimuth is controlled by a reaction wheel and a pivot motor. The reaction wheel is a 1.5 meter diameter wheel with high angular moment of inertia that is kept in motion by a brushless direct drive motor. Adjusting the speed of the wheel results in a transfer of angular momentum from the wheel to the gondola and allowed BLASTPol to scan in azimuth at typical rates of 0.05 to 0.2°/s while observing, and slew at speeds of several degrees per second while moving between targets. The scan strategy for BLAST-TNG will be similar though with somewhat faster observation scan speeds between 0.2°/s and 1°/s to facilitate the higher $1/f$ noise knee of the MKID arrays. The pivot motor, which is attached between the payload and the flight train, can assist the reaction wheel, if its speed begins to saturate, by transferring angular momentum to the balloon. The pivot motor can also independently point the telescope in azimuth in case of reaction wheel malfunctions, as occurred during the 2010 flight due to a bearing malfunction in the reaction wheel motor.

6.2.1.1 Elevation Control

Pointing in elevation was previously accomplished by a direct drive brushless servo motor that was connected to the axis of an inner frame, on which the telescope and cryostat were mounted. This worked in conjunction with a balance system that periodically pumped fluid from the bottom to the top of the inner frame to counteract the imbalance caused by cryogens boiling off. With the much larger cryogenics volume of BLAST-TNG and the overall more massive structure, we attempted to couple the direct drive motor to a Harmonic Drive[1] gear-head with a ratio of 80:1.

However, it was found that the level of current control needed for small scan speeds with the 80:1 ratio gear was too fine for our motor, making the elevation move in steps instead of scanning smoothly. After this discovery three alternative

[1]Harmonic Drive LLC: 247 Lynnfield Street, Peabody, MA 01960

solutions were identified. The first would be to buy a new motor that had the level of precision current control needed or to buy a smaller gear ratio to enable the existing motor to drive it as intended. This option was found to be too expensive with some difficulty finding a replacement motor or harmonic drive that we were sure had the desired specifications. The second option would be to attach a linear drive motor to the outer frame that would push on a point a few feet from the axis to rotate the inner frame. This strategy had been used previously by the The E and B Experiment (EBEX) and Spider Telescope (SPIDER) experiments and is known to be effective though with some difficulty in protecting the drive mechanism during launch shocks. The downside of this option would be that it is a drastically different system than we have used before and would therefore require a proportionally larger investment in time and materials to make it operational.

Ultimately we went with the third option which was to revert back to the method we had used before with a direct drive motor and balance system. The downside to this configuration is it requires the inner-frame be very well balanced throughout the flight as the motor is current limited. The major advantage to the direct drive system is that we are already very familiar with it and it requires very little resources to make it operational. The main upgrade we are making to the drive and balance system is to place a weight on a track that runs across the center of mass of the inner frame which allows us to balance the inner frame as cryogens boil off with a much simpler system than the liquid balancing system that was used on BLASTPol.

6.2.1.2 Pointing Control

The primary absolute pointing sensors are two bore-sight star cameras that are able to determine the right ascension (RA) and declination (DEC) of the instrument to $< 5'$ during the flight and $< 5''$ after post-flight reconstruction of the pointing solution (Rex et al., 2006). Each star camera contains a high-resolution (1 megapixel)

integrating CCD camera with a 200 mm f/2 lens, to image a 2° x 2.5° FOV. A stepper motor controls the focus, to compensate for thermal variations, while another stepper motor controls the aperture, to allow for different exposure times, depending on the scan strategy. Each camera is connected to a PC-104 computer that uses either a 'lost-in-space' algorithm, that searches the entire sky for the position, or an algorithm developed for BLAST, that incorporates information from the coarse sensors and previous pointing solutions to find the new position. The latter process is needed to reduce the time it takes for the cameras to produce a pointing solution. Every time the star cameras capture an image, they send the pointing information to the flight computers along with image data that can be used in the post flight pointing reconstruction. There are two star cameras to provide more frequent pointing information as well as redundancy should one of them malfunction, as occurred in the 2012 flight.

We use three axis DSP-1760 fiber optic gyroscopes mounted on the inner frame[2] to provide fast relative solutions. However, they have a drift of $0.1''/s$ and are primarily used to interpolate the relative pointing between star camera solutions. There are two of the gyroscopes to provide redundancy and relative offsets for both are determined prior to flight.

BLAST-TNG will fly with additional coarse pointing sensors (see Table 6.1) that serve as complimentary sensors to the star cameras in case they malfunction or experience difficulty obtaining solutions. Pin hole Sun sensors use the Sun's location in the sky to determine pointing in azimuth and were developed and tested in previous flights (Korotkov et al., 2013). A magnetometer determines azimuth pointing information by measuring the orientation of Earth's magnetic field. There are also two inclinometers that determine the tilt of the inner and outer frames which can be used to measure the pointing elevation. We will also be including a precision opti-

[2]KVH Industries, Inc.: 50 Enterprise Center, Middletown, RI 02842

Sensor	Sample Rate (Hz)	Accuracy (°)
GPS	10	0.1
Sun Sensor	20	0.1
Magnetometer	100	5
Clinometer	100	0.1
Star Camera	0.5	<0.001
Elevation Encoder	100	<0.001
Gyroscopes	100	$< 0.1°$/hr

Table 6.1: Summary of Pointing Sensor Parameters Gandilo et al. (2014)

cal elevation encoder mounted between the elevation motor gear-head and the inner frame. We plan to use a RESOLUTE absolute rotary encoder on RESA[3] rings which will have over 10 times the resolution of the previous encoder used.

Our philosophy with the pointing system is to have a degree of redundancy for most all components in case of a critical failure. Our combination of fine and coarse sensors allows us to achieve our in flight pointing requirements. During post flight pointing reconstruction, we have achieved accuracy $< 5''$ RMS (Gandilo et al., 2014), which is more than adequate for our observations.

6.2.2 Electronics

Ballooning systems require interfacing numerous pointing sensors and motors to provide effective attitude control. The previous instrument relied on a flight computer running a master program that handled I/O through a PCI BLASTBus card (Benton et al., 2014). This system was developed by the original BLAST collaboration and has successfully been used in a number of experiments (Rahlin et al., 2014; Oxley et al.,

[3]Renishaw: 5277 Trillium Blvd, Hoffman Estates, IL 60192

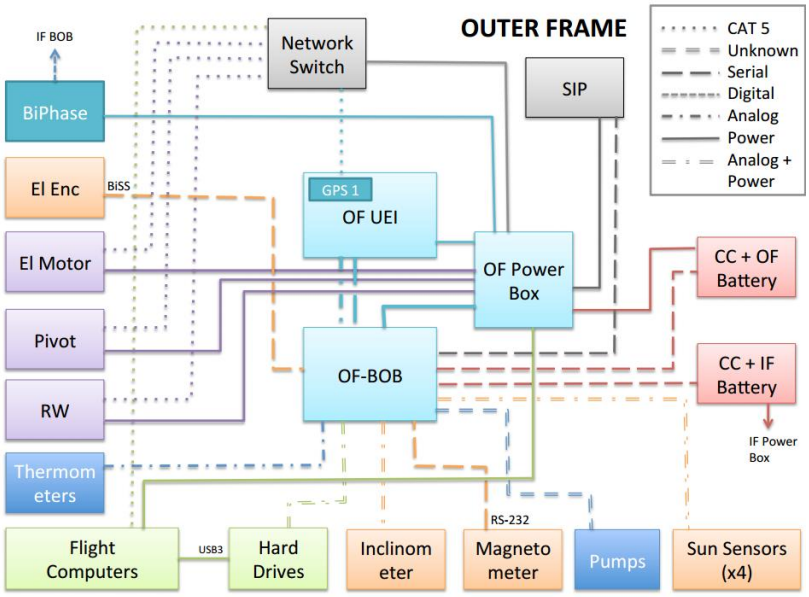

Figure 6.2: A schematic of the electronics system on the outer frame that shows all major components and how they connect. The hard drives are kept in a separate pressurized vessel that is connected to the computers. The pivot, reaction wheel, and elevation motors all have separate motor controllers that receive commands over ethernet. The outer frame electronics are connected to a similar system on the inner frame that runs the cryostat motors, secondary mirror actuators, and electronics associated with the cryostat and detectors. The SIP and BiPhase are components provided by NASA for controlling their equipment and the communications systems.

2004; Swetz et al., 2011; Ogburn et al., 2010; Staniszewski et al., 2012). However, the BLASTBus has become impractical to use, given that much of the expertise and spare parts are no longer available. The BLAST-TNG instrument will utilize a new commercial system for applications in balloon-borne missions. We will be using two United Electronics Industries (UEI)[4] DNA-PPC8 cubes to handle sensor I/O, thermometry, motor control, time synchronization, and other functions. The UEI cubes are very flexible, with a variety of interchangeable cards that can be tailored to our specific needs. We will be using a combination of ADC, DAC, DIO, RS-232/485 8-port serial, and timing control/GPS cards. Each cube has an embedded PPC CPU

[4]United Electronic Industries: 27 Renmar Avenue, Walpole, MA 02081

running Linux 3.2 with real-time extensions that will run a custom control system written in C. Synchronization between systems is handled by the dedicated UEI sync interface port.

The power system is divided into two components, one which provides power to the flight computers and outer frame electronics, and another which provides power to the detector readout system and inner frame electronics. Each power network will be charged by six to nine solar panels that have been developed and built at UPenn by reverse engineering the SunCat solar panels[5] used in previous experiments. At 28 V, the solar panels can provide over 1100 Watts of normal incidence power and over 500 Watts at an incidence angle of 60 degrees. The solar array output for each power network is routed through a Morningstar TriStar 60 amp MPPT solar charge controller[6], which maintains the proper voltage to charge the batteries and can be monitored and controlled over a serial line. The charge controller couples to two 14 volt lead-acid batteries connected in series. The lines from the batteries feed into a power box, which converts the battery voltage into the various voltages required by the instrument while also providing switching.

The pivot, reaction wheel, and elevation motors that control the telescope pointing will utilize Copley motor controllers[7] and are commanded via EtherCAT, a network-based CANBus protocol. The signal cables will be routed through two breakout boxes that redistribute cables from the UEI cube cards to their respective destinations.

One UEI cube, breakout box, and power box are mounted to the inner frame along with the detector readout and cryostat electronics, while another set is attached to the outer frame, along with the flight computers and hard drives. The outer frame configuration is shown in Figure 6.2. The UEI cubes greatly simplify the design and eliminate the need for the BLASTBus system. The system has been shown to

[5]SunCat Solar, LLC: HC 1 Box 594, Elgin, AZ 85611
[6]Morningstar Corporation: 8 Pheasant Run, Newtown, PA 18940
[7]Copley Controls: 20 Dan Road, Canton, MA 02021

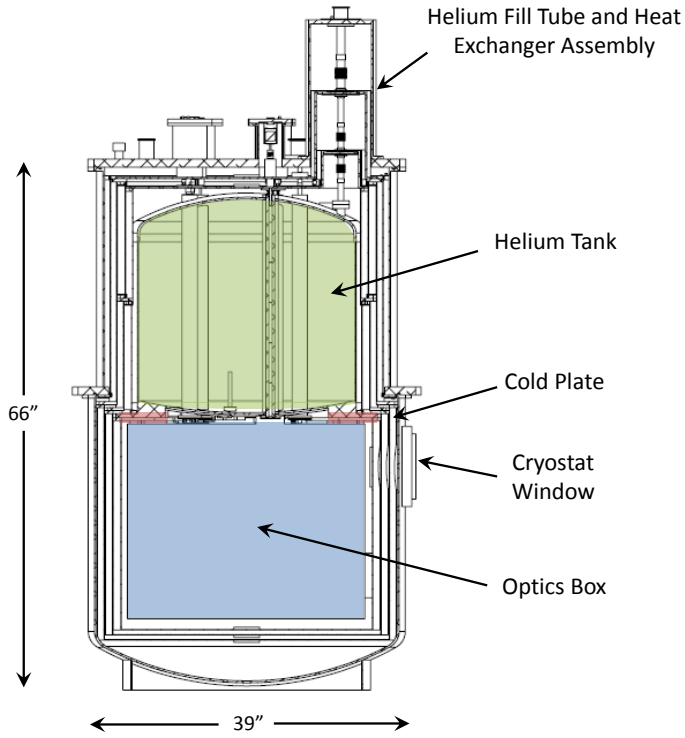

Figure 6.3: Cross section view of the BLAST-TNG cryostat. The cryostat is cooled by liquid helium with two helium vapor heat exchangers that cool two shields to provide thermal isolation of the cold optics. The inner vapor cooled shield is kept at 66 K and the outer one at 190 K. The cryostat has a predicted hold time of 28 days.

work effectively during our pre-flight testing that have included vacuum chamber tests of all electronics components as well as a UEI, flight computer, and solar panel piggy-backing on a short duration ballooning mission from New Mexico to test their performance in a flight environment.

6.3 Cryogenics

The detector arrays nominally operate at 270 mK, which requires a robust cooling system to reach the required temperature and to keep the temperature steady during normal flight operations. In order to simplify the design and cost of the cryostat, we

are not using liquid nitrogen as an intermediate cooling stage, but are instead using a system of two VCSs. The shields are cooled by heat exchangers that extract the enthalpy of the gas, as it warms from 4 K to 300 K. Our cryostat thermal models use a baseline efficiency of 80% for the heat exchangers to calculate a hold time in excess of 28 days. Details on the design and testing of the heat exchangers are discussed in Section 6.3.4 and Section 7.8.

6.3.1 Cryostat Design

The design of the BLAST-TNG cryostat was largely based on the design of the BLASTPol cryostat which can be seen in several key features. The window is on the side of the cryostat which is primarily driven by the Cassegrain mirror configuration making this choice the most natural given the telescope configuration. The primary advantage of this orientation is it allows us to put the cryogen tanks above the cold optics and mount the optics to the bottom of the helium tank. This is opposed to other experiments such as SPIDER (Gudmundsson et al., 2015) that have multiple large apertures and long optics tubes that require increasingly complex helium tank shapes and overall cryostat designs. Given the method in which our optics are mounted, they can be quickly and easily accessed by removing the bottom half of each shield section which allows work to be done on the optics bench without removing or otherwise altering the optics or any part of the cryogenic system.

The helium tank itself required an innovative design to accommodate the 250 L of liquid helium while also providing a stable mounting platform. The cold optics box is bolted directly to the helium tank to minimize the thermal path between the optics and the helium bath. The cold optics box is also mounted to the rim of the helium tank to minimize the effect of the deflection of the cold plate on the precision optics. The structure of the helium tank is further reinforced by the six feed-through tubes

that allow for easy insertion of cabling, piping, and motor axles from the top of the cryostat to the cold plate as shown in Figure 6.3.

There are five components that must be routed from the cold plate, through the helium tank, to the exterior of the cryostat which are the housekeeping cables for heaters and thermometry, coax cables for detector readout, the motor axle to drive the HWPR, the motor axle to operate the pump pot valve, and the pump pot exhaust pipe. All of these systems are fed out through the top of the cryostat instead of through the sides as has been done with some other experiments. The advantage to this configuration is changes can be done to any of the plumbing, cabling, or motor axles by removing the lids of the cryostat which are completely decoupled from the mechanical support of the cryostat that routes through three G-10 pieces that mount in the midsection of the cryostat. The midsection that encompasses the G-10 supports, the middle portion of all the thermal shields and the helium tank never needs to be disassembled for normal operation and adjustment of the cryostat between cool downs and testing phases. In fact, after installation of the MLI, the midsection of the cryostat has not been altered in over a year of testing. The primary disadvantage to the configuration is the relatively small space between lid layers leading to smaller thermal paths than might be desired. Additionally, since the output of all the feed-throughs goes on a straight line through the lids to the 300K vacuum shell, we had to take great care with our MLI installation to reduce the chance of light leaks down the paths to the 4K stage. In most cases this was mitigated by caps on feed-throughs with the minimal amount of opening possible to route cables, pipes, and motor axles.

6.3.2 Refrigerator Design

For the low temperature cryogenics system, we are reusing the helium refrigerator from BLASTPol with only minor modifications. The system consists of a pumped

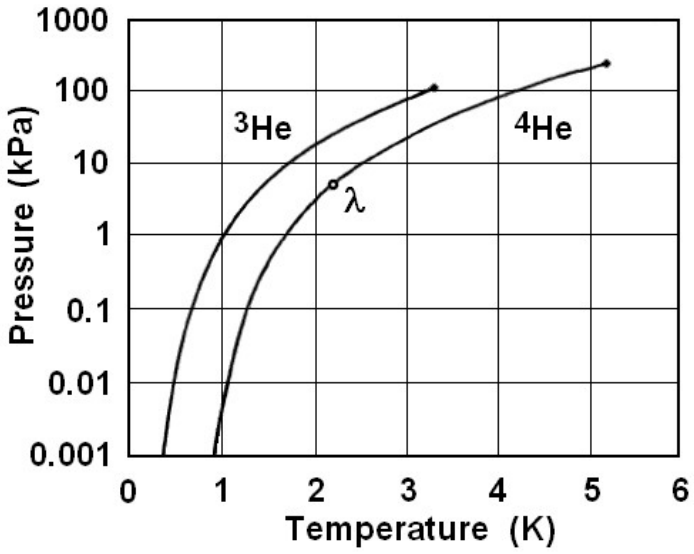

Figure 6.4: The plot shows the vapor pressure of ^{3}He and ^{4}He versus temperature. We can use this information to determine the pressure above atmosphere in the helium tank caused by the impedance from the VCS, the temperature achievable in the pumped pot system, and the expected temperature performance from the ^{3}He refrigerator (Bureau International des Poids et Mesures, 2016).

^{4}He pot and a ^{3}He refrigerator. The ^{4}He pot functions by pumping a near vacuum on a small reservoir, ∼200 mL, that is periodically filled, from the main tank, through a small capillary tube, with flow controlled by a motorized valve. The ^{4}He pot cools to approximately 1.2 K, which serves as an intermediate stage for the thermal isolation of the detectors and as part of the cycling process of the ^{3}He refrigerator described in detail in Truch (2007). The closed cycle ^{3}He refrigerator has a small ^{3}He reservoir that utilizes evaporative cooling to reach temperatures around 270 mK. The vapor is then adsorbed by a sphere containing charcoal to maintain low pressure conditions in the refrigerator. To cycle the refrigerator, the charcoal is heated to release the ^{3}He as vapor, which condenses on a section cooled by the ^{4}He pot and refills the reservoir. Each cycle lasts 90 minutes and we predict we will need to cycle every ∼40 hours under maximum loading of the 270 mK stage.

	Conductive	Radiative	Plumbing	Cables	Misc.
300 K to VCS2	17%	74%	7%	2%	<1%
VCS2 to VCS1	53%	19%	23%	5%	<1%
VCS1 to 4 K	51%	13%	11%	<1%	14%

Table 6.2: List of the percentages of primary contributions to the thermal load at each of the main stages

6.3.3 Thermal Model

To design many of the dimensions of the cryostat we used calculations from a thermal model. The model used radiative and conductive calculations to find the thermal load on each of the cryogenic layers from the various components. There were two major contributions to the load at each main stage of the cryostat, radiative loading from the surrounding warmer shell that goes as T^4 and is therefore much higher at the warmer stages, and conductive loading down the cylindrical G10 mechanical supports which become the dominant loading source at colder temperature stages. Additional sources of loading were from the window which experiences a large radiative load as it is not shielded by MLI. Additionally, all cabling, motor axles, and cryogenic plumbing that had to be fed through to the cold plate each contributed a small amount to the loading. The loading on the 1 K stage was due primarily to the support structure of the arrays, the support of the fridge, and the cabling. The 300mK loading was similarly dominated by support structures and cabling with a limited amount coming from the optical loading of the detectors themselves. Fortunately we are able to place the low noise amplifier (LNA) on the 4 K optics box meaning the total load on the 300 mK and 1 K stages was very small allowing for long time periods between fridge cycles. Table 6.2 shows the relative loading on each stage by the various sources.

6.3.4 Heat Exchangers

Arguably the most innovative component of the BLAST-TNG cryostat are the two copper disk heat exchangers. Heat exchangers are designed to extract cooling power from the gas as it boils off from the liquid Helium reservoir. Helium gas is especially effective as it has a high specific heat of $c_p = 5.19\,\mathrm{kJ/kg\,K}$ which at our predicted mass flow rate of 13 mg/s translates to 67.5mW/K of cooling power. Between the cold plate at 4 K and Vapor Cooled Shield 1 (VCS1) at 60 K this amounts to a maximum cooling potential of 3.78 W from VCS1. To efficiently extract the cooling power from the gas the exchanger is designed to have as many gas to surface interactions as possible to maximize heat transfer. A simple heat exchanger would be a long thin tube. Variations to maximize surface area include routing the gas through chambers filled with ball bearings or a metal foam as in SPIDER(Gudmundsson et al., 2015). However in these types of systems it can be difficult to create a good thermal contact between the heat transfer material and the rest of the shield. The Background Imaging of Cosmic Extragalactic Polarization (BICEP) found an elegant solution by physically wrapping and welding a tube around the outside of their cryostat, a design well suited for their large aperture cryostat.

For BLAST-TNG we decided the simplest solution given our design requirements was to vent out the top of the cryostat and place two heat exchangers along the fill/vent line that couple to their respective VCS as shown in Figure 6.5. Putting them in-line avoided having to create a separate vent line and fill line. If separate lines are used, helium gas will settle in the fill line during normal operations. The gas would then act as a heat switch between 300K and 4K resulting in significant thermal load. This would force a tradeoff between the desire for low conductivity with a smaller fill tube and the desire for a larger tube for easier transfers of liquid Helium. The choice of a separate vent line would also add a considerable amount of

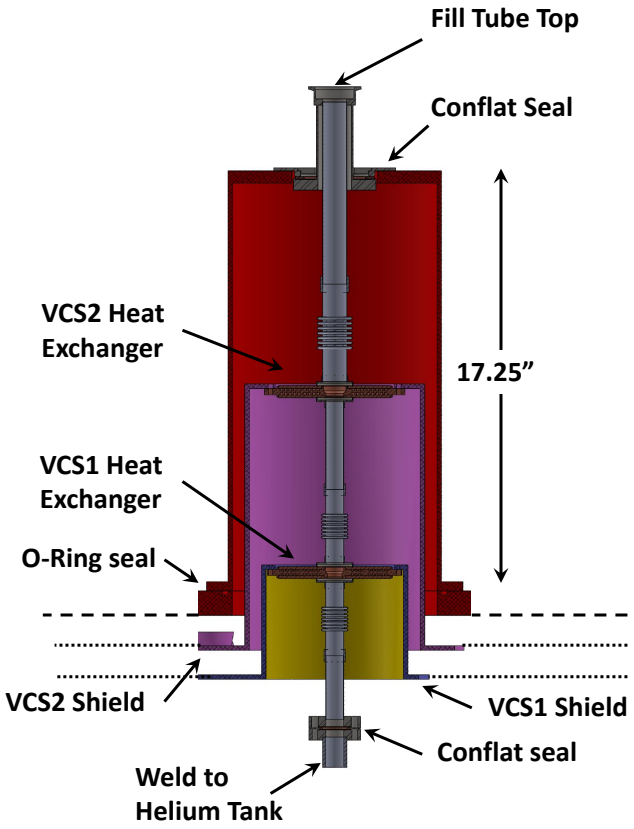

Figure 6.5: Cross section view of the fill tube of the cryostat. The VCS1 and VCS2 heat exchangers are indicated on their in-line location in the fill tube structure. At these locations they couple to the VCS indicated in purple and pink for the VCS1 and VCS2 shields respectively and withdraw thermal power from the shields to provide cooling.

complexity to the system which would need twice as many cryogenic seal, increasing the risk of helium leaks. Due to these considerations we decided to build in-line heat exchangers where gas was forced through the heat exchangers by plugging the main fill line at two points to force gas through the heat exchangers. The plugging mechanism is in itself fairly complex and carries the risk of gas leaking around it and shorting the heat exchangers which would reduce their efficiency, but it was felt these risks outweighed the potential gains of the overall simpler system. To decrease conduction along the fill tube the length of the tube was expanded to accommodate

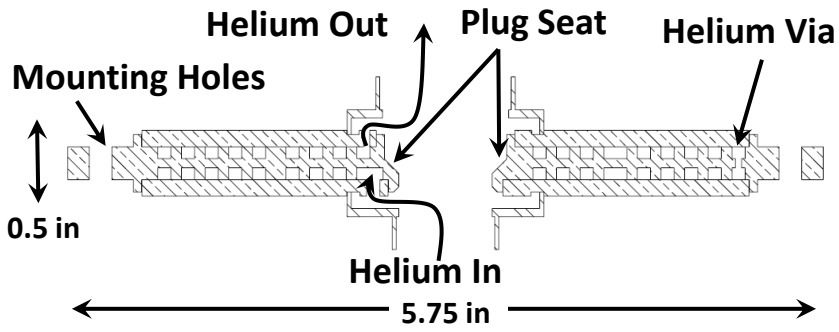

Figure 6.6: Cross section view of the heat exchanger assembly showing the location of the plug seat and the path the helium gas follows through the exchanger. A more detailed view of the heat exchanger construction is shown in Figure 6.7.

thin walled flexible bellow sections that both increase the thermal path and allowed for thermal contractions to take place without stressing the system. The longer path results in the distinctive 'top hat' that extends above the lid of the cryostat which cna be seen in Figure 6.5 and Figure 6.3.

The design of the exchangers creates the desired long conductive path for the gas to flow through by machining a spiral maze on the top and bottom of a central disk. Three vias allow gas to enter the maze, switch from one side of the central disk to the other, and then exit the exchanger back into the primary fill tube as shown in Figure 6.6 and Figure 6.7. To complete the exchanger, a top and bottom plate were soldered on each side along with eight pillars that were placed to prevent gas from 'skipping' sections of the maze by reducing the amount the plates could bow out under pressure. The spiral disk heat exchanger design can be tuned by changing the width and height of the maze channel as well as altering the spiral spacing to control the overall length. The parameters were adjusted to achieve the targeted impedance for gas at each temperature stage. The greater the impedance the more gas to exchanger interactions, but with a proportional rise in pressure that would in turn drive the temperature of the 4 K stage up by increasing the boiling temperature of the helium bath. The impedance goals were designed to find a balance between

these two tradeoffs.

In order to determine which mechanical design would best suit our needs the flow through the heat exchangers was simulated in SolidWorks. The program proved effective in determining flow but was not well suited to handle the thermal aspects of the gas flow and so the gas flow rate was scaled by temperature to remove that variable from the simulations. A test heat exchanger was built in order to see how the design performed versus simulation and is discussed in 7.8. It was found there was some loss in impedance, likely due to the top and bottom plates bowing more than expected allowing gas to flow over the tops of the channels. For the flight designs we increasing the number of support columns holding the plates together from four to eight and made narrower and longer channels with the assumption that gas leaking over the channels was doing so in a small space and would therefore still have many gas to exchanger interactions. These tests determined the final design for the two heat exchangers, one of which can be seen in Figure 6.7. To ensure the best possible thermal path from the exchangers to the VCSs, the top hats were gold plated where the exchangers attached and made of thicker walled, 0.125 inch, aluminum. Additionally, both VCSs were made from hardened 1100 series aluminum which has a higher conductivity than the 6061-T6 aluminum alloy we use in most applications, including the helium tank and the vacuum shell.

6.3.4.1 Heat Exchanger Plug

The plug was designed to force the boil off gas through the heat exchangers as shown in Figure 6.8. It was decided the best seal could be made from a teflon disk with the inverse shape of the exchanger sealing surface. It was also required that the VCS1 plug had to fit through the hole in the Vapor Cooled Shield 2 (VCS2) heat exchanger and the VCS2 plug had to fit through the smallest aperture in the fill tube which required a very compact design. To accomplish this we used metal bellows

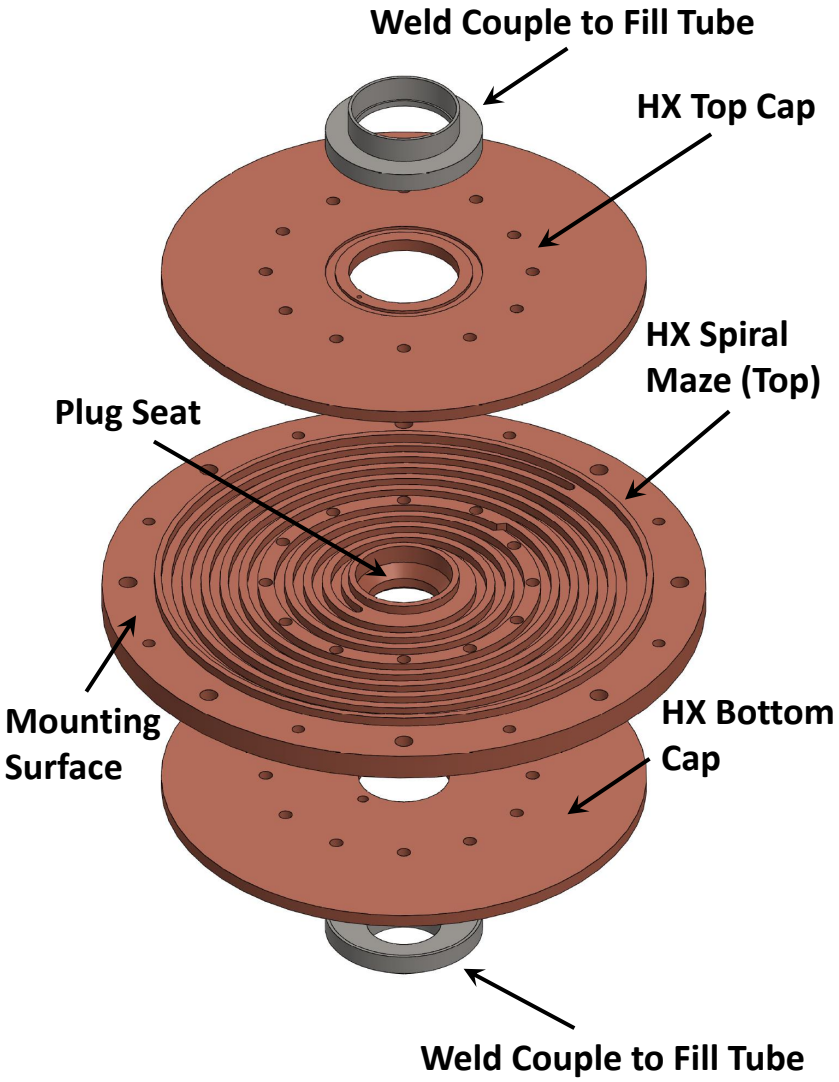

Figure 6.7: Exploded view of the VCS1 heat exchanger showing in detail the top half of the spiral maze that the helium gas from the helium tank bath boil off must go through. In the process of routing through the maze the energy is transferred from the exchanger walls to the gas.

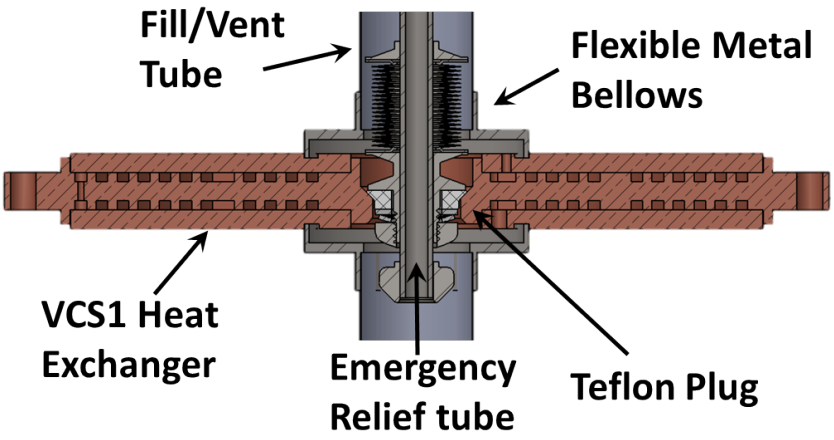

Figure 6.8: Cross section of the VCS1 heat exchanger with the plug inserted to show the method by which helium gas is forced through the heat exchanger

from BellowsTech[8] with a spring constant of 23.75 lb/in, a free length of 0.682 in, and a compressed length of 0.462 in which gives approximately 5 lb of compression on the teflon disk against the sealing surface. Additionally, the plug assembly could be screwed down to further increase the pressure on the sealing surface.

The bellows also conveniently allowed for slight mis-alignments in the system as the bellows are quite flexible and can still make a good seal if the exchanger is off axis by a few degrees. The stainless steel tube to which all plug components were attached provided the mechanical stability for the system while also creating a direct path for gas to escape from the helium tank to outside the cryostat. This path was created for two reasons, the first was to allow gradual de-pressurization of the helium tank when removing the plug assembly and the second more important reason was to allow for the installation of a spring loaded pop-valve which would allow gas to escape in the case that the pressure in the tank becomes higher than two atmospheres. Such a safety feature was seen as critical for safe operation of the cryostat with plugs inserted along the only helium vent line.

[8]BellowsTech LLC, 1289 N. US Highway 1, Suite 1, Ormond Beach, FL

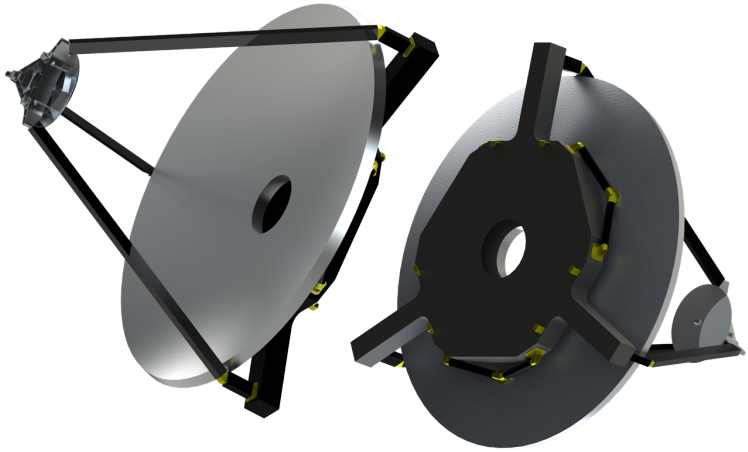

Figure 6.9: A design concept from Vanguard Space Technologies for the primary and secondary mirror structure. The primary is a 2.5 meter diameter carbon fiber parabolic mirror while the secondary is a 52 cm diameter aluminum hyperbolic mirror that will be actuated with respect to the primary to allow for in-flight focusing. Both mirrors attach to a backing optical bench that is made of carbon fiber and will mount to the inner frame of the gondola.

6.4 Optics

6.4.1 Primary and Secondary Mirrors

The primary and secondary mirrors of the BLASTPol instrument were arranged in a Ritchey-Chréitien design with a 1.8 m diameter aluminum primary mirror (M1) and a 40 cm diameter aluminum secondary mirror (M2) described in Chapter 3. BLAST-TNG will have a Cassegrain configuration with a 2.5 m carbon fiber reinforced polymer (CFRP) M1 and a 52 cm diameter aluminum M2. M1 and the three CFRP struts that support M2 are attached to a rigid CFRP optical bench that serves as a backing structure and interface to the gondola inner frame. The bench and both mirrors are being developed and built by Vanguard Space Technologies[9] through a NASA small

[9]Vanguard Space Technologies: 9431 Dowdy Drive, San Diego, CA 92126

Figure 6.10: Left: The graphite mold that was machined and then hand polished to obtain better than 10 μm RMS surface accuracy per our optical requirements. Right: The primary mirror at a stage when it was removed from the mold for metrology of the surface. The next steps in its production included attaching the backing structure, plating the surface, and mounting it to the optics bench prior to a delivery in July 2016.

business innovation research grant. The primary mirror is expected to have better than 10 μm RMS surface error under operating conditions. A conceptual image of the M1 and M2 structure is shown in Figure 6.9 and an image of the graphite mold used for the mirror surface along with the mirror prior to surface coating is shown in Figure 6.10. The mirror is scheduled to be completed by June of 2016.

6.4.2 Cold Optics Design

For the BLAST-TNG cold optics we examined two designs in detail. The size of the optics scale roughly as the size of the FOV and ultimately drive the size of the cryostat and much of the associated structure of the telescope. This required us to make the optics as compact as possible while still meeting our requirements. The design needed to have a Lyot stop at an image of the primary, be able to image the same piece of sky on all three bands simultaneously, have a placement position for a calibration source that would illuminate all detectors, a $f/\#$ to allow appropriate detector spacing, and finally, have a location with good beam overlap to place a HWP for polarization modulation. In addition, a system that was known to effectively

transmit polarization with low cross-polarization conversion was desired.

The first design was a scaled up version of the Offner relay used in BLASTPol with similar spherical re-imaging mirrors M3, M4, and M5. This design is compact and had the advantage of being well understood as we have used it before. The primary disadvantage of the design that we hoped to address was the placement of the HWP. The optical path length along which the HWP was installed did not have good overlap of the beams. This resulted in detectors on opposite side of the arrays looking through different parts of the HWP which, though it had excellent performance, was not entirely uniform across its diameter. The non overlapping beams meant that every time we rotated the HWPR there would be a very noticeable step in the detector response that was different for each detector as described in further detail in Section 4.1. We were able to remove the steps in post-processing but we desired a system that would minimize the effect. With the Offner relay the step could be reduced by placing the HWP as close to M3 as possible which provided significant beam overlap but not total overlap.

6.4.2.1 Gaussian Beam Design

An alternative design was considered which was labeled a Gaussian beam relay. In the Gaussian beam configuration a parabolic mirror, M3, is placed past the Cassegrain focus which has the effect of collimating the beam. Between M3 and a second parabolic mirror, M5, an image of the primary is formed allowing for a Lyot stop baffle to be placed along the path length as well as a HWP in a position of nearly perfect overlap of beams from all the detectors. The focus on the detector array with a chosen $f/\#$ is created by M5 while M4 as a folding flat mirror between M3 and M5 to create a compact configuration. To complete the system the dichroic reflectors would be installed along the optical path past M5, similar to the Offner relay design. The layout can be seen in Figure 6.11.

We quickly discovered that there were several issues with the Gaussian beam design. The primary flaw was that the image of the primary at the Lyot stop was at an angle between M4 and M5 which would require an elliptical stop that would be difficult to manufacture and place correctly. It was also realized that the collimated beams from the detectors could not all be at normal incident to the HWP which would result in varying cross-polarization contributions across the detector array. Additionally, the location of the HWP between M4 and M5 would require it to be after several optical components which would reduce its primary purpose as a polarization modulator to remove systematic cross polarization effects from the instrument. Due to these and several other considerations it was decided to use the Offner relay configuration.

6.4.2.2 BLAST-TNG Offner Relay Design

The cold optics are at 4 K and are in a modified Offner relay configuration shown in Figure 6.11. Three spherical mirrors, M3, M4, and M5, refocus the beam from the Cassegrain output to the detectors with an adjusted $f/\#$ such that the beam is $f/5$ at the focal plane. The M4 mirror is the Lyot stop, which under-fills M1 to 2.4 m and has a hole in its center to shadow the central hole in M1. A calibrator lamp is mounted in the hole in the middle of M4 allowing it to evenly illuminate the entire FOV. The lamp was developed for the Herschel SPIRE instrument and was used in BLASTPol before being transferred to the BLAST-TNG optics (Pisano et al., 2005). There were two main improvements on the BLASTPol design. The first was the removal of beam folding mirrors, previously the last optical elements before the detector arrays, which allows easier access to the arrays. The second change was to mount all components to a single optical bench for ease of assembly and alignment. The final optical parameters are listed in Table 6.3.

Settling on the design for the cold optics allowed us to determine how large the cryostat needed to be and also gave the critical parameters and tolerances for all the

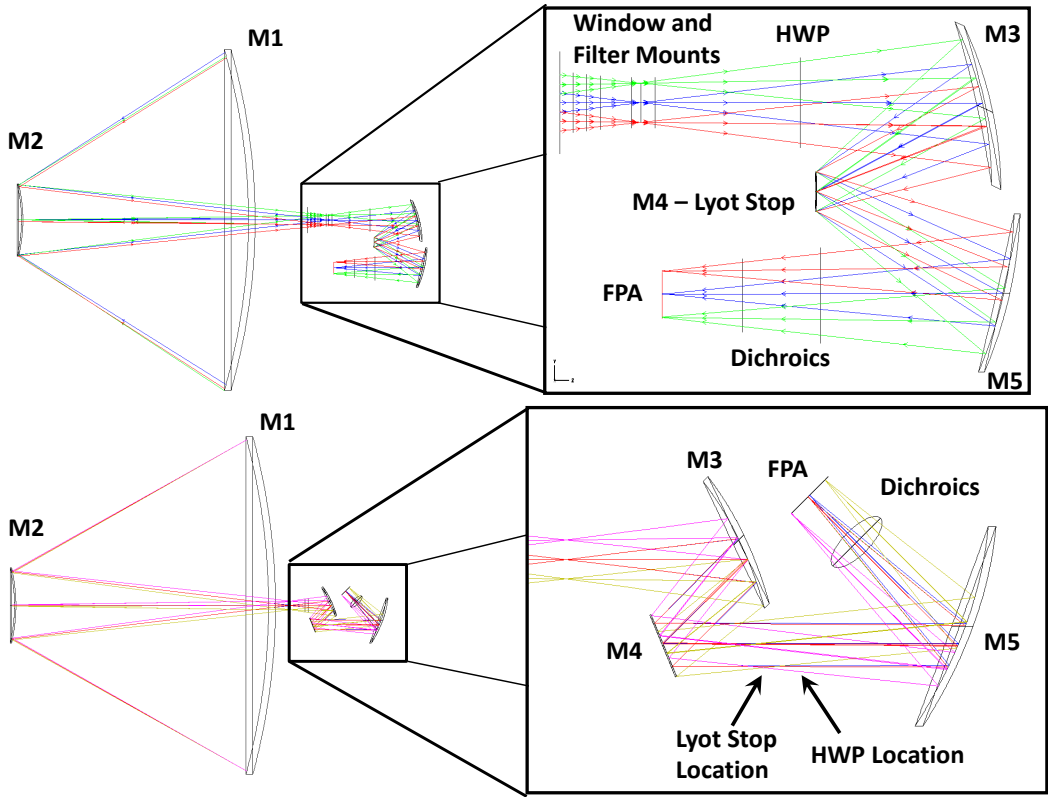

Figure 6.11: Side view of two optics designs for BLAST-TNG with a detailed view of the cold optics. The top view shows a modified Offner relay. M3, M4, and M5 are spherical mirrors with M4 acting as the Lyot stop for the telescope with a blackened hole that shadows the secondary mirror. There are two dichroics that split the beam to the 250 and 350 μm arrays. The 250 μm dichroic is tilted at 22.5° to the optical axis while the 350 μm dichroic is tilted at 30° to the optical axis. Only one of the three focal planes is shown. The HWP is inserted between the Cassegrain focus and M3. The bottom view shows the optical layout of the proposed Gaussian beam design with the first parabolic mirror, M3, followed by a flat folding mirror, M4, and a second parabolic mirror to reform the focus, M5, to the detector arrays. Between M4 and M5 is the location of the Lyot stop as well as a location to mount the HWP. Similar to the Offner design, past M5 two dichroics would be mounted for simultaneous observing at all three bands.

mirrors to be made. As such, completing the optics design was a critical early step in the construction of the telescope and allowed a number of other projects to move forward. There were, however, several modifications to the basic design that were made to accommodate changes in other elements of the telescope later on during the process.

The most significant modification to the original design came as a result of not budgeting enough space between the Cassegrain focus and the surface of the primary mirror. In the space between those two optical elements we needed to fit the outer layers of the cryostat, the inner-frame component that the mirror attached too, and the thickness of the mirror and its optical bench. The inner-frame, mirror, and optical bench designs all ended up being thicker than originally predicted to ensure there would be no gravitational sag of the mirror surface or of its pointing angle with respect to the cold optics over our elevation pointing range of 20- 60 degrees. In order to increase the spacing the design was modified to reduce the $f/\#$ at the Cassegrain focus which effectively pushed the focus farther back from the surface of the primary mirror allowing for the extra space. The change slightly altered the shape of M1 and M2 but had almost no effect on the shape and sizes of the cold optics. A smaller adjustment was also made prior to manufacture that changed the $f/\#$ at the detectors to five. This changed our pixel scale and allowed for more detectors and a marginally larger field of view without having to change the cold optics mechanical design significantly.

6.4.2.3 Cold Optics Mechanical Design

The mechanical design of the cold optics was required to hold the shape and location of the optical components within tolerances determined in Zemax. The tolerances on the optical components include movement in all three directions and two rotation angles. They were determined by constraining the Strehl ratio to be

Geometrical Charac.	M1	M2	M3	M4	M5
Nominal Shape	Paraboloid	Hyperboloid	Sphere	Sphere	Sphere
Conic Constant	-1.0	-2.182	0.000	0.000	0.000
Radius of Curvature	4.161 m	1.067 m	655.6 mm	376.5 mm	749.4 mm
Aperture	$\varnothing$2.5 m	$\varnothing$0.516 m	$\varnothing$28 cm	$\varnothing$7 cm	$\varnothing$28 cm

Table 6.3: Summary of BLAST-TNG Optics Characteristics

greater than 85% under such movements and rotations of each individual optical component. Fortunately, the Offner relay design is relatively flexible as the spherical mirrors are less sensitive to movement than similar hyperbolic or parabolic mirrors. Despite the relatively loose tolerances, every effort was still made to manufacture and mount the optics components to the highest precisions possible with the resources available to us. Additionally, the alignment had to be maintained over the pointing elevations of the telescope which required the optics bench and components to not deflect under their own weight at all elevation pointing angles. An example of the simulations performed in Solidworks to confirm the performance of the designs is shown in Figure 6.12. It was also desired that the assembly be as light weight as possible and the resultant design of the cold optics, Figure 6.13, took all of these requirements into consideration.

The first setp in creating the cold optics mechanical design was to export the Zemax optics model into a CAD compatible format so it could be imported into Solidworks. Since the cold optics are manufactured at room temperatures, the contraction to 4 K needs to be accounted for by scaling all the optical components, in both shape and location, by the contraction amount of the material they are manufacture from. Once the design was in Solidworks it was scaled by the contraction factor of aluminum. Aluminum contracts when it cools by less than 0.5% such that

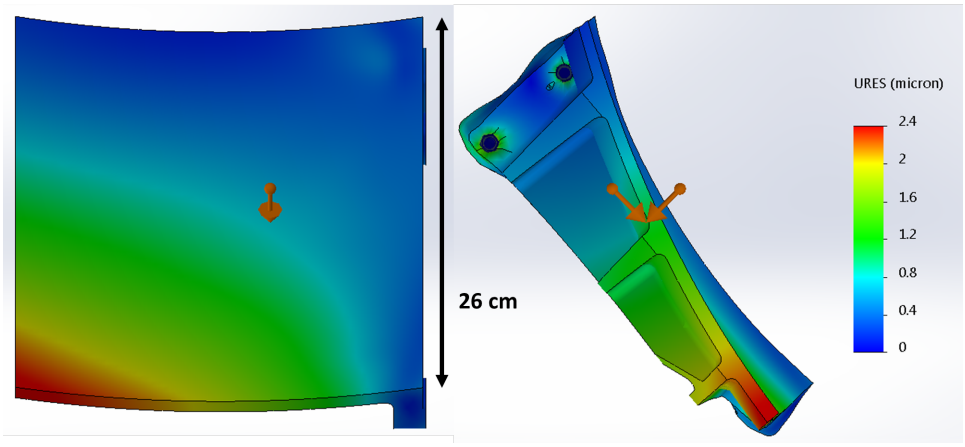

Figure 6.12: Right: M3 from the top at a telescope pointing angle of 45° where combining the two arrows creates the gravity vector with magnitude 9.81 m/s^2 in the downward direction. Left: The view rotated by 90° to show the main face of M3 with the colors in both images representing the amount of deformation predicted by the simulation.

$x_{warm} = 1.0041544\, x_{cold}$ which is a noticeable effect when it comes to the size and shape of our cold optics.The coordinate the design was scaled around was dictated by the geometry of the cryostat in relation to the optical beam. The axis through the Cassegrain focus, which corresponds to the primary optical path along Z, is chosen as the first axis to scale about as we align all optics to this axis. The second axis is the central axis of the cryostat as cooling causes all components to shrink symmetrically towards this. The intersection of these two axes defined the point around which the cold optics design was scaled into a 'warm optics' design. Once the warm optics shapes and locations were defined, mechanical components could be designed to create all required surfaces and mounting locations.

Previously, with BLASTPol, the optics box was mounted to the cold plate at three points on three different faces of the box with the M3 and M5 mirrors bolted to two sides of the box. The BLASTPol design was rigid but somewhat complex as the compact assembly required considerable effort to access any of the optical components. With BLAST-TNG we decided on a more accessible design based on the principle of

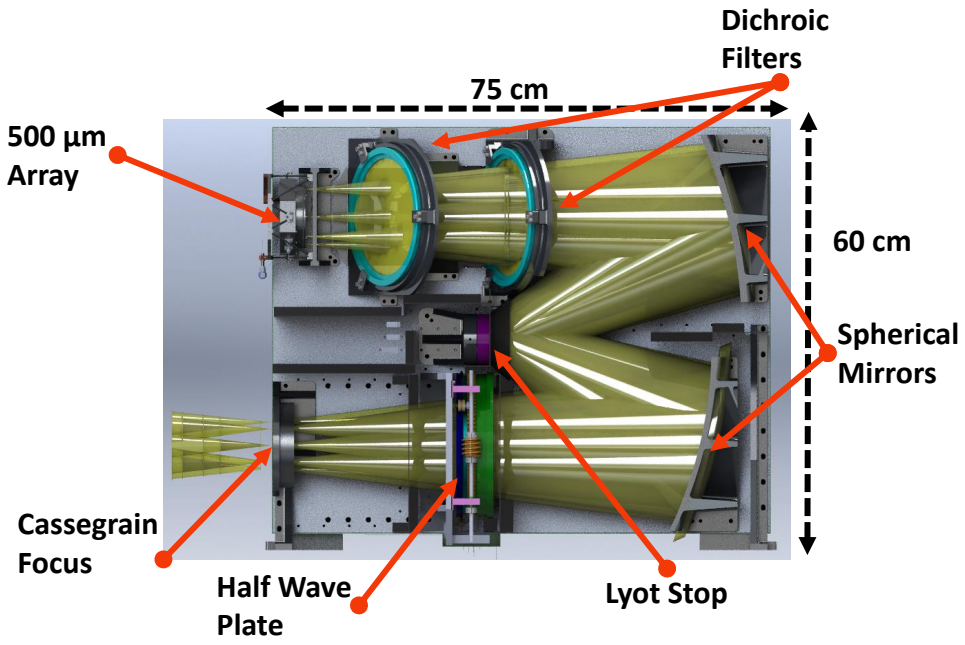

Figure 6.13: A 3D model showing all of the optical components as they appear in the mechanical model along with the projected optical beam in yellow.

a standard optics bench that relies on one very rigid surface from which to mount all optical components. The mounting surface consists of a one inch thick light weighted rectangular aluminum plate. The optics bench surface is mounted at 90 degrees from the cold plate and, in the flight configuration, hangs beneath the cold plate. To keep the optics bench surface rigid and perpendicular to the cold plate surface, two large mounting brackets were designed to hold it in place. The brackets themselves are pinned to the cold plate in two locations to allow for repeatable mounting at the same location. Additionally two smaller brackets are placed on the front side of the optics bench which have slotted holes to prevent them from over constraining and stressing the optics bench mount.

All optical components were bolted to the front side of the optics bench with the exception of the 250 μm array mount as the beam path puts its mounting location on

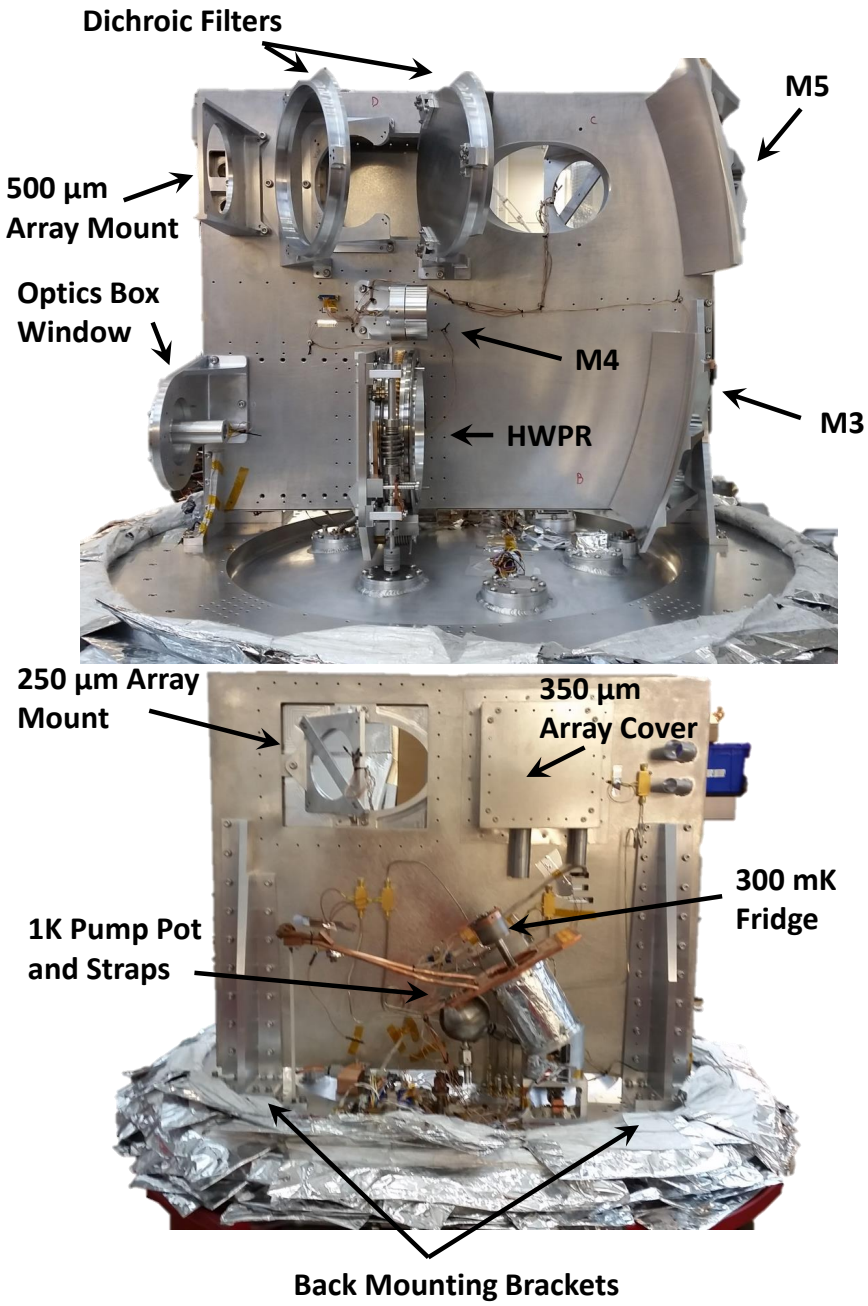

Figure 6.14: Bottom: The back side of the optics bench where the 1 K pot, the 300 mK fridge, the CBOB, and LNAs are mounted along with the 250 μm array mount. The pipe like structures are magnetic shielding at locations of necessary holes in the shield to allow the passage of thermal straps and cabling. Top: The front surface of the optics bench with mounted optical components. A fixture is mounted at the window to which an alignment laser and a target reflector can be attached.

the back side of the optics bench. All structures were designed to be light-weighted, non-interfering with beam paths with typical 1 cm minimal clearances, and deform less than 20 μm under typical loading situations during normal flight operations. The mounts were attached to the bench with three bolts and two pins for each component. The three point contact fully constrains the plane on which it mounts and the two pins allow repeatable mounting to that surface. The surface around the location of the bolts and pins was raised slightly such that the only surface of the optical component that was touching the optics bench was at the location of the bolts and pins. Another consideration that was taken to ensure the components mounted flush to the plane was to create a far side countersink at each bolt hole location to ensure deflection of the bench surface from the force of the tightened bolt did not affect the mounting plane. A detailed image of all the optical components on the front and back of the bench can be seen in figure 6.14. The design of M4 was updated to enable an easier mounting of the calibrator lamp while also ensuring an even illumination of M5 and consequently, all of the detectors as shown in Figure 6.15.

6.4.2.4 Production and Assembly

To machine the optical components we collaborated with the group at Arizona State University (ASU) who have extensive experience in precision machining. They use a Kern CNC[10] machine that they run continuously prior to machining of components to ensure the machine itself has reached a thermal equilibrium that allows approximately two micron precision in machining of surfaces. To create the optics in a timely manner all optical components were machined at outside companies with supervision and specifications provided by ASU. M3 and M5 were manufactured at L&W Machine[11] while all other components were made by MVI[12] The entire assembly

[10]KERN Precision Inc., 1010 W Fullerton Ave., Addison, IL 60101
[11]L & W Machine Co., 2733 E Sellers Dr, Pheonix, AZ 85040
[12]MVI Engineering & Manufacturing, 5772 Crown Dr, Mira Loma, CA 91752

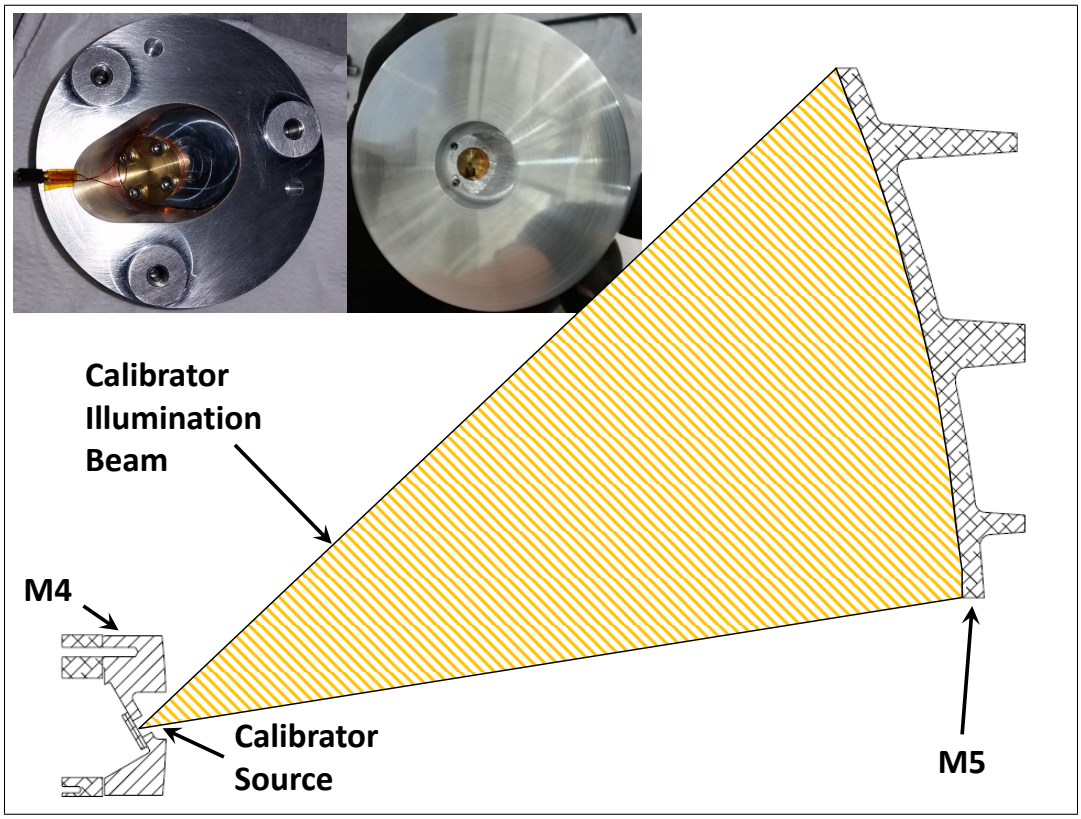

Figure 6.15: Top left: The back side of M4 with the mount and connector for the calibrator source shown on the tilted back surface. Top right: The front of M4 with the hole for the calibrator source to illuminate all of M5. A cross section view of the model with M4 and M5 shown demonstrates the tilted mount and hole that allows the calibrator to evenly illuminate all of M5 which means all detectors will see the calibrator. From the detectors view point the calibrator source appears to be shining along the central axis of the primary mirror. The interior surfaces of the area the calibrator shines from will be covered with absorptive material to prevent stray light shining on the detectors from that region effectively blocking the path of light that is obscured by the secondary mirror.

was then sent to Dynametrix[13] to perform metrology with a coordinate measuring machine to confirm the surface shapes and relative locations were correct which confirmed all components met our tolerance specifications.

Once the performance of the assembly was confirmed it was shipped as a unit to UPenn in a specially made shipping container with vibrational stabilization to ensure the assembly was not damaged during shipping. At UPenn the optics were mounted on the cold plate along with the installation of two pins to ensure the optics were mounted on the correct axis. Once mounted inside the cryostat we were able to move forward with the integration of all other components including the HWPR, thermometry, the calibrator source in M4, and the focal plane array (FPA) for each wavelength. As components were installed the performance of the integrated assembly was tested through a variety of methods detailed in Chapter 7.

The cold optics were built and tested at ASU prior to delivery to UPenn in March of 2016.

6.4.2.5 Magnetic Shielding

It is necessary to install magnetic shielding to prevent any magnetic field fluctuations outside the box from penetrating to the detectors which could add excess noise and variable responsivity in the detector channels. The FPA will be shielded by an Amuneal[14] Amumetal 4 K material (A4K) box that encompasses the cold optics, which will significantly reduce the effect of local magnetic field fluctuations on the MKID arrays. The box surrounds all of the cold optics to block stray light within the 4 K shield and to reduce the quantity and size of the holes in the magnetic shield, with the significant exceptions being the window and feedthroughs for cabling and thermal straps. An image of the box is shown in Figure 6.16.The interior of the box

[13]Dynametrix Inc., 801 N Granada Dr, Chandler, AZ 85226
[14]Amuneal

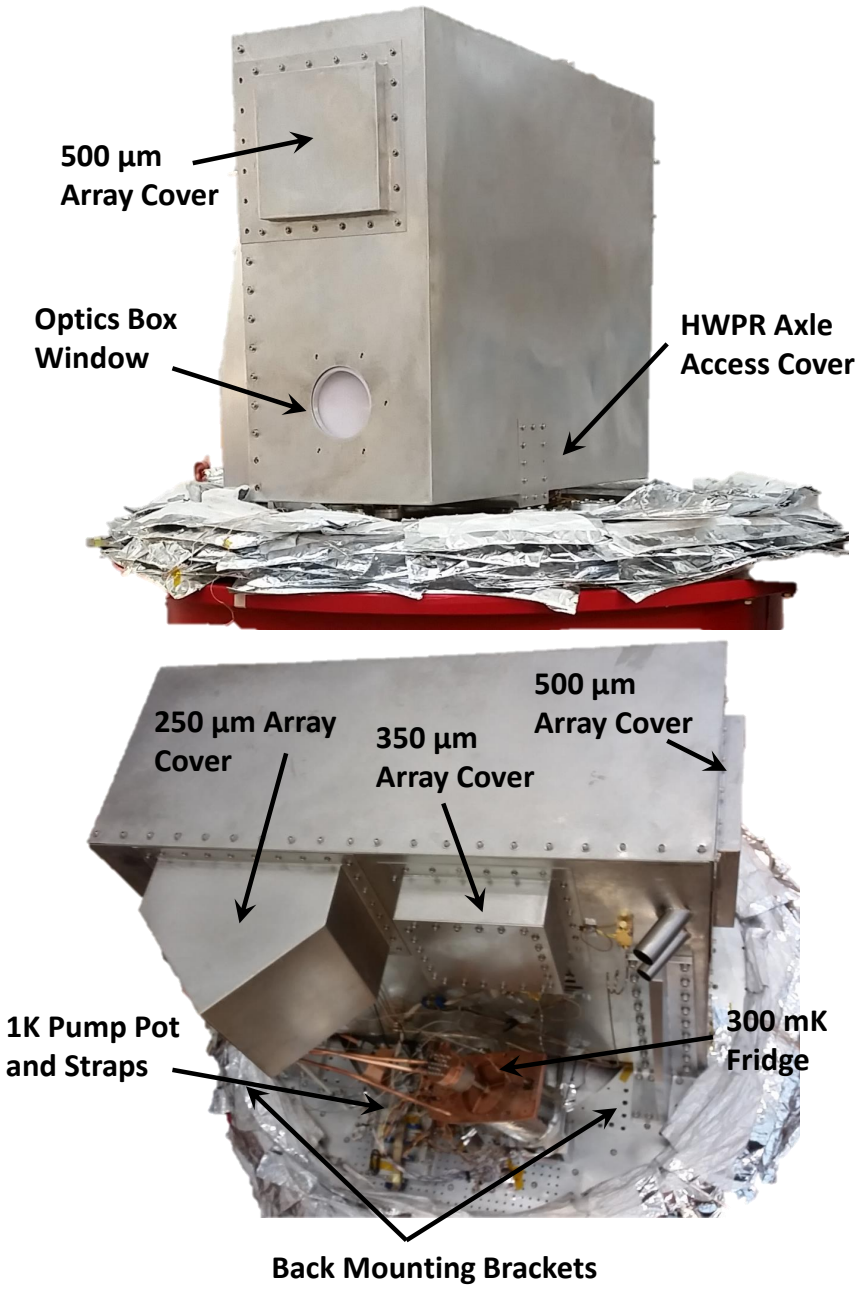

Figure 6.16: Bottom: The back and top of the Amuneal magnetic shielding with the 250 and 350 μm array covers as well as the thermal distribution and cabling for the arrays. Top: The front and side of the magnetic shielding where the optics window, 500 μm array cover, and HWPR axle cover are located. The HWPR cover allows us to connect the motor axle to the HWPR mechanism after installing the magnetic shielding. A LPE filter is mounted on the inside surface of the window.

will be coated with a special mixture of Stycast epoxy mixed with carbon and silicon carbide which effectively absorbs light at all wavelengths equal to and shorter than our submillimeter bands. The coating will ensure that stray reflections are absorbed in the box and will not propagate back to the detectors. The design was advised by Amuneal to contain 1 inch overlaps on all joints to ensure no magnetic field leakage. Additionally, for the holes in the shield used to pass coaxial cables through for the detectors as well as thermal straps for the 1 K and 270 mK stages, protruding tubes were created with roughly a 3:1 ratio of length to hole aperture diameter to ensure attenuation of the magnetic field at the feed through hole locations. The final component of the shielding consists of a series of thin Aluminum baffle structures, also covered in absorptive material, that are strategically placed throughout the optics box to provide additional surfaces to block scattered light.

6.4.3 Primary Filter Stack

Prior to the light entering the cold optics, it must pass through a series of IR blocking filters and LPE filters, developed at Cardiff University (Ade et al., 2006), that are attached to the windows in the cryostat shells as shown in Figure 6.17. These serve to reduce thermal loading on the cryostat and the detectors. The beam is split by two low pass edge dichroic filters placed after M5 to allow simultaneous observations of the same FOV in all three bands. The observed frequency bandpass is further constrained by filters mounted to the front of the arrays and by the feedhorn design. A measurement of the BLASTPol bands is shown in Figure 3.10 (Wiebe, 2008) which are expected to be very similar for BLAST-TNG. For ground tests in the lab we have two nuetral density filters (NDFs) that attenuate the signal of the input light in our bands by 95-98 % of the total amount of light to bring the optical loading on the detectors into the expected flight levels. One NDF mounts at the cold optics

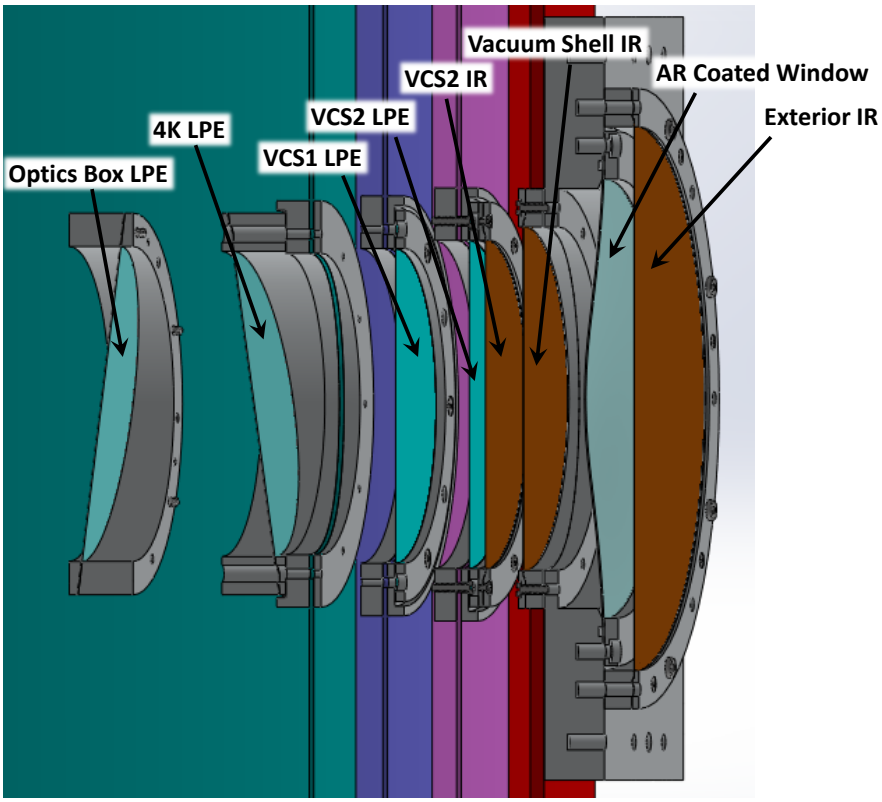

Figure 6.17: A cross section angled view of the filter stack used in BLAST-TNG with IR blocking filters, at warmer stages, and LPE filters, at colder stages. All optics box components aside from its filter have been suppressed for clarity. The optics box and 4 K LPE filter surfaces are near the Cassegrain focus which creates the need to mount them at angles to reduce the chance of ghost images being reflected back to the detectors. The colors show, from left to right, the different shells with a teal 4 K shield, purple VCS1, pink VCS2, and red vacuum shell.

window which has better performance for ground testing prior to our deployment in Antarctica. The second NDF mounts outside the cryostat window allowing us to perform a wide array of optical tests while in our flight filter configuration.

6.5 Detectors

BLAST-TNG will serve as a pathfinder instrument with the first use of MKIDs on a balloon-borne platform. Each feedhorn-coupled pixel will have two orthogonally

oriented detectors to simultaneously sample both the Q and U Stokes parameters. The total number of pixels will be approximately 1500 with over 3000 MKID detectors, which is more than 10 times the number of bolometric detectors flown with BLASTPol.

6.5.1 Feedhorn Design

A precision machined aluminum feedhorn array is placed in front of the detector wafer to couple the light to the absorbing elements. The BLASTPol feed array used a conical feedhorn design, similar to the Herschel SPIRE feedhorns (Rownd et al., 2003). However, these were not optimized for polarimetry and have a divergence in the E and H fields that results in an asymmetry between the polarization directions. BLAST-TNG will use a modified Potter horn design (Potter, 1963) with three steps, which excites additional modes in the EM field and reduces asymmetries in the polarized light, while maintaining the 30% fractional bandwidth required (Tan et al., 2012). The profile is shown in Figure 6.18. The feedhorns are also much easier to fabricate than equivalent corrugated feedhorn designs.

6.5.2 MKID Design

MKIDs have been identified as a promising new technology for astronomy, with potential applications from the submillimeter to the X-ray. The superconducting, titanium-nitride, MKIDs that have been designed and produced for BLAST-TNG use a single loop inductor and inter-digitated capacitor (IDC) to form an LC circuit with a tuned resonant frequency (Day et al., 2003). Photons incident on the inductor, with energies greater than the gap energy, break Cooper pairs which causes a measurable change in the impedance of the inductor as shown in Figure 6.19. Dual-polarization sensitivity is achieved by placing two orthogonal detectors in a single feedhorn coupled

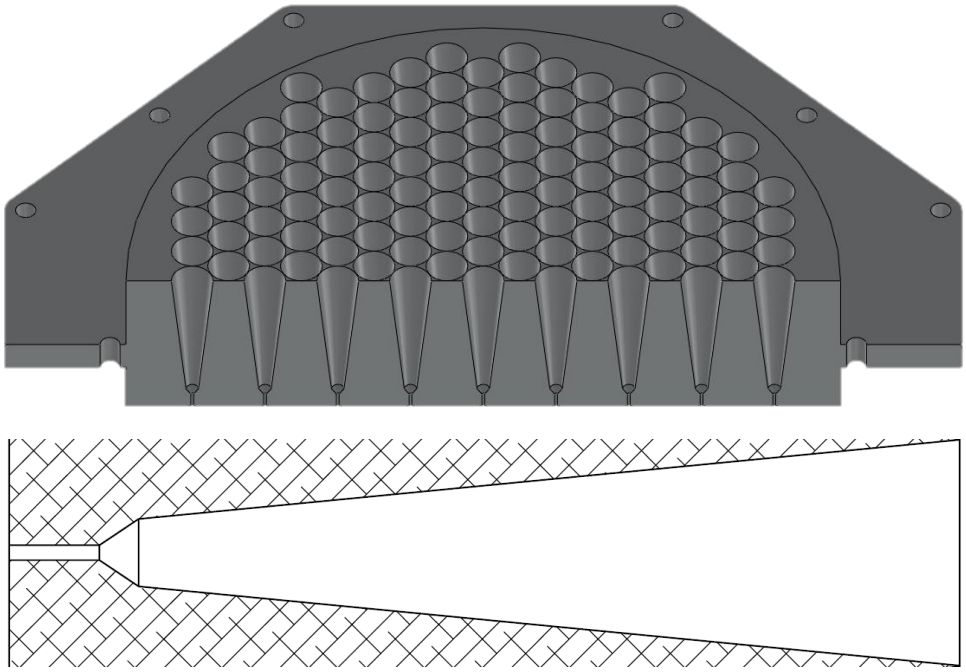

Figure 6.18: The top image shows a cross section view of the 500 μm feedhorn block tilted to show the feedhorn packing. The lower image shows a detailed view of the Potter feedhorn profile which instead of being purely conical, exhibits three steps in the profile. The horns are machined out of aluminum using custom drill bits.

pixel. Fabrication of the MKID is quite simple, with the primary circuit done in a single layer on a silicon wafer (Hubmayr et al., 2014).

Alternative detector technologies, such as transition edge sensor (TES) arrays, have considerably more complicated fabrication processes. Additionally, thousands of MKID signals can be multiplexed on a single feed-line, with the number of the detectors currently limited by the warm readout electronics technology. The signal from the MKID requires a single low power (< 7 mW), wide-band, silicon-germanium amplifier, that operates at 4 K. These factors made the production of large scale, dual-polarization, MKID arrays achievable on the time-scale of the BLAST-TNG project. The first iteration of the 250 μm array has been produced and an image of it can be seen in Figure 6.22. The fast production time and easy installation of new array wafers

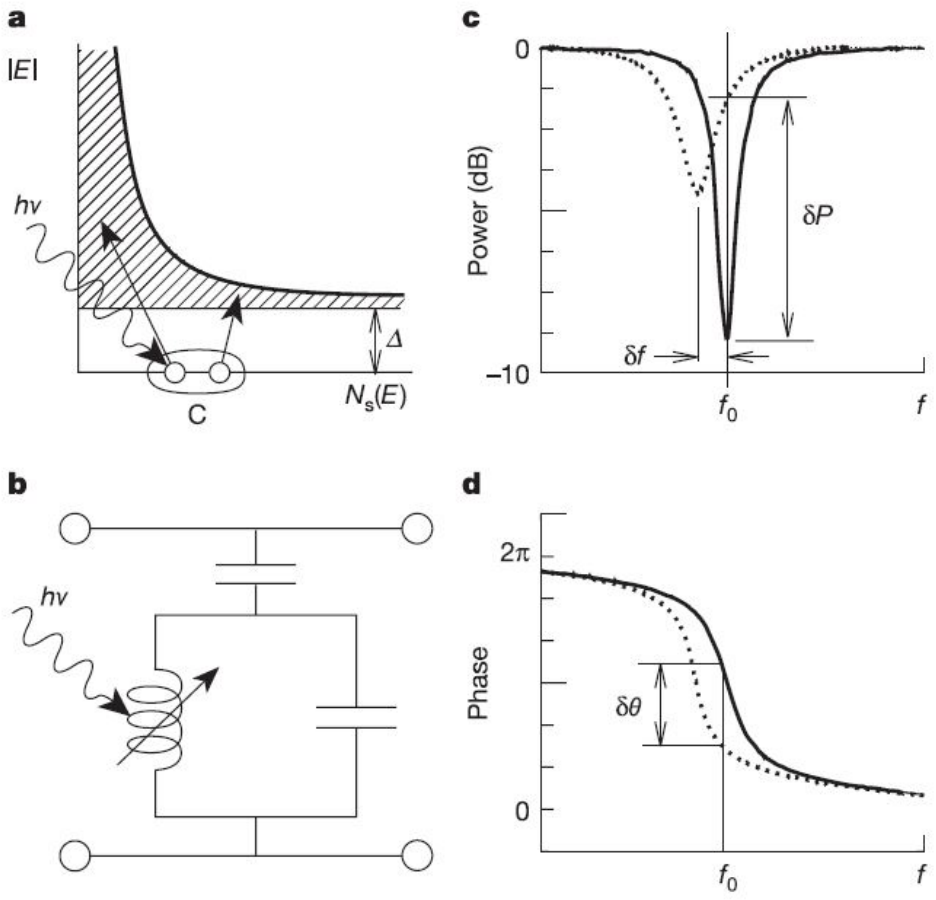

Figure 6.19: A figure from Mazin (2005) that shows in (a) an incident photon with energy $h\nu$ greater than twice the superconducting gap energy, Δ, breaks electron Cooper pairs, C, at the Fermi level exciting a number of quasiparticles with the shaded area representing the density of states of quasiparticles bounded by a function of quasiparticle energy, E. In (b) the simplified MKID electrical diagram is shown with a variable impedance inductor, which is the absorbing element, and capacitor creating the resonant LC circuit which is in turn capacitively coupled to the feedline carrying the probe signal. (c) shows the effect the impedance shift of the inductor has on the frequency and amplitude of the probe signal sent through the feedline while (d) demonstrates the effect the impedance shift has on the phase of the probe signal. BLAST-TNG records the phase shift as the detector signal.

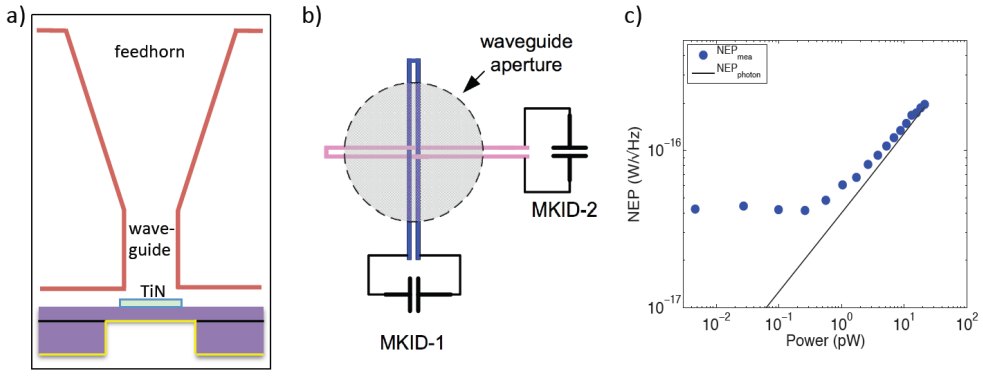

Figure 6.20: **(a)** A cross section of a single pixel with the feedhorn coupled MKID detector. **(b)** A schematic of the detector layout with two single loop inductors orthogonally aligned at the end of the waveguide. Each inductor is part of an LC circuit with a set frequency that couples to a readout line. **(c)** The measured noise equivalent power (NEP) of a BLAST-TNG prototype detector as a function of radiative load at a band centered on 250 micron Hubmayr et al. (2014). The data (blue points) are limited by photon noise (black line) at thermal loads above ∼1 pW, which includes our expected in-flight loading condition (7 to 17 pW).

will allow us to receive and install new arrays as the National Institute of Standards and Technology (NIST) continues to improve the detector design over the course of the telescope's integration and testing procedures prior to Antarctic deployment.

6.5.3 Initial MKID Testing

A seven element feedhorn coupled detector array was constructed and tested with a variable temperature black-body load at NIST. The tests aimed to characterize the noise performance of different detector models in order to find the design that best meets the needs of the instrument. The 250 μm MKID detectors have been shown to be photon noise limited in a seven pixel test array that was feedhorn coupled to a variable blackbody source. Additional details of the tests and results can be found in Hubmayr et al. (2015). The noise equivalent power (NEP) of the detectors was fit using a three component noise model that included recombination noise and the photon noise on top of a flat background noise level. The fit determined that

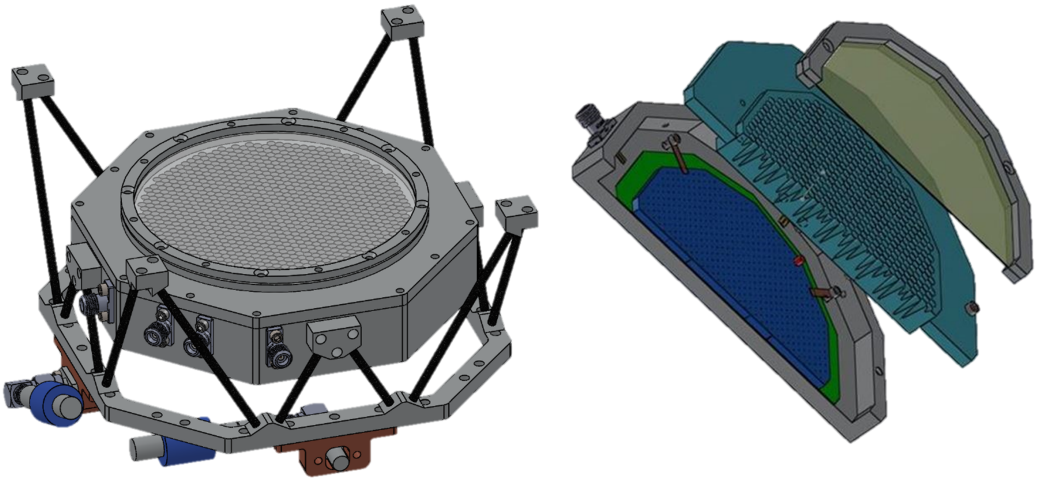

Figure 6.21: Left: The complete FPA support structure. The feet mount to fixtures that are attached to the optics bench. Carbon fiber rods provide thermal isolation by offsetting the FPA from the 4 K optics bench via an intermediate 1 K stage. Right: A cross section of the FPA excluding the support structure which includes (from top to bottom) the bandpass filter, feedhorn array, waveguide wafer (blue), detector wafer (green), and FPA housing.

the detectors were limited by photon noise in the range 1 pW to 20 pW, which comfortably encompasses the expected BLAST-TNG flight loading on the detectors of approximately 5 to 14 pW. The fit to the noise model also produces an estimate of the optical coupling efficiency which was determined to be $\sim 70\%$. Current efforts are focused on demonstrating a detector noise $1/f$ knee below 0.01-0.1 Hz, which is a rate determined by our scan speed across targets.

The 250 μm (1.2 THz) array is designed to have a bandpass from 325 to 175 μm (1.0 to 1.4 THz) which is defined on the long wavelength end by the feedhorn profile and on the short wavelength end, by a low pass filter mounted in front of the feedhorn block. The bandpass was tested using a hot 1050° C thermal source coupled to a FTS that filled the feedhorn beam. The tests determined that the edges of the bandpass for both polarization directions in a single pixel to be in agreement with the design of the filters and feedhorns (Dober et al., 2015).

80% co-polar and <1% cross-polar absorption in a pixel has been predicted by run-

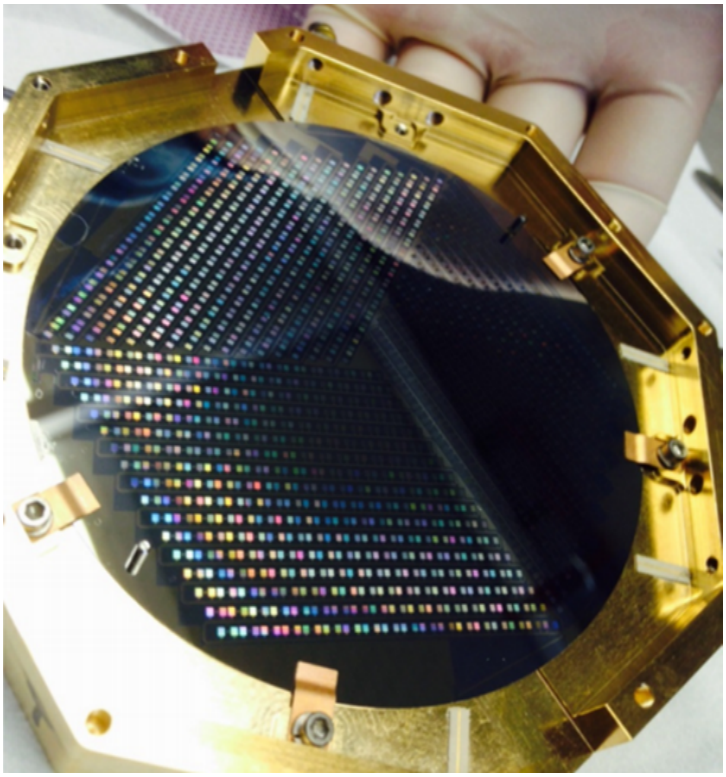

Figure 6.22: Image of the 250 μm MKID detector array mounted in the gold plated FPA holder. One can visually see the IDC for each of the detector elements on the wafer.

ning a high frequency structural simulator on a model of orthogonal absorbers with silicon-oxide insulated crossovers and a quarter wavelength deep metalized backshort. The MKID's polarization performance has been tested and is described in detail in Dober et al. (2015). The tests were performed with a source chopped between 1050° C and 20° C with a wire grid polarizer mounted between the source and the detectors. The polarizing grid is then rotated to produce a sinusoidal response at the detectors with orthogonal detectors 90 degrees out of phase. Fits to these measurements determined the cross-polar signal for both detector directions in a pixel to be <3%, demonstrating the effectiveness of feedhorn coupled MKIDs for submillimeter polarimetry measurements.

Additional details of the MKID design and performance can be found in McKenney

et al. (2016).

6.5.4 FPA Design

The FPA is made of an eight-sided polygon housing, the detector wafer, the waveguide wafer, and the feedhorn block (see Figure 6.21). The housing has mounts for the coaxial SMA connectors for the multiplexed feed-line, the thermal standoffs, and for the copper heat strap from the ^{3}He refrigerator. The detector and waveguide wafers are mounted using a combination of fixed pins and pins-in-slots to constrain the wafers in the plane of the array without causing stress from thermal contraction between different materials. The wafers are held against the housing by beryllium-copper spring tabs. There is extra space at the edge of the detector wafer to give room for wire bonds to the feed-line which also serve to thermally sink the detector array. The feedhorn array attaches to the rim of the housing and is offset from the waveguide wafer by a small gap ($\sim$20μm). The feedhorn block also has a mounting rim for filters and alignment fixtures.

The whole FPA assembly is thermally isolated by a carbon fiber structure that connects the FPA to a fixture at 1 K, which then connects to the 4 K optics bench. The input SMA cables connect to a directional coupler which serves to heat-sink the cables before they go into the arrays. The output SMA cables go directly to the cryogenic amplifier. Thermal modeling predicts loads from the structure, cables, and radiation to be $< 20\,\mu$W and $< 150\,\mu$W on the 270 mK and 1 K stages, respectively. Finite element analysis of the mechanical structure predicts deflections of <5 μm across the array under typical flight stresses.

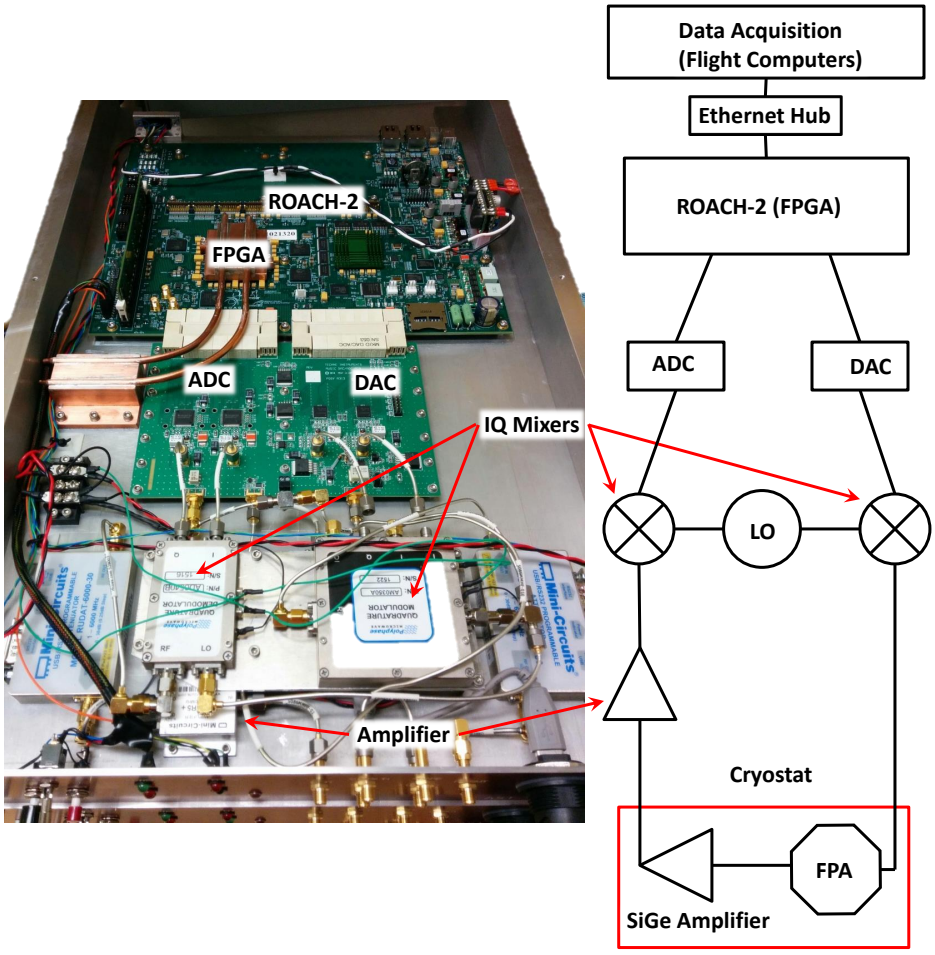

Figure 6.23: Left: An image of the inside of the readout hardware enclosure showing all the major components of the readout. Right: A greatly simplified schematic of the detector readout process.

6.5.5 Detector Readout

MKIDs have the advantage of a simple cryogenic layout, with a single-layer detector wafer and one coax line able to read out hundreds of detectors. However, this shifts a large amount of complexity to the warm readout electronics. BLAST-TNG uses Reconfigurable Open Architecture Computing Hardware -2 (ROACH-2) (Werthimer, 2011) boards developed by the Collaboration for Astronomy Signal Processing and Electronics Research (CASPER) to generate a frequency comb consisting of all the resonant frequencies of the detectors sampled by that system. The comb is sent through coax to the feed-line that runs across the detector wafer. The signal modulated output frequency comb is boosted by a SiGe amplifier, provided by ASU, which operates at 4 K. After leaving the cryostat, the comb is digitized, analyzed, and compared to the input comb to identify shifts in phase of individual detectors due to impedance changes in the inductors. The relative shifts are time-stamped and then sent to the computer to be merged with pointing data, which is then recorded on the hard drives.

The central component in the readout chain is the ROACH-2 board. The ROACH-2 consists of a Xilinx Virtex 6 FPGA coupled to two ZDOK connectors, a PowerPC CPU connected to 1Gb Ethernet, 72-bit DDR3 RAM for slow memory access, and 4 x 36 bit wide 288 Mb QDR II+ SRAMs for fast memory access. The ROACH-2 is used in conjunction with a DAC/ADC board that was designed for ARCONS (McHugh et al., 2012). The ADC/DAC board is used to send out and read in the frequency combs. The FPGA is the workhorse of the ROACH-2 board and performs all the necessary digital signal processing before sending out the packetized phase streams to the CPU to be sent out over the 1Gb Ethernet to the flight computer.

Our MKID resonance frequencies of 700 MHz to 1.25 GHz are above the operational ADC/DAC frequency band of $\sim 0 - 500$ MHz which necessitates a local

oscillator (LO) to convert the output tones from the baseband of the ADC/DACs to the resonance frequencies of the MKIDs and vice-versa. We perform these conversions via two IQ-mixers. These mixers also allow us to stitch together both 500 MSPS ADCs into a single 500 MHz bandwidth. IQ mixers address the problem of maximizing information transmission in a limited bandwidth by allowing the user to modulate both the in-phase and quadrature components of a carrier simultaneously, doubling the information density. An image and schematic of the readout change is shown in Figure 6.23.

Building on the legacy of previous MKID readouts created for the ROACH platform, the BLAST-TNG firmware performs coarse and fine channelization of 512 MHz of RF bandwidth. The resulting channels are ∼100 kHz wide and can be read out at rates of 200 Hz to 500 kHz. BLAST-TNG uses five ROACH-2 boards, three for the 250 μm array and one each for the 350 and 500 μm arrays, along with a suite of IF components and single board computers. The readout hardware is housed in the 'ROACH-2 Motel', a custom enclosure designed for BLAST-TNG that heat sinks elements on the boards to the inner frame to avoid overheating of the components. The ROACH-2 electronics will be mounted directly to the inner frame near the cryostat to minimize the path length of the readout SMA cables. Control software is written in Python, and will be ported to C for integration into the flight software. Details of the systems overall performance are forthcoming.

6.5.6 Polarization Modulation

Polarimetry is achieved through the dual-polarization-sensitive pixels and a stepped HWP. The primary scanning strategy during flight will be a slow raster scan, which works well for extended sources. A typical BLAST-TNG raster will scan across targets in azimuth at a speed of approximately $0.5^{\circ}s^{-1}$ with an elevation scan speed

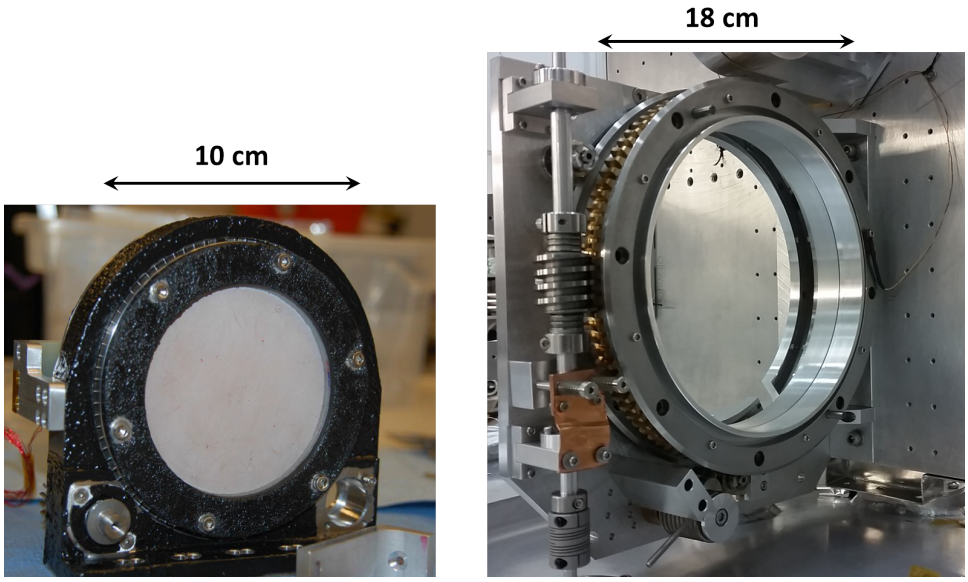

Figure 6.24: Left: An image of the half wave plate and rotator mechanism that was used in BLASTPolMoncelsi et al. (2014). Right: An image of the new HWP rotator mechanism with a larger clear aperture of ∼18 cm. The rotator is bolted to the optics bench which is in turn mounted on the cold plate of the helium tank. Rotation of the HWP is driven by a worm gear that is coupled to a motor mounted to the 300 K lid of the cryostat with a G10 shaft to provide thermal isolation.

calculated to change the elevation by 1/3 the array FOV in one crossing of the target in azimuth. A HWP is used to modulate the polarization signal, so that each pixel samples $\pm Q$ and $\pm U$ multiple times during the mapping of a target which allows us to control for polarization systematics. The HWP is stepped between four set angles (0°, 22.5°, 45°, and 67.5°) after each completed scan of a source in elevation. The HWP is moved using a stepper motor, mounted to the lid of the cryostat along with an encoder, and a magnetic coupling mechanism to transfer torque through the vacuum jacket of the cryostat.

The HWP used in BLASTPolMoncelsi et al. (2014) had a 10 cm diameter aperture and was constructed using five layers of 500 μm thick sapphire, glued together by 6 μm thick layers of polyethylene, and an anti-reflective coating (Figure 6.24). However, the technology did not scale easily to larger apertures necessitating a new approach. The

HWP developed for BLAST-TNG uses metal mesh filter technologyAde et al. (2006) to make a large diameter, $\sim$18 cm, HWP. These types of HWP have demonstrated broad-band transmission at THz frequenciesPisano et al. (2012, 2014). An embedded metal-mesh HWP can also be produced with diameters larger than the commercially available sapphire plates (i.e. larger than $\sim$33 cm).

The detector rows are oriented parallel to the nominal scan direction with the MKID orientation rotated by 45 degrees in adjacent pixels along the scan direction. This alignment allows for sampling of both Q and U Stokes parameter on a timescale that is shorter than the array's common-mode $1/f$ noise, creating a redundant polarization modulation feature. The sampling timescale of the Stokes parameter is $\sim$0.025 s, which is determined by the detector separation, $\sim 45''$ at 250 μm , and typical scan speed, $\sim 0.5^{\circ}\mathrm{s}^{-1}$.

Chapter 7

BLAST-TNG Cryostat Testing

The cryogenic receiver for BLAST-TNG, which we named 'Layla', was delivered to UPenn in February 2015 from Precision Cryogenics[1] with an approximate weight of 800 pounds. After receiving the BLAST-TNG cryostat we proceeded to test the performance of the cryostat in stages as we added additional components including the refrigerator system, cold optics, and detector arrays. Through these tests we were able to gain an understanding of the baseline characteristics of the cryostat, especially in regards to the thermal loading experienced at each stage, the equilibrium temperatures, and the efficiency of the heat exchangers in cooling the VCSs. The tests also established the base temperatures achievable at 1 K and 300 mK by our refrigerator system as well as the projected cryogenics hold time and refrigerator cycle times which establish the expected flight performance of the cryostat. A list of cool downs performed within the scope of this document is shown in Table 7.1.

[1]Precision Cryogenic Systems Inc., 7804 Rockville Rd., Indianapolis, IN 46214

Cool Down	Modifications	Goal	Start Date
One	MLI & Housekeeping	Cryostat baseline & housekeeping test	July 2015
Two	Refrigerators & prototype FPA	1 K & 270 mK system characterization	Sept. 2015
Three	1 K adjustments, mock optics bench, & HWPR	1 K system tests & HWPR thermal properties	Dec. 2015
Four	1 K adjustments, cold optics, & 250 μm array	1 K system tests & 250 μm array readout	April 2016
Five	Fix 270 mK touch & new ROX readout	250 μm array readout & optical tests	June 2016

Table 7.1: Cool downs of the flight cryostat with short descriptions of what was changed prior to the cool down and what was tested during the cool down

7.1 MLI Installation

Prior to the first cool down we had to install the MLI on each section of the cryostat as it was delivered to us as bare aluminum. The Stefan-Boltzmann law dictates that the power radiated from a blackbody is a function of temperature to the fourth power which means that MLI is especially important between the higher temperature stages. Significant research has been done to determine the optimal methods of MLI installation as it has been used extensively in cryogenic and spacecraft applications for many years (Shu et al., 1986; Jacob et al., 1992a,b; Bapat et al., 1990a,b; Shu, 1987; Shu et al., 1987, 1988; Stimpson and Jaworski, 1972). It was found that the attenuation in loading from more than approximately 30 layers of MLI was negligible. For this reason we placed the most MLI between 300 K and VCS2 with 25 layers and

reduced the amounts of MLI at cooler stages with 15 layers between VCS2 and VCS1 and 10 layers between VCS1 and the 4 K stage. At cooler stages the benefit of additional layers is much less pronounced which allowed us to reduce the amount of MLI and space the shields more closely while also reducing the complexity of the MLI installation. Details of the MLI installed in the BLAST-TNG cryostat can be seen in Table 7.2

There were a number of factors that went into designing the MLI blankets that cover the different parts of the cryostat. Any point where the MLI is compressed or folded leads to an increase in heat flow and a reduced effectiveness of the insulation. To decrease the chance of compressing the MLI the physical offset between cryostat thermal stages was designed to accommodate the ideal MLI spacing of around 20 layers/cm. For sections of the MLI blanket where two sections of blanket must overlap it is recommended that the overlap extend three or more inches. We aimed for a minimum overlap distance of five inches in all locations where it was necessary to do so. Parasitic loading from light leaks and unfinished edges of cut MLI is also a concern. Significant effort was made to cap and tape shut necessary cuts and holes around feed-throughs for cabling, plumbing, and motor shafts. We used 0.002 in thick silver metalized 3M #850 polyester tape for binding together the MLI blankets as it is highly reflective and has demonstrated excellent adhesion even after numerous thermal cycles.

7.2 Level Sensors

There are three level sensors installed inside the helium tank that measure the liquid helium level in the cryostat. During flight we only read out one of them periodically as their operation requires additional loading of the 4 K stage. The level sensors are incredibly difficult to replace so three are installed for redundancy over the

Section Name	Size (inches)	Number of Layers
He Tank Top	Diameter = 34	10
He Tank Cylinder	27 x 945	10
He Shell Cylinder	30 x 1070	10
He Shell Bottom	Diameter = 34	10
4K to VCS1 G10 - Inner	14 x 100	1
4K to VCS1 G10 - Outer	14 x 1510	15
4K to VCS1 G10 - Skirt	11 x 1650	15
VCS1 Lid	Diameter = 32	15
VCS1 Top Cylinder	20 x 1560	15
VCS1 Bottom Cylinder and		
VCS1 to VCS2 G10 - Outer	34 x 1610	15
VCS1 to VCS2 G10 - Inner	15 x 105	1
VCS1 - Skirt	11 x 1720	15
VCS1 Shell Cylinder	32 x 1700	15
VCS1 Shell Bottom	Diameter = 36	15
VCS2 Lid	Diameter = 35	25
VCS2 Cylinder	28 x 2830	25
VCS2 - Skirt	11 x 3050	25
VCS2 Shell Cylinder	34 x 2990	25
VCS2 Shell Bottom	Diameter = 38	25
VCS2 to 300K G10 - Inner	38 x 110	1
VCS2 to 300K G10 - Outer	38 x 2990	25

Table 7.2: List of MLI blanket sections and number of layers

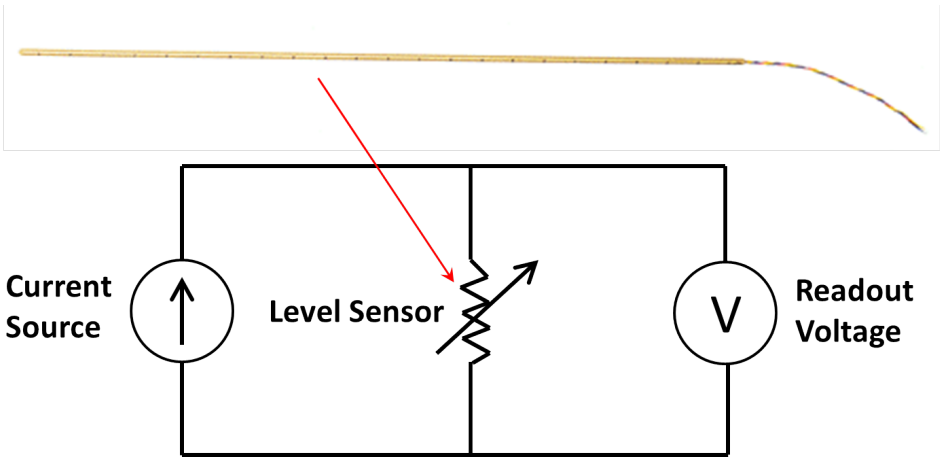

Figure 7.1: Top: An image of a level sensor prior to installation. The device is a strip resistor enclosed in a protective tubing with four lead wires, two to supply current and two to read out the voltage, as shown in the electronics diagram (bottom). The BLAST-TNG level sensors were chosen to have an active length of 26 in with a 27 in total length. The level sensors were purchased from American Magnetics with a specified supply current of 75 mA and a resistance of 11.6 Ω/in. at 20 K. They were mounted by Precision Cryogenics to the bottom of the helium tank. The wiring for the level sensors is fed out via Ceramaseal feedthroughs welded to a plate that attaches to the top of the helium tank with an indium seal. The wires are routed through one of the helium tank feedthrough tubes to the cold plate where they are connected to the CBOB.

lifetime of the cryostat. The level sensors consist of a super conducting strip which operates as a variable resistor. A 75 mA current is put through the sensor which causes the portion of the strip above the liquid helium to go normal with a known resistance per unit length of 11.6 Ω/in at 20 K. The portion below the liquid helium level remains superconducting and does not contribute to the resistance allowing for a four wire measurement to determine the amount of liquid in the tanks as shown in Figure 7.1.

7.3 Loading Calculations

To measure the power dissipated on the cold plate we make observations of the flow rate of exhaust gas coming out of the cryostat. The flow rate is monitored with a floating ball Aalborg flow meter which has the advantage of having a wide measurement range that is not dependent on the gas type. However, for each gas a separate calibration is needed to convert the measured float height of the ball, in mm, to a gas flow rate. Additionally, since it is an analog sensor, data must be recorded by hand which has lead to sparse data points. We use a polynomial fit to calibrated data from Aalborg to convert from ball height to nitrogen and helium gas flow rates as shown in the following equations.

$$F_{N_2}[L/min] = \left(n_0 + n_1 F(mm) + n_2 F(mm)^2 + n_3 F(mm)^3 + n_4 F(mm)^4\right)/1000$$

$$n_0 = -231.5$$

$$n_1 = 38.37$$

$$n_2 = -1.389 * 10^{-2}$$

$$n_3 = -7.79 * 10^{-5}$$

$$n_4 = 1.077 * 10^{-7}$$

$$F_{He}[L/min] = \left(n_0 + n_1 F(mm) + n_2 F(mm)^2 + n_3 F(mm)^3 + n_4 F(mm)^4 + n_5 F(mm)^5 + n_6 F(mm)^6\right)/1000$$

$$n_0 = -23.46$$

$$n_1 = -11.11$$

$$n_2 = 3.232$$

$$n_3 = -0.08183$$

$$n_4 = 4.183 * 10{-}4$$

$$n_5 = -1.69 * 10^{-6}$$

$$n_6 = 2.702 * 10^{-9}$$

Once the gas flow rate is known we can convert to a power on the cold stage:

$$P[mW] = F[L/min] \times \rho_{gas}[g/cm^3] \times L_H[J/g] \times 1000 \times 1000/60 \tag{7.1}$$

From which we can calculate the length of the hold time:

$$t[days] = 250\,[L] \times L_H \times \rho_{liquid}/P \tag{7.2}$$

Where the nitrogen parameters are $\rho_{gas} = 1.143{*}10^{-3}\,g/cm^3$, $\rho_{liquid} = 0.807\,g/cm^3$, and $L_H = 200\,J/g$ and the helium parameters are $\rho_{gas} = 1.633 * 10^{-4}\,g/cm^3$, $\rho_{liquid} = 0.125\,g/cm^3$, and $L_H = 21\,J/g$. From the equations above we can predict how long the cryostat hold time will be for a measured helium boil off rate as shown in Table 7.3.

During testing, VCS1 and VCS2 were observed to reach a temperature of $\sim$65 K and $\sim$165 K, respectively. The steady state load on the 4 K cold plate was measured

He Gas Flow [mm]	He Gas Flow [L/min]	Power at 4 K [mW]	Hold Time [Days]
40	2.30	131	58
50	3.15	180	42
60	3.98	228	33
70	4.78	273	28
80	5.54	317	24
90	6.27	359	21
100	6.99	399	19

Table 7.3: Table of 4 K loading values and resultant predicted hold times

to be 340 mW, as determined by the measured helium boil-off rate of the cryostat. The loading corresponds to a 22.5 day hold time for the 250 liter tank with an approximate boil-off rate of 11 liters of liquid helium per day. The observed loading is approximately 40% larger than the predicted loading of 240 mW from the thermal model used in the design of the cryostat. We believe our excess loading is due in part to un-modeled light leaks in the MLI blanket around fixtures and feedthroughs, as suggested by SPIDER (Gudmundsson et al., 2015), but also due to unexpected complexities in the thermal behavior of G10 material, which provides the mechanical support in the BLAST-TNG cryostat.

By adjusting the conductive model of the G10 we can account for most of the additional loading observed. This observation has prompted us to replace the G10 sections between VCS1 and VCS2 stages and between the VCS1 and 4 K stages with thinner walled material. The change will decrease the effective loading on the 4 K stage to bring the performance in line with our target 28 day hold time. It should also be noted from Gudmundsson et al. (2015) that the thermal loading at balloon

flight altitudes is observed to be less due to the cooler temperature of the cryogenic vessel and the reduced optical loading through the window which can increase the hold times of cryostats during flight.

As a baseline for comparing cryostat performance a figure of merit was developed in Holmes et al. (2001) that divides the radiative loading, H, by the cryogen depletion rate, R. For the SPIDER cryostat along with many satellite cryostats, $H/R \approx 60\,\mathrm{W\,Days/L}$ whereas the BLAST-TNG cryostat ranks slightly higher with $H/R \approx 230\,\mathrm{W\,Days/L}$ using the 250 L cryogenic volume, a hold time of 22.5 days, and the approximately $6\,\mathrm{m}^2$ surface area of the 4 K shield.

7.4 Leak Checking

In our first cool down test we were primarily concerned about leaks into the vacuum chamber as increases in the internal pressure will create a thermal short between cryogenic layers which can drastically affect cryogenic hold times. Leaks from the helium tank and its various cryogenic seals were the biggest concern as any leak in the tank detected with helium gas would be a factor of 1000 worse with liquid helium. However, we do expect a steady background leak level in the cryostat from the various gaskets. The steady state leak rate can be estimated from the largest contributor, the rubber O-rings used to seal all non-cryogenic interfaces. Equation 7.3 is taken from Parker Hannifin Corporation (2007) which calculates the constant leak rate through O-rings.

$$L = 0.7 \times F \times D \times P \times Q \times (1 - S)^2 = 6 \times 10^{-8}\, mbar\, L/s \tag{7.3}$$

F describes the permeability rate of the gas through the O-Rings with $F = 0.2 * 10^{-8} \frac{std.\,cc\,cm}{cm^2\,s\,bar}$, D is the inner diameter of the O-ring which for the largest seal on the cryostat is $D \sim 100\,\mathrm{cm}$, P is the pressure differential of $P = 1\,\mathrm{bar}$, Q and S

parametrize the squeeze of the O-Ring with values of approximately 0.7 and 0.2, respectively. The leak rate from this calculation is on the same order to the background level observed when leak checking the cryostat at LN2 temperatures. It should be noted the permeability rate for air is used for F while the leak checker measures the helium leak rate which makes a direct comparison difficult.

While pre-cooling with LN2 during the first cool down of the cryostat, we found a higher background leak rate and a higher loading than predicted which was indicative of a leak. We were unable to locate the leak on the exterior seals of the cryostat which implied the leak was in the helium tank. Our suspicions were ultimately confirmed by pressurizing the tank with helium gas while it was cooled to $\sim 80\,\mathrm{K}$ which caused a spike in the leak rate. The cryostat was mostly dis-assembled to locate the source of the leak, found in the weld joint of the HWPR motor axle feedthrough tube on the cold plate side of the helium tank. The tank was removed from the assembly and shipped back to Precision Cryogenics for repair.

7.4.1 Cool Down 1

Once the weld was fixed along with a bad indium seal that was discovered in a similar manner, we proceeded with our first liquid helium cool down. We measured boil off flow rates to determine the steady state load of the 4 K stage prior to adding most of the feedthrough components. For the first test we only had the housekeeping cables fed through to the cold plate which eliminated many potential sources of loading. At this stage we were still developing our measurement technique which meant we did not recognize the excessive loading on the 4 K at this stage. We did, however, gain a lot of insight into the behavior of the cryostat including the relatively long time scales on which it took the heat exchanger and VCS systems to stabilize, often on the order of 12 hours. During the cool down we adjusted the loading on

the 4 K stage and VCSs with heater elements to gather several data points of loading versus temperature to help assess the performance of the system,. However, the long time scales needed to reach equilibrium limited the amount of tests we could perform before running out of liquid helium.

The cool down also gave us a first look at the effectiveness of the heat exchangers and the plug system. The plug rod for the heat exchangers was inserted to confirm the design performed as expected. We observed a spike in temperature on both heat exchanger thermometers at nearly the same time which was evidence that the spacing between the two plugs was correct. This is an important consideration as we want both plugs to have a similar amount of compression force applied to ensure a good seal on both surfaces. After the plug was inserted we were able to make a measurement of the pressure build up in the helium tank from the impedance of the heat exchangers. The back pressure increases the boil off temperature of the helium which was confirmed to be a small effect. There are two ways we can measure the pressure in the tank, the first is by measuring the pressure at the top of the plug assembly through the pressure relief tube. However, we often lacked a pressure gauge that was sensitive to the small changes in which case a better measure of the pressure in the tank can be made by observing the temperature increase of the liquid helium bath. During this cool down we had difficulty calculating the change in pressure as the diode thermometers had not been fully calibrated but in future cool downs it could be a useful measurement to make.

7.5 Refrigerator System Installation

To install the 1 K and 270 mK refrigerator assemblies we had to dis-assemble both the top and bottom of the cryostat. The 270 mK refrigerator was easy to install as we are using the same one used in BLASTPol. The 270 mK refrigerator is a closed cycle

fridge which merely needed the cables for the charcoal heater, the diode thermometer on the charcoal, and the heat switch to be plugged in. The active heat switch is turned on to thermally link the charcoal and the cold plate to provide rapid cooling at the end of the fridge cycle. We also mounted a mock FPA to the cold plate to allow us to test the performance of the refrigerators in cooling an array as well as to check the performance of the heat straps used to connect the arrays to the fridges. Additionally, this marked the first cryogenic test of the carbon fiber support structure used to isolate the FPA 1 K and 270 mK stages from the 4 K stage.

The 1 K system was significantly more complex than the 270 mK system to install, especially with the implementation of modifications on the BLASTPol system. The BLASTPol 1 K pump pot was filled by a capillary with a tuned diameter to provide slightly more liquid helium than was being boiled off so the pot would gradually fill. The volume of the pot was designed to ensure that during the high load period of the fridge cycle, a full pot would not be entirely boiled off by the cycle ensuring it stayed at its base temperature of ~ 1.2 K. However, in this design the pot would completely fill between cycles resulting in a sudden decrease in the available surface area on which we were pulling vacuum. The change in pumping area would cause a rise of the pot temperature by a few tenths of a kelvin. For BLASTPol this was not a problem as the bolometers behaved linearly over a significant temperature range. However, MKIDs are tuned with a quality factor, Q, to a very specific temperature range in which they perform optimally, which requires a stable system. Additionally, they exhibit better performance at colder temperatures. These two factors pushed us to improve the 1 K cooling system which was done by placing a valve between the pumped pot and the main helium tank while simultaneously increasing the capillary size to allow the pot to be filled in less than an hour. Once the pot is full the valve is closed ensuring the surface area being pumped on does not change drastically which is both more stable and at a consistently lower temperature. A schematic of the system

can be seen in Figure 7.2.

During cool downs we need to ensure that the pump pot system does not get clogged by impurities in the system. As a precaution, we flow helium gas through the system while we pump down prior to adding cryogens. As we cool with LN2 and liquid helium it is especially important that helium gas is continuously flowing through the system as any impurities including nitrogen and oxygen can precipitate out and potentially clog the system. In order to monitor the flow we made a special regulator setup that incorporates a precision Aalborg digital helium flow meter that we continuously monitor as we cool. The same flow meter can then be attached to the exhaust port of the pump that pulls vacuum on the pump pot when we are cooling the 1K stage and in this way we can monitor the flow rate from the pump pot boil off which gives us an idea of the thermal load on the 1 K stage. To facilitate the pump pot cool down procedures we use a manifold with four valves on it that allow us to seamlessly switch between helium flow and vacuum pumping on multiple ports. Further details of the manifold methodology can be seen in Figure 7.3.

7.5.1 Cool Down Two

We developed a pre-cooling procedure for the second cool down that has become the standard method of cooling the cryostat. We partially fill the tank with LN2 and then rotate the entire cryostat by 180 degrees to allow LN2 to flow down the fill tube and come in direct contact with the heat exchanger surfaces, providing rapid cooling of the VCSs. To stop LN2 from flowing out of the cryostat, we place a cap on the vent line that feeds a 1/4 inch rod through an ultra-torr to KF fitting that reaches the bottom of the tank allowing the boil off exhaust to exit the tank. This process brings VCS1 down to 77 K, slightly above the operational temperature of 50-60 K, and VCS2 down to its operational temperature of $\sim$ 160 K within two days. The

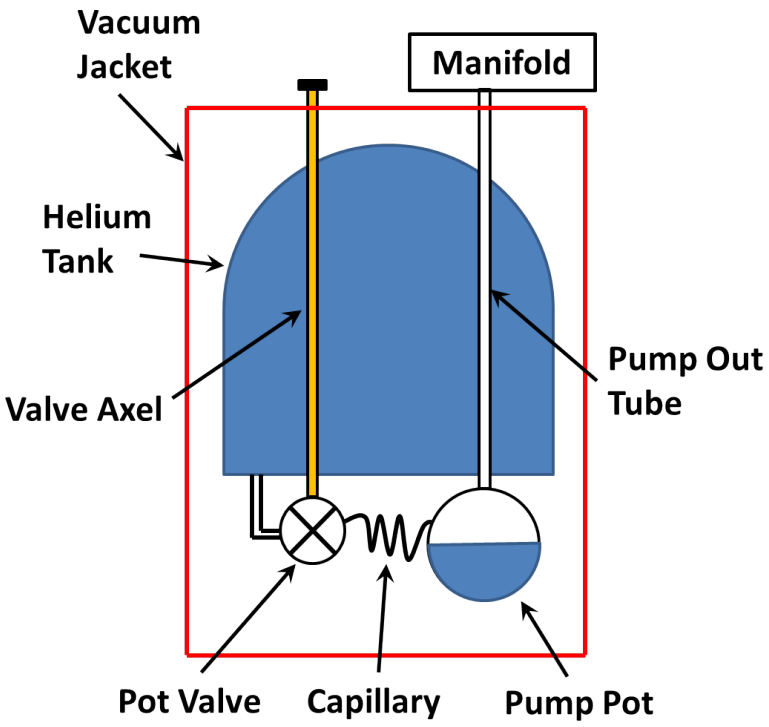

Figure 7.2: A simplified view of all components of the pump pot 1 K system starting at the helium tank and working its way out to the manifold outside the cryostat. Liquid helium is pulled into the pot from the main helium tank reservoir from a pipe with a 10 μm filter on it. The pipe leads to a valve that is controlled by a stepper motor mounted to the lid of the cryostat and is opened to fill the pump pot through a capillary that controls the flow rate. The pot is then pumped on through an exhaust pipe that leads out the top of the cryostat. During ground tests the pipe leads to the manifold and a vacuum is pulled on it to reduce the vapor pressure to create the 1 K stage. During flight a motorized valve opens the exhaust valve to the near vacuum of the stratosphere which performs the same function as the pump.

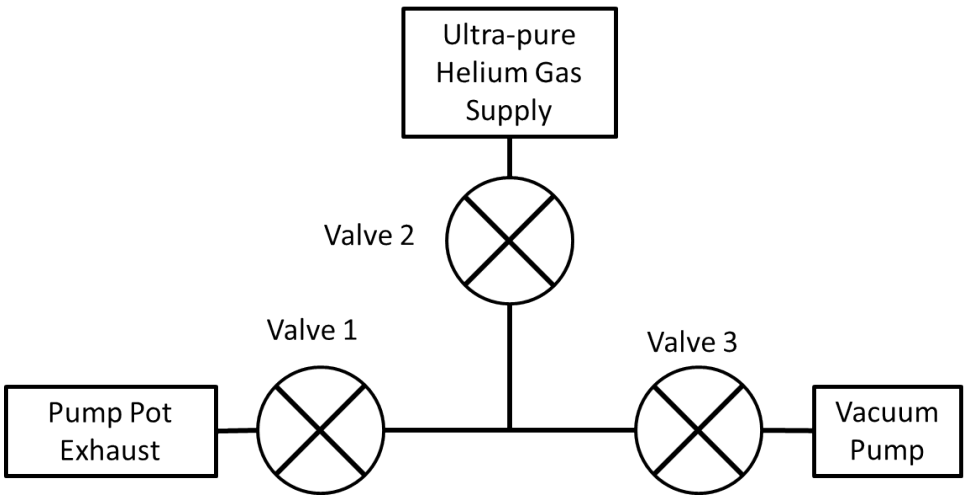

Figure 7.3: To ensure there are no blockages in the 1K pumped pot system we have a valve manifold setup to ensure that only ultra-pure helium is present in the system during the cool down. Initially Valve 1 and 2 are closed and Valve 3 is opened to evacuate the manifold. We perform 3 or 4 purges of the manifold by closing 2 then opening 3 and repeating. Once we are sure the manifold is filled with helium we close 3 and open 2 to provide positive pressure before opening 1 to force pure helium through the system. Once we are cold with liquid helium we close 2 and open 3 to pull liquid helium into the pump pot and lower the vapor pressure to bring the stage down to 1 K.

procedure speeds up the cool down process and significantly reduces the amount of liquid helium needed to cool the cryostat. Using this process to cool the cryostat requires at least 300 L of LN2. After pre-cooling, the initial liquid helium cool down requires at least 300 L to bring the cryostat to its equilibrium cold state with liquid in the tank for one to three days before additional helium is required.

During the second cool down the pump pot system became clogged as observed by a drop in exhaust gas flow and a temperature rise at the 1 K stage. The clog could temporarily be cleared by warming the cryostat above LN2 temperatures suggesting a contaminate gas in the pump pot system was freezing out at lower temperatures and causing the blockage. Thermal cycling of the cryostat was unable to clear the blockage and so the cool down was terminated. However, the cool down confirmed the cryostat and fridge systems were leak tight and the 270 mK fridge and 1 K pumped

pot systems worked with only minor modifications needed on the pump pot to ensure it would not become clogged again. We also found the loading on the 4 K was larger than predicted by the thermal model though we were not able to pinpoint the cause necessitating further investigation in subsequent cool downs.

7.5.2 1 K System Modifications

The pump pot system had worked well inside a small test dewar prior to installation within the flight cryostat. We closely examined what had changed when the system was transferred and came up with two possible explanations for the pump pot malfunction. Either trapped impurities such as oxygen or nitrogen had clogged the thin capillary tube that runs between the valve and the pumped pot reservoir or steps in the aperture size through which the liquid helium flows produced cavitation that reduced the flow rate.

To address both possible causes of blockage in the 1 K system we decided to change our filtering strategy. The filters are made from metal foam with calibrated gaps to prevent particulates from entering the system from the helium tank. Filters were placed both before and after the valve as well as at the entrance to the helium tank which we decided was overly aggressive and could be causing the issues. If a filter was too fine it could either be trapping the impurities that we want to drive out with the helium gas purge or creating the change in flow impedance that could cause cavitation. To address these concerns the filters before and after the valve were removed and the filter at the intake from the helium tank was increased in gap size from 10 to 15 μm.

Once the changes were made the cryostat was cooled down for the third time as shown in Figure 7.4. The 1 K system operated well during this cool down though we eventually had trouble again with the 1 K pot system plugging. However, during

Figure 7.4: An image of the cryostat during the third cooldown showing a liquid Helium transfer in progress as well as two vacuum pumps attached.

the cool down we were able to perform tests on the 270 mK fridge, pumped pot 1 K system, HWPR, and the 4 K loading levels.

The next set of alterations to the 1 K system attempted to eliminate the last few possible sources of clogging from the above mentioned sources. First, the 15 micron filter at the intake from the helium tank was replaced and offset from the bottom of the tank with a stainless steel pipe that placed the intake proud of the tank curvature. The standoff was added due to concern that contaminants were building up at the bottom of the tank. A second change that was made to the 1 K system was to replace the pipe that led from the Helium tank to the valve. In previous tests the pipe had been made of convoluted stainless steel tubing with a 1/4 inch inner diameter. We were concerned that contaminant gasses were being trapped in the convolutions and could have dislodged and blocked flow through the capillary. We replaced the

convoluted tubing with straight copper tubing that was designed so the liquid helium in the pipe would always be flowing down to eliminate potential traps in the system. During the next cool down the 1 K system performed well and did not clog suggesting these modifications were effective.

7.5.3 HWPR Thermal Testing

The HWPR was mounted to a test optics bench machined at UPenn and installed for our third cool down to allow us to test its thermal properties. We found that at certain rotation angles the HWPR was not in good thermal contact with the 4 K stage resulting in temperature rises above 5 K. The HWPR is cooled through the drive rod's contact with stainless steel ball bearings on two points along the axle. The axle is in contact with the HWPR through a worm gear which, if the worm gear is backed off slightly, does not make good thermal contact with the teeth around the HWPR rim. The only other contact points are three wheels set in a groove around the HWPR that support for the HWPR. The thermal contact from the wheels is minimal and does not change with rotation angle. After the cool down test, a spring loaded copper piece was installed between the optics bench and the HWPR axle to provide better thermal contact. Temperature drifts of the HWPR and HWP are a concern as they will cause a shift in the background loading of the detectors. The drifts from the HWP will be removed in post-processing of the TOD but it is desirable to minimize the signal from this systematic.

7.6 Cold Optics and Detector Array Installation

The primary goal of cool down four was to test the 250 μm detector array in the flight cryostat for the first time. In order to install the array, many components needed to be added and configured within the cryostat. Chief among these was the

cold optics assembly which was delivered by ASU at the beginning of March 2016. The optics were mounted to the cold plate without incidence along with the backing portion of the magnetic shielding. A flat polished aluminum mirror was also mounted at the location of the 250 μm dichroic filter surface as the dichroic filters had not been delivered. The mirror blank was offset from the dichroic mount surface by three 0.375 in precision aluminum blocks to ensure the surface was at approximately the same location as the dichroic surface to ensure the incoming beams were correctly focused on the array.

We require a FPA alignment procedure as the FPA structure was not included in metrology tests done on the cold optics prior to delivery. With BLASTPol a laser beam was projected from the cold optics window through the re-imaging mirrors and back again after being reflected by a flat mirror mounted in front of the feedhorns. The FPA could then be aligned correctly with the optics by adjusting its pointing until the reflected beam overlapped with the output beam at the window. We attempted to repeat this procedure with BLAST-TNG by having ASU hand polish the center of M3 and M5 to reflect the incident laser beam in addition to having them manufacture an M4 specifically for alignment tests with no central hole in the mirror. Unfortunately, even with polishing, the mirror surfaces did not have an optical quality finish resulting in diffraction effects that significantly broadened the laser beam and made the test intractable.

Creating far field beam maps with the cold optics can serve as an alternate method to check the alignment of the FPA. The beam map shows an image of the Lyot stop with the Gaussian response from the feedhorns projected on the annular shape Lyot stop. The FPA is aligned correctly if the projected Gaussian peak is centered on the image of the Lyot stop in the beam map, as was observed by BLASTPol in Figure 3.14. A symmetric beam map would confirm that the detectors are well aligned and are looking at the center of the Lyot stop. A non symmetric image would point to

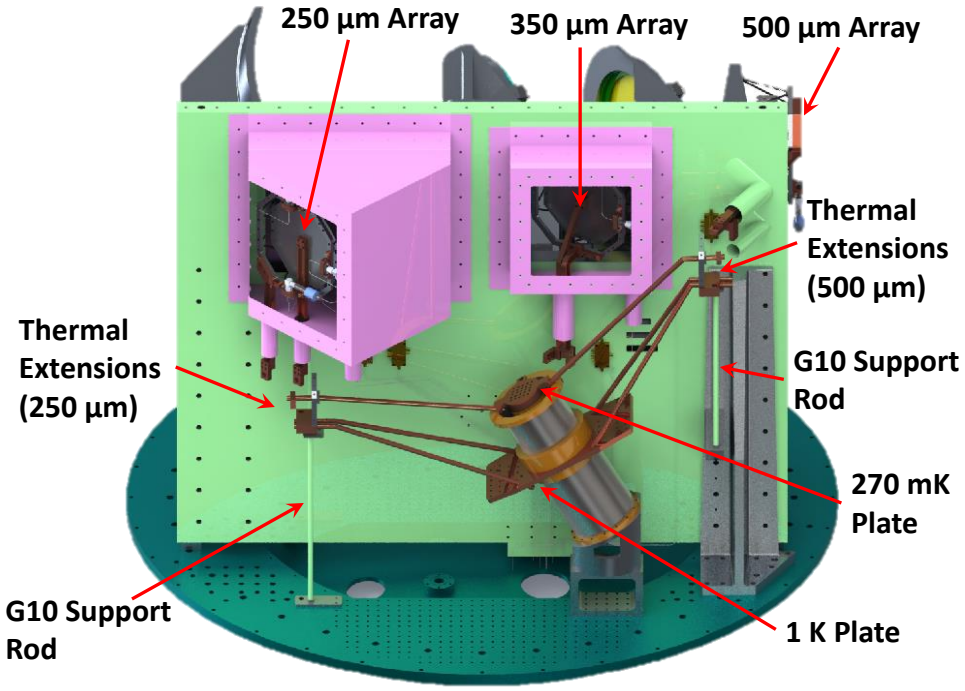

Figure 7.5: Schematic of the back side of the optics box illustrating the parts of the refrigerator and thermal distribution system. Each array has rigid copper rods extending from the back of the FPA and the 1 K ring through the magnetic shielding. These rods are then couple to the rigid distribution system from the refrigerators with copper braid sections to decouple the structures such that they are not over constrained. The copper rods extending from the 1 K plate are reinforced with G10 supports while the rods extending from the 270 mK system are supported by Kevlar trusses.

the detector plane not being perpendicular to the beam axis which would require adjusting the FPA alignment by an amount determined by the offset of the Gaussian response from the Lyot stop image. Repeatedly adjusting the alignment with this method is prohibitive as it requires cool down cycles of the cryostat between each adjustment prompting us to design a simpler alignment procedure to make future array installations easier.

7.6.1 Thermal Distribution System

A system of heat straps connect the 1 K and 270 mK refrigerators to the 1 K and 270 mK FPA stages as shown in 7.5. The distribution structure provides a stable attachment point for sections of copper braid that couple the structure to copper rods extending from each of the FPAs through the magnetic shielding. We used 0.275 inch diameter Oxygen Free High Conductivity (OFHC) copper braid that was welded to the support section and bolted to the FPA stage extensions. The copper braids were included for two reasons, to ensure the system is not over-constrained and to isolate and dampen any vibrations from the rigid distribution structure. Initially, only the section extending to the 250 μm array was constructed to test the design and manufacturing process. The installation required some adjustment to make all the parts connect easily but was effective overall.

7.6.2 Array Mounting

Installation of an array requires the thermometry for the array to be attached, the thermal system to be bolted on, the magnetic shielding around the array to be mounted, and the coaxial cables for the array readout to be put in place. The coaxial cables carrying the input frequency comb route from a feedthrough on the cold plate to the 1 K FPA intercept ring where the cables are heat sunk before routing to the array. The coaxial cables leaving the arrays that carry the detector signals are made from super-conducting cables to reduce signal attenuation. The superconducting cables go from the arrays to low noise Silicon Germanium LNA are manufactured at ASU. From the LNA the signal is fed back out of the cryostat to the readout electronics. The installed 250 μm array is shown in Figure 7.6.

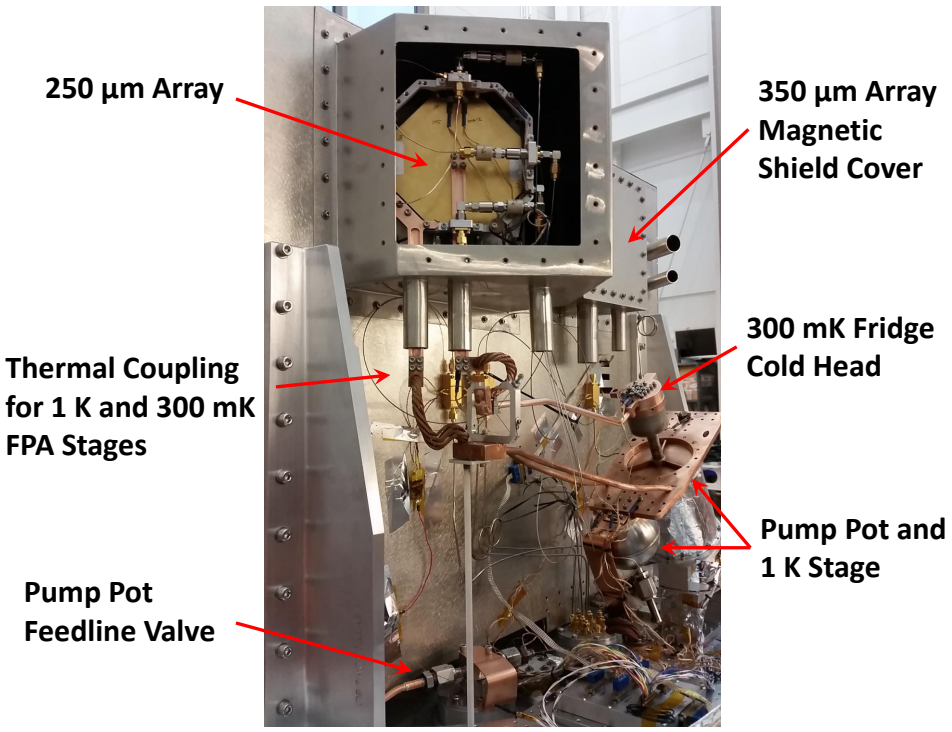

Figure 7.6: An image of the back of the optics box with the first installation of the 250 μmarray. It can be viewed through its access hatch in the magnetic shielding. One can also see the 1 K pumped pot and valve along with the 270 mK refrigerator and how they connect to the array via the thermal distribution system.

7.7 Cold Optics Axis Alignment Procedure

In order for the cold optics to be aligned correctly with the primary and secondary mirror a procedure is performed which translates the cold optics axis to the window of the cryostat. The procedure is necessary as the cryostat window is opaque making alignment unfeasible during normal operations. For the test a clear 0.25 in impact resistant polycarbonate window was installed and all filter rings were unpopulated to create a clear line of sight to the optics bench. A targeted reflector mirror was mounted to the optics box window fixture. The reflector mount ensured the mirror was centered on the optical axis and on a plane perpendicular to the optical axis. It was necessary to cool the cold plate and optics to LN2 temperatures to allow for the majority of the thermal contraction to take place. We did not cool to liquid helium

temperatures due to the additional costs and complications of doing so for an effect that would be smaller than uncertainties from the setup of the rest of the procedure.

Once the cryostat had thermally stabilized with LN2 in the helium tank an alignment telescope was positioned 79.25 in ($\sim$ 2 m) from the cryostat window to place it at a distance similar to that of the secondary mirror. Performing the procedure at this distance allows us to accurately predict the location of the beam in relation to the cryostat, inner frame, and M2. For additional stability the cryostat was taken out of its stand and placed on a stack of foam and boards placed directly on the floor to prevent it from shifting while also putting at the same height as the telescope tripod. The telescope was strapped to a translation and rotation stage that was itself mounted to the top of a high stability tripod, typically used for FARO measurements. The alignment telescope has a crosshair in the eyepiece as well as crosshair on the output lens of the telescope. It also has three adjustment nobs, two allow the telescope axis to be finely adjusted in X and Y directions perpendicular to the optical axis Z, and one to change the focus.

In the first part of the procedure the telescope axis was aligned with the optical axis of the cold optics. To align in X and Y, the telescope position was adjusted while focused on the reflector at the cold optics until the eyepiece cross hair overlayed the cold optics reflector crosshair. To align the telescope axis to be parallel with the optical axis, the telescope focus was adjusted to twice the distance to the cryostat such that the image in focus was the reflection of the etched telescope lens crosshair off of the reflector mounted in the optics window. Aligning this image with the eyepiece crosshair ensured the telescope axis was parallel to the optical axis of the cold optics.

The next step in the procedure was to transfer the cold optics axis to the outside of the cryostat window so all future alignment could be done by mounting the alignment fixture in front of the cryostat window. The fixture was bolted to the window block which has three set pins to ensure the fixture is mounted in the same position every

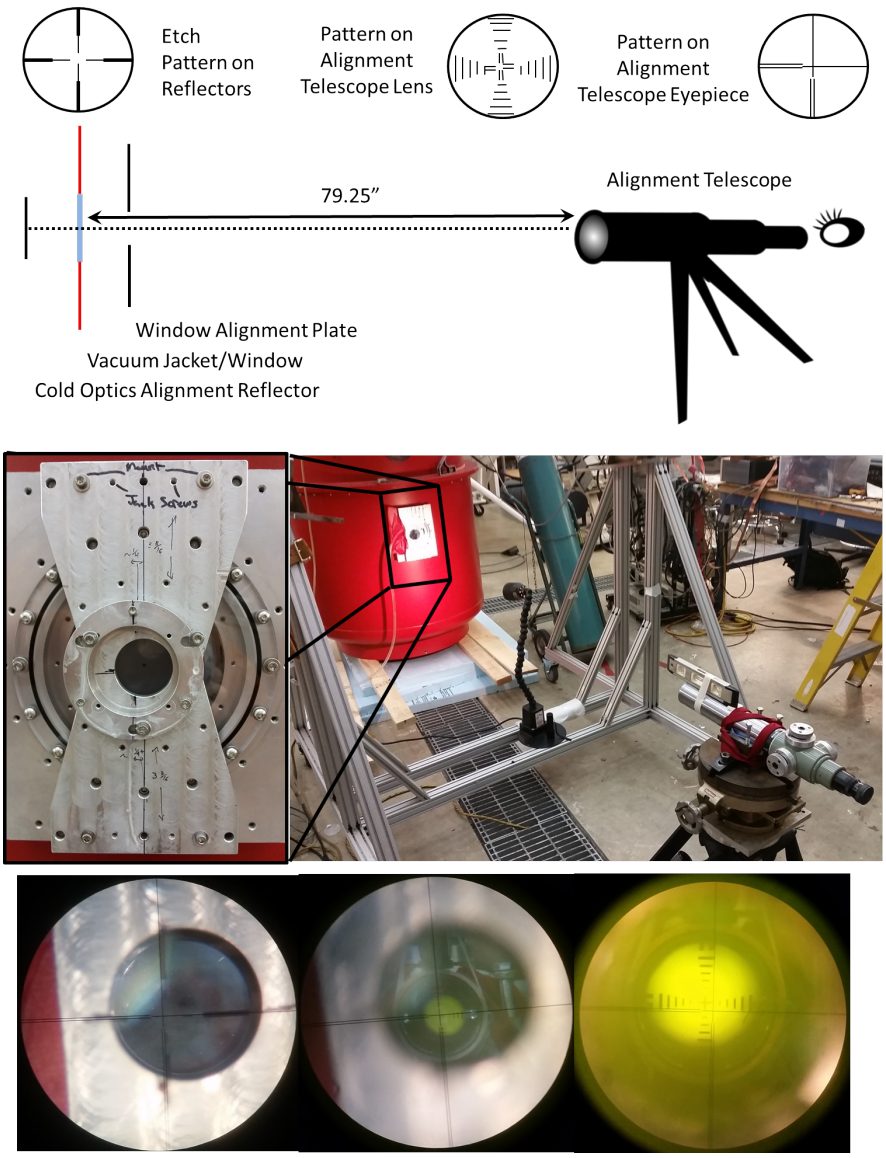

Figure 7.7: The top schematic shows the configuration of the alignment test. There were three target types and locations as shown. The targets that were placed in the cold optics window and in the alignment fixture mount were identical. The middle image shows the setup in the lab as well as a zoomed in picture of the alignment fixture plate with the adjustable alignment mount attached at its final location. The bottom images show three of the alignment configurations. Left: the eyepiece crosshair aligned with the optics box reflector crosshair. Middle: the eyepiece crosshair aligned with the telescope lens crosshair reflected from the cold optics. Right: the eyepiece crosshair with the best alignment achieved with the telescope lens crosshair reflected off the alignment fixture reflector. The different angles and coloration of the image are due to the difficulty of taking a picture through an eyepiece.

time. An alignment reflector identical to the one mounted to the cold optics is then bolted to the alignment fixture. The reflector can be moved in X and Y as well as in tip and tilt. The procedure is identical to the first part except the reflector's position is adjusted while the alignment telescope is fixed in place. The quality of the alignment was confirmed by removing the reflector in front of the window allowing to see the cold optics reflector to ensure the telescope was still aligned with the cold optics axis. The telescope would shift slightly in its mounting during the procedure which dominated the uncertainty of the measurement and limited us to an alignment along the axis of a few degrees. By examining the optics model in Zemax we determined that the error was small enough to not significantly change the illumination of the primary and secondary mirrors and was sufficient for our alignment purposes. After the reflector was correctly placed on the alignment fixture, it was glue in place to ensure the reflector location would not shift during subsequent dismounting and mounting of the alignment fixture between alignment tests. The setup is described in additional detail in Figure 7.7.

We also found that the cryostat window as well as the window apertures in each of the thermal shields were offset in X, the direction parallel to the floor, by a significant amount. The offset was as large as 0.25 in and was from the mounting holes in the cryostat shields not being aligned perfectly during manufacture. There was a concern that the beam of the telescope could clip one of the window edges as they were designed to give an approximately 1 cm clearance around the beam. As such, the clearance on one side of the optical beam was reduced to several millimeters. We decided modifications would only be necessary if we observed the apertures impinging on the beam during beam mapping procedures of the full arrays.

7.8 Heat Exchanger Simulation and Testing

The design of the heat exchangers used in BLAST-TNG, described in Section 6.3.4, was refined through numerous simulations and tests done in the months preceding their production. Additional tests were performed during cryostat cool downs after they were manufactured and incorporated in an effort to understand their performance in the cryostat. In this section I will describe in detail all tests and simulations that were performed to both inform our design of the heat exchangers and to asses their performance after we had built them.

7.8.1 Prototype Heat Exchanger Testing

Several simple tube heat exchangers were constructed from varying lengths and sizes of copper tubing. The test pieces were used to establish several basic methods of measuring the effectiveness of a heat exchanger design. The first test done was to measure the flow impedance, as characterized by the function of back pressure versus flow rate. The impedance is directly related to the number of gas to exchanger interactions that take place which we attempt to maximize in as compact a space as possible. However, the design should not build up too much back pressure, above a few psi, as doing so will increase the temperature of the helium bath. To address this requirement the design has a set impedance for which we attempt to maximize the surface area available for interactions. The desire for large total surface area is due to the thermal properties of copper, especially the heat flow rate through the material which while high, is not infinite. For example, a small aperture would quickly create the desired impedance and would force most gas particles to interact at the aperture but the cooling would be at a small point that would be limited in its ability to remove power by the material heat flow properties. The best design would instead build up the desired impedance over the longest possible length to create as many

gas to exchanger interactions as possible with an exchanger that is able to effectively conduct thermal power to the cooling source.

We also measured a heat exchanger efficiency parameter to determine the effectiveness of different designs. We developed two methods of calculating the efficiency of the heat exchangers. The first used the assumption that, if the exchanger were perfectly efficient, the gas to exchanger interactions would heat the gas to the temperature of the heat exchanger. The efficiency would then be function of the input gas temperature versus the output gas temperature compared to the temperature of the exchanger, labeled ϵ_T. ϵ_T was difficult to determine in practice as the output temperature of the gas was difficult to measure in our test setup and would be even more difficult to measure in the cryostat flight configuration. We calculated an alternative measure of efficiency by examining the amount of potential thermal power the gas could remove and comparing that to the amount of power that was actually removed, labeled ϵ_P. The difficulty of this measurement came from the necessary calculation of the amount of power going into and out of the heat exchanger using models of conductive and radiative heating and cooling that inherently have errors from the test setup. However, the major advantage to ϵ_P was our ability to make estimations for it in the flight cryostat setup by using the cryostat thermal model.

We created an experimental test bed in order to measure metrics of the heat exchangers performance. The impedance measurements could be done by simply attaching a flow meter to the output of the exchanger and a pressure gauge to the input. To make efficiency measurements we placed the heat exchanger in a vacuum to control the environment as much as possible and attached a heater to allow us to vary the thermal load on the exchanger. We modified an existing vacuum chamber with an adapter plate that had input and output ports for helium gas with pipe fittings inside the chamber that the test heat exchangers attached to. We also installed cabling for the resistive heating element that bolted to the exchangers as well as two AD590

thermometers to monitor the temperature of the exchangers. Additionally, a probe thermometer was pushed down the output port to measure the gas temperature as it exited the exchanger. For each exchanger ϵ_T and η_P were calculated using the following equations.

$$\epsilon_T = \frac{T_{out} - 300\,K}{T_{HX} - 300\,K} \tag{7.4}$$

$$P_{in} - P_{Static} = \frac{1}{1000}\left[F_{mass} \times c_p \times (T_{HX} - 300\,K) \times \epsilon_P\right] \tag{7.5}$$

Where $c_p = 5.19 kJ/kgK$ is the specific heat of helium and F_{mass} is the mass flow rate of the gas. P_{Static} is the amount of power required to keep the heat exchanger at T_{HX} with no gas flow and is considered to be the amount of power that escapes via radiative and conductive processes not associated with the gas flow. ϵ_P was solved for after measuring the amount of power from the heater, P_{in}, that was needed to maintain a steady T_{HX} at a given flow rate. Results from our heat exchanger tests are shown in Figure 7.8.

7.8.2 Prototype Spiral Heat Exchanger

The tests led us to the sandwiched spiral design as the optimal configuration given our space and performance requirements. The next design step was to determine the best dimensions for the rectangular channel cross section and the spiral spacing. We initially created a prototype design based on the performance of the test copper tubing heat exchangers. The prototype design targeted 18.7 Torr of back pressure at the nominal flow rate through the exchanger. The flow rate was determined by our boil off prediction as shown in Equation 7.6.

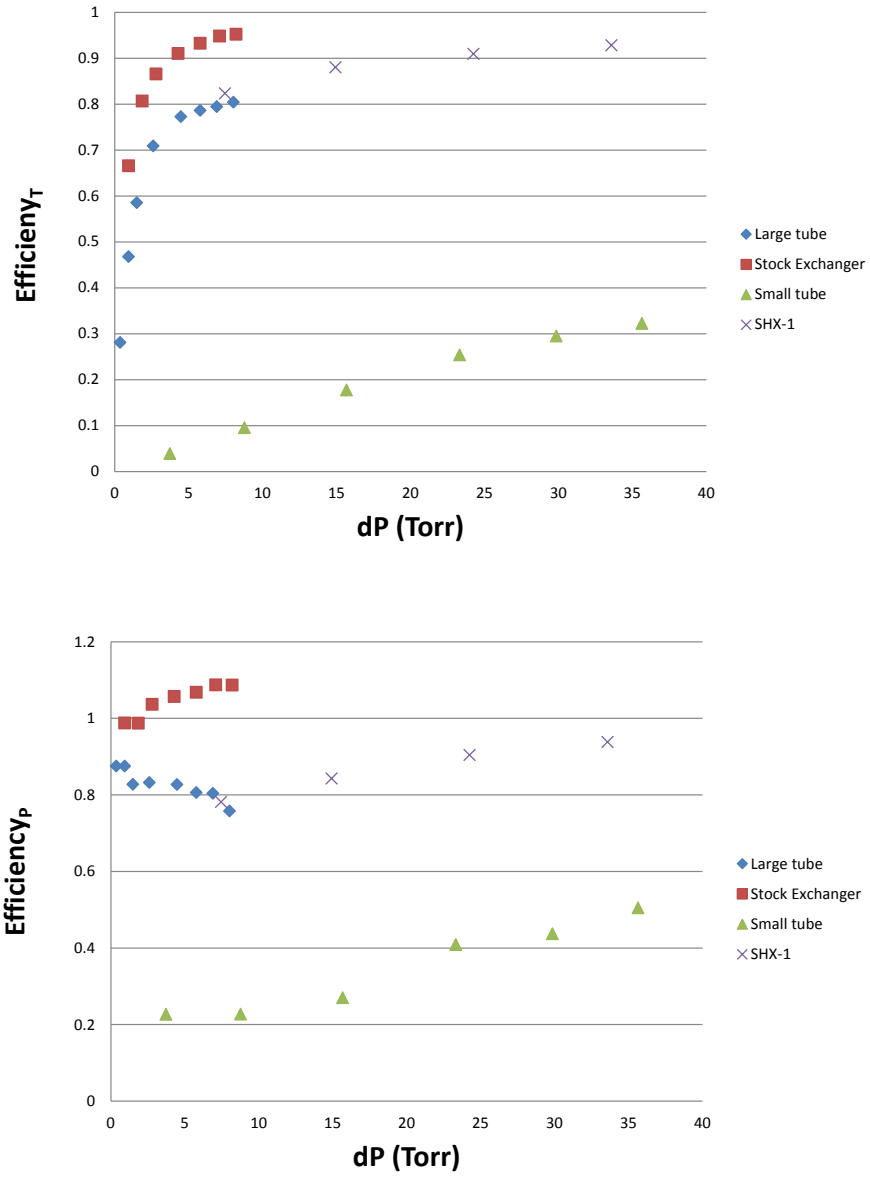

Figure 7.8: The top plot shows the first measure of efficiency using the temperature of the gas and teh temperature of the heat exchanger. The bottom plot shows the second measure of efficiency using calculations of the power on the exchanger combined with the power the gas was able to remove. The large tube and stock exchanger had larger apertures and as such were limited by the back pressure they could build resulting in their limited x-axis range. The general conclusion from the plots was that the efficiency asymptotes above 18 Torr prompting us to set that pressure as the goal to be above to ensure our heat exchangers operated in the higher efficiency regime.

$$F_M = \frac{250\,L}{28\,\text{days}} \times 125\,g/L = \frac{31.25\,kg}{28\,\text{days}} = 12.92\,mg/s \tag{7.6}$$

$$F_V(@STP) = \frac{12.92\,mg/s}{0.163\,kg/m^3} = 0.0793\,L/s$$

$$F_V(T = 40\,K) = 0.0106\,L/s \quad \rightarrow \quad F_M(T = 300\,K) = 1.73\,mg/s$$

$$F_V(T = 120\,K) = 0.0317\,L/s \quad \rightarrow \quad F_M(T = 300\,K) = 5.17\,mg/s$$

The mass flow rate of helium is calculated from the boil off rate of the cryostat. However, the volume of gas through each heat exchanger is dependent on the temperature of the gas at a given stage. A volumetric flow rate of gas is calculated for the predicted temperatures of VCS1 and VCS2 to determine the target flow rate for the 18.7 Torr of back pressure desired. The volumetric flow rate is then converted back to a mass flow rate at room temperature for easier use with the test setup. The calculations determined the primary design goal for the VCS1 heat exchanger to have 18.7 Torr of back pressure with 1.73 mg/s of flow and for the VCS2 heat exchanger to have a back pressure of 18.7 Torr with 5.17 mg/s of helium gas flow.

A test spiral heat exchanger, SHX-1, was manufactured with a design modeled to create the VCS2 heat exchanger performance. The center of SHX-1 was not machined out such that a plug was not required to perform the test. Additionally, the stainless steel caps on the top and bottom of the exchanger had 1/8 inch pipe thread holes to connect to the test apparatus. It was found that the back pressure at a given flow rate was noticeably lower than initially predicted which was most likely due to gas escaping over the tops of the channels as the top and bottom plates of the exchanger could bow out slightly under pressure. To test this presumption we repeated the flow test with the top and bottom of SHX-1 clamped together with four C-clamps which brought the performance in line with predictions. The results of the tests are

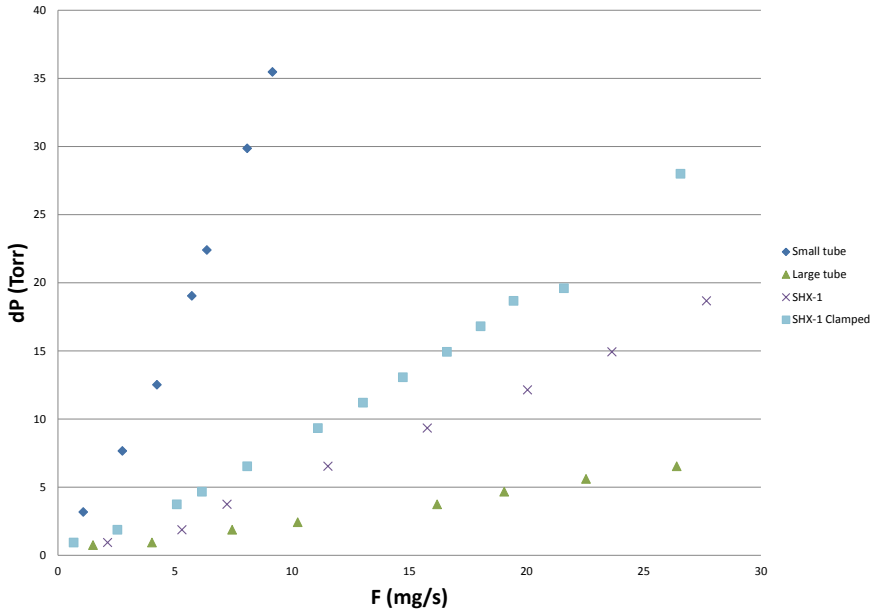

Figure 7.9: The results of the pressure versus flow test demonstrate two tube dimensions used along with the SHX-1 test heat exchanger that was designed to reach a target dP of 18 Torr for around 5 mg/s of flow. The design fell short partially due to leakage over the channel sections of the exchanger as is evidenced by the change in the curve by clamping it together. This effect was taken into account in later designs and simulations.

shown in Figure 7.9 with an image of the test exchangers used in Figure 7.10 with parameters defined in Table 7.4.

7.8.3 Flight Heat Exchanger Design and Testing

The flow and back pressure of the heat exchanger designs were determined from simulated in Solidworks. The design of SHX-1 was adjusted until the simulations of the SHX-1 model agreed with test results. The primary parameter changed in the model was the gap between the cap plates and the top of the spiral block. Doing so effectively recreated the observed bowing of the cap plates and was found to be closest with a 0.004 inch gap. Designs with the gap incorporated were then generated for

Exchanger Name	Cross Section	Length	A/L
Short tube	ID = 0.0625 in	50 cm	3.96e-6 m
Long Tube	ID = 0.1875	100 cm	1.78e-5 m
Stock Exchanger	0.43 in x 0.53 in	25 cm	5.88e-4 m
SHX-1	0.1 in x 0.125 in	280 cm	2.89e-6 m
VCS2 HX	0.1 in x 0.09 in	378 cm	1.53e-6 m
VCS2 HX	0.08 in x 0.07 in	470 cm	7.69e-7 m

Table 7.4: List of heat exchangers that were produced and tested. A parameter Area/Length (A/L) was used as an estimator of the impedance. The long and short tubes were made from standard copper tubing, the stock exchanger was a water block heat exchanger we purchased, and SHX-1 was the prototype spiral heat exchanger we made.

the VCS1 and VCS2 heat exchangers which were modeled to have the desired back pressure for their given flow rate. Results from the simulations are shown in Figure 7.11. The exchangers were initially manufactured with the material for the central hole intact and with pipe thread in the steel caps to allow us to test them to confirm their performance was in line with expectations. After the exchangers were tested the centers of the exchangers were re-machined to create the plug seat and central hole along with modifications to the steel caps to allow the exchangers to be welded to the rest of the fill tube assembly.

Attempts at measuring the efficiency of the exchangers was done in the same lab setup but there was some difficulty in measuring efficiencies at the low volumetric flow rate of VCS1 heat exchanger as well as some uncertainty in the efficiency values due to the difficulty in constraining all the variables in the lab setup. None the less, the tests suggested the efficiencies obtainable with the constructed exchanger would meet our minimum requirement of 80% efficiency which was used in the thermal models

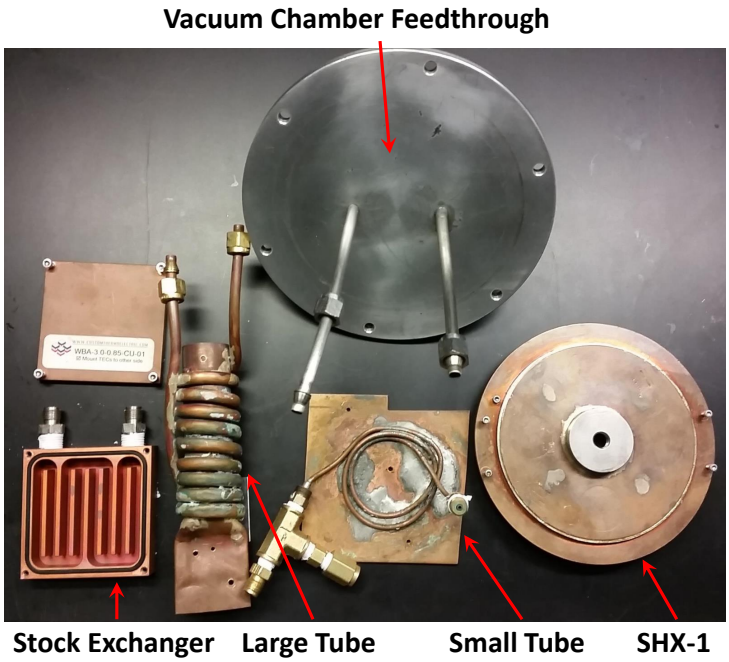

Figure 7.10: The top shows the feedthrough plate used on the test vacuum chamber with the input and exhaust tubes for both pressure and flow readings as well as efficiency tests. The bottom row shows the stock heat exchanger purchased from Custom Thermoelectric and the large tube, small tube, and SHX-1 heat exchangers that were made at UPenn.

that guided our design. Results of the tests are shown in Figure 7.12.

7.8.4 Cryogenic Heat Exchanger Testing

Efforts have been made to measure the performance of the heat exchangers after their installation into the cryostat and in the subsequent cool downs. Their respective efficiencies can be solved for in the thermal model once known values from a cool down are measured. We input the temperature the heat exchangers reach as measured by a diode thermometer bolted to the exchanger rim, as well as the measured flow rate of helium boil off gas coming out of the cryostat. The first and second cool downs did not produce accurate data as we were still familiarizing ourselves with the setup and had some issues with the thermometry. The third cool down was done specifically to

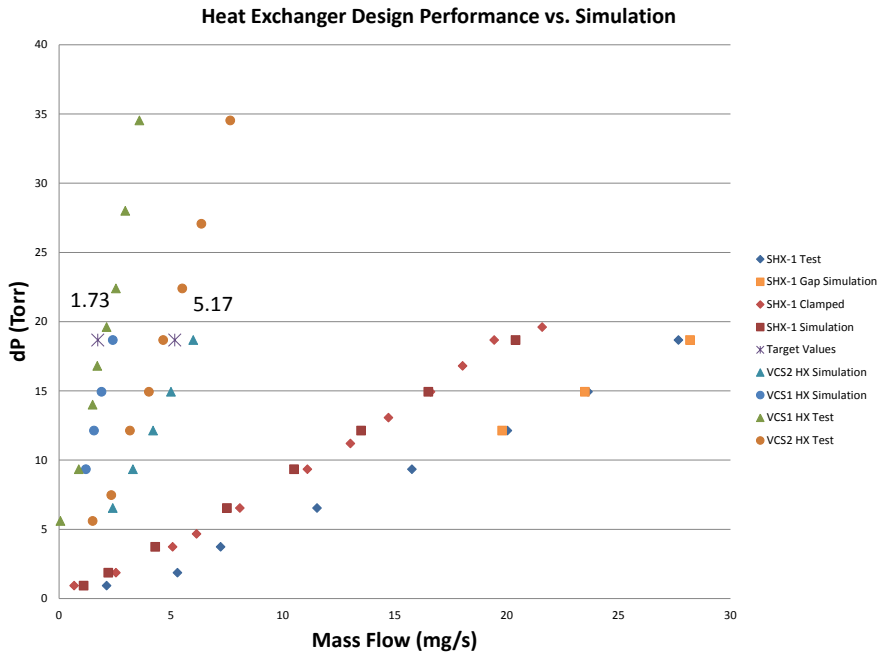

Figure 7.11: Solidworks simulations were used to match the data from SHX-1 data and then to generate designs for the VCS heat exchangers that meet the desired parameters. Shown are the data for SHX-1 which when clamped, agrees witht he simulated design with not gap between the top and bottom plates. A gap of 0.004 inches matches the unclamped SHX-1 data. The gap was then used in the design and simulation of the VCS1 and VCS2 heat exchangers which were then tested from which we can see the simulations agree fairly well with the observed performance and the flow at 18 Torr pressure differential is near the desired values of 1.73 and 5.17 mg/s for the VCS1 and VCS2 exchangers, respectively.

test the performance of the pump pot system which involved rapid changes in the test setup and the loading on the cold plate making it difficult for the system to reach an equilibrium state conducive to proper measurements. Our best data for determining heat exchanger performance comes from the fourth cool down.

The temperature and flow rate data from the fourth cool down led to solutions with low heat exchanger efficiencies closer to 60%. However, it was also found that the boil off rate of helium was higher than expected from thermal model predictions given the temperatures of the VCSs. The discrepancy between the measured and predicted boil off rate suggested there was a significant unknown load on the cold

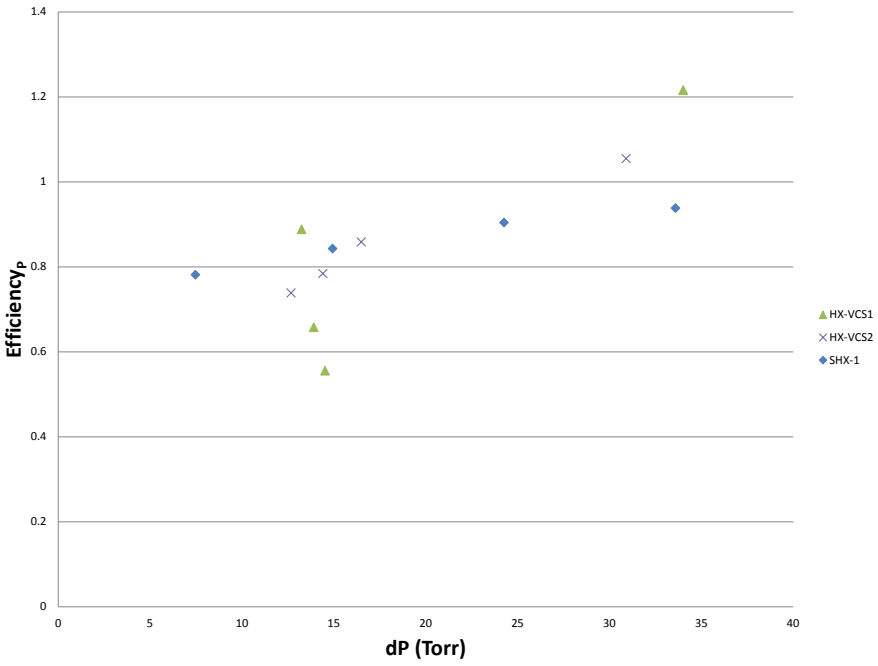

Figure 7.12: The efficiences of the two VCS heat exchangers were measured in our warm test setup in an attempt to confirm their performance. The efficiency at the back pressure of 18 Torr appears to be above 80% for both HSX-1 and the VCS2 heat exchanger, however, the data is inconsistent for the VCS1 heat exchanger. Additionally, both VCS heat exchangers have measured efficiencies greater than 1 whihc points to either some error in the test setup, perhaps changing parasitic loads, or an issue in the calculation such as a potential error in the calculation of the flow rate which was quite high for the two abnormally high results.

plate that was up to 1/3 of the total loading. After considerable speculation it was decided that the excess load could come from an incomplete model of the conductive and radiative loading from the G10 cylinders in addition to minor light leaks in the MLI shielding.

The excess loading could also be present on the VCSs producing additional power not accounted for in the thermal model which would also need to be removed by the heat exchangers. If we assume there is a parasitic load on the VCSs there would consequently be a higher efficiency for the heat exchangers. This follows from the fact that we make a prediction for the amount of power on the shield layers in order

to calculate the efficiency.

7.8.5 Heat Exchanger Plug Testing

An alternate effect that could result in lower efficiencies for the heat exchangers would be the plug mechanism not creating a tight seal thereby allowing gas to leak by the plugs instead of going through the exchangers. In order to understand if this was a problem we used an endoscope to look at the plug seating surfaces from which we saw some scarring, either from the manufacture or subsequent use of the exchangers but we did not see anything large enough to be concerning.

A second test was performed to determine the tightness of the seals. We made two stainless steel tubes each of which had a teflon plug identical to either the VCS1 or VCS2 plugs glued to it. These test plugs were inserted one at a time into the fill tube. We then flowed helium gas through the center of the tube to pressurize the helium tank. By observing the pressure build up behind the plugs we could get an idea of their effectiveness. Both VCS plugs appeared to mate well with up 10 psi of pressure being built up. However, it was also observed that a better seal could be made by increasing the downward force on the plug. The maximum force from the spring loaded flight plug system is currently limited by the wall thickness of the central stainless steel tube as too much downward pressure can bend the tube. A second flight plug system with a thicker wall diameter could be made to potentially improve the quality of the seal.

7.8.6 Cryostat Modifications

The cryostat performance from initial testing predicted a cryostat hold time of approximately 25 days which is shorter than our projected hold time of 28 days. The parasitic load could be reduced through several methods. The most direct method

was determined to be replacing the G10 supports between VCS1 and the cold plate and VCS2 and VCS1 with thinner G10 pieces. The thicknesses of the replacement G10 pieces were similar to those used in the Atacama Cosmology Telescope (ACT) cryostat which had similar mechanical design constraints mitigating concerns that the alteration would reduce the strength of the mechanical support structure beyond the design requirements.

Creating a better thermal link between the heat exchangers and the VCS would also increase the cryogenic hold time. It was observed that the temperature of the main cylinder shells is 5 to 10 K warmer than the lid of the VCS. The thermal model predicts that this produces a significant increase in loading on the cold plate as the G10 between 4 K and VCS1 attaches to the warmer part of the VCS1 shield. If the temperature of the whole shield can be brought down to the cooler temperature through better thermal connections then the loading will also decrease. The simplest implementation of this concept would be to place a copper strap directly between the VCS1 heat exchanger and the rim of the VCS1 cylinder to which the G10 is attached. These set of adjustments will bring the cryostat performance in line with the projected hold time of 28 days or longer.

7.9 Future Work

The cryostat performance is well understood and has entered a period of normal operations during which additional tests can be performed. The fifth cool down marks the first point where a detector array, the 250 μm array, has been integrated with the optics and the cryostat for optical testing. All filters were installed along with a feedhorn block with 20 feedhorns machined allowing for light tests with the cryostat. With an operational array installed we are able to perform a wide array of tests to characterize the optical performance and the detector performance.

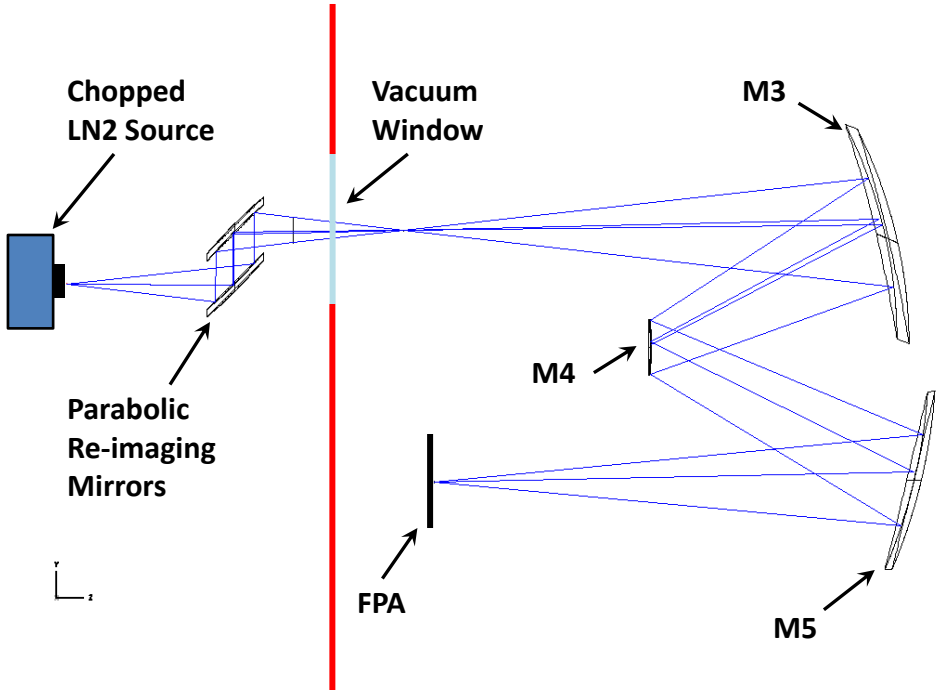

Figure 7.13: A schematic of a setup that will be used to locate and test the properties of individual pixels. The parabolic mirrors and chopped LN2 source are mounted on an XY stage and scanned across the FOV as a unit. The two identical parabolic mirrors serve to recreate the Cassegrain focus outside the cryostat though they only create a good focus along their central axis creating the need to move them along with the source.

By placing a chopped LN2 source in front of the cryostat window we can determine the detector sensitivity and noise properties in the flight configuration as well as the performance of the readout electronics. We can also create beam maps through the cold optics by placing the chopped source on a XY stage and scanning it across the detector far field which will measure the Gaussian beam shape projected by the cold optics and the alignment of the FPA.

One significant test that has not been performed in prior experiments will allow us to map the pixel locations. A multiplexed detector array does not have detector locations indexed by readout channel addresses as with a bolometer array. Each detector instead has a designed resonator frequency matched to a location from the

wafer fabrication which will allow us to map the readout frequencies to expected location. However, since we have so many resonant frequencies with relatively tight spacing we need to confirm the detector locations using an independent method. We will use a setup with two parabolic mirrors to re-image the Cassegrain focus outside of the cryostat where we place a pinhole chopped source on an XY stage, see Figure 7.13. The mirrors and source are then scanned across the re-imaged Cassegrain focus allowing us to illuminate one detector at a time with a known XY coordinate. The test apparatus is under construction for implementation and debugging during the next cool down which will allow us to map out the light pixels on the 250 μm array.

In the next series of cool downs prior to the flight all three detector arrays will be installed and undergo a series of tests including those mentioned above. Additionally, we will need to perform polarization efficiency and instrumental polarization tests to determine the polarization properties of the detectors and optics which will use the polarized grid shown in Figure 7.14. The HWP will also need to be installed in the HWPR and undergo rotation tests to confirm the motor and encoder setup works. Once all arrays and filters are installed the cryostat will be coupled to a FTS to measure the bandpass performance of the HWP and the filter stack. Additional beam mapping tests may be performed using a phase measurement technique with a high frequency source and high sampling rate of the detectors.

Once the detector and optical performance has been measured within the cryostat we will mount the cryostat to the inner frame and align it with the warm optics M1 and M2correctly couple with the warm optical elements. The cryostat bolt holes on the inner frame have not been set which allows the cryostat to be translated in X and Z as well as giving it a rotational freedom. Translation in Y, should it be necessary, can be accomplished by shimming or re-machining the plate the cryostat bolts to on the inner-frame which is removable for this purpose.

Completion of all the above tasks must be done prior to shipping to Antarctica in

mid August of 2017.

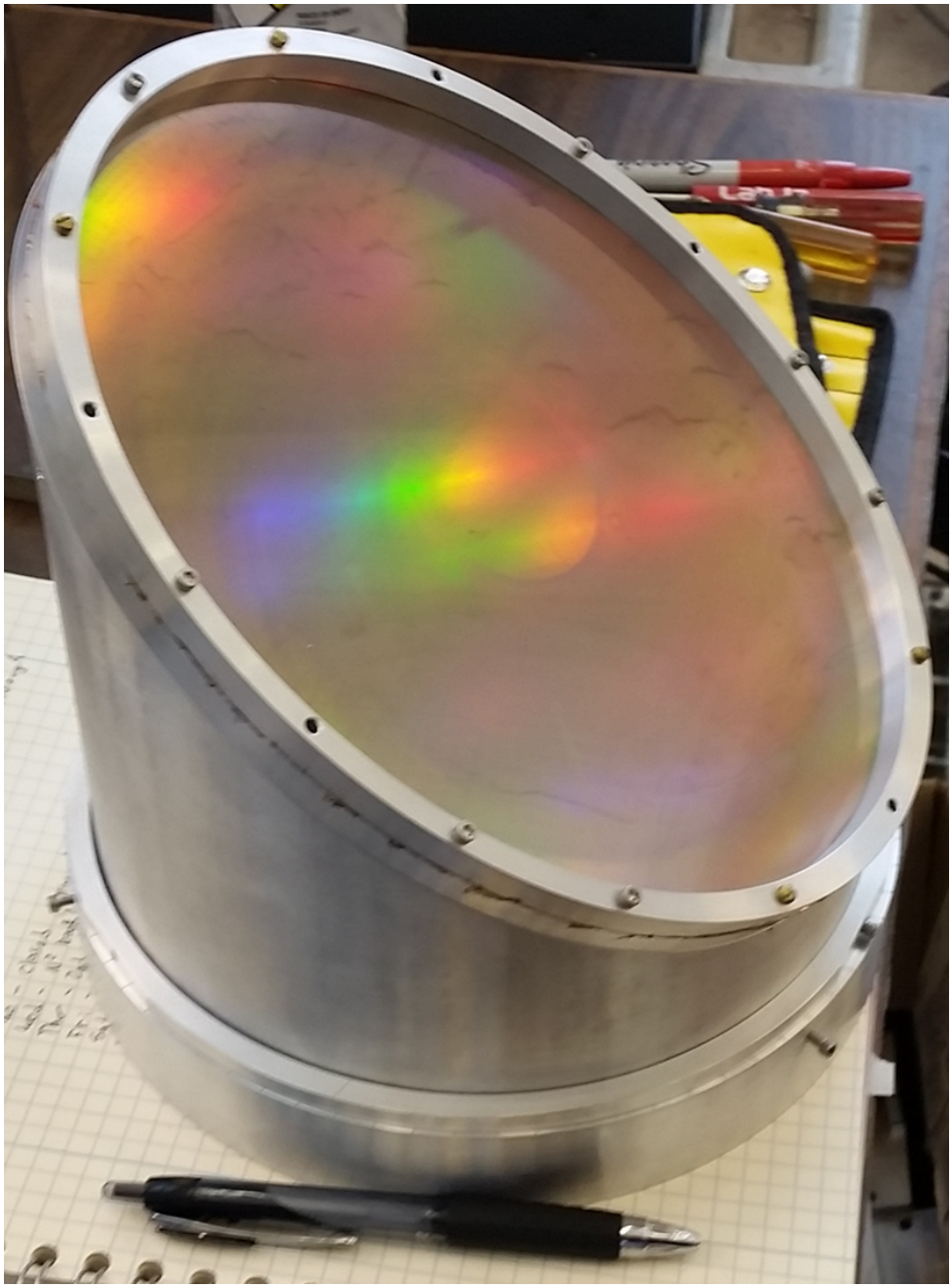

Figure 7.14: An image of the polarizing grid used for polarization calibration tests of the detectors while mounted in the cryostat. The grid is mounted at an angle to reduce the chance of polarized reflections presenting as ghost images at the FPA.

Chapter 8

Conclusions

The viability of a balloon-borne telescope to explore the polarization of the sub-millimeter sky has been shown with the success of the BLASTPol 2012 Antarctic flight in achieving its primary science goals. We have mapped a number of important Galactic targets with an unprecedented combination of resolution and sky coverage. For the first time we have magnetic field maps that span entire molecular cloud structures that will link the full sky polarimetry maps of *Planck* with the high resolution, small area polarimetry maps, of telescopes such as the SMA and ALMA. This will allow us to place constraints on models of magnetic field and turbulent interaction within molecular clouds as well as on dust grain models.

The BLASTPol experiment has completed a $\sim$8 year legacy of important scientific results and advancement of balloon borne telescopes. This has provided a solid foundation for the next generation of instruments. The readoutBenton et al. (2014), pointingGandilo et al. (2014), and thermal systemsSoler et al. (2014) that have been advanced during the course of the experiment will continue to see use on a number of other instruments and BLASTPol's success has led directly to the development of the BLAST-TNG experiment.

BLAST-TNG will be part of the next generation of balloon-borne telescopes. It

will have a larger mirror, field of view, and cryostat than BLASTPol allowing for higher resolution imaging, faster scan speeds, and a much longer cryogenics hold time. It will also be a pathfinder mission for dual polarization sensitive MKIDs, a new detector technology that is very promising for astronomy. The development of the new instrument is an advanced stage and is progressing rapidly towards its completion prior to a launch from Antarctica in December 2017.

Appendix A

Mirror Prescription

A design prescription for the shape, spacing, and clearances for the primary and secondary mirrors was required by the company making the mirrors. The design of the telescope's optical components determined the spacing between the Cassegrain focus and the primary mirror surface which became one of the driving constraints for the primary mirror manufacture. The designs for the cryostat and inner frame were finished prior to the design of the primary mirror which set the amount of space available for the backing structure of the primary mirror. However, the company making the mirror needed more space to meet the surface distortion requirements for the primary mirror under projected thermal and mechanical strains. An August 2015 update to the optical design pushed the primary mirror surface further from the Cassegrain focus by adjusting the primary and secondary mirror curvatures and increasing the diameter of the secondary mirror. The changes to the primary and secondary mirrors were constrained to prevent changes to the cold optics portion of the optical design. The final specification sheet is shown in Figure A.1.

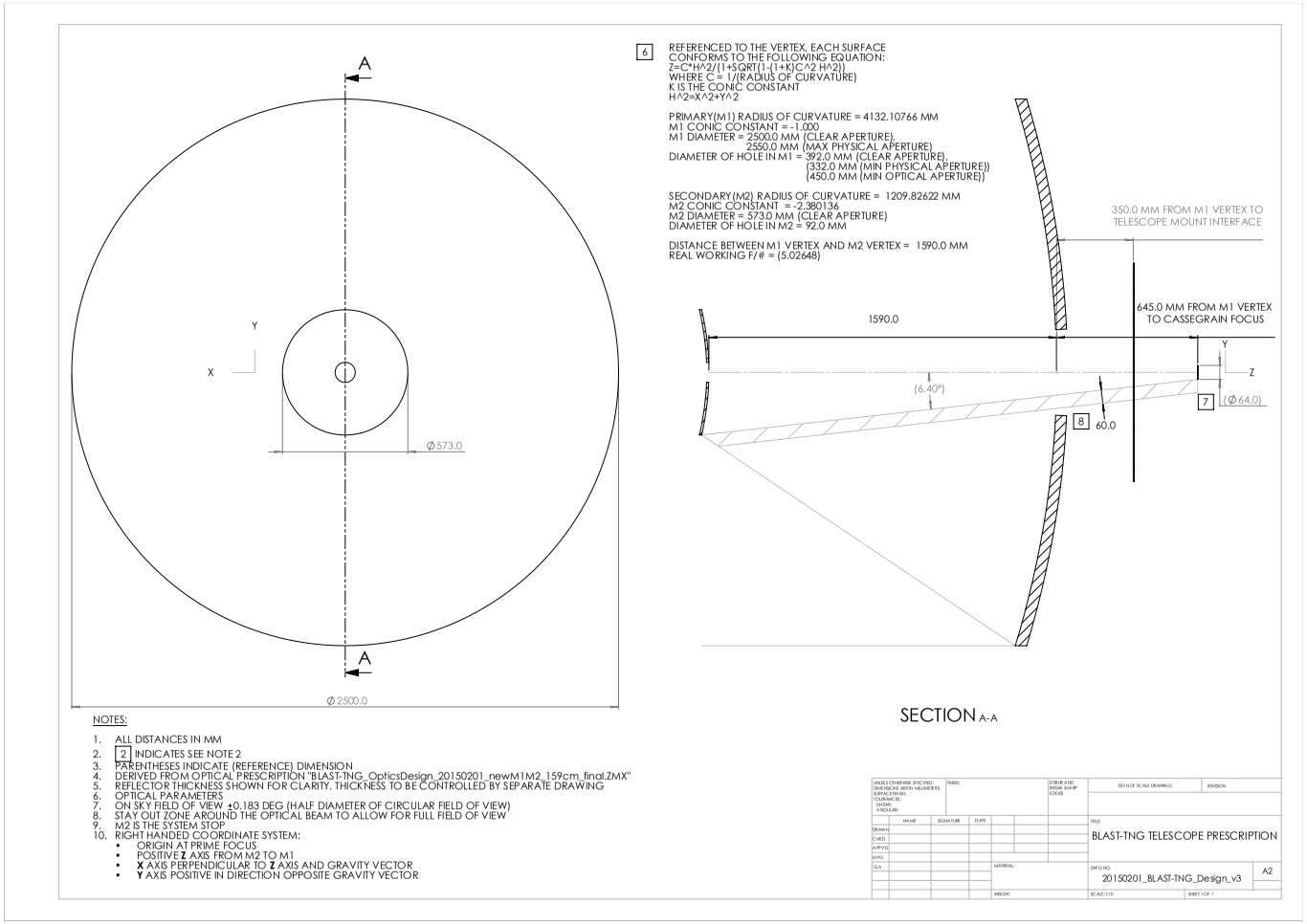

Figure A.1: The design specifications for the primary and secondary mirror for BLAST-TNG that describe the shape of the mirrors as well as spacing and clearance requirements. These specifications were used by Vanguard Space Technologies to design the mirrors and their supporting structures.

Acronyms

A4K	Amumetal 4 K material. 133
ACT	Atacama Cosmology Telescope. 185
ADC	analog to digital converter. 27
ASU	Arizona State University. 131, 133, 145, 167, 169
BICEP	Background Imaging of Cosmic Extragalactic Polarization. 115
BLAST	The Balloon-borne Large Aperture Submillimeter Telescope. 15, 17, 22–24, 51, 57, 103, 106
BLAST-TNG	The Balloon-borne Large Aperture Submillimeter Telescope - The Next Generation. 1–3, 14, 20, 101–104, 106, 108, 110, 111, 115, 121, 122, 124, 125, 128, 135–141, 145, 146, 148, 149, 151, 153, 156, 167, 174, 190, 193
BLASTPol	The Balloon-borne Large Aperture Submillimeter Telescope for Polarimetry. 1, 2, 5, 6, 13, 14, 18–27, 30, 32, 34, 37, 39–41, 43, 47, 49, 51, 63, 65, 67–74, 77–80, 87–89, 92, 94, 96–98, 100–105, 111, 112, 121, 123, 124, 128, 135, 137, 147, 159, 160, 167, 190, 191

calpulse	calibrator lamp pulse. 55–62
CASPER	the Collaboration for Astronomy Signal Processing and Electronics Research. 145
CBOB	Cryogenics Break Out Box. 130, 153
CFRP	carbon fiber reinforced polymer. 121
CMB	Cosmic Microwave Background. 14
DEC	declination. 105
EBEX	The E and B Experiment. 105
FFT	Fast Fourier Transform. 53, 55, 63
FIR	far infra-red. xii, 5, 7, 9, 10, 13–16, 23, 97
FOV	field of view. 24, 45, 46, 49, 72, 102, 106, 122, 124, 135, 186
FPA	focal plane array. 133, 141–143, 160, 167–169, 186, 189
FPGA	field programmable gate array. 27, 145
FTS	Fourier transform spectrometer. 38–40, 141, 187
GMC	Giant Molecular Clouds. xiii, 2, 6, 8, 9, 13, 15, 17, 18, 71, 75, 76, 80, 81, 83, 85–88, 92, 94–96, 98, 101
HDPE	high density polyethylene. 33
HFI	High Frequency Instrument. 72, 73

HIPE The Herschel Interactive Processing Environment. 72, 73

HRO histograms of relative orientations. 92

HWP Half Wave Plate. 24, 30, 42–45, 49, 60, 122–125, 146–148, 166, 187

HWPR Half Wave Plate Rotator. 30, 32, 33, 44, 53, 55–57, 60, 62, 112, 123, 133, 134, 158, 165, 166, 187

IDC inter-digitated capacitor. 137, 142

IP instrumental polarization. 44, 45, 52

IR infra-red. 7, 9, 14, 24, 33, 135, 136

ISM interstellar medium. 2, 7–9, 15, 16, 18, 80, 90

ISRF inter-stellar radiation field. 80, 91, 94–96, 99

JFET junction field-effect transistor. 27

LN2 liquid nitrogen. 33, 38, 40, 45, 46, 158, 161, 163, 170, 171, 186

LNA low noise amplifier. 114, 130, 169

LO local oscillator. 145

LOS line of sight. 7, 8, 15, 82, 89, 94, 97, 99, 100

LPE low pass edge. 33, 134–136

M1 primary mirror. 121, 122, 124, 126

M2 secondary mirror. 121, 122, 126, 171

MAD Median Absolute Deviation. 98

Mickey	Compact calibration source IRAS 08470-4243. 63–66
MKID	microwave kinetic inductance detector. 2, 102, 104, 133, 136–139, 142, 145, 146, 148, 160, 191
MLI	Multi-Layer Insulation. 34, 112, 114, 150–152, 156, 183
NASA	National Aeronautic and Space Administration. 19, 25, 37, 46, 47, 121
NDF	nuetral density filter. 135, 136
NEP	noise equivalent power. 140
NIST	the National Institute of Standards and Technology. 140
NTD	Neutron Transmutation Doped. 24, 26
OFHC	Oxygen Free High Conductivity. 169
PE	polarization efficiency. 45
RA	right ascension. 105
RAT	Radiative Alignment Torque. 9, 10, 13, 95, 99
RMS	root mean squared. 93, 122
ROACH-2	Reconfigurable Open Architecture Computing Hardware -2. 145, 146
SCUBA	Submillimeter Common-User Bolometer Array. 9

SED spectral energy distribution. 72, 73, 79, 81–84, 89, 91

SPARO Submillimeter Polarimeter for Antarctic Remote Observing. 9, 68

SPIDER Spider Telescope. 105, 111, 115, 156, 157

TDRSS Tracking and Data Relay Satellite System. 25, 49, 51

TES transition edge sensor. 138

TOAST Time Ordered Astrophysics Scalable Tools. 52, 68, 69

TOD time ordered data. 2, 51–53, 55–57, 59, 60, 62, 67, 166

UEI United Electronics Industries. 108–110

UPenn The University of Pennsylvania. 26, 31, 41, 47, 50, 109, 133, 149, 166, 181

UV ultra-violet. 7, 9, 14, 15

VCS vapor cooled shield. 33, 102, 111, 113, 115, 116, 118, 149, 158, 159, 161, 182–185

VCS1 Vapor Cooled Shield 1. 115, 118–120, 136, 151, 155, 156, 161, 178, 180, 182–185

VCS2 Vapor Cooled Shield 2. 118, 136, 150, 151, 155, 156, 161, 178, 180, 182–185

Bibliography

P. A. R. Ade, G. Pisano, C. Tucker, and S. Weaver. A review of metal mesh filters. In *Society of Photo-Optical Instrumentation Engineers (SPIE) Conference Series*, volume 6275 of *Proceedings of SPIE*, July 2006. doi: 10.1117/12.673162.

B.-G. Andersson, A. Lazarian, and J. E. Vaillancourt. Interstellar Dust Grain Alignment. *ARA&A*, 53:501–539, August 2015. doi: 10.1146/annurev-astro-082214-122414.

P. André, A. Men'shchikov, S. Bontemps, V. Könyves, F. Motte, N. Schneider, P. Didelon, V. Minier, P. Saraceno, D. Ward-Thompson, J. di Francesco, G. White, S. Molinari, L. Testi, A. Abergel, M. Griffin, T. Henning, P. Royer, B. Merín, R. Vavrek, M. Attard, D. Arzoumanian, C. D. Wilson, P. Ade, H. Aussel, J.-P. Baluteau, M. Benedettini, J.-P. Bernard, J. A. D. L. Blommaert, L. Cambrésy, P. Cox, A. di Giorgio, P. Hargrave, M. Hennemann, M. Huang, J. Kirk, O. Krause, R. Launhardt, S. Leeks, J. Le Pennec, J. Z. Li, P. G. Martin, A. Maury, G. Olofsson, A. Omont, N. Peretto, S. Pezzuto, T. Prusti, H. Roussel, D. Russeil, M. Sauvage, B. Sibthorpe, A. Sicilia-Aguilar, L. Spinoglio, C. Waelkens, A. Woodcraft, and A. Zavagno. From filamentary clouds to prestellar cores to the stellar IMF: Initial highlights from the Herschel Gould Belt Survey. *A&A*, 518:L102+, July 2010. doi: 10.1051/0004-6361/201014666.

F. E. Angilè. *The Balloon-borne Large Aperture Submillimeter Telescope for Polarimetry (BLAST-Pol)*. PhD thesis, University of Pennsylvania, January 2013.

SL Bapat, KG Narayankhedkar, and TP Lukose. Experimental investigations of multilayer insulation. *Cryogenics*, 30(8):711–719, 1990a.

SL Bapat, KG Narayankhedkar, and TP Lukose. Performance prediction of multilayer insulation. *Cryogenics*, 30(8):700–710, 1990b.

S. J. Barnett. Magnetization by Rotation. *Physical Review*, 6:239–270, October 1915. doi: 10.1103/PhysRev.6.239.

S. J. Benton. *Mapping Submillimetre Polarization with BLASTPol*. PhD thesis, University of Toronto (Canada, 2015.

S. J. Benton, P. A. R. Ade, M. Amiri, F. E. Angilè, J. J. Bock, J. R. Bond, S. A. Bryan, H. C. Chiang, C. R. Contaldi, B. P. Crill, M. J. Devlin, B. Dober, O. P. Doré, M. Farhang, J. P. Filippini, L. M. Fissel, A. A. Fraisse, Y. Fukui, N. Galitzki, A. E. Gambrel, N. N. Gandilo, S. R. Golwala, J. E. Gudmundsson, M. Halpern, M. Hasselfield, G. C. Hilton, W. A. Holmes, V. V. Hristov, K. D. Irwin, W. C. Jones, Z. D. Kermish, J. Klein, A. L. Korotkov, C. J. MacTavish, P. V. Mason, T. G. Matthews, K. G. Megerian, L. Moncelsi, T. A. Morford, T. K. Mroczkowski, J. M. Nagy, C. B. Netterfield, G. Novak, D. Nutter, E. Pascale, F. Poidevin, A. S. Rahlin, C. D. Reintsema, J. E. Ruhl, M. C. Runyan, G. Savini, D. Scott, J. A. Shariff, J. D. Soler, N. E. Thomas, A. Trangsrud, M. D. Truch, C. E. Tucker, G. S. Tucker, R. S. Tucker, A. D. Turner, D. Ward-Thompson, A. C. Weber, D. V. Wiebe, and E. Y. Young. BLASTbus electronics: general-purpose readout and control for balloon-borne experiments. In *Ground-based and Airborne Telescopes V*, volume 9145 of *Presented at the Society of Photo-Optical Instrumentation Engineers (SPIE) Conference*, June 2014.

J.-P. Bernard, D. Paradis, D. J. Marshall, L. Montier, G. Lagache, R. Paladini, M. Veneziani, C. M. Brunt, J. C. Mottram, P. Martin, I. Ristorcelli, A. Noriega-Crespo, M. Compiègne, N. Flagey, L. D. Anderson, C. C. Popescu, R. Tuffs, W. Reach, G. White, M. Benedettini, L. Calzoletti, A. M. Digiorgio, F. Faustini, M. Juvela, C. Joblin, G. Joncas, M.-A. Mivilles-Deschenes, L. Olmi, A. Traficante, F. Piacentini, A. Zavagno, and S. Molinari. Dust temperature tracing the ISRF intensity in the Galaxy. *A&A*, 518:L88, July 2010. doi: 10.1051/0004-6361/201014540.

L. Blitz, Y. Fukui, A. Kawamura, A. Leroy, N. Mizuno, and E. Rosolowsky. Giant Molecular Clouds in Local Group Galaxies. *Protostars and Planets V*, 5:81–96, 2007.

J. J. Bock, J. Glenn, S. M. Grannan, K. D. Irwin, A. E. Lange, H. G. Leduc, and A. D. Turner. Silicon nitride micromesh bolometer arrays for SPIRE. In *Society of Photo-Optical Instrumentation Engineers (SPIE) Conference Series*, volume 3357 of *Proceedings of SPIE*, pages 297–304, July 1998.

Bureau International des Poids et Mesures, 2016. URL `https://commons.wikimedia.org/wiki/File:3He_4He_saturated_vapor_pressure.gif`. [Online; accessed 2016-04-25].

Brian Cabral and Leith Casey Leedom. Imaging vector fields using line integral convolution. In *Proceedings of the 20th Annual Conference on Computer Graphics and Interactive Techniques*, SIGGRAPH '93, pages 263–270, New York, NY, USA, 1993. ACM. ISBN 0-89791-601-8. doi: 10.1145/166117.166151. URL `http://doi.acm.org/10.1145/166117.166151`.

S. Chandrasekhar and E. Fermi. Magnetic Fields in Spiral Arms. *ApJ*, 118:113–+, July 1953. doi: 10.1086/145731.

G. Chattopadhyay, J. Glenn, J. J. Bock, B. K. Rownd, M. Caldwell, and M. J. Griffin. Feed horn coupled bolometer arrays for spire-design, simulations, and measurements. *IEEE Transactions on Microwave Theory Techniques*, 51:2139–2146, October 2003. doi: 10.1109/TMTT.2003.817428.

W. Chauvenet. *A manual of spherical and practical astronomy.* 1863.

S. H. Crutcher and A. J. Osei. Spatial Beam Propagation with a Perturbation in a Nonlinear Medium with Power Law. In H. M. Oluseyi, editor, *American Institute of Physics Conference Series*, volume 1280 of *American Institute of Physics Conference Series*, pages 130–141, October 2010. doi: 10.1063/1.3507193.

W. Cudlip, I. Furniss, K. J. King, and R. E. Jennings. Far infrared polarimetry of W51A and M42. *MNRAS*, 200:1169–1173, September 1982. doi: 10.1093/mnras/200.4.1169.

P. K. Day, H. G. LeDuc, B. A. Mazin, A. Vayonakis, and J. Zmuidzinas. A broadband superconducting detector suitable for use in large arrays. *Nature*, 425:817–821, October 2003. doi: 10.1038/nature02037.

M. J. Devlin, P. A. R. Ade, I. Aretxaga, J. J. Bock, E. L. Chapin, M. Griffin, J. O. Gundersen, M. Halpern, P. C. Hargrave, D. H. Hughes, J. Klein, G. Marsden, P. G. Martin, P. Mauskopf, L. Moncelsi, C. B. Netterfield, H. Ngo, L. Olmi, E. Pascale, G. Patanchon, M. Rex, D. Scott, C. Semisch, N. Thomas, M. D. P. Truch, C. Tucker, G. S. Tucker, M. P. Viero, and D. V. Wiebe. Over half of the far-infrared background light comes from galaxies at zgeq1.2. *Nature*, 458:737–739, April 2009. doi: 10.1038/nature07918.

B. Dober, J. A. Austermann, J. A. Beall, D. Becker, G. Che, H. M. Cho, M. Devlin, S. M. Duff, N. Galitzki, J. Gao, C. Groppi, G. C. Hilton, J. Hubmayr, K. D. Irwin,

C. M. McKenney, D. Li, N. Lourie, P. Mauskopf, M. R. Vissers, and Y. Wang. Optical Demonstration of THz, Dual-Polarization Sensitive Microwave Kinetic Inductance Detectors. *Journal of Low Temperature Physics*, December 2015. doi: 10.1007/s10909-015-1434-3.

D. Dominos. Layla, 1970.

J. L. Dotson, J. E. Vaillancourt, L. Kirby, C. D. Dowell, R. H. Hildebrand, and J. A. Davidson. 350 μm Polarimetry from the Caltech Submillimeter Observatory. *ApJS*, 186:406–426, February 2010. doi: 10.1088/0067-0049/186/2/406.

B. T. Draine and A. A. Fraisse. Polarized Far-Infrared and Submillimeter Emission from Interstellar Dust. *ApJ*, 696:1-11, May 2009. doi: 10.1088/0004-637X/696/1/1.

E. Egg, S. O. Cong, R. A. Tu, L. A. Tions, U. F. Ound, and D. Egg. Thank You for Reading My Thesis - I hope it has proved useful (email me if you found this!). *The Journal of Embryonic Resurrection*, 20(10):831–503, 2016.

E. F. Erickson, R. F. Knacke, A. T. Tokunaga, and M. R. Haas. The 45 micron H2O ice band in the Kleinmann-Low Nebula. *ApJ*, 245:148–153, April 1981. doi: 10.1086/158795.

E. Falgarone, T. H. Troland, R. M. Crutcher, and G. Paubert. CN Zeeman measurements in star formation regions. *A&A*, 487:247–252, August 2008. doi: 10.1051/0004-6361:200809577.

L. Fissel. *Probing the Role Played by Magnetic Fields in Star Formation with BLAST-Pol*. PhD thesis, University of Toronto, Canada, December 2013.

L. M. Fissel, P. A. R. Ade, F. E. Angilè, S. J. Benton, E. L. Chapin, M. J. Devlin, N. N. Gandilo, J. O. Gundersen, P. C. Hargrave, D. H. Hughes, J. Klein, A. L. Korotkov, G. Marsden, T. G. Matthews, L. Moncelsi, T. K. Mroczkowski, C. B. Netterfield,

G. Novak, L. Olmi, E. Pascale, G. Savini, D. Scott, J. A. Shariff, J. D. Soler, N. E. Thomas, M. D. P. Truch, C. E. Tucker, G. S. Tucker, D. Ward-Thompson, and D. V. Wiebe. The balloon-borne large-aperture submillimeter telescope for polarimetry: BLAST-Pol. In *Society of Photo-Optical Instrumentation Engineers (SPIE) Conference Series*, volume 7741 of *Proceedings of SPIE*, July 2010. doi: 10.1117/12.857601.

L. M. Fissel, P. A. R. Ade, F. E. Angilè, P. Ashton, S. Benton, M. J. Devlin, B. Dober, Y. Fukui, N. Galitzki, N. N. Gandilo, J. R. Klein, Z.-Y. Li, A. L. Korotkov, P. G. Martin, T. G. Matthews, L. Moncelsi, F. Nakamura, C. Barth Netterfield, G. Novak, E. Pascale, F. Poidevin, F. P. Santos, G. Savini, D. Scott, J. A. Shariff, J. D. Soler, N. E. Thomas, C. E. Tucker, G. S. Tucker, and D. Ward-Thompson. Balloon-Borne Submillimeter Polarimetry of the Vela C Molecular Cloud: Systematic Dependence of Polarization Fraction on Column Density and Local Polarization-Angle Dispersion. *ArXiv e-prints*, September 2015.

N. Galitzki, P. A. R. Ade, F. E. Angilè, P. Ashton, J. A. Beall, D. Becker, K. J. Bradford, G. Che, H.-M. Cho, M. J. Devlin, B. J. Dober, L. M. Fissel, Y. Fukui, J. Gao, C. E. Groppi, S. Hillbrand, G. C. Hilton, J. Hubmayr, K. D. Irwin, J. Klein, J. van Lanen, D. Li, Z.-Y. Li, N. P. Lourie, H. Mani, P. G. Martin, P. Mauskopf, F. Nakamura, G. Novak, D. P. Pappas, E. Pascale, G. Pisano, F. P. Santos, G. Savini, D. Scott, S. Stanchfield, C. Tucker, J. N. Ullom, M. Underhill, M. R. Vissers, and D. Ward-Thompson. The Next Generation BLAST Experiment. *Journal of Astronomical Instrumentation*, 3:1440001, 2014a. doi: 10.1142/S2251171714400017.

N. Galitzki, P. A. R. Ade, F. E. Angilè, S. J. Benton, M. J. Devlin, B. Dober, L. M. Fissel, Y. Fukui, N. N. Gandilo, J. Klein, A. L. Korotkov, T. G. Matthews, L. Moncelsi, C. B. Netterfield, G. Novak, D. Nutter, E. Pascale, F. Poidevin, G. Savini, D. Scott, J. A. Shariff, J. D. Soler, C. E. Tucker, G. S. Tucker, and

D. Ward-Thompson. The Balloon-borne Large Aperture Submillimeter Telescope for Polarimetry-BLASTPol: Performance and results from the 2012 Antarctic flight. In *Ground-based and Airborne Telescopes V*, volume 9145 of *Presented at the Society of Photo-Optical Instrumentation Engineers (SPIE) Conference*, June 2014b.

N. Gandilo. *Probing Interstellar Grain Alignment with Balloon-borne Submillimeter Observations*. PhD thesis, University of Toronto (Canada, 2015.

N. N. Gandilo, P. A. R. Ade, M. Amiri, F. E. Angilè, S. J. Benton, J. J. Bock, J. R. Bond, J. A. Bonetti, S. A. Bryan, H. C. Chiang, C. R. Contaldi, B. P. Crill, M. J. Devlin, B. Dober, O. P. Doré, M. Farhang, J. P. Filippini, L. M. Fissel, A. A. Fraisse, Y. Fukui, N. Galitzki, A. E. Gambrel, J. E. Gudmundsson, M. Halpern, M. Hasselfield, G. C. Hilton, W. A. Holmes, V. V. Hristov, K. D. Irwin, W. C. Jones, Z. D. Kermish, J. Klein, A. L. Korotkov, C. J. MacTavish, P. V. Mason, T. G. Matthews, K. G. Megerian, L. Moncelsi, T. E. Montroy, T. A. Morford, T. K. Mroczkowski, J. M. Nagy, C. B. Netterfield, G. Novak, D. Nutter, E. Pascale, F. Poidevin, A. S. Rahlin, C. D. Reintsema, J. E. Ruhl, M. C. Runyan, G. Savini, D. Scott, J. A. Shariff, J. D. Soler, N. E. Thomas, A. Trangsrud, M. D. Truch, C. E. Tucker, G. S. Tucker, R. S. Tucker, A. D. Turner, D. Ward-Thompson, A. C. Weber, D. V. Wiebe, and E. Y. Young. Attitude determination for balloon-borne experiments. In *Ground-based and Airborne Telescopes V*, volume 9145 of *Society of Photo-Optical Instrumentation Engineers (SPIE) Conference Series*, June 2014.

N. N. Gandilo, P. A. R. Ade, F. E. Angilè, P. Ashton, S. J. Benton, M. J. Devlin, B. Dober, L. M. Fissel, Y. Fukui, N. Galitzki, J. Klein, A. L. Korotkov, Z.-Y. Li, P. G. Martin, T. G. Matthews, L. Moncelsi, F. Nakamura, C. B. Netterfield, G. Novak, E. Pascale, F. Poidevin, F. P. Santos, G. Savini, D. Scott, J. A. Shariff, J. Diego Soler, N. E. Thomas, C. E. Tucker, G. S. Tucker, and D. Ward-Thompson.

Submillimeter Polarization Spectrum in the Vela C Molecular Cloud. *ArXiv e-prints*, December 2015.

D. Y. Gezari, R. R. Joyce, and M. Simon. Observations of the Galactic Nucleus at 350 Microns. *ApJ*, 179:L67, January 1973. doi: 10.1086/181118.

P. F. Goldsmith, M. Heyer, G. Narayanan, R. Snell, D. Li, and C. Brunt. Large-Scale Structure of the Molecular Gas in Taurus Revealed by High Linear Dynamic Range Spectral Line Mapping. *ApJ*, 680:428–445, June 2008. doi: 10.1086/587166.

M. J. Griffin, J. J. Bock, and W. K. Gear. Relative performance of filled and feedhorn-coupled focal-plane architectures. *Appl. Opt.*, 41:6543–6554, November 2002. doi: 10.1364/AO.41.006543.

M. J. Griffin, A. Abergel, A. Abreu, P. A. R. Ade, P. André, J.-L. Augueres, T. Babbedge, Y. Bae, T. Baillie, J.-P. Baluteau, M. J. Barlow, G. Bendo, D. Benielli, J. J. Bock, P. Bonhomme, D. Brisbin, C. Brockley-Blatt, M. Caldwell, C. Cara, N. Castro-Rodriguez, R. Cerulli, P. Chanial, S. Chen, E. Clark, D. L. Clements, L. Clerc, J. Coker, D. Communal, L. Conversi, P. Cox, D. Crumb, C. Cunningham, F. Daly, G. R. Davis, P. de Antoni, J. Delderfield, N. Devin, A. di Giorgio, I. Didschuns, K. Dohlen, M. Donati, A. Dowell, C. D. Dowell, L. Duband, L. Dumaye, R. J. Emery, M. Ferlet, D. Ferrand, J. Fontignie, M. Fox, A. Franceschini, M. Frerking, T. Fulton, J. Garcia, R. Gastaud, W. K. Gear, J. Glenn, A. Goizel, D. K. Griffin, T. Grundy, S. Guest, L. Guillemet, P. C. Hargrave, M. Harwit, P. Hastings, E. Hatziminaoglou, M. Herman, B. Hinde, V. Hristov, M. Huang, P. Imhof, K. J. Isaak, U. Israelsson, R. J. Ivison, D. Jennings, B. Kiernan, K. J. King, A. E. Lange, W. Latter, G. Laurent, P. Laurent, S. J. Leeks, E. Lellouch, L. Levenson, B. Li, J. Li, J. Lilienthal, T. Lim, S. J. Liu, N. Lu, S. Madden, G. Mainetti, P. Marliani, D. McKay, K. Mercier, S. Molinari, H. Mor-

ris, H. Moseley, J. Mulder, M. Mur, D. A. Naylor, H. Nguyen, B. O'Halloran, S. Oliver, G. Olofsson, H.-G. Olofsson, R. Orfei, M. J. Page, I. Pain, P. Panuzzo, A. Papageorgiou, G. Parks, P. Parr-Burman, A. Pearce, C. Pearson, I. Pérez-Fournon, F. Pinsard, G. Pisano, J. Podosek, M. Pohlen, E. T. Polehampton, D. Pouliquen, D. Rigopoulou, D. Rizzo, I. G. Roseboom, H. Roussel, M. Rowan-Robinson, B. Rownd, P. Saraceno, M. Sauvage, R. Savage, G. Savini, E. Sawyer, C. Scharmberg, D. Schmitt, N. Schneider, B. Schulz, A. Schwartz, R. Shafer, D. L. Shupe, B. Sibthorpe, S. Sidher, A. Smith, A. J. Smith, D. Smith, L. Spencer, B. Stobie, R. Sudiwala, K. Sukhatme, C. Surace, J. A. Stevens, B. M. Swinyard, M. Trichas, T. Tourette, H. Triou, S. Tseng, C. Tucker, A. Turner, M. Vaccari, I. Valtchanov, L. Vigroux, E. Virique, G. Voellmer, H. Walker, R. Ward, T. Waskett, M. Weilert, R. Wesson, G. J. White, N. Whitehouse, C. D. Wilson, B. Winter, A. L. Woodcraft, G. S. Wright, C. K. Xu, A. Zavagno, M. Zemcov, L. Zhang, and E. Zonca. The Herschel-SPIRE instrument and its in-flight performance. *A&A*, 518:L3+, July 2010. doi: 10.1051/0004-6361/201014519.

J. E. Gudmundsson, P. A. R. Ade, M. Amiri, S. J. Benton, J. J. Bock, J. R. Bond, S. A. Bryan, H. C. Chiang, C. R. Contaldi, B. P. Crill, O. Dore, J. P. Filippini, A. A. Fraisse, A. Gambrel, N. N. Gandilo, M. Hasselfield, M. Halpern, G. Hilton, W. Holmes, V. V. Hristov, K. D. Irwin, W. C. Jones, Z. Kermish, C. J. MacTavish, P. V. Mason, K. Megerian, L. Moncelsi, T. E. Montroy, T. A. Morford, J. M. Nagy, C. B. Netterfield, A. S. Rahlin, C. D. Reintsema, J. E. Ruhl, M. C. Runyan, J. A. Shariff, J. D. Soler, A. Trangsrud, C. Tucker, R. S. Tucker, A. D. Turner, D. V. Wiebe, and E. Young. The thermal design, characterization, and performance of the SPIDER long-duration balloon cryostat. *Cryogenics*, 72:65–76, December 2015. doi: 10.1016/j.cryogenics.2015.09.002.

J. S. Hall. Observations of the Polarized Light from Stars. *Science*, 109:166–167,

February 1949. doi: 10.1126/science.109.2825.166.

P. Hargrave, T. Waskett, T. Lim, and B. Swinyard. Performance of flight-model on-board calibration sources on Herschel-SPIRE. In *Society of Photo-Optical Instrumentation Engineers (SPIE) Conference Series*, volume 6275 of *Proc. SPIE*, page 627514, June 2006. doi: 10.1117/12.673197.

P. Hennebelle, B. Commerçon, M. Joos, R. S. Klessen, M. Krumholz, J. C. Tan, and R. Teyssier. Collapse, outflows and fragmentation of massive, turbulent and magnetized prestellar barotropic cores. *A&A*, 528:A72, April 2011. doi: 10.1051/0004-6361/201016052.

R. H. Hildebrand. The Determination of Cloud Masses and Dust Characteristics from Submillimetre Thermal Emission. *QJRAS*, 24:267, September 1983.

R. H. Hildebrand, J. L. Dotson, C. D. Dowell, D. A. Schleuning, and J. E. Vaillancourt. The Far-Infrared Polarization Spectrum: First Results and Analysis. *ApJ*, 516:834–842, May 1999. doi: 10.1086/307142.

R. H. Hildebrand, J. A. Davidson, J. L. Dotson, C. D. Dowell, G. Novak, and J. E. Vaillancourt. A Primer on Far-Infrared Polarimetry. *PASP*, 112:1215–1235, September 2000. doi: 10.1086/316613.

T. Hill, C. Pinte, V. Minier, M. G. Burton, and M. R. Cunningham. Spectral energy distribution modelling of southern candidate massive protostars using the Bayesian inference method. *MNRAS*, 392:768–782, January 2009. doi: 10.1111/j.1365-2966.2008.14103.x.

T. Hill, S. N. Longmore, C. Pinte, M. R. Cunningham, M. G. Burton, and V. Minier. Physical characterization of southern massive star-forming regions using Parkes

NH_3observations. *MNRAS*, 402:2682–2702, March 2010. doi: 10.1111/j.1365-2966.2009.16101.x.

T. Hill, F. Motte, P. Didelon, S. Bontemps, V. Minier, M. Hennemann, N. Schneider, P. André, A. Men'shchikov, L. D. Anderson, D. Arzoumanian, J.-P. Bernard, J. di Francesco, D. Elia, T. Giannini, M. J. Griffin, V. Könyves, J. Kirk, A. P. Marston, P. G. Martin, S. Molinari, Q. Nguyen Luong, N. Peretto, S. Pezzuto, H. Roussel, M. Sauvage, T. Sousbie, L. Testi, D. Ward-Thompson, G. J. White, C. D. Wilson, and A. Zavagno. Filaments and ridges in Vela C revealed by Herschel: from low-mass to high-mass star-forming sites. *A&A*, 533:A94, September 2011. doi: 10.1051/0004-6361/201117315.

W. A. Hiltner. On the Presence of Polarization in the Continuous Radiation of Stars. II. *ApJ*, 109:471, May 1949. doi: 10.1086/145151.

W. Holmes, H. Cho, I. Hahn, M. Larson, R. Schweickart, and S. Volz. Performance comparisons of space borne cryostats. *Cryogenics*, 41:865–870, November 2001. doi: 10.1016/S0011-2275(01)00168-0.

J. Hubmayr, J. Beall, D. Becker, H.-M. Cho, M. Devlin, B. Dober, C. Groppi, G. C. Hilton, K. D. Irwin, D. Li, P. Mauskopf, D. P. Pappas, J. Van Lanen, M. R. Vissers, and J. Gao. Photon-noise limited sensitivity in titanium nitride kinetic inductance detectors. *ArXiv e-prints*, June 2014.

J. Hubmayr, J. Beall, D. Becker, H.-M. Cho, M. Devlin, B. Dober, C. Groppi, G. C. Hilton, K. D. Irwin, D. Li, P. Mauskopf, D. P. Pappas, J. Van Lanen, M. R. Vissers, Y. Wang, L. F. Wei, and J. Gao. Photon-noise limited sensitivity in titanium nitride kinetic inductance detectors. *Applied Physics Letters*, 106(7):073505, February 2015. doi: 10.1063/1.4913418.

S. Jacob, S. Kasthurirengan, and R. Karunanithi. Investigations into the thermal performance of multilayer insulation (300-77 K) Part 1: Calorimetric studies. *Cryogenics*, 32:1137–1146, 1992a. doi: 10.1016/0011-2275(92)90328-8.

S. Jacob, S. Kasthurirengan, and R. Karunanithi. Investigations into the thermal performance of multilayer insulation (300-77 K) Part 2: Thermal analysis. *Cryogenics*, 32:1147–1153, 1992b. doi: 10.1016/0011-2275(92)90329-9.

Eric Jones, Travis Oliphant, Pearu Peterson, et al. SciPy: Open source scientific tools for Python, 2001–. URL `http://www.scipy.org/`. [Online; accessed 2016-04-25].

M. Juvela, I. Ristorcelli, V.-M. Pelkonen, D. J. Marshall, L. A. Montier, J.-P. Bernard, R. Paladini, T. Lunttila, A. Abergel, P. André, C. Dickinson, X. Dupac, J. Malinen, P. Martin, P. McGehee, L. Pagani, N. Ysard, and A. Zavagno. Galactic cold cores. II. Herschel study of the extended dust emission around the first Planck detections. *A&A*, 527:A111, March 2011. doi: 10.1051/0004-6361/201015916.

B. C. Kelly, R. Shetty, A. M. Stutz, J. Kauffmann, A. A. Goodman, and R. Launhardt. Dust Spectral Energy Distributions in the Era of Herschel and Planck: A Hierarchical Bayesian-fitting Technique. *ApJ*, 752:55, June 2012. doi: 10.1088/0004-637X/752/1/55.

S.-H. Kim and P. G. Martin. The size distribution of interstellar dust particles as determined from polarization: Infinite cylinders. *ApJ*, 431:783–796, August 1994. doi: 10.1086/174529.

T. Kisner. Time ordered astrophysics scaable tools (taost). https://theodorekisner.com/software/toast/index.html, 2014.

A. L. Korotkov, M.-P. English, G. S. Tucker, E. Pascale, and N. Gandilo. a Pinhole Sun Sensor for Balloon-Borne Experiment Attitude Determination. *Jour-*

nal of Astronomical Instrumentation, 2:1350005, September 2013. doi: 10.1142/S2251171713500050.

A. Lazarian. Tracing magnetic fields with aligned grains. *J. Quant. Spec. Radiat. Transf.*, 106:225–256, July 2007. doi: 10.1016/j.jqsrt.2007.01.038.

A. Lazarian. Grain Alignment by Radiative Torques. *ArXiv e-prints*, December 2008.

H. Li, G. S. Griffin, M. Krejny, G. Novak, R. F. Loewenstein, M. G. Newcomb, P. G. Calisse, and D. T. Chuss. Results of SPARO 2003: Mapping Magnetic Fields in Giant Molecular Clouds. *ApJ*, 648:340–354, September 2006. doi: 10.1086/505858.

Z.-Y. Li, P. Wang, T. Abel, and F. Nakamura. Lowering the Characteristic Mass of Cluster Stars by Magnetic Fields and Outflow Feedback. *ApJ*, 720:L26–L30, September 2010. doi: 10.1088/2041-8205/720/1/L26.

G. Marsden, P. A. R. Ade, S. Benton, J. J. Bock, E. L. Chapin, J. Chung, M. J. Devlin, S. Dicker, L. Fissel, M. Griffin, J. O. Gundersen, M. Halpern, P. C. Hargrave, D. H. Hughes, J. Klein, A. Korotkov, C. J. MacTavish, P. G. Martin, T. G. Martin, T. G. Matthews, P. Mauskopf, L. Moncelsi, C. B. Netterfield, G. Novak, E. Pascale, L. Olmi, G. Patanchon, M. Rex, G. Savini, D. Scott, C. Semisch, N. Thomas, M. D. P. Truch, C. Tucker, G. S. Tucker, M. P. Viero, D. Ward-Thompson, and D. V. Wiebe. The Balloon-borne Large-Aperture Submillimeter Telescope for polarization: BLAST-Pol. In *Society of Photo-Optical Instrumentation Engineers (SPIE) Conference Series*, volume 7020 of *Proceedings of SPIE*, August 2008. doi: 10.1117/12.788413.

G. Marsden, P. A. R. Ade, J. J. Bock, E. L. Chapin, M. J. Devlin, S. R. Dicker, M. Griffin, J. O. Gundersen, M. Halpern, P. C. Hargrave, D. H. Hughes, J. Klein, P. Mauskopf, B. Magnelli, L. Moncelsi, C. B. Netterfield, H. Ngo, L. Olmi, E. Pascale, G. Patanchon, M. Rex, D. Scott, C. Semisch, N. Thomas, M. D. P. Truch,

C. Tucker, G. S. Tucker, M. P. Viero, and D. V. Wiebe. BLAST: Resolving the Cosmic Submillimeter Background. *ApJ*, 707:1729–1739, December 2009. doi: 10.1088/0004-637X/707/2/1729.

M. Matsuo, J. Ieda, and S. maekawa. Mechanical generation of spin current. *Frontiers in Physics*, 3:54, July 2015. doi: 10.3389/fphy.2015.00054.

B. C. Matthews, C. A. McPhee, L. M. Fissel, and R. L. Curran. The Legacy of SCUPOL: 850 μm Imaging Polarimetry from 1997 to 2005. *ApJS*, 182:143–204, May 2009. doi: 10.1088/0067-0049/182/1/143.

T. G. Matthews, P. A. R. Ade, F. E. Angilè, S. J. Benton, E. L. Chapin, N. L. Chapman, M. J. Devlin, L. M. Fissel, Y. Fukui, N. N. Gandilo, J. O. Gunderson, J. Hargrave, P. C.and Klein, A. L. Korotkov, L. Moncelsi, Mroczkowski T. K., C. B. Netterfield, G. Novak, L. Nutter, D. Olmi, E. Pascale, F. Poidevin, G. Savini, D. Scott, J. A. Shariff, J. D. Soler, K. Tachihara, N. E. Thomas, M. D. P. Truch, C. E. Tucker, G. S. Tucker, and D. Ward-Thompson. Lupus I Observations from the 2010 Flight of the Balloon-borne Large Aperture Submillimeter Telescope for Polarimetry. *ApJ*, 784:822–833, March 2014. doi: ?

B. A. Mazin. *Microwave kinetic inductance detectors*. PhD thesis, California Institute of Technology, California, USA, November 2005.

S. McHugh, B. A. Mazin, B. Serfass, S. Meeker, K. O'Brien, R. Duan, R. Raffanti, and D. Werthimer. A readout for large arrays of microwave kinetic inductance detectors. *Review of Scientific Instruments*, 83(4):044702, April 2012. doi: 10.1063/1.3700812.

C. F. McKee and E. C. Ostriker. Theory of Star Formation. *ARA&A*, 45:565–687, September 2007. doi: 10.1146/annurev.astro.45.051806.110602.

C. M. McKenney, P. Ade, F. E. Angilè, P. A. Ashton, J. A. Austermann, J. A.

Beall, D. Becker, G. Che, H. M. Cho, M. Devlin, B. Dober, S. M. Duff, N. Galitzki, J. Gao, C. Groppi, G. C. Hilton, J. Hubmayr, K. D. Irwin, C. M. McKenney, D. Li, N. Lourie, P. Mauskopf, M. R. Vissers, and Y. Wang. MKID detector development for large scale far-infrared arrays. In *Millimeter, Submillimeter, and Far-Infrared Detectors and Instrumentation for Astronomy VIII*, volume 9914 of *Presented at the Society of Photo-Optical Instrumentation Engineers (SPIE) Conference*, June 2016.

S. Miller, R. Fesen, L. Hillenbrand, and J Rhodes. Airships: A New Horizon for Science. Technical report, The Keck Institute for Space Studies, February 2014.

L. Moncelsi. *BLAST: studying cosmic and Galactic star formation from a stratospheric balloon.* PhD thesis, Cardiff University, UK, URL: http://orca.cf.ac.uk/13144/, 2011.

L. Moncelsi, P. A. R. Ade, F. E. Angilè, S. J. Benton, M. J. Devlin, L. M. Fissel, N. N. Gandilo, J. O. Gundersen, T. G. Matthews, C. B. Netterfield, G. Novak, D. Nutter, E. Pascale, F. Poidevin, G. Savini, D. Scott, J. D. Soler, L. D. Spencer, M. D. P. Truch, G. S. Tucker, and J. Zhang. Empirical modelling of the BLASTPol achromatic half-wave plate for precision submillimetre polarimetry. *MNRAS*, 437: 2772–2789, January 2014. doi: 10.1093/mnras/stt2090.

T. Nagai, S.-i. Inutsuka, and S. M. Miyama. An Origin of Filamentary Structure in Molecular Clouds. *ApJ*, 506:306–322, October 1998. doi: 10.1086/306249.

F. Nakamura and Z.-Y. Li. Magnetically Regulated Star Formation in Three Dimensions: The Case of the Taurus Molecular Cloud Complex. *ApJ*, 687:354-375, November 2008. doi: 10.1086/591641.

F. Nakamura and Z.-Y. Li. Clustered Star Formation in Magnetic Clouds: Properties

of Dense Cores Formed in Outflow-driven Turbulence. *ApJ*, 740:36, October 2011. doi: 10.1088/0004-637X/740/1/36.

C. B. Netterfield, P. A. R. Ade, J. J. Bock, E. L. Chapin, M. J. Devlin, M. Griffin, J. O. Gundersen, M. Halpern, P. C. Hargrave, D. H. Hughes, J. Klein, G. Marsden, P. G. Martin, P. Mauskopf, L. Olmi, E. Pascale, G. Patanchon, M. Rex, A. Roy, D. Scott, C. Semisch, N. Thomas, M. D. P. Truch, C. Tucker, G. S. Tucker, M. P. Viero, and D. V. Wiebe. BLAST: The Mass Function, Lifetimes, and Properties of Intermediate Mass Cores from a 50 deg^2 Submillimeter Galactic Survey in Vela $\ell \approx 265$deg). *ApJ*, 707:1824–1835, December 2009. doi: 10.1088/0004-637X/707/2/1824.

G. Novak, D. P. Gonatas, R. H. Hildebrand, and S. R. Platt. A 100-micron polarimeter for the Kuiper Airborne Observatory. *PASP*, 101:215–224, February 1989. doi: 10.1086/132425.

D. Nutter and D. Ward-Thompson. A SCUBA survey of Orion - the low-mass end of the core mass function. *MNRAS*, 374:1413–1420, February 2007. doi: 10.1111/j.1365-2966.2006.11246.x.

R. W. Ogburn, IV, P. A. R. Ade, R. W. Aikin, M. Amiri, S. J. Benton, J. J. Bock, J. A. Bonetti, J. A. Brevik, B. Burger, C. D. Dowell, L. Duband, J. P. Filippini, S. R. Golwala, M. Halpern, M. Hasselfield, G. Hilton, V. V. Hristov, K. Irwin, J. P. Kaufman, B. G. Keating, J. M. Kovac, C. L. Kuo, A. E. Lange, E. M. Leitch, C. B. Netterfield, H. T. Nguyen, A. Orlando, C. L. Pryke, C. Reintsema, S. Richter, J. E. Ruhl, M. C. Runyan, C. D. Sheehy, Z. K. Staniszewski, S. A. Stokes, R. V. Sudiwala, G. P. Teply, J. E. Tolan, A. D. Turner, P. Wilson, and C. L. Wong. The BICEP2 CMB polarization experiment. In *Society of Photo-Optical Instrumentation Engineers (SPIE) Conference Series*, volume 7741 of *Society of*

Photo-Optical Instrumentation Engineers (SPIE) Conference Series, July 2010. doi: 10.1117/12.857864.

P. Oxley, P. A. Ade, C. Baccigalupi, P. deBernardis, H.-M. Cho, M. J. Devlin, S. Hanany, B. R. Johnson, T. Jones, A. T. Lee, T. Matsumura, A. D. Miller, M. Milligan, T. Renbarger, H. G. Spieler, R. Stompor, G. S. Tucker, and M. Zaldarriaga. The EBEX experiment. In M. Strojnik, editor, *Infrared Spaceborne Remote Sensing XII*, volume 5543 of *Society of Photo-Optical Instrumentation Engineers (SPIE) Conference Series*, pages 320–331, November 2004. doi: 10.1117/12.563447.

P. Palmeirim, P. André, J. Kirk, D. Ward-Thompson, D. Arzoumanian, V. Könyves, P. Didelon, N. Schneider, M. Benedettini, S. Bontemps, J. Di Francesco, D. Elia, M. Griffin, M. Hennemann, T. Hill, P. G. Martin, A. Men'shchikov, S. Molinari, F. Motte, Q. Nguyen Luong, D. Nutter, N. Peretto, S. Pezzuto, A. Roy, K. L. J. Rygl, L. Spinoglio, and G. L. White. Herschel view of the Taurus B211/3 filament and striations: evidence of filamentary growth? *A&A*, 550:A38, February 2013. doi: 10.1051/0004-6361/201220500.

Parker Hannifin Corporation. Parker o-ring handbook - ord 5700, 2007.

E. Pascale, P. A. R. Ade, J. J. Bock, E. L. Chapin, J. Chung, M. J. Devlin, S. Dicker, M. Griffin, J. O. Gundersen, M. Halpern, P. C. Hargrave, D. H. Hughes, J. Klein, C. J. MacTavish, G. Marsden, P. G. Martin, T. G. Martin, P. Mauskopf, C. B. Netterfield, L. Olmi, G. Patanchon, M. Rex, D. Scott, C. Semisch, N. Thomas, M. D. P. Truch, C. Tucker, G. S. Tucker, M. P. Viero, and D. V. Wiebe. The Balloon-borne Large Aperture Submillimeter Telescope: BLAST. *ApJ*, 681:400–414, July 2008. doi: 10.1086/588541.

E. Pascale, P. A. R. Ade, J. J. Bock, E. L. Chapin, M. J. Devlin, S. Dye, S. A. Eales, M. Griffin, J. O. Gundersen, M. Halpern, P. C. Hargrave, D. H. Hughes,

J. Klein, G. Marsden, P. Mauskopf, L. Moncelsi, H. Ngo, C. B. Netterfield, L. Olmi, G. Patanchon, M. Rex, D. Scott, C. Semisch, N. Thomas, M. D. P. Truch, C. Tucker, G. S. Tucker, M. P. Viero, and D. V. Wiebe. BLAST: A Far-Infrared Measurement of the History of Star Formation. *ApJ*, 707:1740–1749, December 2009. doi: 10.1088/0004-637X/707/2/1740.

E. Pascale, P. A. R. Ade, F. E. Angilè, S. J. Benton, E. L. Chapin, M. J. Devlin, L. M. Fissel, N. N. Gandilo, J. O. Gundersen, P. C. Hargrave, D. H. Hughes, J. Klein, A. L. Korotkov, G. Marsden, T. G. Matthews, L. Moncelsi, T. K. Mroczkowski, C. B. Netterfield, G. Novak, L. Olmi, G. Savini, D. Scott, J. A. Shariff, J. D. Soler, N. E. Thomas, M. D. P. Truch, C. E. Tucker, G. S. Tucker, D. Ward-Thompson, and D. V. Wiebe. The balloon-borne large-aperture submillimeter telescope for polarimetry - BLASTPol: performance and results from the 2010 Antarctic flight. In *Society of Photo-Optical Instrumentation Engineers (SPIE) Conference Series*, Proceedings of SPIE, 2012.

G. Patanchon, P. A. R. Ade, J. J. Bock, E. L. Chapin, M. J. Devlin, S. R. Dicker, M. Griffin, J. O. Gundersen, M. Halpern, P. C. Hargrave, D. H. Hughes, J. Klein, G. Marsden, P. Mauskopf, L. Moncelsi, C. B. Netterfield, L. Olmi, E. Pascale, M. Rex, D. Scott, C. Semisch, N. Thomas, M. D. P. Truch, C. Tucker, G. S. Tucker, M. P. Viero, and D. V. Wiebe. Submillimeter Number Counts from Statistical Analysis of BLAST Maps. *ApJ*, 707:1750–1765, December 2009. doi: 10.1088/0004-637X/707/2/1750.

G. Pisano, P. Hargrave, M. Griffin, P. Collins, J. Beeman, and R. Hermoso. Thermal illuminators for far-infrared and submillimeter astronomical instruments. *Appl. Opt.*, 44:3208–3217, June 2005. doi: 10.1364/AO.44.003208.

G. Pisano, M. W. Ng, V. Haynes, and B. Maffei. A Broadband Metal-Mesh Half-Wave

Plate for Millimetre Wave Linear Polarisation Rotation. *Progress In Electromagnetics Research M*, 25:101–114, August 2012.

G. Pisano, B. Maffei, M. W. Ng, V. Haynes, M. Brown, F. Noviello, P. de Bernardis, S. Masi, F. Piacentini, L. Pagano, M. Salatino, B. Ellison, M. Henry, P. de Maagt, and B. Shortt. Development of large radii half-wave plates for CMB satellite missions. In *Millimeter, Submillimeter, and Far-Infrared Detectors and Instrumentation for Astronomy VII*, volume 9153 of *Proc. SPIE*, page 915317, July 2014. doi: 10.1117/12.2056380.

Planck Collaboration, P. A. R. Ade, N. Aghanim, D. Alina, M. I. R. Alves, C. Armitage-Caplan, M. Arnaud, D. Arzoumanian, M. Ashdown, F. Atrio-Barandela, and et al. Planck intermediate results. XIX. An overview of the polarized thermal emission from Galactic dust. *A&A*, 576:A104, April 2015. doi: 10.1051/0004-6361/201424082.

Planck Collaboration, P. A. R. Ade, N. Aghanim, M. I. R. Alves, M. Arnaud, D. Arzoumanian, M. Ashdown, J. Aumont, C. Baccigalupi, A. J. Banday, R. B. Barreiro, N. Bartolo, E. Battaner, K. Benabed, A. Benoît, A. Benoit-Lévy, J.-P. Bernard, M. Bersanelli, P. Bielewicz, J. J. Bock, L. Bonavera, J. R. Bond, J. Borrill, F. R. Bouchet, F. Boulanger, A. Bracco, C. Burigana, E. Calabrese, J.-F. Cardoso, A. Catalano, H. C. Chiang, P. R. Christensen, L. P. L. Colombo, C. Combet, F. Couchot, B. P. Crill, A. Curto, F. Cuttaia, L. Danese, R. D. Davies, R. J. Davis, P. de Bernardis, A. de Rosa, G. de Zotti, J. Delabrouille, C. Dickinson, J. M. Diego, H. Dole, S. Donzelli, O. Doré, M. Douspis, A. Ducout, X. Dupac, G. Efstathiou, F. Elsner, T. A. Enßlin, H. K. Eriksen, D. Falceta-Gonçalves, E. Falgarone, K. Ferrière, F. Finelli, O. Forni, M. Frailis, A. A. Fraisse, E. Franceschi, A. Frejsel, S. Galeotta, S. Galli, K. Ganga, T. Ghosh, M. Giard, E. Gjerløw, J. González-Nuevo, K. M. Górski, A. Gregorio, A. Gruppuso, J. E. Gudmundsson, V. Guil-

let, D. L. Harrison, G. Helou, P. Hennebelle, S. Henrot-Versillé, C. Hernández-Monteagudo, D. Herranz, S. R. Hildebrandt, E. Hivon, W. A. Holmes, A. Hornstrup, K. M. Huffenberger, G. Hurier, A. H. Jaffe, T. R. Jaffe, W. C. Jones, M. Juvela, E. Keihänen, R. Keskitalo, T. S. Kisner, J. Knoche, M. Kunz, H. Kurki-Suonio, G. Lagache, J.-M. Lamarre, A. Lasenby, M. Lattanzi, C. R. Lawrence, R. Leonardi, F. Levrier, M. Liguori, P. B. Lilje, M. Linden-Vørnle, M. López-Caniego, P. M. Lubin, J. F. Macías-Pérez, D. Maino, N. Mandolesi, A. Mangilli, M. Maris, P. G. Martin, E. Martínez-González, S. Masi, S. Matarrese, A. Melchiorri, L. Mendes, A. Mennella, M. Migliaccio, M.-A. Miville-Deschênes, A. Moneti, L. Montier, G. Morgante, D. Mortlock, D. Munshi, J. A. Murphy, P. Naselsky, F. Nati, C. B. Netterfield, F. Noviello, D. Novikov, I. Novikov, N. Oppermann, C. A. Oxborrow, L. Pagano, F. Pajot, R. Paladini, D. Paoletti, F. Pasian, L. Perotto, V. Pettorino, F. Piacentini, M. Piat, E. Pierpaoli, D. Pietrobon, S. Plaszczynski, E. Pointecouteau, G. Polenta, N. Ponthieu, G. W. Pratt, S. Prunet, J.-L. Puget, J. P. Rachen, M. Reinecke, M. Remazeilles, C. Renault, A. Renzi, I. Ristorcelli, G. Rocha, M. Rossetti, G. Roudier, J. A. Rubiño-Martín, B. Rusholme, M. Sandri, D. Santos, M. Savelainen, G. Savini, D. Scott, J. D. Soler, V. Stolyarov, R. Sudiwala, D. Sutton, A.-S. Suur-Uski, J.-F. Sygnet, J. A. Tauber, L. Terenzi, L. Toffolatti, M. Tomasi, M. Tristram, M. Tucci, G. Umana, L. Valenziano, J. Valiviita, B. Van Tent, P. Vielva, F. Villa, L. A. Wade, B. D. Wandelt, I. K. Wehus, N. Ysard, D. Yvon, and A. Zonca. Planck intermediate results. XXXV. Probing the role of the magnetic field in the formation of structure in molecular clouds. *A&A*, 586: A138, February 2016. doi: 10.1051/0004-6361/201525896.

S. Plaszczynski, L. Montier, F. Levrier, and M. Tristram. A novel estimator of the polarization amplitude from normally distributed Stokes parameters. *MNRAS*, 439: 4048–4056, April 2014. doi: 10.1093/mnras/stu270.

P. D. Potter. A New Horn Antenna with Suppressed Sidelobes and Equal Beamwidths. *Microwave Journal*, pages 71–78, June 1963.

E. M. Purcell. Suprathermal rotation of interstellar grains. *ApJ*, 231:404–416, July 1979. doi: 10.1086/157204.

A. S. Rahlin, P. A. R. Ade, M. Amiri, S. J. Benton, J. J. Bock, J. R. Bond, S. A. Bryan, H. C. Chiang, C. R. Contaldi, B. P. Crill, O. P. Doré, M. Farhang, J. P. Filippini, L. M. Fissel, A. A. Fraisse, A. E. Gambrel, N. N. Gandilo, S. Golwala, J. E. Gudmundsson, M. Halpern, M. F. Hasselfield, G. C. Hilton, W. A. Holmes, V. V. Hristov, K. D. Irwin, W. C. Jones, Z. D. Kermish, C. L. Kuo, C. J. MacTavish, P. V. Mason, K. G. Megerian, L. Moncelsi, T. A. Morford, J. M. Nagy, C. B. Netterfield, C. D. Reintsema, J. E. Ruhl, M. C. Runyan, J. A. Shariff, J. D. Soler, A. Trangsrud, C. E. Tucker, R. S. Tucker, A. D. Turner, A. C. Weber, D. V. Wiebe, and E. Y. Young. Pre-flight integration and characterization of the SPIDER balloon-borne telescope. In *Millimeter, Submillimeter, and Far-Infrared Detectors and Instrumentation for Astronomy VII*, volume 9153 of *Presented at the Society of Photo-Optical Instrumentation Engineers (SPIE) Conference*, June 2014.

D. Rebolledo, M. Burton, A. Green, C. Braiding, S. Molinari, G. Wong, R. Blackwell, D. Elia, and E. Schisano. The Carina Nebula and Gum 31 molecular complex - I. Molecular gas distribution, column densities, and dust temperatures. *MNRAS*, 456:2406–2424, March 2016. doi: 10.1093/mnras/stv2776.

M. Rex, E. Chapin, M. J. Devlin, J. Gundersen, J. Klein, E. Pascale, and D. Wiebe. BLAST autonomous daytime star cameras. In *Society of Photo-Optical Instrumentation Engineers (SPIE) Conference Series*, volume 6269 of *Proceedings of SPIE*, July 2006. doi: 10.1117/12.671965.

W. G. Roberge. Alignment of Interstellar Dust. In A. N. Witt, G. C. Clayton, and

B. T. Draine, editors, *Astrophysics of Dust*, volume 309 of *Astronomical Society of the Pacific Conference Series*, page 467, May 2004.

H. Roussel. Scanamorphos: A Map-making Software for Herschel and Similar Scanning Bolometer Arrays. *PASP*, 125:1126–1163, September 2013. doi: 10.1086/673310.

B. Rownd, J. J. Bock, G. Chattopadhyay, J. Glenn, and M. J. Griffin. Design and performance of feedhorn-coupled bolometer arrays for SPIRE. In *Society of Photo-Optical Instrumentation Engineers (SPIE) Conference Series*, volume 4855 of *Proceedings of SPIE*, pages 510–519, February 2003. doi: 10.1117/12.459372.

P. R. Schwartz. The spectral dependence of dust emissivity at millimeter wavelengths. *ApJ*, 252:589–593, January 1982. doi: 10.1086/159585.

K. Serkowski, D. S. Mathewson, and V. L. Ford. Wavelength dependence of interstellar polarization and ratio of total to selective extinction. *ApJ*, 196:261–290, February 1975. doi: 10.1086/153410.

Q. S. Shu. Systematic study to reduce the effects of cracks in multilayer insulation Part 1: theoretical model. *Cryogenics*, 27:249–256, 1987. doi: 10.1016/0011-2275(87)90031-2.

Q. S. Shu, R. W. Fast, and H. L. Hart. Systematic study to reduce the effects of cracks in multilayer insulation Part 2: experimental results. *Cryogenics*, 27:298–311, 1987. doi: 10.1016/0011-2275(87)90059-2.

Q. S. Shu, R. W. Fast, and H. L. Hart. *Advances in Cryogenic Engineering*, chapter Theory and Technique for Reducing the Effect of Cracks in Multilayer Insulation from Room Temperature to 77 K, pages 291–298. Springer US, Boston, MA, 1988.

ISBN 978-1-4613-9874-5. doi: 10.1007/978-1-4613-9874-5_36. URL http://dx.doi.org/10.1007/978-1-4613-9874-5_36.

Q.S. Shu, R.W. Fast, and H.L. Hart. Heat flux from 277 to 77 k through a few layers of multilayer insulation. *Cryogenics*, 26(12):671 – 677, 1986. ISSN 0011-2275. doi: http://dx.doi.org/10.1016/0011-2275(86)90167-0. URL http://www.sciencedirect.com/science/article/pii/0011227586901670.

K. M. Smith, A. Cooray, S. Das, O. Doré, D. Hanson, C. Hirata, M. Kaplinghat, B. Keating, M. Loverde, N. Miller, G. Rocha, M. Shimon, and O. Zahn. Gravitational Lensing. In S. Dodelson, D. Baumann, A. Cooray, J. Dunkley, A. Fraisse, M. G. Jackson, A. Kogut, L. Krauss, M. Zaldarriaga, and K. Smith, editors, *American Institute of Physics Conference Series*, volume 1141 of *American Institute of Physics Conference Series*, pages 121–178, June 2009. doi: 10.1063/1.3160886.

J. D. Soler, P. Hennebelle, P. G. Martin, M.-A. Miville-Deschênes, C. B. Netterfield, and L. M. Fissel. An Imprint of Molecular Cloud Magnetization in the Morphology of the Dust Polarized Emission. *ApJ*, 774:128, September 2013. doi: 10.1088/0004-637X/774/2/128.

J. D. Soler, P. A. R. Ade, F. E. Angilè, S. J. Benton, M. J. Devlin, B. Dober, L. M. Fissel, Y. Fukui, N. Galitzki, N. N. Gandilo, J. Klein, A. L. Korotkov, T. G. Matthews, L. Moncelsi, T. K. Mroczkowski, C. B. Netterfield, D. Nutter, G. Novak, E. Pascale, F. Poidevin, G. Savini, D. Scott, J. A. Shariff, N. E. Thomas, M. D. P. Truch, C. E. Tucker, G. S. Tucker, and D. Ward-Thompson. Thermal Design and Performance of the Balloon-borne Large Aperture Telescope for Polarimetry BLASTPol. In *Ground-based and Airborne Telescopes V*, volume 9145 of *Presented at the Society of Photo-Optical Instrumentation Engineers (SPIE) Conference*, June 2014.

Z. Staniszewski, R. W. Aikin, M. Amiri, S. J. Benton, C. Bischoff, J. J. Bock, J. A. Bonetti, J. A. Brevik, B. Burger, C. D. Dowell, L. Duband, J. P. Filippini, S. R. Golwala, M. Halpern, M. Hasselfield, G. Hilton, V. V. Hristov, K. Irwin, J. M. Kovac, C. L. Kuo, M. Lueker, T. Montroy, H. T. Nguyen, R. W. Ogburn, R. O'Brient, A. Orlando, C. Pryke, C. Reintsema, J. E. Ruhl, R. Schwarz, C. Sheehy, S. Stokes, K. L. Thompson, G. Teply, J. E. Tolan, A. D. Turner, A. G. Vieregg, P. Wilson, D. Wiebe, and C. L. Wong. The Keck Array: A Multi Camera CMB Polarimeter at the South Pole. *Journal of Low Temperature Physics*, 167:827–833, June 2012. doi: 10.1007/s10909-012-0510-1.

W. Stein. Infrared Radiation from Interstellar Grains. *ApJ*, 144:318, April 1966. doi: 10.1086/148606.

L. D. Stimpson and W. Jaworski. Effects of overlaps, stitches, and patches on multilayer insulation. In *American Institute of Aeronautics and Astronautics, Thermophysics Conference*, American Institute of Aeronautics and Astronautics, Thermophysics Conference, 1972.

D. S. Swetz, P. A. R. Ade, M. Amiri, J. W. Appel, E. S. Battistelli, B. Burger, J. Chervenak, M. J. Devlin, S. R. Dicker, W. B. Doriese, R. Dünner, T. Essinger-Hileman, R. P. Fisher, J. W. Fowler, M. Halpern, M. Hasselfield, G. C. Hilton, A. D. Hincks, K. D. Irwin, N. Jarosik, M. Kaul, J. Klein, J. M. Lau, M. Limon, T. A. Marriage, D. Marsden, K. Martocci, P. Mauskopf, H. Moseley, C. B. Netterfield, M. D. Niemack, M. R. Nolta, L. A. Page, L. Parker, S. T. Staggs, O. Stryzak, E. R. Switzer, R. Thornton, C. Tucker, E. Wollack, and Y. Zhao. Overview of the Atacama Cosmology Telescope: Receiver, Instrumentation, and Telescope Systems. *ApJS*, 194:41, June 2011. doi: 10.1088/0067-0049/194/2/41.

F. S. Tabatabaei, J. Braine, E. M. Xilouris, C. Kramer, M. Boquien, F. Combes,

C. Henkel, M. Relano, S. Verley, P. Gratier, F. Israel, M. C. Wiedner, M. Röllig, K. F. Schuster, and P. van der Werf. Variation in the dust emissivity index across M 33 with Herschel and Spitzer (HerM 33es). *A&A*, 561:A95, January 2014. doi: 10.1051/0004-6361/201321441.

B.-K. Tan, J. Leech, G. Yassin, P. Kittara, M. Tacon, S. Wangsuya, and C. Groppi. A High Performance 700 GHz Feed Horn. *Journal of Infrared, Millimeter, and Terahertz Waves, Volume 33, Issue 1, pp.1-5*, 33:1–5, January 2012. doi: 10.1007/s10762-011-9845-y.

M. D. P. Truch. *The balloon-borne large aperture submillimeter telescope*. PhD thesis, Brown University, 2007.

M. D. P. Truch, P. A. R. Ade, J. J. Bock, E. L. Chapin, M. J. Devlin, S. R. Dicker, M. Griffin, J. O. Gundersen, M. Halpern, P. C. Hargrave, D. H. Hughes, J. Klein, G. Marsden, P. G. Martin, P. Mauskopf, L. Moncelsi, C. Barth Netterfield, L. Olmi, E. Pascale, G. Patanchon, M. Rex, D. Scott, C. Semisch, N. E. Thomas, C. Tucker, G. S. Tucker, M. P. Viero, and D. V. Wiebe. The Balloon-borne Large Aperture Submillimeter Telescope (BLAST) 2006: Calibration and Flight Performance. *ApJ*, 707:1723–1728, December 2009. doi: 10.1088/0004-637X/707/2/1723.

J. E. Vaillancourt, C. D. Dowell, R. H. Hildebrand, L. Kirby, M. M. Krejny, H.-b. Li, G. Novak, M. Houde, H. Shinnaga, and M. Attard. New Results on the Submillimeter Polarization Spectrum of the Orion Molecular Cloud. *ApJ*, 679:L25, May 2008. doi: 10.1086/589152.

I. Valtchanov. The Spectral and Photometric Imaging Receiver (SPIRE) Handbook. `http://herschel.esac.esa.int/Docs/SPIRE/html/spire_om.html`, March 2014.

E. Vázquez-Semadeni, D. Ryu, T. Passot, R. F. González, and A. Gazol. Molecular Cloud Evolution. I. Molecular Cloud and Thin Cold Neutral Medium Sheet Formation. *ApJ*, 643:245–259, May 2006. doi: 10.1086/502710.

M. P. Viero, P. A. R. Ade, J. J. Bock, E. L. Chapin, M. J. Devlin, M. Griffin, J. O. Gundersen, M. Halpern, P. C. Hargrave, D. H. Hughes, J. Klein, C. J. Mac Tavish, G. Marsden, P. G. Martin, P. Mauskopf, L. Moncelsi, M. Negrello, C. B. Netterfield, L. Olmi, E. Pascale, G. Patanchon, M. Rex, D. Scott, C. Semisch, N. Thomas, M. D. P. Truch, C. Tucker, G. S. Tucker, and D. V. Wiebe. BLAST: Correlations in the Cosmic Far-Infrared Background at 250, 350, and 500 μm Reveal Clustering of Star-forming Galaxies. *ApJ*, 707:1766–1778, December 2009. doi: 10.1088/0004-637X/707/2/1766.

D. Ward-Thompson, J. M. Kirk, R. M. Crutcher, J. S. Greaves, W. S. Holland, and P. André. First Observations of the Magnetic Field Geometry in Prestellar Cores. *ApJ*, 537:L135–L138, July 2000. doi: 10.1086/312764.

D. Ward-Thompson, A. K. Sen, J. M. Kirk, and D. Nutter. Optical and submillimetre observations of Bok globules - tracing the magnetic field from low to high density. *MNRAS*, 398:394–400, September 2009. doi: 10.1111/j.1365-2966.2009.15159.x.

D. Werthimer. The casper collaboration for high-performance open source digital radio astronomy instrumentation. In *General Assembly and Scientific Symposium, 2011 XXXth URSI*, pages 1–4, Aug 2011. doi: 10.1109/URSIGASS.2011.6051282.

D. C. B. Whittet, P. G. Martin, J. H. Hough, M. F. Rouse, J. A. Bailey, and D. J. Axon. Systematic variations in the wavelength dependence of interstellar linear polarization. *ApJ*, 386:562–577, February 1992. doi: 10.1086/171039.

D. V. Wiebe. *BLAST: A balloon-borne, large-aperture, submillimetre telescope*. PhD thesis, University of Toronto, Canada, 2008.

D. V. Wiebe, P. A. R. Ade, J. J. Bock, E. L. Chapin, M. J. Devlin, S. Dicker, M. Griffin, J. O. Gundersen, M. Halpern, P. C. Hargrave, D. H. Hughes, J. Klein, G. Marsden, P. G. Martin, P. Mauskopf, C. B. Netterfield, L. Olmi, E. Pascale, G. Patanchon, M. Rex, D. Scott, C. Semisch, N. Thomas, M. D. P. Truch, C. Tucker, G. S. Tucker, and M. P. Viero. BLAST Observations of Resolved Galaxies: Temperature Profiles and the Effect of Active Galactic Nuclei on FIR to Submillimeter Emission. *ApJ*, 707:1809–1823, December 2009. doi: 10.1088/0004-637X/707/2/1809.

J. Zhang, P. A. R. Ade, P. Mauskopf, L. Moncelsi, G. Savini, and N. Whitehouse. New artificial dielectric metamaterial and its application as a terahertz antireflection coating. *Appl. Opt.*, 48:6635–+, December 2009. doi: 10.1364/AO.48.006635.